Investigating Disk-Jet Structure around Supermassive Black Hole through Polarization Images

Yuh Tsunetoe

Dissertation Adviser: Professor Shin Mineshige

Department of Astronomy, Kyoto University

A thesis submitted for the degree of Doctor of Philosophy

December 2022

This page intentionally left blank.

Abstract

The realization of direct imaging of supermassive black holes has opened up a new horizon for understanding the enigmatic mechanism of magnetically driven jets in active galactic nuclei. In order to investigate the structure of jet and accretion disk close to the black hole, at this opportunity, I present theoretical predictions of polarimetric images in the horizon scale through polarized general relativistic radiative transfer calculation based on fluid model by general relativistic magnetohydrodynamics simulations.

For the M87 jet, I find that linear polarization (LP) vectors by synchrotron emission are scrambled and depolarized by Faraday rotation in outer cold disk. It is also confirmed that circular polarization (CP) components, weak at the emission, are increased due to Faraday conversion in innermost hot disk with ordered magnetic fields. I also predict polarimetric images of Sgr A*, which has no outstanding jet, modifying electron temperature prescription so that the emissions from hot disk suppress those from jets relatively. I point out that CP image show a sign-flipping with a vertical border line, termed as "separatrix". Correspondingly, LP fluxes are bright along the separatrix. These features are due to the dependence of Faraday rotation, which induces Faraday conversion here, on the angle between light path and helical magnetic field line.

Based on the above results, I construct a description of the jet-disk structure near the black hole, consisting of synchrotron-emitting jet, inner Faraday-conversion disk and outer Faraday-rotation disk. As an observational feature of this description, a separation between LP and CP is presented along the jet. That is, the LP intensity is distributed downwards compared to the total intensity, since the image is dominated by the emissions from the downstream of the foreground jet, not passing through the disk and not Faraday-rotated. Meanwhile, the CP intensity is shifted upwards due to the increased components from the upstream, Faraday-converted from LP in inner disk. These results are confirmed to be consistent with exiting LP observations by the Event Horizon Telescope and other global-scale VLBIs. Future high-resolutive linear and circular polarimetric observations will give a stronger constraint on the magnetic and plasma properties. Furthermore, surveying wavelengths and model parameters, I establish a unified description according to the optical thickness for Faraday rotation and conversion, and synchrotron self-absorption. Accumulating both observational and theoretical results will lead to a unified description for a diversity of the active galactic nucleus jets.

Acknowledgement

This doctoral dissertation has been completed with the generous help and support of many researchers, administrative staff, student colleagues, friends and family. Even in a modest way, I would like to express my gratitude to them here.

First of all, I would like to show my greatest appreciation to my supervisor, Prof. Shin Mineshige. He always guided me to the way an astrophysicist should be, and set the examples in every aspect including research discussions, scientific writings, presentations, and documentations. Without his considerable assistance, I would not have been able to carry out the research activities since the final year of my undergraduate. Secondly, I owe a very important debt to Prof. Ken Ohsuga and Tomohisa Kawashima. They fully supported my research from the early stages of the code implementation to the following astrophysics discussions. Through weekly discussions with them, I was able to constantly review the progress of my project and stay motivated in my research. Thirdly, I would like to offer my special thanks to Kazunori Akiyama for discussions based on observational knowledges and frequent warm interactions. He also motivated me for research activities overseas as my career path through his kind and practical advices. In addition, I am deeply grateful to Hiroyuki R. Takahashi and Masanori Nakamura for provision of simulation data sets and stimulating discussions. Their pleasant cooperations have made my researches more fruitful.

I am deeply grateful to all the members of Mineshige-Group and Black Hole Lunch seminar for discussions and knowledge of wide range of fields; Keiichi Maeda, Mami Machida, Norita Kawanaka, Yuta Asahina, Kotaro Moriyama, Misaki Mizumoto, Takumi Ogawa, Eishun Takeo, Mariko Kimura, Yoshihiro Makino, Takaaki Kitaki, Taiki Ogihara, Takumi Ohmura, Haruka Sakemi, Mutsuko Inoguchi, Kazuma Ijima, Haruo Yasuda, Nacho Botella Lasaga, Yasuaki Kohda, Hiroki Okino, Masayuki Furuno, Akihiro Inoue, Aoto Utsumi, Mikiya Takahashi, Erika Ogata, Takuya Mushano, and Shogo Yoshioka. I am also indebt to all the administrative staff members for their daily smooth document processing and paperwork management with patience; Yukiko Nakanishi, Erika Toma, Noriko Itoh, Miyuki Kawamoto, Keiko Ohara and Ayako Nagaoka. I thank all the staff and students of the Department of Astronomy, Kyoto University for the enjoyable and fruitful Ph.D. student life through everyday conversations, parties, trips, and so on.

Further, my deepest appreciation goes to my family, Kaoru, Go, and Raku. Their unceasing devotion and hospitality have always encouraged and inspired me, regardless of the geographi-

cal distance between us. I would not be where I am today without their help. Finally, I sincerely thank all the people who have touched, inspired, and energized me throughout my life.

This dissertation was supported in part by Japan Society for the Promotion of Science (JSPS) Grant-in-Aid for JSPS Research Fellow; Grant Number JP20J22986. Numerical computations and analyses were in part carried out on Cray XC30 “ATERUI”, XC50 “ATERUI II”, and analysis servers at Center for Computational Astrophysics, National Astronomical Observatory of Japan.

Contents

This page intentionally left blank.

Chapter 1

Introduction

1.1 Black Holes

1.1.1 Concepts

Black holes (BH) have attracted a great deal of interest due to their simplicity of description and the variety of phenomena they produce. The origin of the concept of black hole can be traced back to the literatures in the close of the eighteenth century, Michell (1784) and Laplace (1796), in which the authors independently introduced hypothetical massive objects whose escape velocity on their surface exceeds the speed of light, and thus non-luminous.

In 1915, Albert Einstein published the theory of general relativity (GR; Einstein 1915), which predicts that the path of light will follow the curvature of spacetime around a body. A few months later, Karl Schwarzschild found the first exact solution (except the trivial flat spacetime) to the Einstein equations of GR that describes the gravitational field of a static, spherically symmetric, and non-charged body (Schwarzschild 1916). The Schwarzschild solution has the characteristic radius of $r_{\rm S}$ ($\equiv 2GM/c^2$; G is the gravitational constant, c is the speed of light, and M is the mass of the body) demarcating the surface of a black hole, or the *event horizon*, within which no particle or light can escape. An object with a radius lower than or equal to this Schwarzschild radius $r_{\rm S}$ is thought to form a black hole (e.g., $r_{\rm S} \sim 3$ km for the Solar mass $M_\odot$).

Although the Schwarzschild solution has a singularity at $r = r_{\rm S}$, it is an unphysical coordinate singularity that can be removed by proper coordinate transformations (e.g., Lemaître 1933; Kruskal 1960). Thus an observer passing through the event horizon does not feel anything strange and continue to fall inwards, while it can no longer send (but can receive) any information to (from) the outside. Meanwhile, another singularity at $r = 0$ is a true physical singularity at which the spacetime itself, and the "classical" GR description, are no longer well-defined and ultimately break down (see, for example, Misner et al. 1973).

Further, by calculating geodesics equations for a massless particle, a photon capture radius of the Schwarzschild black hole is obtained as $R_{\rm c} = \sqrt{27}\, r_{\rm g}$. This determines whether a photon

approaching from infinity, with an impact parameter b, will escape to infinity ($b > R_{\rm c}$) or plunge into the event horizon ($b < R_c$; Hilbert 1917). Thus, a non-rotating black hole illuminated by background light is observed as a circular silhouette, or the so-called *black hole shadow*, with a diameter of $2\ R_c$. Photons with $b = R_c$ are captured on an unstable circular orbit at $r = 3\ r_{\rm g}$ and rotate around the black hole. If there are radiating matters near the black hole, they produce the "photon ring" bordering the shadow.

In 1963, Roy Kerr discovered another exact solution to the Einstein equations for a stationary, axi-symmetric (thus allowed to rotate), and non-charged body (Kerr 1963). The event horizon of the Kerr black hole is situated at the radius of $r_{\rm H} = r_{\rm g}\ (1 + \sqrt{1 - a^2})$ in the Boyer-Lindquist (BL) coordinates (Boyer & Lindquist 1967; see equation 2.10 in this thesis). Here $r_{\rm g} \equiv GM/c^2 = r_{\rm S}/2$ is the gravitational radius, $a = J/Mc$ is the dimensionless spin parameter, and J is the angular momentum of the black hole.[1] In the case of $a = 0$, it returns back to the Schwarzschild solution. In astrophysical contexts, the spin parameter a must be lower than or equal to 1. Otherwise the solution includes the *naked singularity*, not enveloped with the event horizon. Since the photon capture radius R_c for the Kerr black hole depends on an incidence angle with respect to the spin axis, the shadow of the rotating black hole is not necessarily circular (Bardeen 1973; Chandrasekhar 1983).

In addition to the event horizon, the Kerr black hole has another characteristic, non-spherical region defined with $r_{\rm ergo} \equiv r_{\rm g}\ (1 + \sqrt{1 - a^2 \cos^2\theta})$, within which any physical (time-like) particle cannot be coordinate-stationary and necessarily co-rotate with the black hole. Further, particles entering this region have access to the "negative energy trajectories". Roger Penrose proposed a thought experiment of energy extraction from the rotating black hole, in which a test particle enter into the *ergosphere*,[2] the region of $r_{\rm H} < r < r_{\rm ergo}$, and split into a fragments plunging into the black hole and another escaping away with a gain of positive energy (Penrose & Floyd 1971). Energy extraction mechanisms from a black hole have also been discussed in the contexts of quantum mechanics and electromagnetics (e.g., Hawking 1974; Blandford & Znajek 1977; see also subsection 1.2.2).

Two years after the Kerr black hole, Ezra Newman found the axi-symmetric solution for a rotating and electrically-charged body, and proposed it as the Kerr-Newman solution, a generalization of the Kerr solution (Newman et al. 1965). It has been established by the *no-hair theorem* that all stationary solutions of the Einstein equations are completely characterized by only three independent parameters of mass, spin, and charge (Israel 1967; Carter 1971). In this sense, the Kerr-Newman solution is referred to as the most general solution of a stationary black hole's spacetime.

[1] For example, $a \sim 0.2$ for the Sun.

[2] This is named from the Greek word *ergon* for work, from which a unit of energy "erg" is also derived.

1.1.2 Astrophysics

Since the BH concepts was presented, the question of their existence has been discussed over a long period of time. To the present day, numerous observations supporting black holes have accumulated in various fields, and we are finally approaching conclusive evidences.

In 1931, Subrahmanyan Chandrasekhar discovered an upper limit of mass of white dwarfs, of an electron-degenerate configuration ($\sim 1.4\ M_\odot$; Chandrasekhar 1931), which implies that a sufficiently massive star cannot resist gravitational collapse and must form a black hole. However, this statement was not necessarily accepted by contemporary scientists, who mostly thought of the black hole solutions as mathematical consequences of the Einstein equations rather than astronomical targets (see, for example, Chandrasekhar 1980). After the proposal of neutron stars, which resist gravitational corruption by neutron degeneracy pressure (Baade & Zwicky 1934), their upper limit mass was newly calculated, the Tolman-Oppenheimar-Volkoff (TOV) limit (Tolman 1939; Oppenheimer & Volkoff 1939; nowadays estimated to be $\sim 1.5 - 3.0\ M_\odot$).

In the middle of the twentieth century, when black holes were becoming accepted as another endpoint of stars, other than white dwarfs or neutron stars, the question of how to observe and identify black holes came up for discussion. While a black hole itself do not emit light, matters falling toward it can do it through release of gravitational energy.

As the most fundamental case, Bondi (1952) introduced a spherically symmetric accretion flow. Some researchers established more energy-effective and observation-favored *accretion disk* models (e.g., Lynden-Bell 1969; Shakura & Sunyaev 1973; Novikov & Thorne 1973; Pringle 1981). In the disk, rotating matters gradually fall inwards, losing its angular momentum and heating up due to the turbulent viscosity. As a result, the heated up disk has a temperature gradient and gives rise to a variety of radiations.

To realize mass supply onto a stellar-mass black hole in the universe, the binary systems were proposed in analogy with the cataclysmic variables, the binaries of a white dwarf and a gas-feeding, normal star. In 1960s, coupled with detection of the X-ray binaries, some of them began thought to be candidates of the black hole binaries. Cygnus X-1 was the first widely accepted one due to its X-ray fluctuations in second-scale and the Doppler shift of its companion star's spectrum, both which demonstrated that it weighs beyond the TOV limit and should be a black hole, not a neutron star (Oda et al. 1971; Webster & Murdin 1972; Bolton 1975).

Independently, another subset of black holes, supermassive black holes (SMBH), has found since the later twentieth century. The quasars, at first displayed like peculiar blue stars, have been found to show much higher luminosity at a cosmological distance than normal galaxies (e.g., Schmidt 1963), in addition to their intense variabilities implying far smaller sizes of a radiation source (e.g., Jones et al. 1974). In explaining these extremely bright but compact objects, the accretion disk model onto a SMBH was called upon, and required a SMBH mass

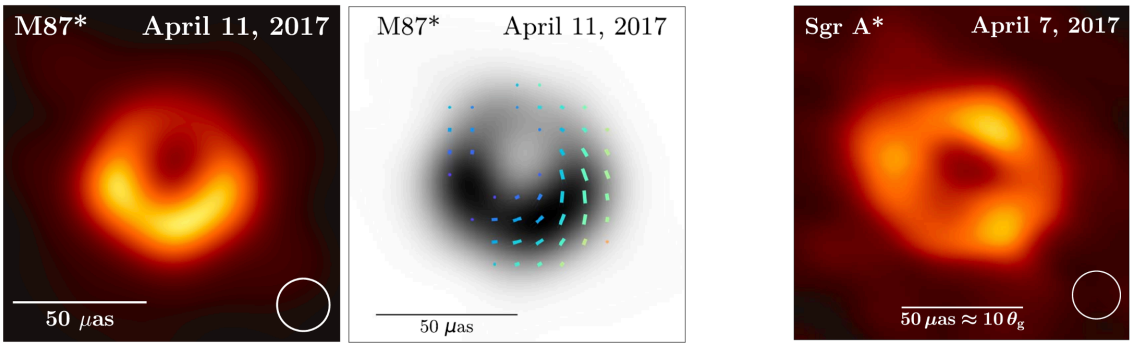

Fig. 1.1: The first images of two SMBHs M87* and Sgr A* obtained by the EHT observation campaigns in 2017. Left: the intensity images of M87* in the center of an elliptical galaxy M87. Center: the linear polarization maps of M87*. Right: the intensity image of Sgr A* in the Galactic center. (Credit: Event Horizon Telescope Collaboration et al. (2019a, 2021a, 2022a))

of roughly $\sim 10^8\ M_\odot$ to match the properties of quasars (Salpeter 1964; Rees 1984).

Through the accretion disk models, it was suggested and has been established that, in addition to quasars, Seyfert galaxies, blazars, and radio galaxies can be interpreted with a unified model of active galactic nuclei (AGN) with different values of the SMBH mass, mass accretion rate, and viewing angle (Lynden-Bell 1969; Barthel 1989; Antonucci 1993; see also subsection 1.2.1). Furthermore, SMBHs have also been found in the center of normal galaxies, including our Milky Way (e.g., Kormendy 1988; Miyoshi et al. 1995; Peterson et al. 1998; Schödel et al. 2002). Today, the mass of SMBHs is known to be distributed in a range of $\sim 10^{5-10}\ M_\odot$. In a range from the stellar-scale to the galactic-scale, one can now say that the existence of black holes is beyond doubt.

In 2016, about a hundred year after the Einstein's GR, LIGO Scientific Collaboration and Virgo Collaboration (2016) reported the first detection of gravitational waves, ripples of space-time predicted by Einstein himself (Einstein 1916). The first event GW150914 matched a merger of two black holes with masses of $\approx 29M_\odot$ and $36M_\odot$ in the waveform, and was also the first observation of a binary black hole merger event.

In 2019, the Event Horizon Telescope (EHT) Collaboration published the first direct images of a SMBH in the center of an elliptical galaxy Messier 87 (M87), the left panel of Figure 1.1 (EHT Collaboration 2019 Paper I). After that, they also presented the linear polarization (LP) maps of the SMBH, referred to as M87* (the central panel; EHT Collaboration 2021 Paper VII), and the images of a SMBH in the Galactic center, Sagittarius (Sgr) A* (the right panel; EHT Collaboration 2022 Paper I). On the images, the SMBH appears in the form of a ring-shaped black hole shadow (see figure 1.2 for a theoretical prediction image) highlighted by radiation from surrounding plasma, which is a consequence of the light bending effects in GR.

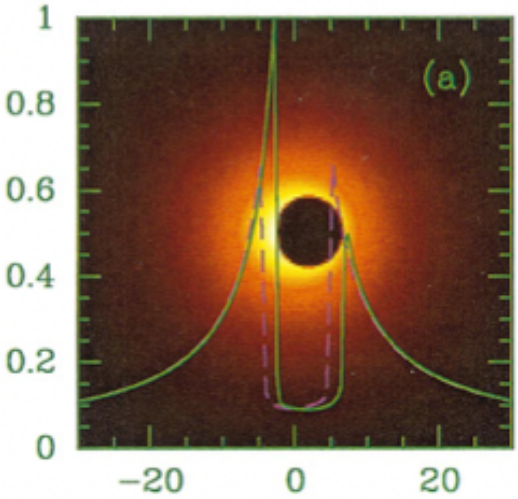

Fig. 1.2: Calculated image of a SMBH and surrounding optically thin, spherical plasma with Sgr A* in mind. Here the spin parameter of the SMBH is $a = 0.998$ and the viewing angle is $i = 45^\circ$ with respect to the BH spin axis. Overlayed are the intensity profiles along the x-axis (solid green) and y-axis (dashed purple). (Credit: Falcke et al. (2000))

1.2 Active Galactic Nuclei

1.2.1 Accretion Flow onto Supermassive Black Holes

As also mentioned above, AGNs have been known to produce energetic phenomena such as intense radiations and powerful outflows (Schmidt 1963; Sanders et al. 1989), and been thought to be driven by a central SMBH onto which matter accretes (Lynden-Bell 1969; Shakura & Sunyaev 1973; Sun & Malkan 1989). Nowadays, observational and theoretical studies have established that AGNs, as much as X-ray binaries, can be categorized into multiple accretion states based on their luminosities (or mass accretion rates) in the Eddington ratio $L/L_{\rm Edd}$ (see Kato et al. 2008 and references therein; see also Ohsuga et al. 2009; Ohsuga & Mineshige 2011 and Figure 1.3 for fluid simulations), although this empirical classification is sometimes ambiguous and can transit each other. Here, the Eddington luminosity

$$L_{\rm Edd} \equiv \frac{4\pi c G M m_{\rm H}}{\sigma_{\rm T}} \approx 1.25 \times 10^{46} \left(\frac{M}{10^8 M_\odot} \right) {\rm erg/s}, \tag{1.1}$$

at which the radiation pressure on ionized hydrogen and gravity of the central object are in equilibrium, and $m_{\rm H}$ and $\sigma_{\rm T}$ are the hydrogen mass and the Thomson scattering cross section, respectively.

For a low luminosity, $L \ll 10^{-2}\ L_{\rm Edd}$, the accretion flow is supposed to be in the advection-dominated state (ADAF; see subsection 1.4.1), which is optically thin and geometrically thick with inefficient radiative cooling effect (see Model C in Figure 1.3). This dim state is related to the low-luminosity AGNs (LLAGN; Ho et al. 1997).

When the luminosity is moderate, $L \sim 0.01 - 0.1\ L_{\rm Edd}$, the flow forms the standard disk as introduced in Shakura & Sunyaev (1973), which is optically thick and geometrically thin (see

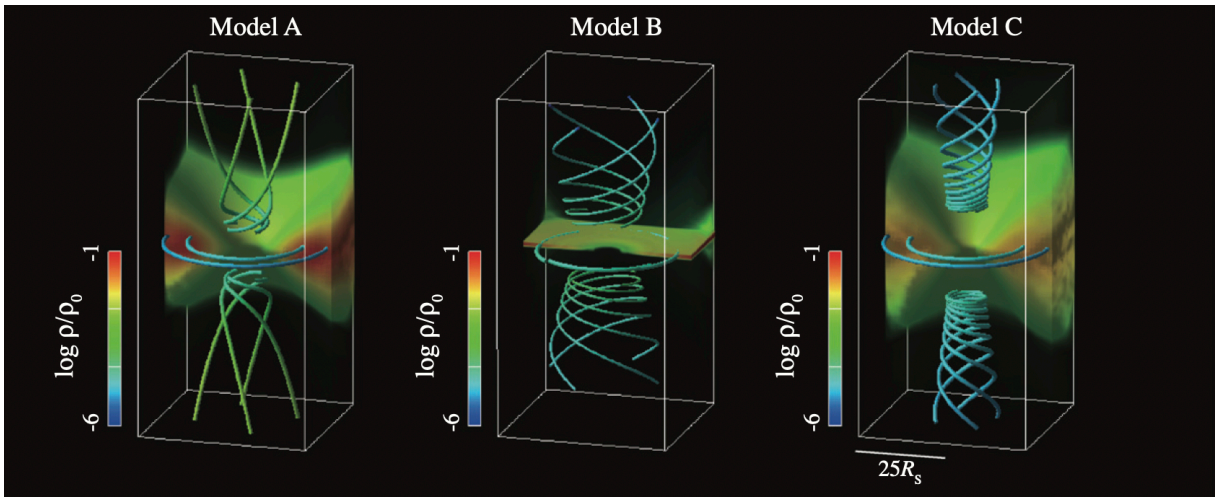

Fig. 1.3: Perspective views of three states of accretion flow obtained from radiation magnetohydrodynamics simulations. The color contours indicate the normalized density distributions, and the streamlines are also overlaid. Model A, B, and C describe the supercritical state, the standard state, and the advection-dominated state, respectively. The (absolute) densities are higher in the order of Model A, B, and C. (Credit: Ohsuga & Mineshige (2011))

Model B in Figure 1.3). The standard state is applied to a range of AGNs such as quasars and Seyfert galaxies.

In the case of a high luminosity, $L \gtrsim L_{\rm Edd}$, the accretion flow is in the radiation-dominant, supercritical (super-Eddington) slim state, which is optically thick and again geometrically thick with the photon trapping effect (see Model A in Figure 1.3). This supercritical state may be related to the narrow-line Seyfert 1 galaxies (NLS1; Osterbrock & Pogge 1985) with a relatively small SMBH mass (e.g., Mineshige et al. 2000; Jin et al. 2017).

1.2.2 Relativistic Jets

In addition, it has been known that a subset of AGNs produce plasma jets. In 1918, Heber Curtis discovered "*a curious straight ray..., apparently connected with the nucleus by a thin line of matter*" in M87 (Curtis 1918), which is today known as the first detection of the jet in the active, giant elliptic galaxy. Since the middle twentieth century, radio interferometry observations have found double lobe structures expanding around the center of galaxies, on a scale of several times the size of host galaxies (e.g., Jennison & Das Gupta 1953 for radio galaxy Cygnus A; Shain 1958 for Centaurus A and Fornax A). With the advent of very long baseline interferometers (VLBI), it has been further revealed that these twin lobes and the nucleus of galaxies are connected with thin, long beam structures, so-called galactic (or AGN) jets (e.g., Perley et al. 1984). In addition, accumulating observations at multi-wavelengths on various size scales have shown that these jets are highly collimated, that is, maintaining their direction and width on a galactic scale, from the base region near the nucleus to the termination in the

intergalactic region (e.g., Bridle & Perley 1984; Zensus 1997; see also Figure 1.4).

Furthermore, VLBI observations have detected the "superluminal motions" of blobs in the AGN jets, which are ejected outwards apparently at beyond the speed of light and often aligned with the jet direction (e.g., Pearson et al. 1981 for quasar 3C 273; Biretta et al. 1995 for M87 jet). These phenomena are understood, coupled with an absent of the receding (background) one of twin jets in the base region, as a consequence of the Doppler beaming effect in observing plasma's motion at a relativistic velocity ($v \sim c$) with a small inclination angle, as predicted in Rees (1966).

Keeping up with the accumulated observational results, theoretical interpretations of the AGN jets have been vigorously discussed. In the early stage of the radio lobes, the "beam model" was suggested, in which relativistic plasmas produced in the nucleus escape in twin opposite directions about the large-scale galactic plane (e.g., Blandford & Rees 1974). The plasmas keep accelerated and collimated by interacting with gas cloud in a mechanism like the De Laval nozzle, and eventually collide with the intergalactic medium to form the observed hot spots. This model was strongly supported by the later detections of thin long jets with VLBI observations. Meanwhile, the essential mechanism of generating relativistic plasmas in the innermost region, and the stability of nozzle-like mechanism were left in discussion.

The two major points in the discussion of the AGN jet mechanism are the acceleration and collimation in the innermost base and nucleus region. Along with the application of accretion disk models to a variety of AGNs (as reviewed in the last subsection), a number of attempts to explain the jets with a system of the SMBH and accretion disk have been suggested.

The thermal-pressure driving models utilize the liberation of thermal gas energy. For example, hot gas in the inner disk can produce intense radiation and heat up the outer disk, to evaporate gas on the surface like the Solar wind ("Compton wind model"; Begelman et al. 1983). However, these are not considered the primary mechanism for the jets because the balance between radiation-heating and gravity, for the gas to escape from the surface, is not accomplished until large radius ($\sim 10^{4-5} r_{\rm g}$), and because of the lack of collimation mechanism. Rather, these scenarios are favored as the mechanism for the expanding, sub-relativistic outflows such as disk winds and coronae, which are thought to be supplementally involved in the jet creation.

The radiation pressure can also be a candidate for the jet-driving mechanism. In the super-Eddington cases (see also the last subsection and Model A in Figure 1.3), plasmas can be accelerated by the radiation force from the disk surface against the gravity of SMBH (e.g., Meier 1979). In these models, the lack of collimation mechanism can be compensated with the geometrically thick accretion flow in the radiation-dominant, supercritical cases (e.g., Abramowicz et al. 1980; Sikora & Wilson 1981). The geometrically thick disk form the funnels around the rotation axis, and radiate tenuous plasmas in the funnel. Due to the axi-symmetry of accretion flow, the plasmas are accelerated outwards in the direction of rotation axis. Meanwhile, the higher the velocity become, the more strongly the plasma are dragged by the radiation itself

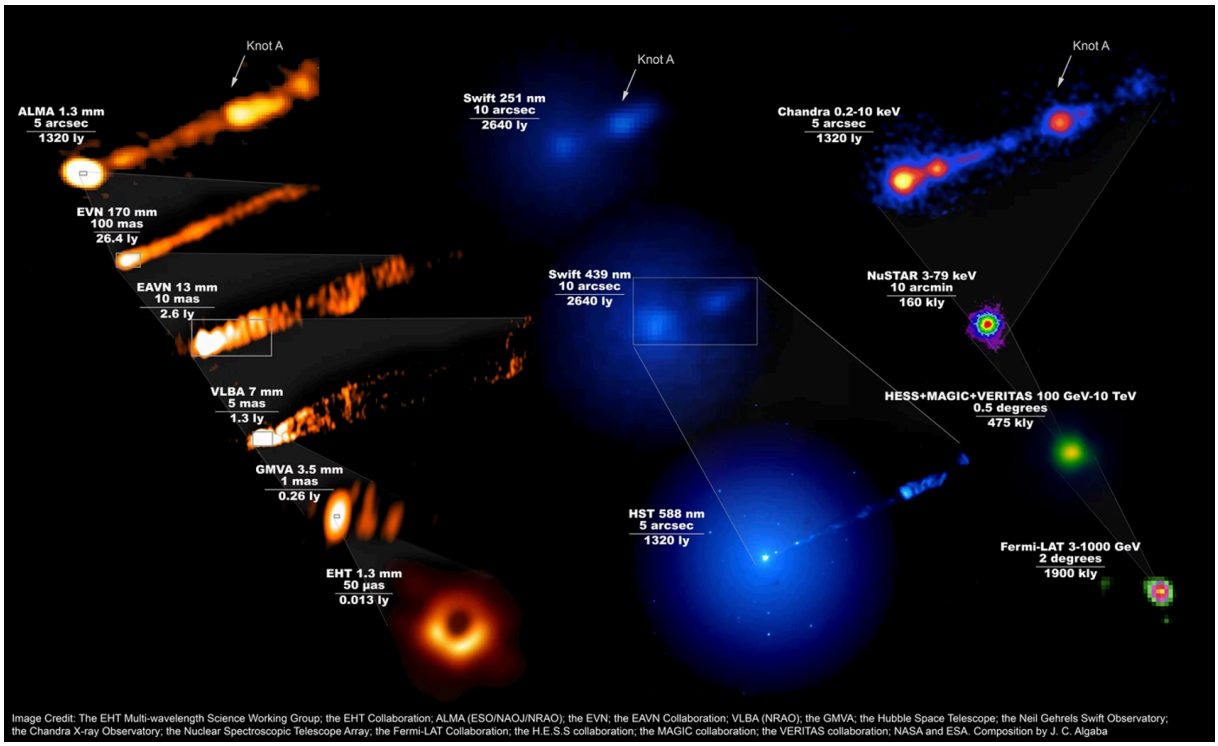

Fig. 1.4: The images of M87 simultaneously observed in various scales at multi-wavelengths (sub-millimeter radio to gamma-ray) during the EHT observations in 2017. (Credit: EHT MWL Science Working Group et al. (2021))

(i.e., numerous photons filling the funnel). As a result, the plasma motion converges into the terminal velocity, which is estimated to be $v \lesssim 0.5c$ and insufficient for the extremely relativistic motion in the AGN jets. Thus, these can be seen as the mechanism for outflows in the supercritical accretion cases (see Takeuchi et al. 2013; Kitaki et al. 2021 for numerical results).

Nowadays, the magnetically driving models are thought to be the most promising description to explain the acceleration and collimation at the same time. In the astrophysical situations of interest, plasmas are "frozen" in magnetic fields and vice versa, that is, the plasma can only move along the magnetic field lines (*ideal magnetohydrodynamics*; ideal MHD; see section 2.1). Thus, the magnetic fields threaded with the accretion disk are dragged with the disk rotation. The plasma frozen in such a field is centrifugally accelerated outwards along the field line, like beads threaded on a swinging wire (magneto-centrifugal acceleration; Blandford & Payne 1982). This description also guarantees the collimation at large distances from the disk by the tension of toroidal magnetic fields. Furthermore, if the magnetic fields are toroidally-dominant around the disk surface, they eject plasmas outwards along the magnetic pressure gradient, also collimating the flow (magnetic pressure acceleration; Shibata & Uchida 1985, 1986)

Analogously, and perhaps ambitiously, one can consider the magnetically driving mechanism with a rotating (Kerr) black hole itself (Blandford & Znajek 1977; Rees et al. 1982; see also Takahashi et al. 1990; Koide et al. 2002 for numerical results). As mentioned in subsection 1.1.1, the rotation energy of a Kerr BH can be extracted by a hypothetical particle designed to

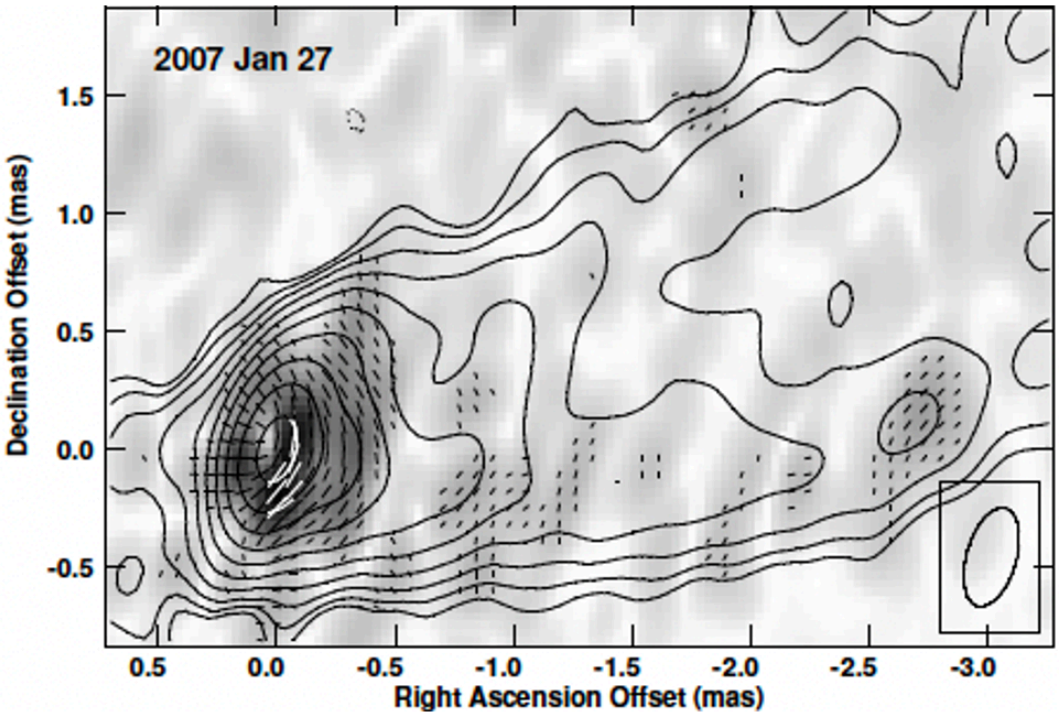

Fig. 1.5: LP map of M87 jet by 43 GHz Very Long Baseline Array (VLBA) observations in 2007. The line and grey contours corresponds to the total intensities (flux densities) and LP intensities, respectively. Overplotted are the ticks of LP vector in EVPA. (Credit: Walker et al. (2018))

split inside the ergosphere (Penrose process). Here, a magnetic field line threaded in the ergosphere is also dragged in prograde to the Kerr BH. Then, its outer part gains positive angular momentum and energy (Poynting) fluxes outwards in the funnel region through the magnetic tension, while its inner part is stretched out by the spinning BH or, in other words, brakes the BH spin. (These two parts of a field line are demarcated by the *light surface*; see, for example, Blandford & Globus 2022.)

The up-to-date, high-resolutive VLBI observations are expected to have access to the magnetic field structure near the SMBH, which is thought to be drive the AGN jet through the mechanisms above (see subsection 1.3.1 and 1.4.3). Furthermore, with the development of computational techniques and resources, the attempts to evolve these magnetically driving mechanisms close to the SMBH have achieved significant progresses (see subsection 1.4.1).

1.3 Case Studies: M87 and Sgr A*

1.3.1 M87; Nearby Low-Luminosity AGN Jet

M87 is the largest elliptical galaxy in the Virgo Cluster, in which our Milky Way galaxy is also located on the outskirts. It is well known that the M87 is categorized into the LLAGNs, and has a jet feature extending to outside the host galaxy and aligned closely to our line of sight

with an inclination angle to the jet axis, $i \sim 20^\circ$ or 160° (Mertens et al. 2016; Walker et al. 2018). Since the discovery in the early twentieth century, the M87 jet has been observed at various length scales over a wide ranges of wavelengths (e.g., Byram et al. 1966; Owen et al. 1989; Ford et al. 1994; Biretta et al. 1995; Macchetto et al. 1997; Marshall et al. 2002; Di Matteo et al. 2003; Aharonian et al. 2006; Abramowski et al. 2012). The bolometric luminosity of M87 has been measured to be $\sim 10^{42}$ erg/s $\sim 10^{-6}\ L_{\rm Edd}$ (Prieto et al. 2016; EHT MWL Science Working Group et al. 2021), which is lower than typical Seyfert galaxies (or quasars) by two (four) orders (Kato et al. 2008). In particular, observations of the jet base with high angular resolution provided by VLBI have provided observational evidences of the persistent relativistic acceleration and collimation (e.g., Junor et al. 1999; Ly et al. 2007; Kovalev et al. 2007; Hada et al. 2011; Asada & Nakamura 2012; Hada et al. 2013; Kino et al. 2014; Mertens et al. 2016; Nakamura et al. 2018; Kim et al. 2018; Park et al. 2019b; see Figure 1.4).

Further, it has been established from the radio core shifts (Blandford & Königl 1979) toward the upstream jet at millimeter wavelengths that the central engine of M87 jet should be a SMBH and accreting matters (Hada et al. 2011). The mass of SMBH has been estimated to be $M \approx 6.2 \times 10^9\ M_\odot$ from the stellar kinematics in the central region at optical wavelengths (Gebhardt et al. 2011), assuming a distance of $D = 16.7$ Mpc (Mei et al. 2007). Thus the angular size of the shadow of SMBH on the celestial sphere will be, if non-rotating, $2\ R_{\rm c}/D = 2\sqrt{27}\ r_{\rm g}/D \approx 38\ \mu$as (This is not largely changed $\lesssim 5\%$ even for a rotating black hole; Takahashi 2004; Johannsen & Psaltis 2010). This suggests that the central SMBH in M87, in addition to that in Sgr A* (see subsection 1.3.2), can be resolved with global-scaled VLBI at 230 GHz and/or 345 GHz (Doeleman et al. 2012; Lu et al. 2014; Akiyama et al. 2015; Chael et al. 2016; Akiyama et al. 2017a,b).

The first ever images of the SMBH M87* by the EHT (the left panel of Figure 1.1; EHT Collaboration 2019 Paper I) are a strong evidence of Einstein's GR theory by themselves. By ring model fitting, the ring diameter of the BH shadow was measured to be $\approx 42\mu$as (EHT Collaboration 2019 Paper VI). This corresponds to the BH mass of $M \approx 6.5 \times 10^9\ M_\odot$, which is similar to the value from the stellar dynamics.

The synchrotron emission, radiated within the inner region of the LLAGN jets at radio wavelengths, is also known to have a polarization component (Baade & Minkowski 1954) which reflects the strength and orientation of the surrounding magnetic fields (see subsection 1.5.1). In M87, VLBI observations also point to the existence of ordered magnetic field structure, potentially driving the large-scaled jet, both through the LP maps (e.g., Hada et al. 2016; Walker et al. 2018; Kravchenko et al. 2020; see Figure 1.5) and analyses of Faraday rotation measure (RM; see subsection 1.5.2) and electric vector position angle (EVPA) orientation (e.g., Owen et al. 1990; Zavala & Taylor 2004; Algaba et al. 2016; Park et al. 2019a). Kuo et al. (2014) gave a constraint of the mass accretion rate $\dot{M} \lesssim 10^{-3}\ M_\odot$/yr near the black hole $\sim 40\ r_{\rm g}$ from measured RM values, assuming Faraday rotation in the outer accretion flow and a power-law

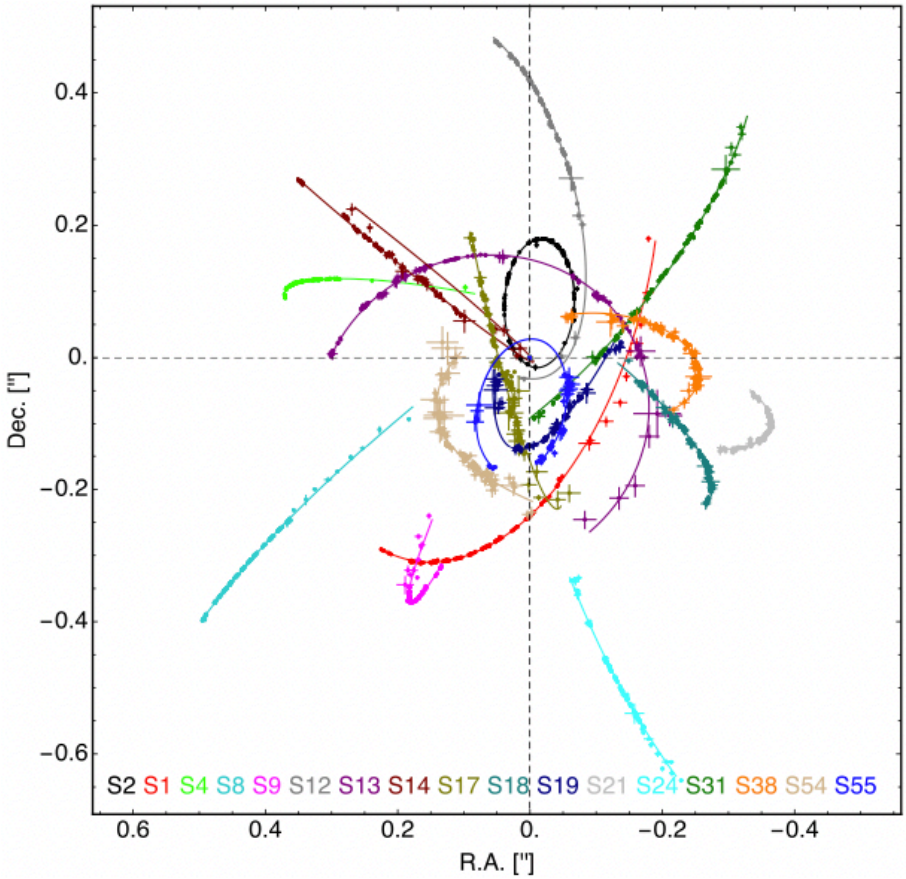

Fig. 1.6: The astrometric data (color points) for some of the S-stars, the stars in the sub-arcsecond scale of the Galactic center Sgr A*, with the best-fitting orbits (solid lines) obtained from the simultaneous multi-star fit. Here the S-stars are used as test particles moving in the gravitational potential of Sgr A*. The coordinate system is adopted such that Sgr A* is at rest on the origin (the intersection of two dash lines). (Credit: Gillessen et al. (2017))

density profile.

Further, the EHT collaboration published LP maps of M87* observed in 2017, which exhibit polarization angles in a nearly azimuthal pattern over a region of the asymmetric ring (the central panel of Figure 1.1). In addition, day-to-day variation evidence for the temporal evolution of the polarization in this inner region over one week (EHT Collaboration 2021 Paper VII). They also found low circular polarization fraction of the M87 core ($< 0.3\%$) from ALMA-only 230 GHz observations (Goddi et al. 2021). These results have opened up a new era with a unique opportunity to study, for the first time, the connection between the powerful relativistic jets and the central SMBH engine.

1.3.2 Sgr A*; the Galactic Center

Closer than the M87*, our Galactic center radio source Sgr A* is also known as an extreme case of LLAGN, hosting a SMBH. Due to its proximity, it has been observed at various wavelengths

as much as M87 (e.g., Balick & Brown 1974; Aitken et al. 2000; Baganoff et al. 2001; Eckart et al. 2004; Daylan et al. 2016; Issaoun et al. 2019). The bolometric luminosity of Sgr A* was measured to be less than $\sim 10^{35-37}$ erg/s $\sim 10^{-(7-9)}\ L_{\rm Edd}$ (Narayan et al. 1998; Baganoff et al. 2003), which is the lowest value in any known LLAGNs and black holes. From the Faraday RM at millimeter and sub-millimeter polarimetry, the mass accretion rate near the black hole has been estimated to be $\sim 10^{-(6-9)}\ M_\odot/{\rm yr}$ (Bower et al. 2003; Marrone et al. 2006, 2007).

A clear difference of Sgr A* from M87 is that it does not have an outstanding (observable) jet feature. Meanwhile, Sgr A* shows a flat spectrum in radio, which is often seen in other LLAGNs with jets (Blandford & Königl 1979). It has been in discussion whether such characteristic spectrum is produced in the jet (even if not observed at the large scales), the accretion flow, or both of them (Falcke et al. 1993; Narayan et al. 1995; Yuan et al. 2002). In this sense, survey of the innermost disk-jet structure near the SMBH is of great importance.

The existence of a SMBH in Sgr A* has been confirmed through the analyses of stellar kinematics as in M87 case, in which the mass of SMBH was estimated to be $M \approx 4 \times 10^6\ M_\odot$ with a distance of $D \approx 8$ kpc (Schödel et al. 2002; Ghez et al. 2003; Gillessen et al. 2009; GRAVITY Collaboration et al. 2018a, 2019; see Figure 1.6). Thus the apparent angular size of the SMBH is $\sim 50\mu$as, comparable to that of M87*, and thus accessible with the EHT array (Doeleman et al. 2008; Fish et al. 2011; Johnson et al. 2015).

In 2022, the EHT collaboration presented the first images of a SMBH in Sgr A* (the right panel of Figure 1.1; EHT Collaboration 2022 Paper I) as an average image of subsets with similar morphologies, overcoming the scattering in the interstellar medium (see, for example, Narayan 1992; Psaltis et al. 2018) and short variability timescale characterized with $t_{\rm g} \equiv r_{\rm g}/c \sim$ mins, both unique to Sgr A*. By accessing both images of M87* and Sgr A*, we can expect to survey two different SMBHs with/without outstanding jets, to find the key factors that determine the existence of jets and the underlying evolutionary scenario of LLAGNs.

1.4 Theoretical Approaches to the LLAGN Jets

1.4.1 Fluid Models

In the LLAGNs with low luminosity and thus low mass accretion rate (Rees et al. 1982), such as M87 and Sgr A*, the accreting material advects the energy released via viscosity inwards, not radiating it away efficiently (Ichimaru 1977). Such optically thin and geometrically thick (due to the high temperature) disks are called as *advection-dominated accretion flows* (ADAF; Narayan & Yi 1994, 1995; Abramowicz et al. 1995; Blandford & Begelman 1999; Yuan & Narayan 2014; see also subsection 1.2.1), or more newly and widely as *radiatively inefficient accretion flows* (RIAF; see, for example, Narayan et al. 2002). Analytical approaches with ADAFs have been successful in reproducing the observed spectra of LLAGNs (e.g., Narayan et al. 1995).

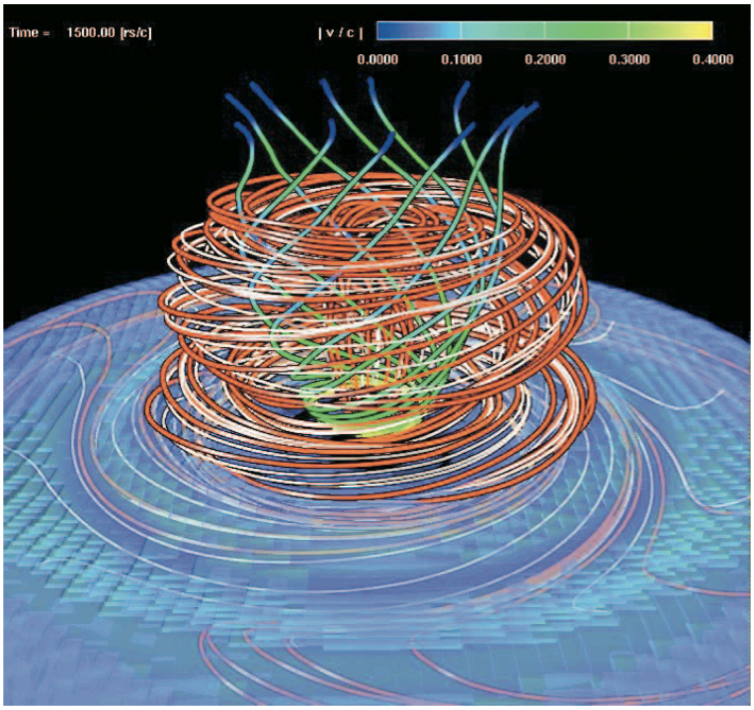

Fig. 1.7: Perspective view of magnetic field lines in a 3D pseudo-Newtonian MHD simulation. Red and white lines indicate magnetic field lines anchored at $(r, z) = (r_{\rm g}, 1.5r_{\rm g})$ and $(56r_{\rm g}, 10r_{\rm g})$ respectively, while green-blue lines denote the streamlines or velocity vectors with the color bar indicating the speed. The blue shaded region shows an iso-density surface. Toroidal fields are accumulated around the disk and driving a jet. Inside the jet, poloidal (vertical) fields are dominant. (Credit: Kato et al. (2004))

As introduced in subsection 1.2.2, some of the most promising models suggest that the AGN jets are powered from rotational energy through magnetic fields threading into the black hole (Blandford & Znajek 1977) or the accretion disk (Blandford & Payne 1982), the so-called "Blandford-Znajek" (BZ) process and "Blandford-Payne" (BP) process, respectively. To survey the mechanism of acceleration and collimation of jets close the black hole such as the BZ and BP processes, multi-dimensional numerical approaches with *general relativistic magneto-hydrodynamics* (GRMHD; Hawley et al. 1984; Koide et al. 1999; see section 2.1) simulation are essential.

GRMHD Simulations: Overview of SANE and MAD Regime

The early (non-GR) MHD simulations suggested that the differentially rotating plasma threaded with magnetic fields gives rise to the *magneto-rotational instability* (MRI; Balbus & Hawley 1991), which triggers MHD turbulence and angular momentum tranport for plasma in RIAFs to accrete inwards (e.g., Balbus & Hawley 1992, 1998; Stone & Pringle 2001). Further, they were also reported to form a global magnetic field structure and magnetically driven jets (e.g., Kato et al. 2004; see Figure 1.7). These results have been also confirmed in several global GRMHD simulations (e.g., De Villiers et al. 2003; Gammie et al. 2003; Narayan et al. 2012).

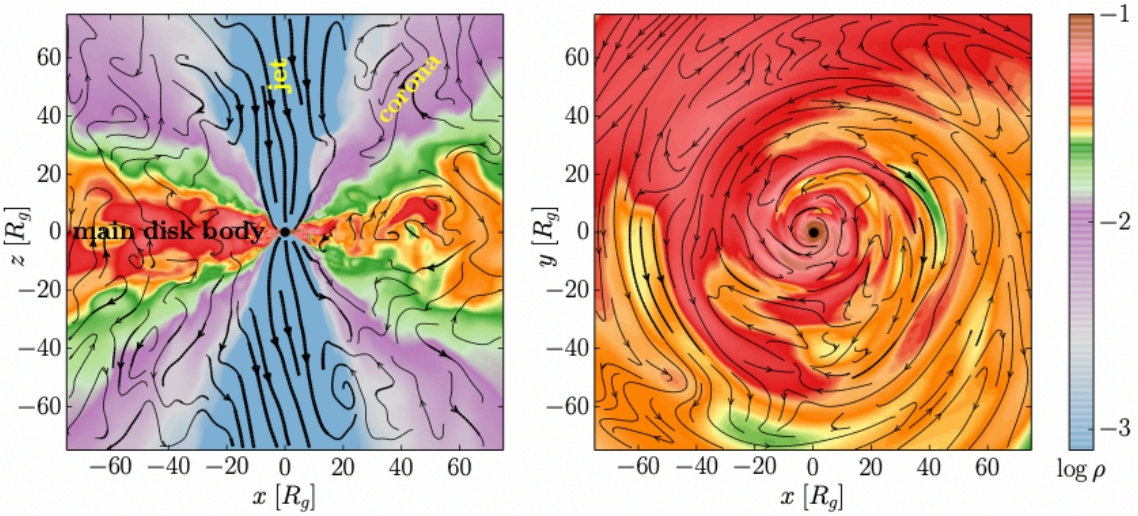

Fig. 1.8: A poloidal (left) and equatorial (right) slice map from a 3D SANE GRMHD simulation. Color contour shows plasma density. Lines and arrows indicates the magnetic field configuration and direction. In the left panel, three regions of the disk body, corona, and jet are identified. (Credit: Yuan & Narayan (2014))

As a typical scenario of jet formation, a GRMHD simulation is initialized with a rotating RIAF torus in a hydrostatic equilibrium and embedded with a weak poloidal magnetic loop (Fishbone & Moncrief 1976). Then, the plasma begins to accrete onto the BH due to MHD turbulence driven by the MRI, amplifying large-scale magnetic fields through a turbulent dynamo (Brandenburg et al. 1995). Finally, the accretion flow is decomposed into three regions, disk body, corona, and axial funnel jet (Yuan & Narayan 2014; see Figure 1.8). The disk body is dense, turbulent, and geometrically thick, consistent with the properties of (semi-)analytical RIAF solutions. Magnetic fields within the disk are chaotic and in sub-equipartition (the plasma-$\beta \equiv p_{\rm gas}/p_{\rm mag} \sim 10 - 100$; gas-pressure dominant, where $p_{\rm gas}$ and $p_{\rm mag}$ are the gas and magnetic pressure, respectively). The corona expands over the disk with lower gas density, in which the magnetic fields are ordered and toroidally dominant with $\beta \sim 1$. The axial funnel jet is magnetically dominated with tenuous gas ($\beta > 1$). The magnetic fields are poloidally dominant close to the BH, and power the jet with a Poynting flux. While the sub-relativistic disk winds in the corona region are thought to be driven by the BP process, the relativistic, Poynting-flux-dominated jets are believed to be driven by the BZ process (McKinney & Gammie 2004; McKinney 2006; McKinney & Blandford 2009; see also Dihingia et al. 2021 for simulations for a thin disk).

The accretion flows of such regularized decompositions are termed as *standard and normal evolution* (SANE; Narayan et al. 2012; Sądowski et al. 2013) models (see Figure 1.8). However, since GRMHD simulations give a diversity of results depending on the BH spin (De Villiers & Hawley 2003), the initial condition of torus size and magnetic field configuration (Hawley & Krolik 2002; Beckwith et al. 2008), numerical resolution (Hawley et al. 2011; Shiokawa et al. 2012), etc., a great number of models have ever been proposed (see Yuan & Narayan 2014;

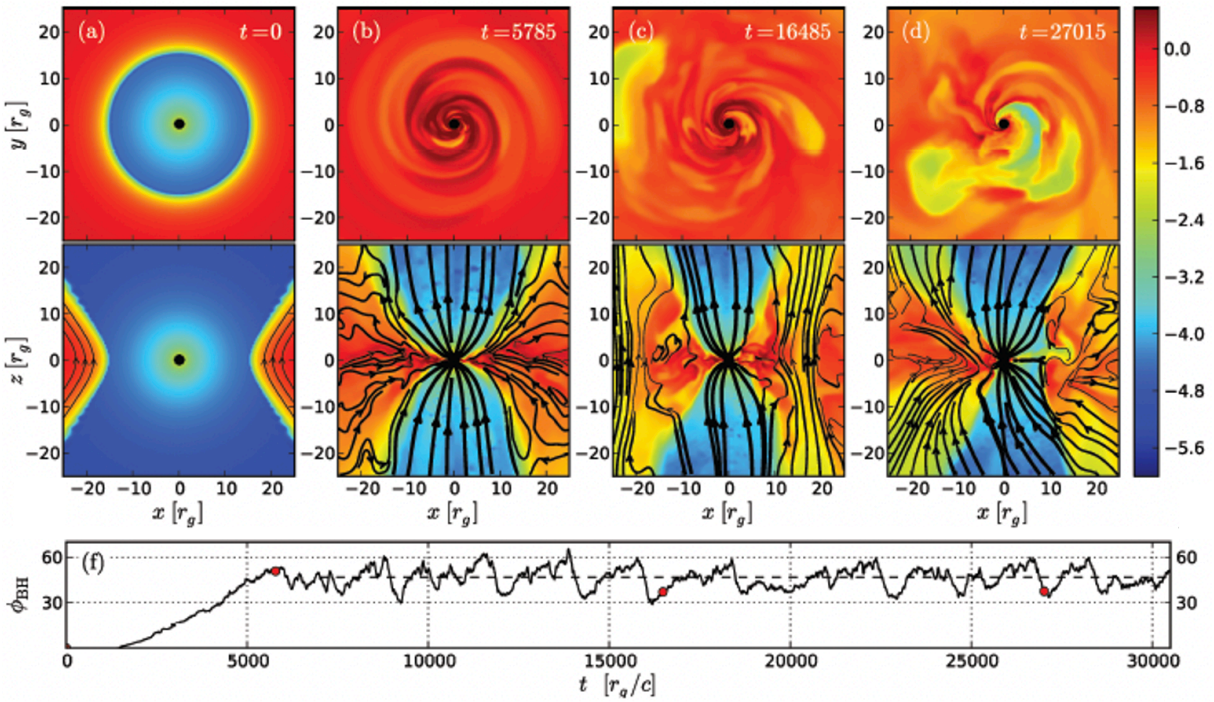

Fig. 1.9: Top; equatorial and poloidal slice maps of four snapshots from a 3D MAD GRMHD simulation, evolving from left to right. Color contour shows the plasma density in the logarithm. Black lines and arrows indicate the magnetic field configuration and direction. Bottom: time evolution of the dimensionless magnetic flux ϕ threading the event horizon. The red circles corresponds to the above snapshots. The magnetic fluxes continue to accumulate around the BH until $t \approx 6000 t_{\rm g}$. After that, the accretion flow become "magnetically arrested" with the magnetic flux saturated, which gives rise to quasi-periodic, non-axisymmetric accumulation and eruption of the magnetic field bundles near the BH as seen in panel (c) and (d). (Credit: Tchekhovskoy et al. (2011), partially modified)

Mizuno 2022 for a review).

There is another subset of GRMHD models in the opposite limit of SANEs in the magnetic flux strength, so called *magnetically arrested disks* (MAD; Igumenshchev et al. 2003; Narayan et al. 2003; Igumenshchev 2008). The MADs are in the opposite limit of the SANEs in the magnetic flux strength, and have the dimensionless magnetic flux $\phi \equiv \Phi_{\rm BH}/\dot{M} {r_{\rm g}}^2 c \sim 50$, where

$$\Phi_{\rm BH} \equiv \frac{1}{2} \int_\theta \int_\phi |B^r| {\rm d}A_{\theta\phi} \tag{1.2}$$

is the absolute magnetic flux threading a hemisphere of the event horizon (see section 2.1 for description of magnetic fields in GRMHD simulations). Such far stronger magnetic fields, than $\phi \sim 5$ in SANEs, enable MADs to produce powerful jets (Tchekhovskoy et al. 2011; McKinney et al. 2012). The dependence of the jet power and shape on the BH spin has been investigated in several works (e.g., Tchekhovskoy & McKinney 2012; Wong et al. 2021; Narayan et al. 2022). In addition, the MADs are also characterized with their dynamically important magnetic flux. By the strong magnetic flux building up close to the BH horizon, the matter accretion is pre-

vented and become no longer stationary or axisymmetric (Igumenshchev et al. 2003; Igumenshchev 2008), rather intermittently erupting magnetic flux tubes (Porth et al. 2021; Ripperda et al. 2022; see Figure 1.9). In this sense, the accretion flows in MADs is not so regularized as those in SANEs, and are worthy of the name.

1.4.2 Theoretical Prediction of SMBH, Disk and Jet Images

As introduced above, the fluid models have been getting to the heart of problems of the LLAGN jet formation. In the next step to directly compare these models with observations, one can consider performing radiative transfer calculation based on the models, to present an image, as well as an energy spectrum, corresponding to them. Since GR predicts that light rays are bent and red-shifted due to gravity of the BH, the calculation is needed to be performed in the BH metric (*general relativistic radiative transfer*; GRRT, see subsection 2.2 for detail).

Numerous works have presented the images from GRRT referring physical quantities in the (semi-)analytical fluid models (e.g., Broderick & Loeb 2009a; Lu et al. 2014; Takahashi et al. 2018b; Kawashima et al. 2019; Jeter et al. 2020; Kawashima et al. 2021b) and calculation fluid models such as GRMHD (e.g., Dexter et al. 2012; Mościbrodzka et al. 2016; Chael et al. 2019; Davelaar et al. 2019; Cruz-Osorio et al. 2022) of M87, as well as Sgr A* (e.g., Broderick & Loeb 2006; Dexter et al. 2010; Shcherbakov et al. 2012; Mościbrodzka et al. 2014; Davelaar et al. 2018; Chael et al. 2018; Pu & Broderick 2018). These images shows the black hole shadow illuminated by emission from surrounding plasma close the horizon, and thus can be an important clue of the jet creation mechanism.

The EHT collaboration compared the M87* image in 2017 with the GRRT images based on their GRMHD library. As a result, those with a rotating black hole were favored due to their powerful jets, implying energy extraction mechanisms from black hole spin like the BZ process, where a wide range of the spin values (including both prograde and retrograde) were yet warranted (EHT Collaboration 2019 Paper V). We here should note that the images in 2017 did not show a prominent jet feature and that the jet power in the model test was referred from larger-scaled observations including the outer jet (see, for example, Tchekhovskoy et al. 2011; Broderick et al. 2015).

In Sgr A* case, the situations of viewing MAD models with a prograde BH and low inclination (i.e., face-on like disk) are favored (EHT Collaboration 2022 Paper V). Such low inclination angle of Sgr A* was also suggested from orbital motion of flares detected by GRAVITY at near-infrared (GRAVITY Collaboration et al. 2018b).

In calculating a GRRT image from a GRMHD model, one of the large uncertainties is how to determine the temperature of electrons, which is thought to produce synchrotron emission at radio wavelengths (see Yuan & Narayan 2014, and references therein). Since the early stage of ADAFs, it has been pointed out that the separation between electron and ion temperatures can occur due to their inefficient Coulomb coupling, and is actually favored to reproduce

the observed spectra (e.g., Narayan & Yi 1995; Manmoto et al. 1997; Mahadevan 1998; Yuan et al. 2003, 2004). Several prescriptions to determine the electron temperature, such as two-temperature calculation (Ressler et al. 2015; Kawazura et al. 2019; Rowan et al. 2017; Chael et al. 2019) or parametrization by post-process (Mościbrodzka et al. 2014; Chan et al. 2015; Mościbrodzka et al. 2016; see section 2.1). Recently Mizuno et al. (2021) confirmed that these two approaches are matched in resultant GRRT images at 230 GHz. Meanwhile, large uncertainty in model parameters remains in both of them. The comparison with observations of the jet creation region may rather give a constraint to this degeneracy in theoretical models.

1.4.3 Polarization Images

In order to extract useful information on the physical processes from the GRRT images, we need to specify the regions producing the emission. However, this is a difficult work especially in the horizon-scale region. Since the light rays from near the black hole are bent and lensed by the gravity, the emissions from the mid-plane disk and twin funnel jets are degenerated into a ring-like shadow image. In this regard, the polarization components can provide powerful tools to verify the disk-jet structure, because they carry out the information regarding the plasma properties not only in the synchrotron-emitting plasma, but also in the intervening plasma through the Faraday effects, rotation and conversion (see subsections 1.5.1 and 1.5.2 for detail). Since the identification of emission region will conclusively connect the detected LP vectors and CP components to the magnetic field configuration, the polarization images have been attracting many attentions and been predicted theoretically.

Mościbrodzka et al. (2017) presented LP images and Faraday RM values through GRRT calculations based on SANE GRMHD models with M87* in mind. Their best-fit, jet-dominated (low electron-temperature disk) model gave consistent values of the LP fraction and RM with observational results in Kuo et al. (2014). Ricarte et al. (2020) also showed resolved RM images, which gave strong, spatial and temporal variabilities. These two studies demonstrated that the LP vectors originated from the counter (receding) jet are scrambled and depolarized by Faraday rotation in the disk, while those from the foreground (approaching) jet can survive from the Faraday depolarization and thus become dominant on the LP maps. On a wide range of scales in the jet observed at multi-wavelengths, the LP vectors and RMs have been theoretically modeled and have given constraints on physical quantities in plasma such as particle density, magnetic field configuration, and proton-electron coupling (e.g., Broderick & Loeb 2009b; Broderick & McKinney 2010; Feng et al. 2016; Jiménez-Rosales & Dexter 2018; Himwich et al. 2020; Dexter et al. 2020; Jiménez-Rosales et al. 2021; Narayan et al. 2021).

The EHT collaboration compared the observed polarization structure with predictions from theoretical models, and attributed low polarization fraction in the image to Faraday rotation internal to the emission region (Event Horizon Telescope Collaboration et al., 2021b). Further, the MAD models are favored over the SANE models in their GRMHD model evaluation.

Meanwhile, Tsunetoe et al. (2020, 2021) suggested that the circular polarization (CP) can be amplified by Faraday conversion process (Jones & O'Dell 1977; see subsection 1.5.2) from the LP in hot and dense plasma with strong magnetic fields near the black hole, up to the extent comparable with the LP. We there introduced an amplification process of the CP through combination of Faraday conversion and rotation (rotation-induced conversion), which produces the CP components with signs imprinting the magnetic fields configuration. Mościbrodzka et al. (2021) also showed the CP images enhanced by Faraday rotation and conversion. Ricarte et al. (2021) introduced a CP conversion process through twist of the magnetic field along the line-of-sight on event horizon scales, in addition to the rotation-induced conversion. These processes of the rotation-induced and field-twist Faraday conversions, as well as intrinsic CP component of synchrotron emission (Legg & Westfold, 1968; Jones & O'Dell, 1977; Jones, 1988), have also been introduced and discussed in the context of CP detection in quasars (Hodge, 1982; Wardle & Homan, 2003; Enßlin, 2003; Gabuzda et al., 2008; Homan et al., 2009).

Furthermore, Tsunetoe et al. (2022a) recently proposed that the LP flux mainly originates from downstream of the jet and the CP flux comes from the counter-side jet, while the total intensity is maximum at the jet base, and that this separation among the total, LP and CP flux along the jet arises from the Faraday rotation in the outer disk and conversion in the inner disk. In this way, accumulating studies have established that the unified interpretation of the LP and CP images is essential for understanding of the magnetic field structure and plasma properties near the black hole (e.g., Shcherbakov et al. 2012; Gold et al. 2017; Anantua et al. 2020; Emami et al. 2021).

1.5 Radiation Processes of Polarization

In the last section, the features in polarization images close to the SMBH were introduced. In this section, elementary radiative processes of polarization are outlined.

1.5.1 Synchrotron Emission and Self-Absorption

Synchrotron Emission

A particle rotating or spiraling in a magnetic field produce emission, so-called gyromagnetic emission. In particular, gyromagnetic emission by highly relativistic particles is referred to as synchrotron emission, while that by non-relativistic particles is known as cyclotron emission. The polarized emission of cyclotron rotating in a plane is characterized, in an intuitive manner, with LP vector observed from the edge-on view to the rotational plane and CP component from the face-on view, which reflect the projection of centrifugally-accelerated motion by the Lorentz force. In the spiraling synchrotron emission, the radiated light is concentrated within a narrow angle towards the particle's motion ($|\theta - \alpha| \lesssim \gamma^{-1}$ if letting γ and $\alpha \equiv \arctan(v_{\parallel}/v_{\perp})$ the

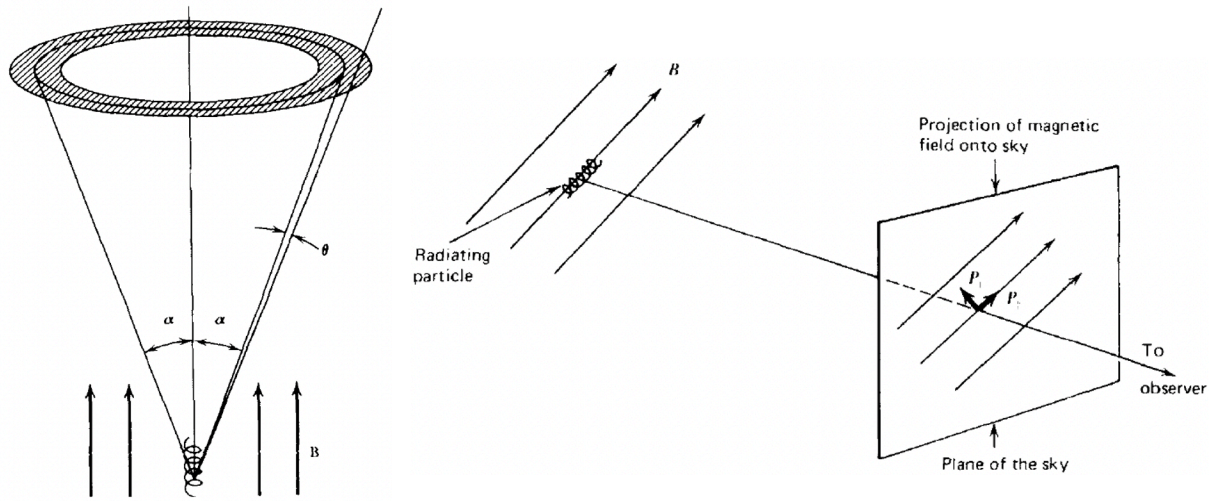

Fig. 1.10: Left: Schematic pictures of the emission from a synchrotron particle with pitch angle α. Radiation is concentrated to the narrow, shaded solid angle around $|\theta - \alpha| \lesssim \gamma^{-1}$ due to the relativistic beaming. Right: Synchrotron polarization vectors on the plane of the sky. One observes two polarization modes of electromagnetic wave perpendicular (electric vector; $\boldsymbol{P}_\perp$) and parallel (magnetic vector; $\boldsymbol{P}_\parallel$) to the projection of magnetic field. (Credit: Rybicki & Lightman (1979))

Lorentz factor and pitch angle of the particle; here $v_\parallel$ and $v_\perp$ are the parallel and perpendicular components of velocity to the magnetic field, respectively) due to the relativistic beaming effect (see, for example, Rybicki & Lightman 1979; see also the left panel of Figure 1.10). As a result, the polarization from a synchrotron is featured with the strong LP emission to near the pitch angle and weak CP emission ($\sim \gamma^{-1}$ in fraction) to small elevation or depression to the pitch angle. In particular, such LP vector has two polarized modes of radiative electromagnetic field perpendicular and parallel with the projected magnetic field on the polarization plane of the sky (see the right panel of Figure 1.10), whose position angles are referred to as the *electric vector position angle* (EVPA) and the *magnetic vector position angle* (MVPA) in polarimetric observations, respectively.[3]

To calculate radiative transfer, one firstly needs to prepare the polarized synchrotron emissivity for a distribution of electrons in a three-dimensional spatial coordinates. Let the magnetic field $\boldsymbol{B} = B(0, 0, 1)$ and the photon wave vector $\boldsymbol{k} = (0, \sin\,\theta_B, \cos\,\theta_B)$, where θ_B is the angle between $\boldsymbol{k}$ and $\boldsymbol{B}$. Then the polarization bases are taken as $\boldsymbol{e}^1 = (1, 0, 0)$ and $\boldsymbol{e}^2 = (0, \cos\,\theta_B, -\sin\,\theta_B)$, such that $\boldsymbol{k}$, $\boldsymbol{e}^1$ and $\boldsymbol{e}^2$ are orthonormal with each other. Here, $\boldsymbol{e}^1$ (or $\boldsymbol{e}^2$) is orthogonal (aligned) with the projection of the magnetic field $\boldsymbol{B}$ onto the polarization plane. The Stokes parameters (I, Q, U, V) are defined with the complex electric field compo-

[3] Since both of these two notations are prevalent equivalently, one should note whether the vectors are described in the EVPA or MVPA on each LP map. For example, while the central panel in Figure 1.1 is in EVPA, Figure 1.5 is in MVPA.

nents E_1 along $\boldsymbol{e}^1$ and E_2 along $\boldsymbol{e}^2$ as follows[4];

$$I = \langle E_1 E_1^* \rangle + \langle E_2 E_2^* \rangle, \tag{1.3}$$
$$Q = \langle E_1 E_1^* \rangle - \langle E_2 E_2^* \rangle, \tag{1.4}$$
$$U = \langle E_1 E_2^* \rangle + \langle E_2 E_1^* \rangle, \tag{1.5}$$
$$V = i \left(\langle E_1 E_2^* \rangle - \langle E_2 E_1^* \rangle \right), \tag{1.6}$$

where I is the total (specific) intensity, Q and U are LP components, and V is a CP component. Here positive Q (with $U = 0$) is defined to correspond to the EVPA perpendicular with the projected magnetic field on the polarization plane of the sky. Inversely, the polarization tensor in the intensity dimension is described with the Stokes parameter as

$$I_{ij} \equiv \langle E_i E_j^* \rangle = \frac{1}{2} \begin{pmatrix} I+Q & U-iV \\ U+iV & I-Q \end{pmatrix}. \tag{1.7}$$

The polarization tensor for the synchrotron emissivity *in vacuo* can be written in the form of (see, for example, Melrose 1980; Dexter 2016);

$$\eta^{ij}(\nu, \theta_B) = \frac{\sqrt{3} e^2}{4c} \nu_B \sin\theta_B H^{ij}(\nu, \theta_B), \tag{1.8}$$

where e is the charge of electron, $\nu_B \equiv eB/m_{\rm e}c$ is the gyromagnetic frequency of electron, $m_{\rm e}$ is the mass of electron, and

$$H^{11}(\nu, \theta_B) = F\left(\frac{\nu}{\nu_c}\right) + G\left(\frac{\nu}{\nu_c}\right), \tag{1.9}$$
$$H^{22}(\nu, \theta_B) = F\left(\frac{\nu}{\nu_c}\right) - G\left(\frac{\nu}{\nu_c}\right), \tag{1.10}$$
$$H^{12}(\nu, \theta_B) = -H^{21}(\nu, \theta_B) = -\frac{4i\cot\theta_B}{3\gamma} H\left(\frac{\nu}{\nu_c}\right). \tag{1.11}$$

Here ν is the emitted frequency, $\nu_{\rm c} \equiv (3/2)\nu_B \gamma^2 \sin\theta_B$ is the critical synchrotron electron frequency (e.g., Rybicki & Lightman 1979), and

$$F(x) = x \int_x^\infty {\rm d}y K_{5/3}(y), \tag{1.12}$$
$$G(x) = x K_{2/3}(x), \tag{1.13}$$
$$H(x) = \int_x^\infty {\rm d}y K_{1/3}(y) + x K_{2/3}(x), \tag{1.14}$$

where $K_\alpha(z)$ is the modified Bessel function of order α.

[4]Here, the IAU/IEEE definition (Hamaker & Bregman 1996) is chosen for the Stokes V, so that the rotation of the electric vector for positive V is counter-clockwise on the observer's screen (i.e., spatially right-handed CP; see also Shcherbakov & Huang 2011).

Finally, the synchrotron emissivity from a distribution of electrons are given by integrating equation 1.8 over the energy distribution;

$$j_\nu^{ij} = \int_1^\infty \mathrm{d}\gamma N(\gamma)\eta^{ij}(\nu,\theta_B). \tag{1.15}$$

Then the polarized emissivities in Stokes parameters are obtained as

$$j_I = j_\nu^{11} + j_\nu^{22}, \tag{1.16}$$
$$j_Q = j_\nu^{11} - j_\nu^{22}, \tag{1.17}$$
$$j_U = j_\nu^{12} + j_\nu^{21}, \tag{1.18}$$
$$j_V = i(j_\nu^{12} - j_\nu^{21}), \tag{1.19}$$

where $j_U = 0$ by the choice of polarization bases (see also section 2.2). In Appendix A, we introduce the polarized emissivities for two kinds of electron distributions commonly used for astrophysical objects, the relativistic thermal (Maxwell-Jüttner) distribution and the power-law distribution, which are implemented into our GRRT code.

Using a relationship among special functions, one can estimate the polarized power radiated per synchrotron electron with energy γ to the direction of the pitch angle, $\theta_B \approx \alpha$, (although this would not be an observable quantity in practical astrophysical situations) by integrating equation 1.8 over frequency (Rybicki & Lightman 1979; Melrose 1980);

$$P^{ij} \equiv \int_0^\infty \mathrm{d}\nu\eta^{ij}(\nu,\alpha). \tag{1.20}$$

With the relation equation between integral of the modified Bessel function and the gamma function,

$$\int_0^\infty \mathrm{d}x x^\beta K_\alpha(ax) = 2^{\beta-1}a^{-\beta-1}\Gamma\left(\frac{1+\alpha+\beta}{2}\right)\Gamma\left(\frac{1-\alpha+\beta}{2}\right), \tag{1.21}$$

and the general properties of the gamma function,

$$\Gamma(z+1) = z\Gamma(z),\ \Gamma(1-z)\Gamma(z) = \frac{\pi}{\sin\pi z}, \tag{1.22}$$

the polarized powers 1.20 yield

$$P^{11} = \frac{7}{8}P,\ P^{22} = \frac{1}{8}P, \tag{1.23}$$
$$P^{12} = -P^{21} = -\frac{\sqrt{3}i\cot\alpha}{2\gamma}P, \tag{1.24}$$

where

$$P \equiv P^{11} + P^{22} = \frac{2}{3}\frac{e^4B^2}{m_e^2c^3}\gamma^2\sin^2\alpha. \tag{1.25}$$

Then the fractions of LP and CP components are evaluated as

$$\frac{P^{11}-P^{22}}{P^{11}+P^{22}} = \frac{3}{4} = 75\%, \tag{1.26}$$
$$\frac{i(P^{12}-P^{21})}{P^{11}+P^{22}} = \frac{\sqrt{3}\cot\alpha}{\gamma}, \tag{1.27}$$

which more quantitatively express the qualitative discussion in the beginning of this subsection. Similar results are obtained for the *realistic*, synchrotron emissivities $j_{(I,Q,U,V)}$ for the power-law distribution (see Appendix A).

Synchrotron Self-Absorption

Synchrotron emitting plasma introduced above, on the other hand, can absorb synchrotron photons by themselves in an interaction with electrons in magnetic field, which is known as the synchrotron self-absorption (SSA). The polarized coefficients of SSA in an isotropic electron population are written with synchrotron emissivities 1.8 by analogy with the Einstein coefficients and the relativistic limit, as follows (Rybicki & Lightman 1979; Melrose 1980);

$$\alpha_{\nu}^{ij} = -\frac{c}{m\nu^2}\int_1^{\infty} \mathrm{d}\gamma\gamma^2 \frac{\mathrm{d}}{\mathrm{d}\gamma}\left\{\frac{N(\gamma)}{\gamma^2}\right\}\eta^{ij}(\nu,\theta_B). \tag{1.28}$$

Then the coefficients for Stokes parameters $\alpha_{(I,Q,U,V)}$ are obtained in the same way with equations 1.16. For the relativistic thermal distribution, it is shown that the polarized emissivities and absorption coefficients naturally follow Kirchhoff's law;

$$j_{(I,Q,U,V)} = \alpha_{(I,Q,U,V)} B_{\nu}(T_{\mathrm{e}}), \tag{1.29}$$

where $B_{\nu}(T)$ is the Planck function, k_{B} is the Boltzmann constant, T_{e} is temperature of electrons, and h is the Planck constant. Meanwhile, for the power-law distribution, the source function for Stokes parameters has a form of

$$S_{\nu} \equiv \frac{j_{\nu(I,Q,U,V)}}{\alpha_{\nu(I,Q,U,V)}} \propto \nu^{\frac{5}{2}}, \tag{1.30}$$

which can be a spectral feature distinguishable from that for the optically thick, thermal synchrotron source with $S_{\nu} \propto \nu^2$ (see Appendix A for concrete expressions).

1.5.2 Faraday Rotation and Conversion

As reviewed in subsection 1.4.3, both of observational and theoretical studies have suggested that the synchrotron radiation from LLAGN jets do not necessarily keep the raw polarization components at emission, but transform them due to the Faraday effects, rotation and conversion, in magnetized plasmas on the way. Qualitatively speaking, the existence of magnetic field makes the plasma *anisotropic*, in which the propagating waves are *responded* dependently on the direction of propagation and polarization relative to the magnetic field.

For example, with a parallel magnetic field to the propagation direction, the right- and left-handed circular polarizations $(E_1, E_2)_{\mp} = E_{\nu}\mathrm{e}^{-i2\pi\nu t}(1, \mp i)$ travel at different phase velocities. Since the linear polarization can be described as a superposition of such CP components (e.g., $\{(E_1, E_2)_{+} + (E_1, E_2)_{-}\}/\sqrt{2} = \sqrt{2}E_{\nu}\mathrm{e}^{-i2\pi\nu t}(1, 0)$), its position angle rotates by the degree

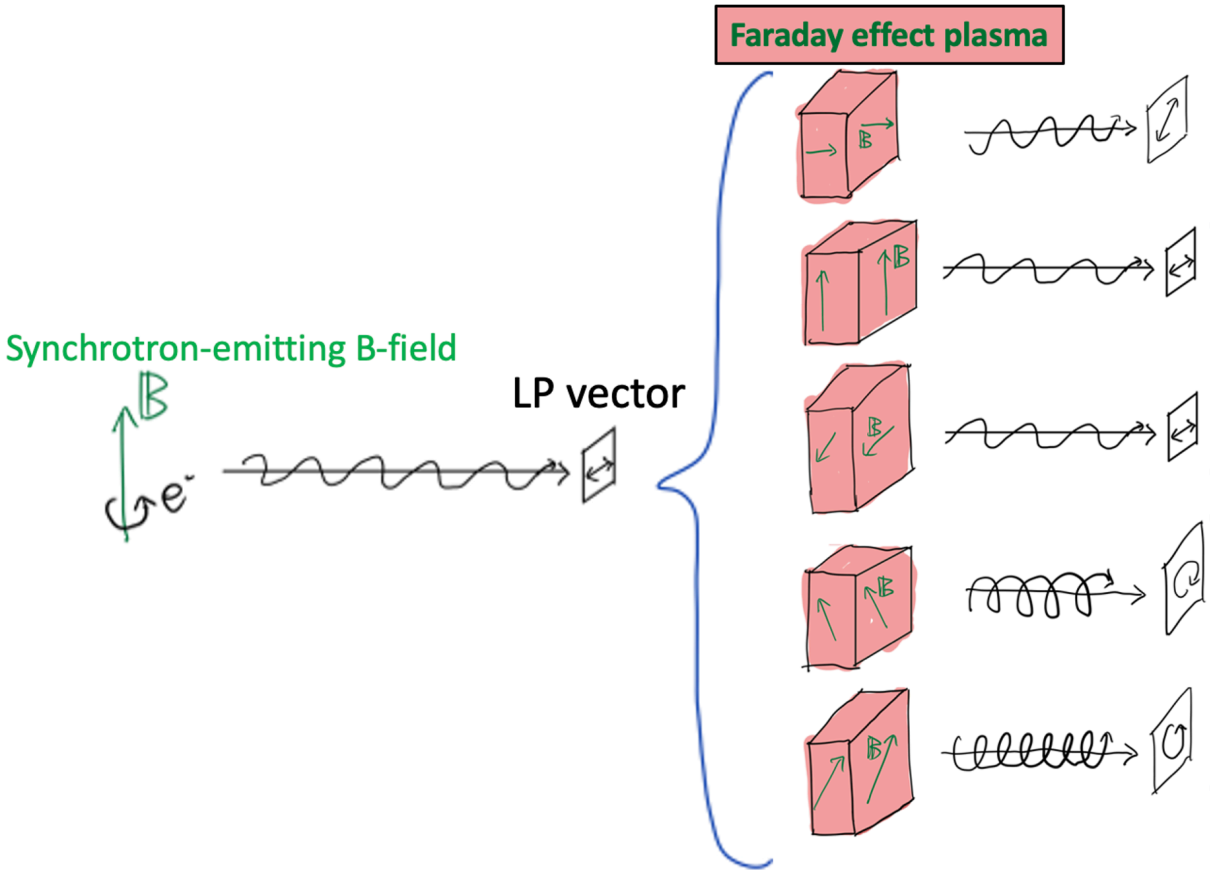

Fig. 1.11: Schematic pictures of propagation of a synchrotron LP vector and Faraday effects in plasmas on the way. Top: a parallel magnetic field to the propagation direction give rise to Faraday rotation of the LP vector. Middle two: parallel or perpendicular magnetic fields to the position angle of LP vector do not affect the polarization. Bottom two: inclined magnetic field to the LP position angle trigger Faraday conversion of LP to CP component.

proportional to the resultant phase gap, which is known as *Faraday rotation* (see, for example, Rybicki & Lightman 1979; see also the top of Figure 1.11).

In a similar way, with a perpendicular magnetic field to its propagation, the linear polarization components parallel and perpendicular with the projection of the magnetic field pass through the plasma at different phase velocities. As a result, the relative phase retardation in a superposition of these components gives rise to development of CP component, or "elliptization" of the polarization, which is termed as *Faraday conversion*, or also known as *Voigt effect* in the context of magneto-optics (see the bottom two panels of Figure 1.11). This can lead to amplification of the CP components, which are weak at the synchrotron emission, through the conversion from the strong LP components. However, a persistent, uniform magnetic field and LP vector position angle cannot trigger the Faraday conversion (see the second and third panel from the top of Figure 1.11). Therefore, the Faraday conversion is induced by the Faraday rotation of LP vector and/or twist of projected magnetic field component on the polarization plane along a light path, as mentioned in subsection 1.4.3 (see chapter 3, 4, and 5 for detail).

In equation, the propagation of electromagnetic wave in a magnetized plasma is described by the 4×4 *response tensor* $\alpha^{\mu\nu}$, which governs the linear proportionality between the induced current density j^μ and the four-vector potential A^μ,

$$j^\mu(\nu) = \alpha^\mu_\beta(\nu) A^\beta(\nu). \tag{1.31}$$

By the choice of Lorenz gauge $A^\mu u_\mu = 0$, where u_μ is four-velocity of the plasma, the spatial components follow $j^i = \alpha^i_j A^j$ in the locally flat plasma-rest frame (Landau & Lifshitz 1975). Radiative transfer equation for the polarization tensor I_{ij} in 1.7 is written with the emissivity tensor 1.15 and the response tensor α^{ij} as (Sazonov 1969)

$$\nu \frac{\mathrm{d}}{\mathrm{d}s} I_{ij} = j_{ij} - i \left({\alpha_i}^n I_{nj} - I_{in} \alpha^{*n}_j \right). \tag{1.32}$$

In the notation of Stokes parameters (I, Q, U, V), the coefficients of Faraday rotation and conversion are described as follows;

$$\rho_V = \frac{2}{\nu} \mathrm{Im}(\alpha^{12}), \tag{1.33}$$

$$\rho_Q = -\frac{1}{\nu} \mathrm{Re}(\alpha^{11} - \alpha^{22}), \tag{1.34}$$

which describe the interactions between Stokes Q and U and between U and V, respectively, and have the same dimension with the absorption coefficients $\alpha_{(I,Q,V)}$ (see also the transfer matrix $\boldsymbol{K}$, equation 2.21 in section 2.2), which can be written as

$$\alpha_I = \frac{1}{\nu} \mathrm{Im}(\alpha^{11} + \alpha^{22}), \tag{1.35}$$

$$\alpha_Q = \frac{1}{\nu} \mathrm{Im}(\alpha^{11} - \alpha^{22}), \tag{1.36}$$

$$\alpha_V = \frac{2}{\nu} \mathrm{Re}(\alpha^{12}). \tag{1.37}$$

The response tensor α_{ij} has been derived, for various particle populations with some assumptions and approximations, in a number of literatures (e.g., Melrose 1980, 2013 and references therein). As an example, that for the thermal electron distribution is described as follows (Trubnikov 1958; Melrose 1997a);

$$\alpha_{\mathrm{th},ij} = i \frac{e^2 n_\mathrm{e}}{m_\mathrm{e} c\, \theta_\mathrm{e}^2 K_2(\theta_\mathrm{e}^{-1})} \int_0^\infty \mathrm{d}\xi \left(T_{ij} \frac{K_2(\mathcal{R})}{\mathcal{R}^2} - R_i \bar{R}_j \frac{K_3(\mathcal{R})}{X_B^2 \mathcal{R}^3} \right), \tag{1.38}$$

where

$$T_{ij} = \begin{pmatrix} \cos X_B\xi & -\sin(X_B\xi)\cos\theta_B \\ \sin(X_B\xi)\cos\theta_B & \cos(X_B\xi)\cos^2\theta_B + \sin^2\theta_B \end{pmatrix}, \tag{1.39}$$

$$\begin{cases} R_i = \sin\theta_B \left[-(1 - \cos X_B\xi), \cos\theta_B (\sin X_B\xi - X_B\xi) \right], \\ \bar{R}_j = \sin\theta_B \left[1 - \cos X_B\xi, \cos\theta_B (\sin X_B\xi - X_B\xi) \right], \end{cases} \tag{1.40}$$

$$\mathcal{R} = \sqrt{\frac{1}{\theta_\mathrm{e}^2} - \frac{2iX_B}{\theta_\mathrm{e}} - X_B^2 \sin^2\theta_B + \frac{2\sin^2\theta_B}{X_B^2} (1 - \cos X_B\xi)}. \tag{1.41}$$

Here $n_{\rm e}$ is number density of thermal electrons, $\theta_{\rm e} \equiv k_{\rm B}T_{\rm e}/m_{\rm e}c^2$ is dimensionless electron temperature, and $X_B \equiv \nu_B/\nu$. Then the coefficients for Faraday rotation and conversion are calculated from equations 1.33 and 1.34. We implement those for the thermal and power-law distributions of electrons into our code (see also Appendix A).

Further, one can obtain an insight about the Faraday rotation and conversion from the relationship between the response tensor and the dielectric tensor;

$$\epsilon_{ij} = \delta_{ij} + \frac{c}{\pi\nu^2}\alpha_{ij}. \tag{1.42}$$

Then the electromagnetic wave equation on the transverse plane can be written as follows;

$$\left[\frac{k^2c^2}{(2\pi\nu)^2}\delta_{ij} - \epsilon_{ij}\right]\begin{pmatrix} E_1 \\ E_2 \end{pmatrix} = 0. \tag{1.43}$$

This yields the dispersion relation (Melrose 1997b; Huang & Shcherbakov 2011);

$$k^2c^2 = (2\pi\nu)^2 + 2\pi c\left\{\alpha_{11} + \alpha_{22} \pm \sqrt{(\alpha_{11}-\alpha_{22})^2 + 4\alpha_{12}\alpha_{21}}\right\}. \tag{1.44}$$

In cases of only Faraday rotation or conversion, for example, this can be written in terms of their coefficients, with the Onsager's principle $\alpha_{12} = -\alpha_{21}$ (Landau & Lifshitz 1980), as

$$k_\pm^2c^2 = (2\pi\nu)^2 + 2\pi c\{{\rm Re}(\alpha_{11}+\alpha_{22}) \pm \nu\rho_V\} \tag{1.45}$$

or

$$k_\pm^2c^2 = (2\pi\nu)^2 + 2\pi c\{{\rm Re}(\alpha_{11}+\alpha_{22}) \pm \nu\rho_Q\}, \tag{1.46}$$

respectively. If assuming two electromagnetic wave propagating in the same direction (i.e., both $k_\pm$ positive/negative), these give two eigenmodes of transverse wave in equation 1.43 with different phase velocities. In each case, these eigenmodes corresponds to the right- and left- handed CP components (in Faraday rotation case) or the parallel and perpendicular LP components to the projected magnetic field (in Faraday conversion case), as exemplified in the beginning of this subsection.

Meanwhile, the term of $2\pi c{\rm Re}(\alpha_{11}+\alpha_{22})$ guarantees that the wave can propagate in the plasma. If its imaginary counterpart $2\pi c{\rm Im}(\alpha_{11}+\alpha_{22}) = 2\pi\nu c\alpha_I$ is dominant, the amplitude of wave decreases exponentially by the absorption effect. In cold, isotropic plasma, this gives the *plasma cutoff frequency* $\omega_{\rm p} \equiv \sqrt{4\pi n_{\rm e}e^2/m_{\rm e}}$ below which electromagnetic wave cannot propagate, and motivates the *dispersion measure* to estimate the interstellar gas densities (see, for example, Rybicki & Lightman 1979; Shcherbakov 2008).

1.6 Our Motivation and Outlook

As outlined above, we have been accessing the important keys to the century-time enigma of the astrophysical jets driven by a SMBH and magnetic fields. However, the observational informations are given in the degenerate form of several effects; GR metric effects by the SMBH, polarized synchrotron emission indicating magnetic field configuration, and SSA and Faraday effects to the polarized lights in plasmas on the way to the Earth. In this dissertation, to resolve these effects and connect the observations with the essential mechanisms of magnetically driven jets, we investigate the structure of SMBH, accretion disk and jet in LLAGNs through theoretical prediction of polarization images by GRRT calculations based on GRMHD simulation models.

This thesis is organized as follows: We outline the methodology for GRMHD simulation and polarized GRRT calculation in chapter 2. Theoretical polarization images of M87 based on two-dimensional GRMHD models with different BH spins are given with discussion of Faraday effects, such as the rotation-induced Faraday conversion into CP, in chapter 3. Next, we show the images of Sgr A* based on the same 2D GRMHD models but with different electron-temperature parameters, and also discuss resultant image features and their relation to the magnetic field configuration in comparison with the M87 cases, in chapter 4. We investigate the relationship among the total, LP and CP intensity distributions on the images of M87 based on a three-dimensional GRMHD model, focusing on the synchrotron emission and Faraday effects in the jet-disk structure, in chapter 5. The dependence of polarimetric features on the observer's viewing (inclination) angles is also discussed with application to a diversity of AGN jets in mind, using the same 3D GRMHD model, in chapter 6. Finally, chapter 7 is devoted to concluding remarks.

Chapter 2

Methods

2.1 GRMHD Simulations

GRMHD simulations evolve an ionized, magnetized plasma in a fixed background metric $g_{\mu\nu}$. The governing equations of GRMHD describes the particle number and energy momentum conservations, and the Maxwell equations;

$$\nabla_\mu(\rho u^\mu) = 0, \tag{2.1}$$

$$\nabla_\mu T^{\mu\nu} = 0, \tag{2.2}$$

$$\nabla_\mu F^{*\mu\nu} = 0, \tag{2.3}$$

where ∇_μ denotes the GR-covariant derivative, ρ is the mass density in the fluid rest frame, u^μ is the plasma four-velocity, $T^{\mu\nu}$ is the stress-energy tensor, and $F^{*\mu\nu}$ is the dual of the electromagnetic Faraday tensor $F^{\mu\nu}$.

Under the ideal MHD assumption, the electric field vanishes in the fluid rest frame ($\boldsymbol{E} + \boldsymbol{v} \times \boldsymbol{B} = \boldsymbol{0}$) due to the high conductivity and large scale of the plasma. In the covariant form, it is equivalently described as

$$u_\mu F^{\mu\nu} = 0. \tag{2.4}$$

By introducing a convenient magnetic field four-vector $b^\mu \equiv (1/2)\epsilon^{\mu\nu\kappa\lambda}u_\nu F_{\lambda\kappa}$ (Gammie et al. 2003), where $\epsilon^{\mu\nu\kappa\lambda}$ is the Levi-Civita tensor, the dual Faraday tensor is written as

$$F^{*\mu\nu} = b^\mu u^\nu - b^\nu u^\mu. \tag{2.5}$$

Since $b^\mu = -F^{*\mu\nu}u_\nu$, one can refer b^μ as four-magnetic field which is measured in the fluid rest frame. It is also useful to introduce the three-vector magnetic field, $B^i \equiv F^{*it}$ and $B^0 \equiv F^{*tt} = 0$[1] (Komissarov 1999).

[1]Note that this form of three-magnetic field is deviated from that measured in the normal observer's frame, as $\mathcal{B}^i \equiv -F^{*i\nu}n_\nu = \alpha F^{it} = \alpha B^i$ (Noble et al. 2006). Here $n_\nu = (-\alpha, 0, 0, 0)$ is four-velocity of the normal observer, and $\alpha \equiv \sqrt{-g_{tt}}$ is the lapse function. After the orthonormalization, the normal observer's frame coincides with the *zero-angular momentum observer* (ZAMO) frame, which is adopted in the context of the 3+1 formalism of the GR spacetime (see Thorne et al. 1986 and references therein).

The stress energy tensor in MHD consists of the two parts of fluid and electromagnetic field;

$$T^{\mu\nu}_{\rm MHD} = T^{\mu\nu}_{\rm fluid} + T^{\mu\nu}_{\rm EM},$$

$$T^{\mu\nu}_{\rm fluid} = (\rho + u + p)u^\mu u^\nu + pg^{\mu\nu},$$
$$T^{\mu\nu}_{\rm EM} = F^{\mu\alpha}F^\nu_\alpha - \frac{1}{4}g^{\mu\nu}F_{\alpha\beta}F^{\alpha\beta}, \tag{2.6}$$

where u is the internal energy and p is the pressure. By expressing equation 2.6 with b^μ, one obtains

$$T^{\mu\nu}_{\rm MHD} = (\rho + u + p + b^2)u^\mu u^\nu + (p + \frac{1}{2}b^2)g^{\mu\nu} - b^\mu b^\nu. \tag{2.7}$$

Here $b^2 \equiv b^\mu b_\mu$ is the magnetic field strength measured in the fluid rest frame.

In a charge-neutral plasma, it is guaranteed that ions and electrons have the same number density n and four velocity u^μ everywhere. Meanwhile, they can have distinct local thermal energy densities $u_{\rm i} \neq u_{\rm e}$ and thus different temperatures $T_{\rm i} \neq T_{\rm e}$, especially in the RIAF cases with inefficient coupling as mentioned in subsection 1.4.2. GRMHD simulations usually ignore the distinction between ions and electrons and handle them together as a single fluid, the single-fluid GRMHD. Then the fluid has a total mass density $\rho = m_{\rm i}n + m_{\rm e}n \approx m_{\rm i}n$, dominated by the ions, a total internal energy density $u = u_{\rm i} + u_{\rm e}$ and a total pressure $p = p_{\rm i} + p_{\rm e}$.

Now the total pressure p and the total internal energy density u is related with the ideal gas law;

$$p = (\Gamma - 1)u, \tag{2.8}$$

where Γ is the adiabatic index (or heat capacity ratio). While $\Gamma = 5/3$ for the non-relativistic monatomic gas, $\Gamma = 4/3$ for the relativistic gas. Since $T \sim 10^{11-12}$ K in the inner region of RIAFs (Yuan & Narayan 2014), the electrons can be relativistic ($k_{\rm B}T/m_{\rm e}c^2 \sim 10 - 100$ while $k_{\rm B}T/m_{\rm i}c^2 \lesssim 0.01$ for the ions; here $k_{\rm B}$ is the Boltzmann constant). In the single-fluid simulations, the effective adiabatic index is thus fixed to a value in the range of $4/3 \leq \Gamma \leq 5/3$ everywhere, or is set to vary in the range depending on the ion and electron temperatures.

Electron Temperature Prescription

As mentioned above and in subsection 1.4.2, the electrons, producing the synchrotron emission in LLAGNs, can have a distinct temperature from that of the ions in RIAFs and GRMHD simulations. This arises from combination of their inefficient Coulomb coupling, the different viscous heating rate of the two, and the cooling of electron by radiation process, which is "dynamically" inefficient in RIAFs. The electron temperature distribution can be obtained by incorporating these thermodynamical effects and evolving energy populations both of ions and electrons, so-called two-temperature GRMHD simulations (e.g., Chael et al. 2018, 2019).

Another approach, being reasonable in computation and allowing us to explore a large parameter domain, is prescribing the electron temperature by post-process after evolving a population of ions, which is predominantly responsible for the fluid dynamics. Mościbrodzka et al.

(2016) proposed a ratio parametrized with two parameters $R_{\rm low}$ and $R_{\rm high}$ and the plasma-β, the R-β prescription;

$$\frac{T_{\rm i}}{T_{\rm e}} = R_{\rm high}\frac{\beta^2}{1+\beta^2} + R_{\rm low}\frac{1}{1+\beta^2}. \tag{2.9}$$

Roughly speaking, $R_{\rm high}$ corresponds to the ratio of proton to electron temperatures in the inner disk with high β, whereas $R_{\rm low}$ corresponds to the same but in the jet region with low β. In comparison with the two-temperature simulation, a range of values $R_{\rm low} \approx 1-10$ and $R_{\rm high} \approx 1-160$ have been suggested in recent works (e.g., Chael et al. 2018; Mizuno et al. 2021). Adopting this approach enables us to apply a GRMHD model to multiple LLAGNs and to discuss them in the same framework (see Chapter 4), since non-radiative GRMHD simulations are scale-invariant (as long as the mass of the accretion flow is negligible relatively to the SMBH mass; EHT Collaboration 2019 Paper V).

2.2 Polarized GRRT Calculation

We perform polarized GRRT calculation in Kerr metric, referring the physical quantities in a GRMHD model. The Kerr metric is, for example, written as follows in the BL coordinates (t, r, θ, ϕ) with the geometric unit system ($c = G = 1$) and $M = 1$ (thus $r_{\rm g} = 1$);

$$\begin{aligned} {\rm d}s^2 &= g_{\mu\nu}{\rm d}x^\mu {\rm d}x^\nu \\ &= -\frac{1}{\rho^2}\left(\Delta - a^2\sin^2\theta\right){\rm d}t^2 - \frac{4ar\sin^2\theta}{\rho^2}{\rm d}t\,{\rm d}\phi + \frac{\rho^2}{\Delta}{\rm d}r^2 + \rho^2{\rm d}\theta^2 + \frac{\Sigma\sin^2\theta}{\rho^2}{\rm d}\phi^2, \end{aligned} \tag{2.10}$$

$$\begin{cases} \rho^2 = r^2 + a^2\cos^2\theta, \\ \Delta = r^2 - 2r + a^2, \\ \Sigma^2 = \left(r^2+a^2\right)^2 - a^2\Delta\sin^2\theta, \end{cases}$$

where ${\rm d}s$ is the line element of a particle. First, we determine light paths from the object to observer's screen by the GR ray-tracing method in the BL coordinates, rewinding the affine parameter (or proper time) λ from each pixel on the screen to the object according to the following equations of the photon propagation;

$$\rho^2\frac{{\rm d}t}{{\rm d}\lambda} = -a\left(a\sin^2\theta - l_z\right) + \frac{\left(r^2+a^2\right)T}{\Delta}, \tag{2.11}$$

$$\rho^2\frac{{\rm d}r}{{\rm d}\lambda} = \pm_r\sqrt{R\left(r\right)}, \tag{2.12}$$

$$\rho^2\frac{{\rm d}\theta}{{\rm d}\lambda} = \pm_\theta\sqrt{\Theta\left(\theta\right)}, \tag{2.13}$$

$$\rho^2\frac{{\rm d}\phi}{{\rm d}\lambda} = -\left(a - \frac{l_z}{\sin^2\theta}\right) + \frac{aT}{\Delta}, \tag{2.14}$$

$$
\begin{aligned}
T &= (r^2 + a^2) - l_z a, \\
R(r) &= T^2 - \Delta[\mu^2 r^2 + (l_z - a)^2 + q], \\
\Theta(\theta) &= q - \cos^2\theta \left(\frac{l_z^2}{\sin^2\theta} - a^2 \right).
\end{aligned}
$$

Here l_z and q are two conserved quantities in each photon trajectory; the angular momentum projected onto the BH spin axis and the Carter constant (Carter 1968) for a photon, respectively (Bardeen et al. 1972; Misner et al. 1973). These are determined from the observer's inclination angle i and the impact parameters (α, β) parallel and perpendicular and with the BH spin axis, or the pixel coordinates on the observer's screen in this case;

$$
l_z = -\alpha \sin i, \tag{2.15}
$$

$$
q = \beta^2 + (\alpha^2 - a^2)\cos^2 i. \tag{2.16}
$$

In equation 2.12 and 2.13, $R(r)$ and $\Theta(\theta)$ are regarded as the radial and angular potentials, whose zeros correspond to turning points of r- and θ-directions, respectively.

Now, in addition to the wave propagation vector $k^\mu = E\frac{\mathrm{d}x^\mu}{\mathrm{d}\lambda}$[2], the polarization basis f^μ, along which the polarization component is measured, is needed to determine by parallel transport along the path. To calculate the basis vector f^μ from the wave vector k^μ, one can exploit the existence of a complex constant in Kerr metric, the Walker-Penrose constant (Walker & Penrose 1970; Connors et al. 1980);

$$
\kappa = \kappa_1 + i\kappa_2 = (r - ia\cos\theta)(\mathscr{A} - i\mathscr{B}), \tag{2.17}
$$

$$
\begin{cases}
\mathscr{A} = k^t f^r - k^r f^t + a\sin^2\theta(k^r f^\phi - k^\phi f^r), \\
\mathscr{B} = \left\{(r^2 + a^2)(k^\phi f^\theta - p^\theta f^\phi) - a(k^t f^\theta - k^\theta f^t)\right\}\sin\theta.
\end{cases}
$$

The real and imaginary parts of the constant, κ_1 and κ_2, determine the direction of the basis on the screen. One can choose $\kappa_1 = \alpha + a\sin i$, $\kappa_2 = -\beta$ and $\kappa_1 = -\beta$, $\kappa_2 = -\alpha - a\sin i$, so that the two polarization bases corresponds to the ϕ- and θ-direction at infinity observer, respectively (Connors et al. 1980; Chandrasekhar 1983). Together with the condition of orthogonality $k^\mu f_\mu = 0$,[3] this equation is solved for f^μ at each point along the path (Dexter 2016).

Once one find the path of each light ray, polarization components are integrated from the object to the screen in the form of Stokes parameters $\boldsymbol{I} = (I, Q, U, V)$. However, the emissivity and radiative coefficients in the transfer matrix is defined and calculated in reference with the propagation vector, polarization basis and magnetic field vector in the fluid rest frame. Thus

[2]Here $E = 2\pi\nu_{\mathrm{obs}}/c$ is a constant photon energy at infinity, and ν_{obs} is the observed frequency. With such normalization of the affine parameter λ, $\mathrm{d}\lambda \approx \mathrm{d}s$ far from the BH (Shcherbakov & Huang 2011).

[3]Here, since f^μ is given *modulo* the null vector k^μ, one can set $f^t = 0$ without loss of generality (Chandrasekhar 1983). Thus the three equations are sufficient.

one here has to transform those (A^μ as an example) in the laboratory frame to those ($\hat{A}^{(\mu)}$) in the fluid rest frame as follow (Shcherbakov & Huang 2011);

$$\hat{A}^{(\mu)} = \eta^{(\mu)(\nu)} g_{\alpha\beta} e^{\alpha}_{(\nu)} A^{\beta}, \tag{2.18}$$

where $\eta^{(\mu)(\nu)} = \mathrm{diag}(-1,1,1,1)$ is the Minkowski (flat spacetime) metric and $e^{\mu}_{(\alpha)}$ is the orthonormal basis of the transformation, tetrads, in Kerr metric in the laboratory frame (Krolik et al. 2005; Beckwith et al. 2008);

$$\begin{aligned}
e^{\mu}_{(t)} &= u^{\mu}, \\
e^{\mu}_{(r)} &= (u_r u^t, -(u_t u^t + u_\phi u^\phi), 0, u_r u^\phi)/N_r, \\
e^{\mu}_{(\theta)} &= (u_\theta u^t, u_\theta u^r, 1 + u_\theta u^\theta, u_\theta u^\phi)/N_\theta, \\
e^{\mu}_{(\phi)} &= (u_\phi, 0, 0, -u_t)/N_\phi,
\end{aligned} \tag{2.19}$$

$$\begin{aligned}
N_r^2 &= -g_{rr}(u_t u^t + u_\phi u^\phi)(1 + u_\theta u^\theta), \\
N_\theta^2 &= g_{\theta\theta}(1 + u_\theta u^\theta), \\
N_\phi^2 &= -(u_t u^t + u_\phi u^\phi)\Delta \sin^2\theta.
\end{aligned}$$

Obviously, the plasma four-velocity u^μ is transformed into $\hat{u}^{(\mu)} = (-1,0,0,0)$ by these. In the plasma rest frame, the synchrotron radiation coefficients for the Stokes parameters can be written in simple form with a basis aligned with the local magnetic field; the polarized synchrotron emissivity is

$$\boldsymbol{j} = \begin{pmatrix} j_I \\ j_Q \\ 0 \\ j_V \end{pmatrix}, \tag{2.20}$$

and the transfer matrix is

$$\boldsymbol{K} = \begin{pmatrix} \alpha_I & \alpha_Q & 0 & \alpha_V \\ \alpha_Q & \alpha_I & \rho_V & 0 \\ 0 & -\rho_V & \alpha_I & \rho_Q \\ \alpha_V & 0 & -\rho_Q & \alpha_I \end{pmatrix}, \tag{2.21}$$

where $(\alpha_I, \alpha_Q, \alpha_V)$ is radiative coefficients of the polarized synchrotron self-absorption (SSA), and (ρ_Q, ρ_V) is those of the Faraday rotation and conversion. Here $j_U = \alpha_U = \rho_U = 0$ by the choice of the basis (see subsection 1.5.1 and Appendix A). Then these emissivity and transfer matrix are rotated from the fluid frame to the observer's frame. If one let χ the angle between the local aligned basis and the global, parallel-transported basis, the rotation matrix is written as

$$R(2\chi) = \begin{pmatrix} 1 & 0 & 0 & 0 \\ 0 & \cos 2\chi & -\sin 2\chi & 0 \\ 0 & \sin 2\chi & \cos 2\chi & 0 \\ 0 & 0 & 0 & 1 \end{pmatrix}. \tag{2.22}$$

This can be calculated with the three-magnetic field $\hat{\boldsymbol{B}}$ and the two global bases $\hat{\boldsymbol{a}}$ and $\hat{\boldsymbol{b}}$ in the fluid rest frame[4] (Shcherbakov & Huang 2011);

$$\sin 2\chi = -2\frac{\left(\hat{\boldsymbol{a}}\cdot\hat{\boldsymbol{B}}\right)\left(\hat{\boldsymbol{b}}\cdot\hat{\boldsymbol{B}}\right)}{\left(\hat{\boldsymbol{a}}\cdot\hat{\boldsymbol{B}}\right)^2+\left(\hat{\boldsymbol{b}}\cdot\hat{\boldsymbol{B}}\right)^2}\,, \tag{2.23}$$

$$\cos 2\chi = \frac{\left(\hat{\boldsymbol{b}}\cdot\hat{\boldsymbol{B}}\right)^2-\left(\hat{\boldsymbol{a}}\cdot\hat{\boldsymbol{B}}\right)^2}{\left(\hat{\boldsymbol{a}}\cdot\hat{\boldsymbol{B}}\right)^2+\left(\hat{\boldsymbol{b}}\cdot\hat{\boldsymbol{B}}\right)^2}\,. \tag{2.24}$$

It should be noted here that $\hat{\boldsymbol{a}}$ and $\hat{\boldsymbol{b}}$ are defined with a offset by the wave vector $\hat{\boldsymbol{k}}$, for example;

$$\hat{\boldsymbol{a}} \equiv \hat{a}_{(i)} - \frac{\hat{a}_{(0)}}{\hat{k}_{(0)}}\hat{k}_{(i)}, \tag{2.25}$$

and normalization[5].

Finally, the polarized radiative transfer equation is written in the invariant form (Mihalas & Mihalas 1984);

$$\frac{d\mathcal{I}}{d\lambda} = \mathcal{J} - \mathcal{K}\mathcal{I}, \tag{2.26}$$

$$\mathcal{I} = g^3\boldsymbol{I},\ \ \mathcal{J} = g^2 R(2\chi)\,\boldsymbol{j},\ \ \mathcal{K} = g^{-1}R(2\chi)\,\boldsymbol{K}\,R(-2\chi)\,, \tag{2.27}$$

where $g \equiv \nu_{\rm obs}/\nu = 1/\hat{k}^{(t)}$ is the combined factor of the gravitational redshift and Doppler effect, and ν is the photon frequency in the fluid rest frame.

Faraday coefficients (ρ_Q, ρ_U, ρ_V) can be so large in the situation of our interest that the calculation are practically impossible. To avoid such difficulty, we adopted the alternative expression of polarized components (Q, U, V), spherical Stokes parameter (R_S, Ψ_S, Φ_S), calculating these on the Poincaré sphere (Shcherbakov et al. 2012);

$$Q = R_S \sin\Psi_S \cos\Phi_S, \tag{2.28}$$

$$U = R_S \sin\Psi_S \sin\Phi_S, \tag{2.29}$$

$$V = R_S \cos\Psi_S. \tag{2.30}$$

Then we can then successfully calculate polarization fraction without divergence nor attenuation. We check the performance of our polarized GRRT code through several tests in Appendix B.

[4]Here we change the notation of magnetic field to the capital letter, $b^\mu \to B^\mu$, to avoid confusion with a basis $\hat{\boldsymbol{b}}$.

[5]This is a result of the choice of the Lorenz gauge (Shcherbakov & Huang 2011; see section 1.5.2).

Chapter 3

Polarization Images of M87: Faraday Rotation and Conversion on Black Hole Ring

Part of text in this chapter was published in Tsunetoe et al. (2020) (Tsunetoe, Y., Mineshige, S., Ohsuga, K., Kawashima, T., & Akiyama, K., *PASJ, 72, 32 (2020)*), titled as "*Polarization imaging of M87 jets by general relativistic radiative transfer calculation based on GRMHD simulations*".

We perform general relativistic radiative transfer (GRRT) calculation, taking into account full polarization in mm-submm wavelengths. The radiation in these wavelength ranges is characterized by high polarization degrees owing to substantial synchrotron emission from relativistic plasma near to the black hole. Since the polarization properties can be described in terms of the four Stokes parameters, we here simulate synchrotron emission, synchrotron self-absorption of each polarization component, and the Faraday effects between Stokes parameters (i.e., the Faraday rotation and the Faraday conversion). The polarization image obtained here reflects the distorted black hole spacetime, as well as the magnetic field configurations and the bulk motions of the plasma. We thus expect to find the black-hole spin dependence of the observed polarization images.

In particular, we here pay special attention to the properties of the circular polarization, which are amplified by the Faraday conversion of the linear polarization, in addition to the liner polarization. We will demonstrate in the present study that the circular polarization, as well as the linear polarization, contains important clues to resolving the magnetic-field structure in the emission region near the BH. Next, our axi-symmetric semi-MAD jets are stronger than SANE jets and are consistent with multi-wavelengths observations in these shape (Nakamura et al. 2018), and this enables us to compare the horizon-scale image with EHT observation more consistently. Finally, we also examine the BH spin dependence of the linear polarization maps.

This chapter is organized in the following way: In section 2, we introduce our models based

on the two-dimensional GRMHD simulation data by Nakamura et al. (2018) and describe our methods of polarized radiative transfer calculation. We then show the results of the calculated polarization images in various parameter ranges in section 3 and present discussion regarding the comparison with observations etc in section 4. A final section is devoted to conclusions.

3.1 Our Models and Methods of Calculations

Our study is in two parts as introduced in chapter 2: (1) GRMHD simulations with data taken from Nakamura et al. (2018) and (2) polarized GRRT calculations. We will outline the models adopted in this work in the following two sections.

3.1.1 GRMHD simulation model of LLAGNs with jet

Nakamura et al. (2018) simulated axisymmetric jet structure, starting with a weakly magnetized torus around a BH, by using the HARM code (Gammie et al. 2003). By adjusting parameters, such as the magnetic configuration of the jets and the minimum plasma-β in torus, they succeeded in reproducing a converging, quasi-stationary jet with a parabolic streamline of $z \propto R^{1.6}$ (with z and R being the half-width of the jet and distance from the black hole), in excellent agreement with the VLBI observations (Asada & Nakamura 2012; Doeleman et al. 2012; Hada et al. 2013;Nakamura & Asada 2013; Akiyama et al. 2015; Hada et al. 2016, and figure 15 in Nakamura et al. 2018).

The 'phi' values of $\phi \equiv \frac{\Phi}{\sqrt{\dot{M}}}$, which is defined as the normalized magnetic flux crossing the BH, are ~ 30 in our models (Nakamura et al. 2018), near to but a bit less than a popular definition of MAD state of 40-60. Therefore we refer the models as 'semi-MAD'. The magnetic field strength reaches its maximum of ≈ 50 Gauss near the black hole in our fiducial model. This value is consistent with the values obtained by the previous works regarding the M87 core region; Kino et al. (2015) report $50\mathrm{G} \leq B_{\mathrm{tot}} \leq 124\mathrm{G}$, while Chael et al. (2019) report $|B|_{r=10r_{\mathrm{g}}} \approx 20\mathrm{G}$.

The model parameters of the GRMHD simulations are the black hole mass, M_{BH}, and the black hole spin, a_{BH}. The mass accretion rate in the horizon $\dot{M}$ is not a free parameter, since we adjust this so as to reproduce the observed intensity of M87 (explained in 3.1.3). Note that density normalization can be taken arbitrarily in non-radiative MHD simulations, since density and field strength square can be scaled, as long as we fix their ratio.

3.1.2 Polarized radiative transfer calculation

We set the screen at $r = 10^4 r_{\mathrm{g}}$ from the central black hole and trace rays with the black hole being at the origin. The numerical box of radiative transfer calculation is $r \leq 100 r_{\mathrm{g}}$ with 512×512 grids. Radiation transfer calculation is made for each radiation frequency, ν. The

Reference name	a_*	$R_{\rm high}$	i	$\dot{M}[M_\odot/{\rm yr}]$	π_{230}	${\rm RM}_{\sim 230}$ [rad/m^2]	Remarks
a09R100	0.9	100	160°	1.4×10^{-3}	2.3%	-2.9×10^{5}	fiducial model
a05R100	0.5	100	160°	6.5×10^{-2}	1.1%	-6.9×10^{6}	low BH spin model
a099R100	0.99	100	160°	1.0×10^{-3}	5.9%	-4.5×10^{5}	high BH spin model
a09R10	0.9	10	160°	9.0×10^{-4}	1.4%	-3.2×10^{5}	hot disk model
a09R100-i135	0.9	100	135°	1.1×10^{-3}	0.82%	1.1×10^{7}	nearly edge-on model
a09R100-i20	0.9	100	20°	1.5×10^{-3}	1.5%	6.3×10^{4}	see section 3.6
a05R100-i20	0.5	100	20°	1.1×10^{-1}	0.55%	-9.2×10^{6}	see section 3.6
a099R100-i20	0.99	100	20°	1.0×10^{-3}	13%	-2.5×10^{4}	see section 3.6
a09R10-i20	0.9	10	20°	1.0×10^{-3}	1.6%	-1.2×10^{6}	see section 3.6
a09R100-i45	0.9	100	45°	1.2×10^{-3}	1.1%	8.1×10^{6}	see section 3.6

Table 3.1: Calculated models and calculated mass accretion rate, $\dot{M}$, polarization fraction, $\pi = \sqrt{Q^2+U^2+V^2}/I$, and rotation measure (RM) calculated from 230 & 235 GHz simulations. In all models we fix the black hole mass to be $M_{\rm BH} = 6.5\times10^9 M_\odot$ and temperature ratio between electron-proton in low-β region to be $R_{\rm low} = 1$. Free parameters are the black hole spin $a_* = a_{\rm BH}/M_{\rm BH}$, temperature ratio in high-β region $R_{\rm high}$ and inclination angle i. The mass accretion rate $\dot{M}$ is a scaling parameter to the 230 GHz-observed flux of M87, ≈ 0.5Jy.

angular diameter of the M87 BH is $r_{\rm g} = 3.8\mu$as for the distance of $D = 16.7$ Mpc (Mei et al. 2007) and the mass of $M_{\rm BH} = 6.5\times10^9 M_\odot$ (Event Horizon Telescope Collaboration et al. 2019a).

Since the GRMHD simulations only give proton temperature ($T_{\rm p}$) distributions, we need to prescribe how to determine electron temperatures, $T_{\rm e}$. In the present study, we calculate the electron temperature by using the following relation (introduced by Mościbrodzka et al. 2016),

$$\frac{T_{\rm p}}{T_{\rm e}} = R_{\rm high}\frac{\beta^2}{1+\beta^2} + R_{\rm low}\frac{1}{1+\beta^2}, \tag{3.1}$$

where β is the ratio of gas pressure to magnetic pressure (so-called plasma-β) and $R_{\rm high}$ and $R_{\rm low}$ ($\equiv 1$) are numerical constants. Roughly, $R_{\rm high}$ corresponds to the ratio of proton to electron temperatures in the inner disk, whereas $R_{\rm low}$ corresponds to the same but in the jet region. Each parameter value of calculated models in the present study will be summarized in section 2.3.

3.1.3 Parameter setting for polarized GRRT calculation

There are many model parameters in the present study, but some of them are not free parameters (see also Table 3.1 for calculated models). We fix the value of $R_{\rm low}(=1)$ in addition to the distance, D, and the black hole mass, M, as are already mentioned, while we vary the black hole spin, a, inclination angle, i (see Fig. 1), and the value of $R_{\rm high}$.

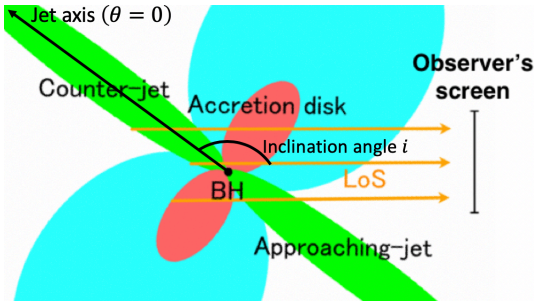

Fig. 3.1: A brief picture of our simulation. Here we defined the inclination angle i as angle between the 'jet axis' (the line of $\theta = 0$ in the coordinates) and the vector pointing from the origin to the center of screen.

Bearing the M87 case in mind, we assign the fiducial parameter (or best-fit one based on our results) set as $(a, R_{\rm high}, i) = (0.9M_{\rm BH}, 100, 160^\circ)$ (i.e., Model "a09R100"). We should also note that the mass accretion rate ($\dot{M}$) is not a free parameter but is determined so as to reproduce the observed flux of M87 core in 230 GHz to be $\simeq 0.5$ Jy (Event Horizon Telescope Collaboration et al. 2019d) in the present study. As a result, the mass accretion rate is distributed in the range of $(0.9 - 65) \times 10^{-3} M_\odot/{\rm yr}$, depending not only on the black hole spin, but also on the inclination angle (since the emission is highly anisotropic), as is shown in table 3.1.

3.2 Polarization Properties

3.2.1 Polarization images: fiducial model

We first show in the top panel of figure 3.2 the $\nu = 230$ GHz intensity (Stokes I, in the brightness temperature $T_{\rm b} \equiv \left(\frac{2k_{\rm B}\nu^2}{c^2}\right)^{-1} I_\nu$) image overlaid with the polarization vectors of our fiducial model. Here we observe the jet from below the equatorial plane ($i = 160^\circ$, see figure 3.1), so the approaching jet (or counter jet) appears in the lower (upper) half of each panel. In the color contours we can observe the black hole "shadow". We also find that the left half of a photon ring is brightened by special relativistic beaming effect due to plasma motion and gravitational blue- and red-shift due to black hole spin $a_{\rm BH} = 0.9M_{\rm BH}$.

We calculated linear polarization vectors from the Stokes Q and U images at 230 GHz and overlay them on the color contours in the upper panel. Here the length of each vector is taken to be proportional to the polarized intensity ($\sqrt{Q^2 + U^2}$). We see a rough tendency that the polarization vectors are vertically ordered on its left side. In contrast, vectors in the outer region are disordered. We should note that linear polarization properties displayed in this figure do not directly reflect magnetic field structure, since they suffer Faraday rotation (discussed in 3.3.1).

We next show the circular polarization (Stokes V) image at 230 GHz in the bottom panel of figure 3.2. The circular polarization component is large only in the side of the background

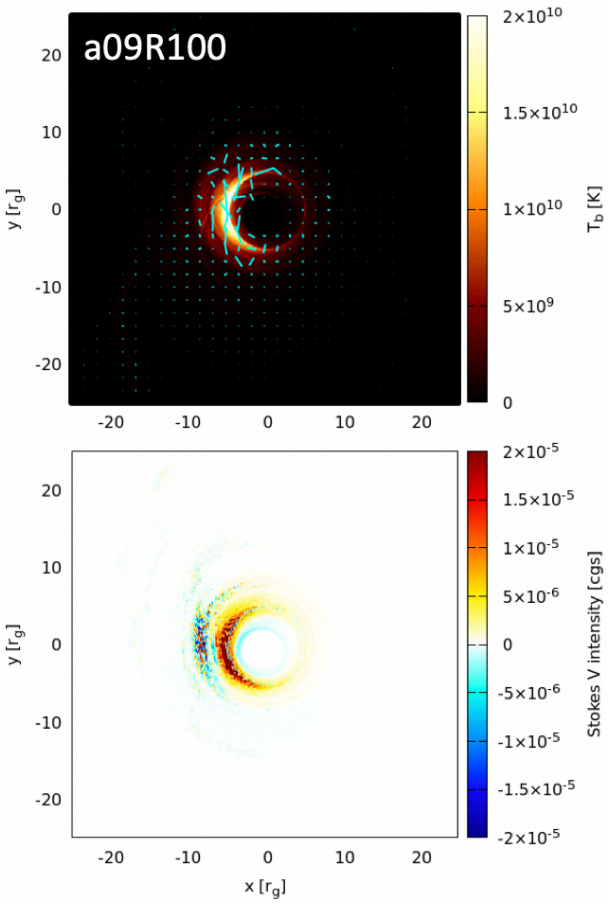

Fig. 3.2: (Top) The 230 GHz intensity map in brightness temperature $T_{\rm b} \equiv \left(2k_{\rm B}\nu^2/c^2\right)^{-1} I_\nu$ (color contours) for the fiducial model (Model a09R100) overlaid with the linear polarization vectors by EVPA (electric vector position angle) weighted with the linear-polarized intensity. (Bottom) The 230 GHz circular polarization (Stokes V, in cgs) image for the same model. The intensity of 2×10^{-5} in cgs at 230 GHz corresponds to the brightness temperature of $\approx 1.2 \times 10^9$K.

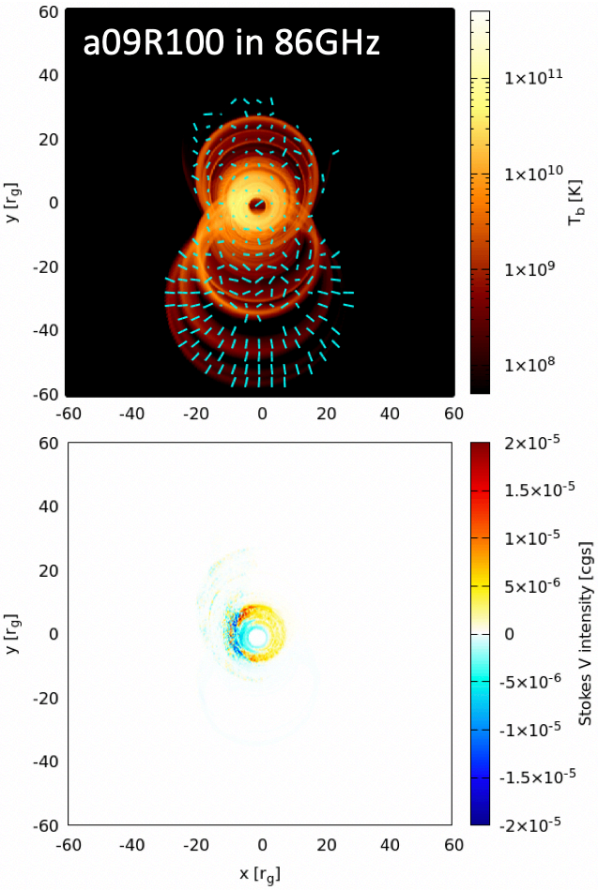

Fig. 3.3: Same as figure 3.2 but the images at 86 GHz. (Upper panel) The intensity map overlaid with the linear polarization vectors (not weighted), of the central region of M87. (Lower panel) The circular polarization (Stokes V) image. Note that the box sizes of both panels are by a factor of 2.5 larger than those in figure 3.2.

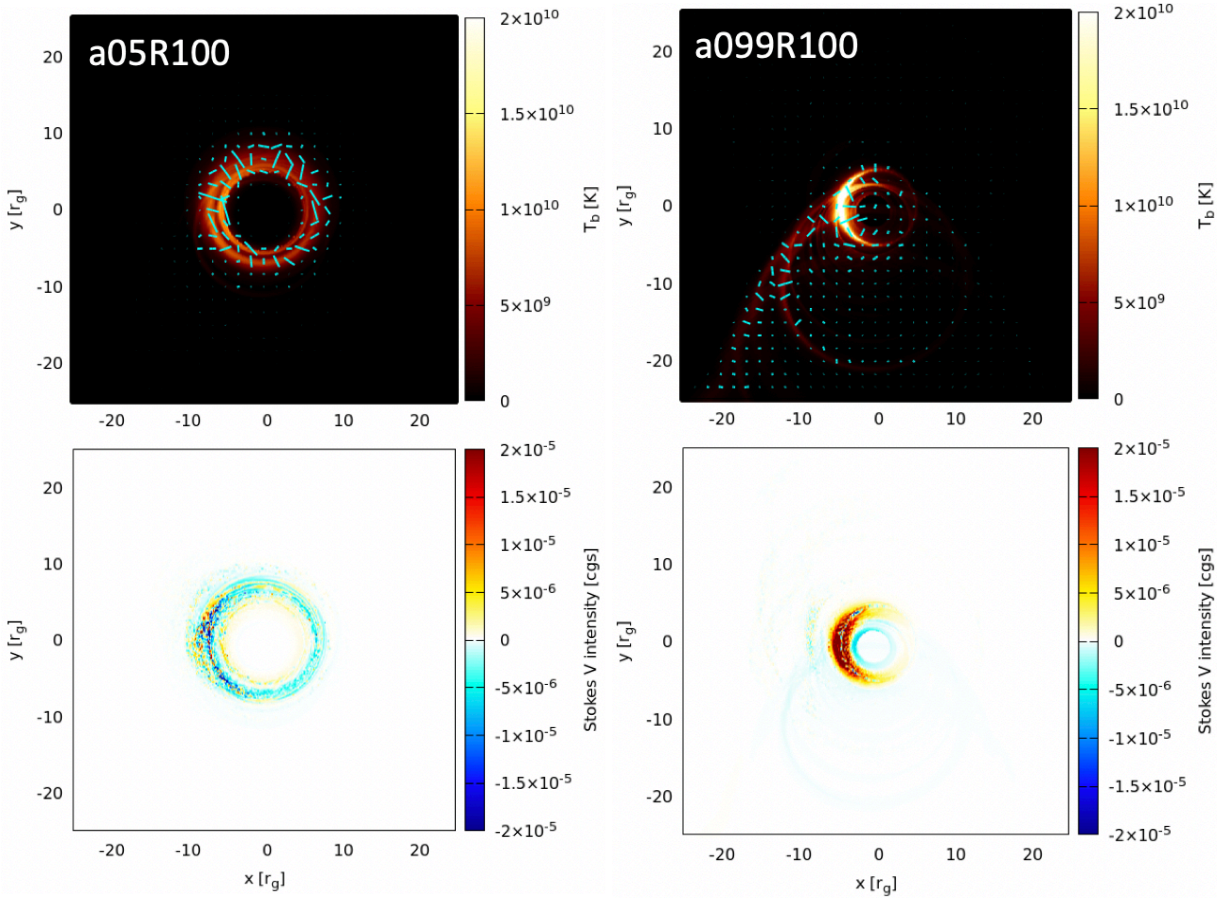

Fig. 3.4: Same as figure 3.2 but for the low-spin model with $a = 0.5M_{\rm BH}$ (left panels) and for the high-spin model with $a = 0.99M_{\rm BH}$ (right panels), respectively.

counter jet, and exhibits monochromatic, red (positive Stokes V) feature around the photon ring.

Event Horizon Telescope Collaboration et al. (2019d) captured the 230 GHz horizon-scale image of M87 showing the black hole shadow without a clear detection of an extended jet structure due to a limited dynamic range of images achievable with the 2017 EHT array. Our fiducial model gives a consistent result with this observation.

3.2.2 Polarization images at 86 GHz

We next show in figures 3.3 the intensity image overlaid with the vectors representing linear polarizations (upper panel) and the circular polarization image (lower panel) at 86 GHz. Note that the spatial scale of this figure is by a factor of 2.5 as large as that of figure 3.2. We should also note in this figure that the length of each vector in the upper panel is taken to be proportional to the linear polarization degree (i.e., $\sqrt{Q^2+U^2}/I$), not to the polarized intensity itself (i.e., $\sqrt{Q^2+U^2}$) as is the case in figure 3.2. This is to clearly display the polarization vectors in the jet regions with low intensity.

In the upper panel of figure 3.3 we can clearly observe both of the approaching jet (in

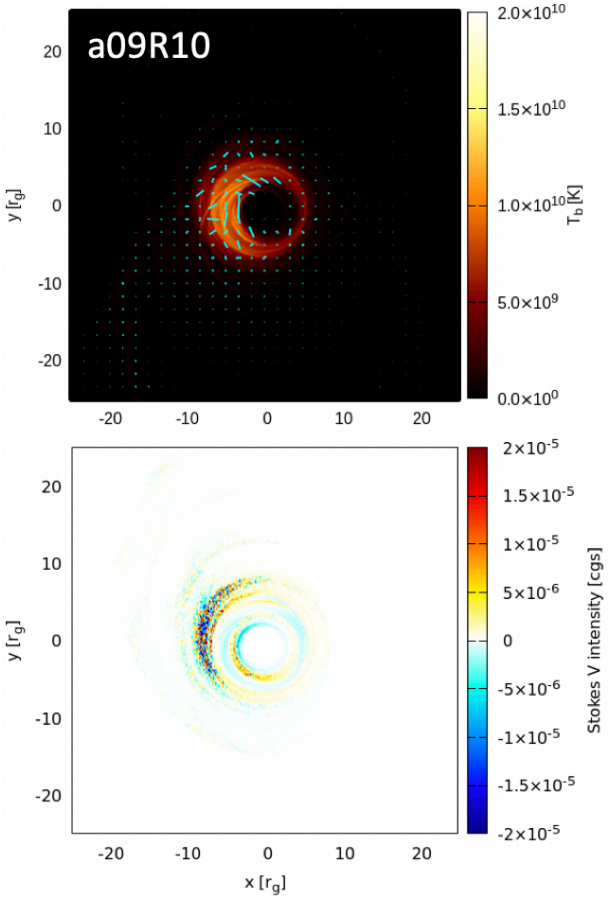

Fig. 3.5: Same as figure 3.2 but for the high-temperature disk ($R_{\rm high} = 10$) model.

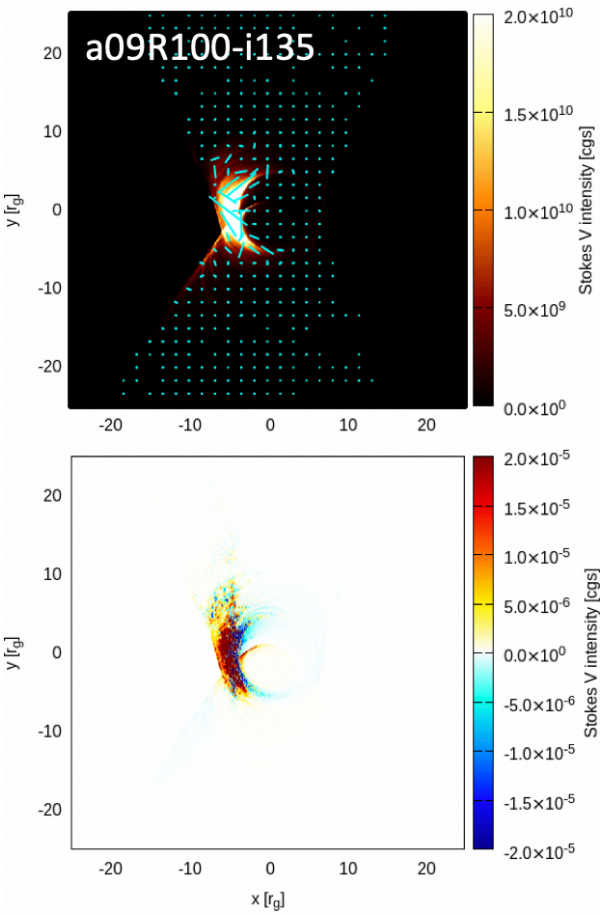

Fig. 3.6: Same as figure 3.2 but for the nearly edge-on model with $i = 135°$.

the lower part) and the counter jet (in the upper part). This contrasts figure 3.2, in which jet components are not clear at 230 GHz. We also notice that the both jets show limb-brightening. This is because high Lorentz factors are achieved at the jet rim (see figure 12 of Nakamura et al. 2018). The counter jet is also bright, and its intensity looks comparable to that of the approaching jet. This is partly because the gravitational lensing effects tend to enhance the light from the counter jet and partly because the bulk Lorentz factor is modest ($\Gamma_L \lesssim 3$) so that the boosting effects of the approaching jet cannot be so large (see also section 3.4 for discussion regarding the consistency of our calculation with the 86 GHz observation).

Let us next examine the linear and circular polarization properties in the upper and lower panels of figure 3.3, respectively. We can see ordered linear polarization vectors in the outer, downstream region in the approaching jet, but they are less ordered in the region nearer to the black hole and in the counter jet. The well-ordered polarization-vector configuration in the outer region of our calculation image agree well with the results of 86 GHz polarimetry by Hada et al. (2016). It is, however, premature to derive any useful constraints on theoretical models from this comparison, since the knot is in the ambivalent location ($\sim 0.1\mathrm{mas} \approx 27 r_{\rm g}$ from BH), where the polarization vectors exhibit a transition from well-ordered to disordered configurations. Furthermore, our simulation region ($\leq 100 r_{\rm g}$) is smaller than the beam size of their observation and the size of the M87 core. In order to make thorough comparison with the polarimetry at 86 GHz and at even lower wavelengths we need larger simulation-box calculations, as well as observation with higher resolution and better sensitivity. We also see that the circular polarization is stronger in the counter jet than in the approaching jet.

3.2.3 Polarization images: low- and high-spin models

In this subsection we compare the results of the low spin model (a05R100) and of the high spin model (a099R100) with those of the fiducial model. Figures 3.4 are the same as figure 3.2.but for the cases with a lower spin of $a = 0.5 M_{\rm BH}$ (in the left panels) and those with a high spin of $a = 0.99 M_{\rm BH}$ (in the right panels), respectively. Note that the mass accretion rate is adjusted so as to give the same total intensity as that of the observation of M87 (see Table 1).

Let us first check the intensity profiles. We immediately notice much more symmetric ring shape in the low-spin model (see the upper left panel) than in the fiducial model. This is partly because the beaming and de-beaming effects are not so large and partly because jet acceleration is not so significant when the spin is small. When the spin parameter is as large as $a = 0.99 M_{\rm BH}$, by contrast, the approaching jet image is clear (see the lower-left zone in the upper-right panel), which was not visible in the fiducial and low-spin models. This is because the plasma bulk motion is accelerated up to the Lorentz factor of $\Gamma_L \sim 3$ when the spin is large, so the approaching jet is more brightened than the counter jet by the beaming and de-beaming gap due to the bulk motion of plasmas in the jet. Further, the toroidal motion of gas blobs gives the crescent-like image. This demonstrate that the jet acceleration process strongly depends on the black hole

spin (see figure 12 of Nakamura et al. 2018).

We next examine the linear and circular polarization properties displayed in the upper and lower panels of figure 3.4. We see that the low-spin model gives rise to a moderately ordered linear polarization vectors across the symmetric ring (at $r \sim 5 - 7r_{\rm g}$ from the BH), while the high-spin model shows highly non-symmetric profile; relatively strong linear polarization is found in the left portions of the half-ring and in the region along the left edge of the approaching jet (see the lower-left region extending from the bright ring) due to the relativistic beaming effect. Circular polarization patterns in the low-spin model exhibit monochromatic structure around the photon ring, with negative Stokes V, which is common feature with the lower panel of figure 3.2. Such circular polarization patterns with positive Stokes V are also seen in the high-spin model (see the lower-right panel of figure 3.4).

3.2.4 Polarization images: hot-disk model

We next calculate the hot-disk model (Model a09R10) and show its intensity map overlaid with polarization vectors and circular polarization map in the upper and lower panels of figure 3.5, respectively. We calculate the electron temperature according to equation (3.1); that is, the smaller value of $R_{\rm high}$ means higher electron temperatures in the low-β region; i.e., the disk region, where thermal energy by far dominates magnetic energy. What happens, when the disk temperature is high? Obviously, the radiation originating from the inner disk contributes much to the total flux, leading to the enhancement of the wider image of the disk region in the intensity map (see the upper panel of figure 3.5). As a result, the photon ring, which was clear in figure 3.2, is no longer visible here. The linear polarization vectors are shorter (low polarization fraction) and show less-ordered structure. Interestingly, the circular polarization properties shown in the lower panel of figure 3.5 exhibit more noisy structure bicolored by red and blue (inconsistent in its sign) .

3.2.5 Polarization images: nearly edge-on model

Finally, we calculate the 230 GHz polarization maps of the nearly edge-on model (Model a09R100-i135) with $i = 135^\circ$ and show the results in the upper and lower panels of figure 3.6.

What are the most remarkable feature that arises by changing inclination angles? The straightforward answer to this question is that the beaming/de-beaming properties are distinct, when we vary the inclination angle, since the relativistic Doppler boosting properties are very sensitive to the line-of-sight direction. We show the linear and circular polarization properties of the low-inclination angle, nearly edge-on model in the upper and lower panels in figure 3.6, respectively, together with the intensity map. The most notable feature in this figure is that the intensity contrast between the left and right sides of the photon ring is more enhanced when i

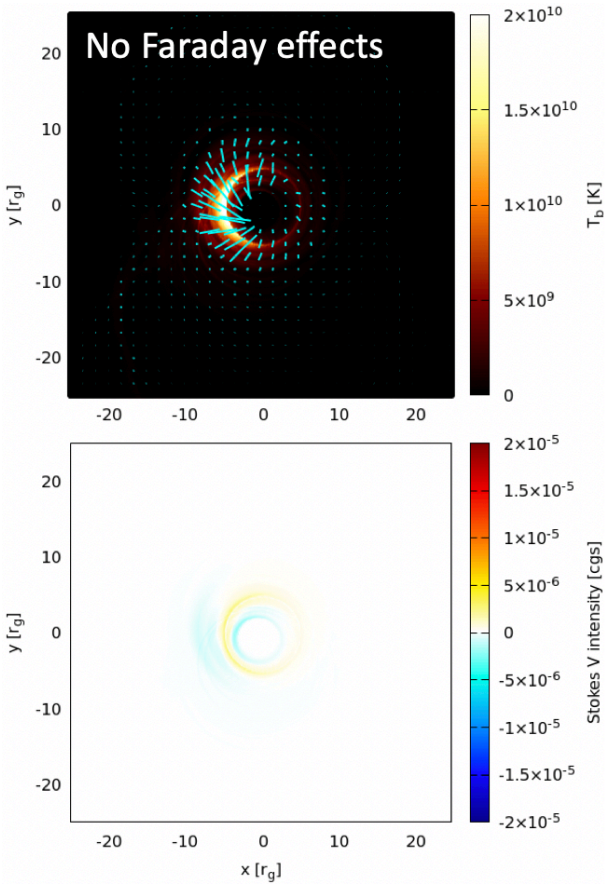

Fig. 3.7: Same as figure 3.2 but without Faraday effect. The observed frequency is 230 GHz.

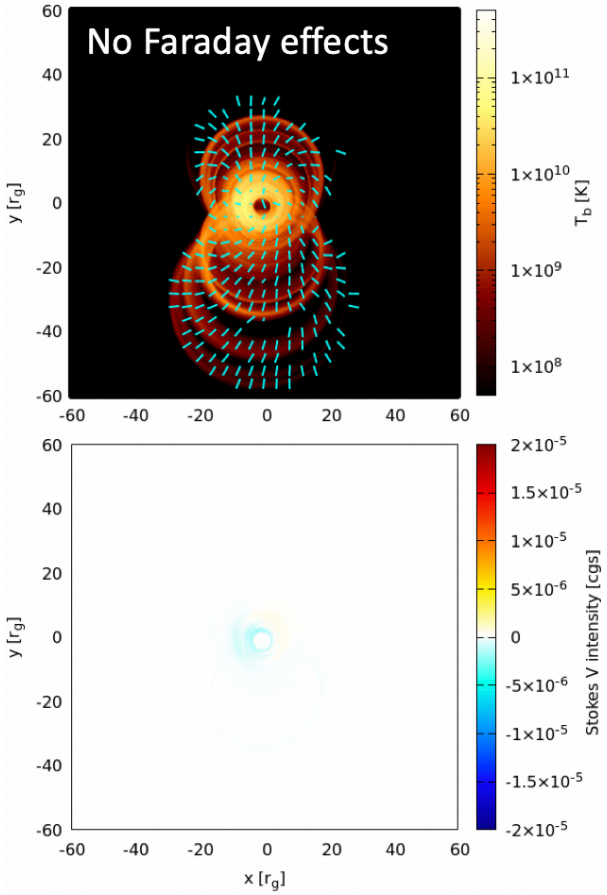

Fig. 3.8: Same as figure 3.7 but at the frequency of 86 GHz.

is large. Moreover, we can see the left-hand-side sheath of both of the approaching and counter jets. The linear polarization component is disordered in the brightest region, the left side of the photon ring. The circularly polarized light is strong in the left-hand side of this figure and in the counter jet region (in the upper part).

3.3 Discussion

3.3.1 Faraday rotation and depolarization in images

The linear polarization properties of synchrotron emission can, in principle, convey the information regarding the magnetic fields in the emitted region, however, the situation is not that simple, since the emission should have experienced the Faraday effects when passing through magnetized plasma before reaching an observer. Therefore, the polarization maps, such as those shown in figures 3.2 and 3.3, may not simply reflect the magnetic structure in the AGN jet.

In order to demonstrate that this is really the case, we performed “fake” ray-tracing calcu-

lations, in which we artificially eliminate the Faraday effects by setting $\rho_Q = \rho_U = \rho_V = 0$ in equation (2.26) and show the results in figures 3.7 and 3.8 for the observational frequencies at 230 GHz and at 86 GHz, respectively. These show the original polarization vectors; i.e., their directions are radial from the BH and thus across the photon ring, since the toroidal magnetic field components dominate near the black hole. The light emitted from the region near the BH actually suffers from Faraday rotation when passing through magnetized plasma to go out and, hence, loses the original information regarding the magnetic fields, though we can still see a hint of the original polarization vectors in the top panel of figure 3.2.

In the 5th column of table 3.1 we show the polarization fraction in the total flux at 230 GHz for each model. We notice in all models that the polarization fraction is rather small, on the order of a few percents. That is, the total polarization fraction π is suppressed, even though local polarization fraction is as large as $\sim 10\%$, since the polarization angle at each narrow area shows a diversity and strong polarizations are cancelled out in the total light in the case of nearly symmetric shape of bright regions. Conversely, asymmetrical images tend to give relatively high polarized fractions (see figure 3.6). Its top panel presents the lowest fraction 0.82% in our models, in spite of its concentrated feature. We interpret this to be a result of rather strong Faraday depolarization (see discussion in section 3.3.2).

At 86 GHz (figure 3.3 (top)), we also see that the linear polarization components from the inner flow and counter jet are largely depolarized (cf. figure 3.8), though there still remains certain amount of linear polarization in the outer approaching jet. We should also note that these lights may suffer further depolarization in the region even outside our calculation box at $r > 100r_g$.

3.3.2 Comparison with the polarimetry

Kuo et al. (2014) observed the core of M87 with the Submilli-meter Array at 230 GHz, aiming to constrain its mass accretion rate by the Faraday rotation measure (RM) measurements. They found its polarization fraction to be $\sim 1\%$ and evaluated the RM to be $-(2.1\pm1.8)\times10^5$ rad/m^2 with a 3σ confidence range between -7.5×10^5 rad/m^2 and 3.4×10^5 rad/m^2, assuming that the Faraday rotation occurs in outer accretion flow rather than in jet interior, and also assuming a power-law density profile and equipartition between the magnetic fields and electrons, they limited the mass accretion $\dot{M}$ to be below $9.2 \times 10^{-4} M_\odot \mathrm{yr}^{-1}$ at $r = 21r_S = 42r_g$.

To compare our results with the polarimetry by Kuo et al. (2014), we calculated the total polarized flux by integrating the Stokes parameters on the screen at two wavelengths, 230 and 235 GHz, and calculated the polarization fraction π and RM through the relationship of

$$\mathrm{RM} = \frac{\chi_{\mathrm{tot},1} - \chi_{\mathrm{tot},2}}{{\lambda_1}^2 - {\lambda_2}^2}, \tag{3.2}$$

where χ_{tot} is the linear polarization degree of the total flux. We summarize the calculation results for all models in the 5th and 6th columns of table 3.1.

There are some noteworthy features found in this table. First, our fiducial model (a09R100) gives reasonable values of $\pi = 2.3\%$ and $\mathrm{RM} = -2.9 \times 10^5 \mathrm{rad/m^2}$, which are fallen in the range given by the polarimetry. In this sense, the fiducial model is consistent with the polarimetry observations.

The mass accretion rate, $\dot{M} = 1.4 \times 10^{-3} M_\odot/\mathrm{yr}$, is, however, outside the allowed range estimated by Kuo et al. (2014). We interpret this discrepancy as a result of different magnetic field strengths and configurations adopted in their study and in ours. Kuo et al. (2014) assumed that (1) the magnetic energy is equal to the internal energy of electrons (i.e., equipartition) and that (2) the field direction is radial, while we found in the GRMHD simulation data that (1) magnetic energy is significantly less than the electron energy and that (2) the field is mostly toroidal. We should caution that the Faraday rotation is proportional to $\int n\vec{B}d\vec{\ell}$ (where n is the electron number density and integration is made along the line of sight vector, $\vec{\ell}$), and that we observe the M87 core from the high inclination angle, $i = 160^\circ$. Therefore, they over-estimated the contribution of magnetic field to the RM, and so under-estimated the electron density and, hence, the mass accretion rate, compared with our evaluation.

Likewise, we find that models a09R10 and a099R100 are also consistent with the polarimetry, whereas the low spin model (a05R100) and nearly edge-on model (a09R100-i135) give much higher RM values by one and two orders of magnitude, respectively. The high value of the low spin model could be associated with its high mass accretion rate, $6.5 \times 10^{-2} M_\odot/\mathrm{yr}$, higher than the constraint by Kuo et al. (2014) and also the values in other models, and this high $\dot{M}$ value could be due to weaker acceleration by weak magnetically driven outflow and jet. High accretion rates means high densities of accretion flow in the region near to the BH, leading to enhancement of the Faraday rotation effects. The high value of nearly edge-on model (a09R100-i135), $1.1 \times 10^7\ \mathrm{rad/m^2}$ can be understood in terms of the orientation effects. That is, the rays which reach us should have passed through the dense and turbulently magnetized flow near the equatorial plane and thus have experienced the Faraday effects more strongly so that they should be extremely depolarized, compared with other cases with $i = 160^\circ$.

3.3.3 Amplification mechanism of circular polarization

We see in all models bright area in the circular polarization image of the counter-jet. Especially in models with low-temperature disk (Models a09R100, a05R100, a099R100), we find a uniform, ring-like structure around the photon ring (see lower panels of figures 3.2 and 3.4). In these images the fraction of circular polarization is $\gtrsim 10\%$, much higher than the original fraction ($\lesssim 1\%$) expected in the synchrotron process. We thus conclude that such high circular polarization degree should be a result of the Faraday conversion from the linear polarization produced by the synchrotron emission. This conclusion is supported by figures 3.7 and 3.8, in which the Faraday effects are removed by hand (setting $\rho_Q = \rho_U = \rho_V = 0$), and which show rather low circular polarization.

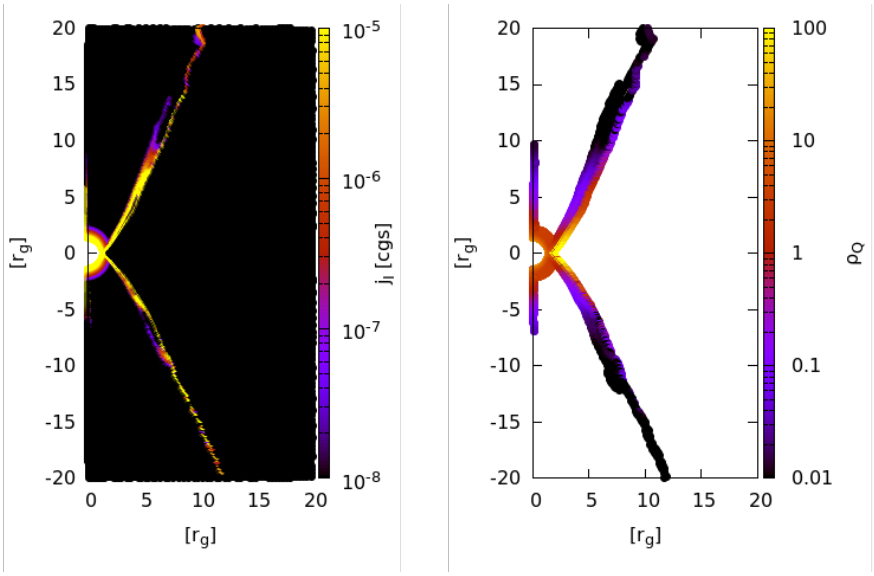

Fig. 3.9: Left: map of synchrotron emissivity (per $r_{\rm g}$) in 230 GHz estimated from magnetic strength and electron density and temperature without the effect of angle between light and field and relativistic effect by bulk motion of plasma, focused on the region near the black hole ($\sim 20r_{\rm g}$). Right: map of the Faraday conversion coefficient (per $r_{\rm g}$) in 230 GHz estimated as emissivity in the right. Only the region where $\rho_Q/\rho_V > 10^{-2}$ is plotted.

We need to make caution that such large circular polarization can be produced, if and only if both of synchrotron emission and Faraday effects occur nearly within the same place which is optically thin for synchrotron self-absorption, Faraday thick, and threaded with ordered magnetic fields. We will explain the reason for this in the following.

Let us first note that strong Faraday conversion is necessary, but is not sufficient, for producing large circular polarization. This is because the Faraday conversion not only causes the conversion from linear polarization to circular polarization, but also yields its back reaction; i.e., conversion from circular polarization to linear polarization. In the limit of very strong Faraday conversion, therefore, both of linear and circular polarization degrees should oscillate from positive to negative and from negative to positive, as radiation propagates (cf. appendix A of Mościbrodzka & Gammie 2018). Such features are not seen, at least in the circular polarization maps of the low-temperature disk models. Then, how is such uniform amplification of circular polarization realized? It will be instructive in this respect to examine the discussion by Dexter (2016) who considered an equation with uniform emission, Faraday rotation, and conversion (without absorption) in his appendix C (see also Appendix C in this thesis for the solution in more general case),

$$\frac{d}{ds}\begin{pmatrix} Q \\ U \\ V \end{pmatrix} = \begin{pmatrix} j_Q \\ j_U \\ j_V \end{pmatrix} - \begin{pmatrix} 0 & \rho_V & 0 \\ -\rho_V & 0 & \rho_Q \\ 0 & -\rho_Q & 0 \end{pmatrix}\begin{pmatrix} Q \\ U \\ V \end{pmatrix}, \tag{3.3}$$

where $j_Q, j_U, j_V, \rho_Q, \rho_V$ are the same as those in section 2.2, s is the distance, and θ_B is an angle

between the magnetic field line and the propagation vector of light-ray (line of sight). Here we can assume $\rho_U = 0$ without loss of generality. These equations have analytic solutions,

$$Q(s) = \frac{\rho_Q}{\rho^2}(j_Q\rho_Q + j_V\rho_V)s - \frac{\rho_V}{\rho^3}(j_V\rho_Q - j_Q\rho_V)\sin\rho s - \frac{j_U\rho_V}{\rho^2}(1-\cos\rho s), \tag{3.4}$$

$$U(s) = \frac{j_U}{\rho}\sin\rho s + \frac{j_Q\rho_V - j_V\rho_Q}{\rho^2}(1-\cos\rho s), \tag{3.5}$$

$$V(s) = \frac{\rho_V}{\rho^2}(j_Q\rho_Q + j_V\rho_V)s - \frac{\rho_Q}{\rho^3}(j_Q\rho_V - j_V\rho_Q)\sin\rho s + \frac{j_U\rho_Q}{\rho^2}(1-\cos\rho s), \tag{3.6}$$

here $\rho \equiv \sqrt{\rho_Q^2 + \rho_V^2}$.

We, here, consider the amplification of $V(s)$ under the condition of $|j_Q|, |j_U| \gg |j_V| \sim 0$. If the path is Faraday thin, $\rho s \ll 1$, the solutions written up to second order of ρs are

$$\begin{aligned} Q(s) &\simeq j_Q s - \frac{j_U}{2\sqrt{2}\rho}(\rho s)^2, \\ U(s) &\simeq j_U s + \frac{j_Q}{2\sqrt{2}\rho}(\rho s)^2, \\ V(s) &\simeq \frac{j_U}{2\sqrt{2}\rho}(\rho s)^2, \end{aligned} \tag{3.7}$$

(Here, we set $\rho_Q = \rho_V = \rho/\sqrt{2}$ for simplicity.) We thus understand that $V(s)$ actually increases but not faster than $Q(s)$ and $U(s)$, as long as the path length (s) is short.

If the path is Faraday thick, $\rho s \gg 1$, conversely, the first term of $Q(s)$ and $V(s)$, which is linear with respect to the path length s, dominates over other terms, and also over the terms in $U(s)$. We thus have

$$Q(s) \sim \frac{1}{2}\frac{\rho_Q^2}{\rho^2}j_Q s, \quad U(s) \sim 0, \quad V(s) \sim \frac{1}{2}\frac{\rho_Q\rho_V}{\rho^2}j_Q s \tag{3.8}$$

from eqs. 3.4 - 3.6, by eliminating the oscillating terms, which should be negligible in the limit of large Faraday optical depth, $\rho s \gg 1$. (Here, we still assume $|\rho_Q| \sim |\rho_V|$ but distinguish ρ_Q and ρ_V for the convenience of later discussion.) As a result, circular polarization degree can grow up to become comparable to that of linear polarization in the condition of balanced Faraday effects, provided that $|\rho_Q| \sim |\rho_V|$ and that Faraday optical depth is large, $\rho s \gtrsim 1$. This occurs even with negligible circular-polarized emission ($|j_V| \ll |j_Q|, |j_U|$).

In detail, the sense of amplification (positive or negative) is associated with that of Faraday rotation, which is proportional to the line-of-sight component of magnetic field ($\rho_V \propto \cos\theta_B$), and suggests the 'direction' (approaching to or away from us) of magnetic field line.

The biggest assumptions made in the above analysis resides in uniform Faraday coefficients; in other words, magnetic field lines are assumed to be well-ordered and their strengths, as well as electron temperatures, do not vary so much from the place of synchrotron emission to that of Faraday conversion. Otherwise, ρ_Q or ρ_U may change their sign, leading to reduction of the

circular polarization degree. Therefore, there are three conditions for the growth of circular polarization: (1) the synchrotron plasma is optically thin but Faraday thick. (2) The Faraday rotation and conversion are balanced there; i.e., $|\rho_Q| \sim |\rho_V|$. (3) Synchrotron emission and Faraday conversion take place roughly in the same region threaded with well-ordered magnetic fields and with nearly uniform electron temperatures.

Let us apply this analysis to our models and search for the regions where the three conditions mentioned above are met. In short, the above three conditions are satisfied in the jet rim near the black hole but only in models with low-temperature disk. We first show the place where synchrotron radiation originates from in the left panel of figure 3.9. Here we plot the contours of synchrotron emissivity at 230 GHz for our fiducial model. (Note that synchrotron emissivity in this plot is estimated simply from magnetic-field strength, electron density in the fluid rest flame, and electron temperature at that point and that relativistic effects are not considered.) Although no sigma-cutoff condition is adopted here, we find that the emission region is concentrated at the jet rim below $z \sim 8r_{\rm g}$, as is indicated by the yellow color. The reason of why no emission is found within the funnel region is that the most luminous region in our model nearly coincides with the funnel wall, where $\sigma \sim 1$, and not the region with high σ values. Note that the same feature is found in other SANE-jet model (see, e.g., Figure 12 of Mościbrodzka et al. 2016). It is important to note that contribution from the disk (inflow) is negligible in this model, since the disk temperature is relatively low ($R_{\rm high} = 100$).

Next, let us examine the place where the Faraday effects are large. We plot such regions in the right panel of figure 3.9, finding that the region similar to the yellow region in the left panel shows large value in the right panel; more precisely, the jet rim but below $z \sim 5r_{\rm g}$ shows high conversion. Thus, the high emissivity region and high conversion region are nearly identical. Furthermore, we confirm that the condition of $|\rho_Q| \sim |\rho_V|$ also holds in this rim region. This is reasonable, given that the ratio of coefficients of the Faraday effects is $|\rho_Q/\rho_V| \propto BT_e^3$ in the limit of high temperature (because we obtain $\rho_Q \propto B^2(\theta_e + K_1(\theta_e^{-1})/6K_2(\theta_e^{-1})) \sim B^2T_e$[1] and $\rho_V \propto BK_0(\theta_e^{-1})/K_2(\theta_e^{-1}) \sim BT_e^{-2}$ (Shcherbakov 2008; Dexter 2016) in the limit of high-temperature, $\theta_e \equiv k_{\rm B}T_e/m_ec^2 \gtrsim 1 \Leftrightarrow T_e \gtrsim 10^{10}$K, where $K_\alpha(x)$ is α-rank modified Bessel function), so the hotter and magnetically stronger, the higher this ratio. Furthermore, we find that only the region of near the black hole ($\lesssim 5r_g$) is Faraday thick, where toroidal magnetic fields are dominant and well-ordered toroidal fields drive the jet.

To conclude, all the conditions for the amplification of circular polarization is satisfied in the jet rim near the black hole, Hence, radiation originating from that region undergoes significant amplification of circular polarization before reaching an observer, thus producing ring-like circular polarization image. In other huge regions with large Faraday rotation circular polarization does not grow appreciably (cf. equation (A5) of Mościbrodzka & Gammie 2018). Focusing

[1]We should note that this linearity to the temperature can be suppressed depending on the balance with the observational and gyromagnetic frequencies. Nonetheless $|\rho_Q|$ are comparable with $|\rho_V|$ in the situation of interest (see also Huang & Shcherbakov 2011).

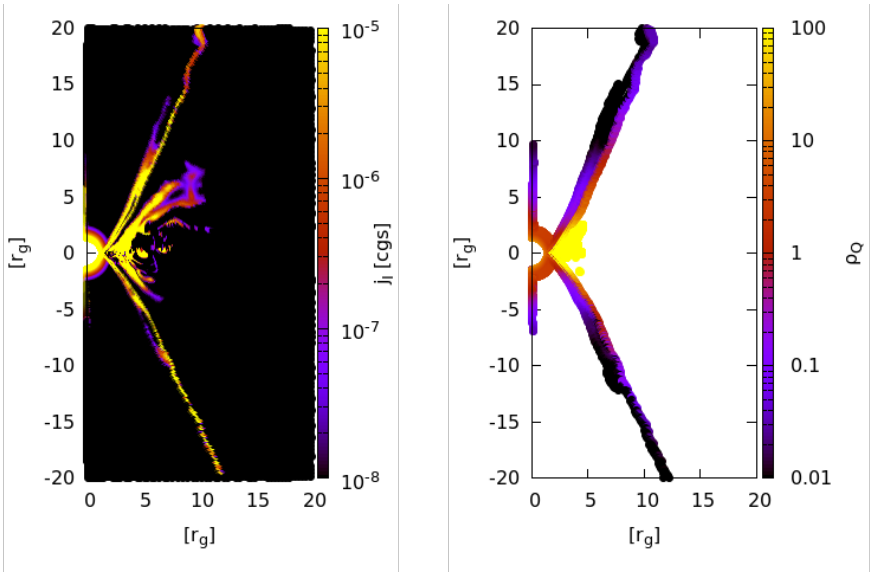

Fig. 3.10: Same maps as figure 3.9, but for the hot disk model (a09R10).

on the sign of amplified circular polarization, we can state that the low spin model a05R100 has magnetic field with different direction from other two models a09R100 and a099R100, as described above.

We finally consider the case of high-temperature disk (a09R10), which exhibits rather noisy and disordered structure in circular polarization image (see Fig. 3.5). We can see that both of the emission region and Faraday region are larger, compared with those of low-temperature models shown in figures 3.9, and extend to the inner disk. This is because the inflow part, which is in the form of RIAF (radiatively inefficient accretion flow; see, e.g., Kato et al. 2008, chap. 9), is now visible. Since the RIAF is threaded with turbulent magnetic field lines, the conditions of ordered field described above are not satisfied there. To be more precise, high temperature, which gives rise to large absolute values of the conversion coefficients (ρ_Q and ρ_U), is not sufficient to enhance CP components by conversion. In addition, magnetic field lines should have ordered structure in the whole conversion region, since otherwise the CP component disorderly varies, changing their sign and absolute values, along each path, so that the integral along the path will get smaller. This is the reason why the CP image of hot disk model (with high turbulence and high temperature) shows chaotic structure with diverse degrees of zero up to $\sim \pm 10\%$, while the CP image of fiducial model (with low turbulent and low temperature) exhibits uniform structure in its sign with the degrees of $\gtrsim 10\%$. We can thus understand why high-temperature disk model yields not so large circular polarization.

In summary, we specify the conditions that circular polarization grows up through the Faraday effects by ordered magnetic field. As a consequence, it will be possible to elucidate the magnetic field direction and temperature distribution of emission plasma, from the observation of circular polarization. It may also be possible to identify the emission regions, either of disk or jet, or both. Comparing the SANE and MAD regimes in terms of circular polarization, we can

infer that Faraday conversions would be stronger in the semi-MAD case than in the SANE case. This is because stronger and better-ordered magnetic field lines make the conversion process more effective.

3.3.4 Comparison with previous studies

Mościbrodzka et al. (2017) calculated a polarized radiative transfer for the SANE (standard and normal evolution) models of M87 for the spin parameter of $a_{\rm BH} \approx 0.94 M_{\rm BH}$, and the inclination angle of $i = 20°$. [Note that the base GRMHD models of our calculation are classified to the semi-MAD (magnetically arrested disk) model.] A big distinction between their results and ours appears in the dependence of the estimated mass accretion rate on the changes of electron temperatures in the disk (or the $R_{\rm high}$ value, see equation 3.1). According to their table 1 $\dot{M}$ varies from $9 \times 10^{-3} M_\odot/{\rm yr}$ to $1 \times 10^{-3} M_\odot/{\rm yr}$ as $R_{\rm high}$ changes from 100 to 10, while $\dot{M}$ only changes by a factor of ~ 1.5 (from $1.4 \times 10^{-3} M_\odot/{\rm yr}$ to $9.0 \times 10^{-4} M_\odot/{\rm yr}$) for the same change in $R_{\rm high}$ in our case. This is because the semi-MAD jet is more powerful than the SANE jet that the contribution of the jet emission relative to the disk emission should be much larger. As a result, the disk temperature is less important in our calculations, than in theirs, when calculating the total flux.

This different dependence also affects the observational properties of the linear polarization vectors. Their figures 6 and 7 show that the original polarization structure survives to some extent in a hot-disk models (their RH1 and RH5), while it is disordered and depolarized in a cold-disk models (RH20 and RH40). In our simulations, by contrast, Faraday rotation and depolarization are fatal even in the hot-disk model (a09R10) due probably to the strong magnetic field in the semi-MAD scheme and due also to the axial symmetry of the GRMHD simulation which we adopted.

As for the Faraday RMs, our absolute values in Models a09R100, a09R10, and a099R100 are in the same order as theirs. In addition, it might be noted that their circular polarization fraction is comparable to the linear one in all models, which is the common feature also in our calculations.

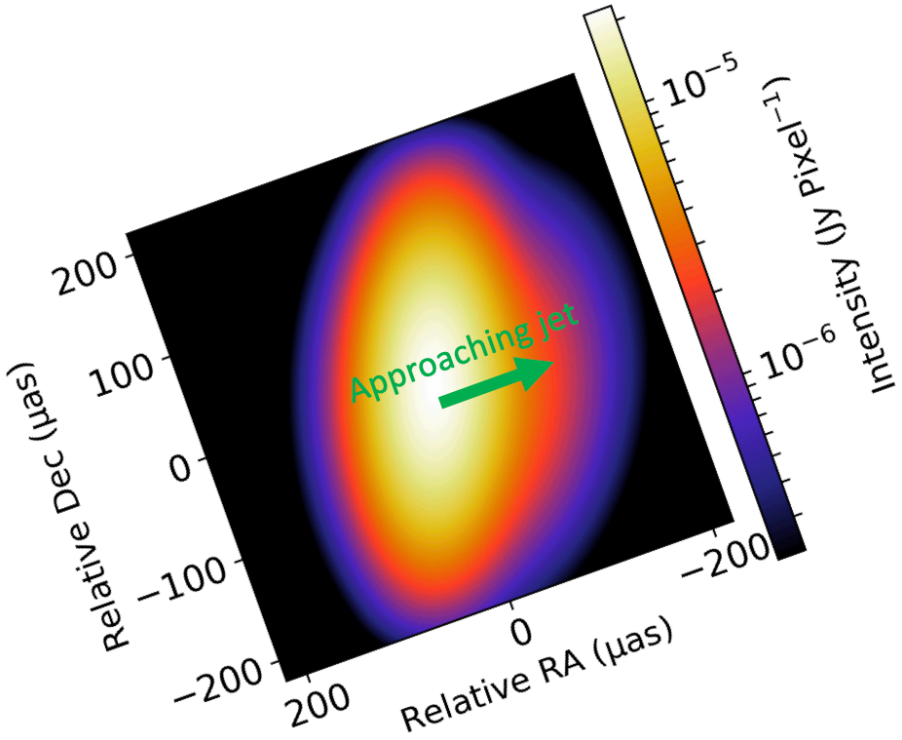

Fig. 3.11: 86 GHz intensity image of our fiducial model (cf. figure 3.3) in log scale, convolved with Gaussian beam of $\approx 70\mu\text{as} \times 200\mu\text{as}$ inclined -20° to the jet axis.

3.4 Convolved image in 86 GHz

The 86 GHz image in figure 3.3 might seem to contradict the well-known feature of M87 jet, an outstanding approaching-component as seen in larger-scale observations (cf. Hada et al. 2016; Kim et al. 2016; Walker et al. 2018). To dispel this doubt, we post-processed 86 GHz image of the fiducial model (the brightness contour of upper panel in figure 3.3) with a python-interfaced library 'SMILI' (Sparse Modeling Imaging Library for Interferometry, Akiyama et al. 2017a; Akiyama et al. 2017b), convolving the original image by Gaussian beam with the size of the 86 GHz observation (Hada et al. 2016), and show it in figure 3.11, finding it in good agreement with the observation in the scale of $\sim 100r_g \approx 0.4\text{mas}$ from the core.

3.5 Sigma cutoff

We took no sigma cutoff in the present study, whereas the sigma cutoff, in which the region with $\sigma \equiv B^2/4\pi\rho_{\rm p}c^2 > \sigma_{\rm cutoff}$ is removed in transfer calculation, is often implemented in order to avoid unphysical effects arising because of low-density floors set in the MHD simulations. To see how the results depend on the values of the sigma cutoff, we performed two additional simulations of the fiducial model (with $R_{\rm high} = 100$): one with the sigma-cutoff of $\sigma_{\rm cutoff} = 20$ and another with $\sigma_{\rm cutoff} = 1$. (The latter condition was adopted by the EHT collaboration.) Note that the mass input rate in the latter case is increased to be $\dot{M} = 2.2 \times 10^{-3} M_\odot {\rm yr}^{-1}$ to give the same radio flux of 0.5 Jy. The results are displayed in figure C1. We find no large differences from that of the fiducial model shown in figure 2, and the conclusions in the present study are not altered.

In a previous work, Chael et al. 2019, they showed different sizes of the BH-shadow among different sigma-cutoff values, since the approaching jet with high-σ values is brighter because of globally higher temperatures (see the central panel of their figure 3) and larger Lorentz factors. In our models, by contrast, the approaching jet is not so luminous to affect the size of the shadow, as seen in figure 3.9 and described in subsection 4.3, and the inclusion of the high-sigma region do not change the size of the shadow.

3.6 Polarization images: the opposite side observers

We here show linear polarization maps and circular polarization images of models in the lower half of table 3.1.3, as below. In these models, we observe the M87 jet from above the equatorial plane with inclinations of $i < 90°$, which corresponds to observations from the opposite side of the text above.

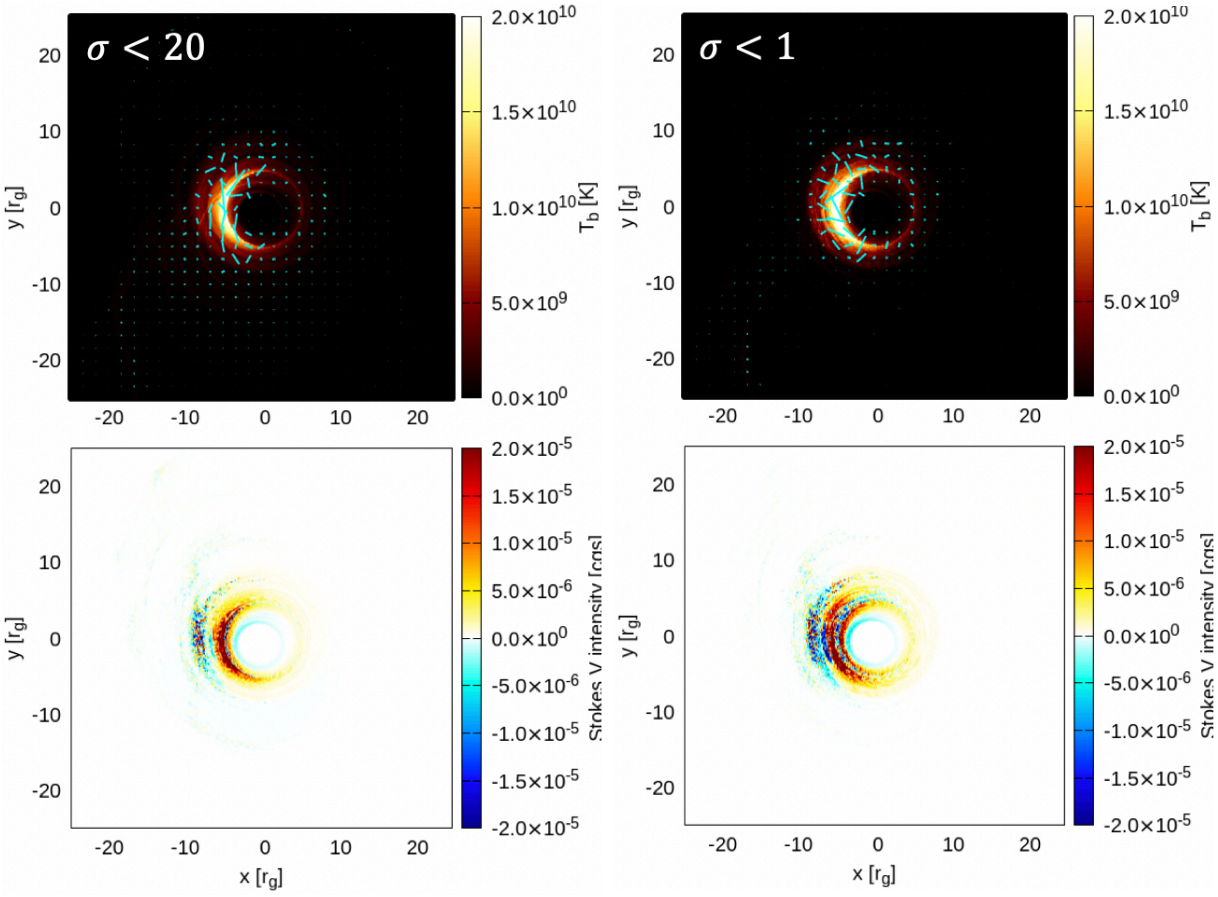

Fig. 3.12: Same as figure 2 but for the case with sigma cutoff of $\sigma_{\rm cutoff} = 20$ and the case with $\sigma_{\rm cutoff} = 1$ in the left and right panels, respectively. The accretion rate is the same as that of the fiducial model in the left panel, while it is increased to be $\dot{M} = 2.2 \times 10^{-3} M_{\odot} {\rm yr}^{-1}$ in the right panel so as to give a total radio flux of 0.5 Jy.

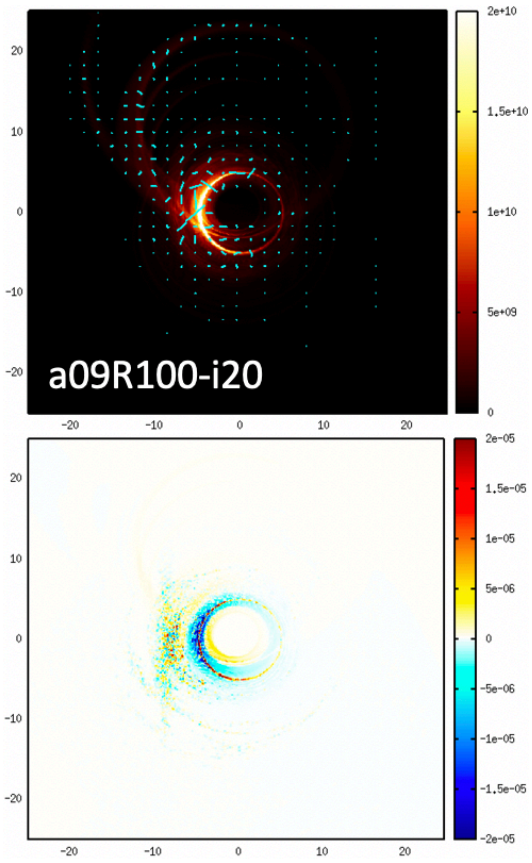

Fig. 3.13: Same as figure 3.2 but for Model a09R100-20.

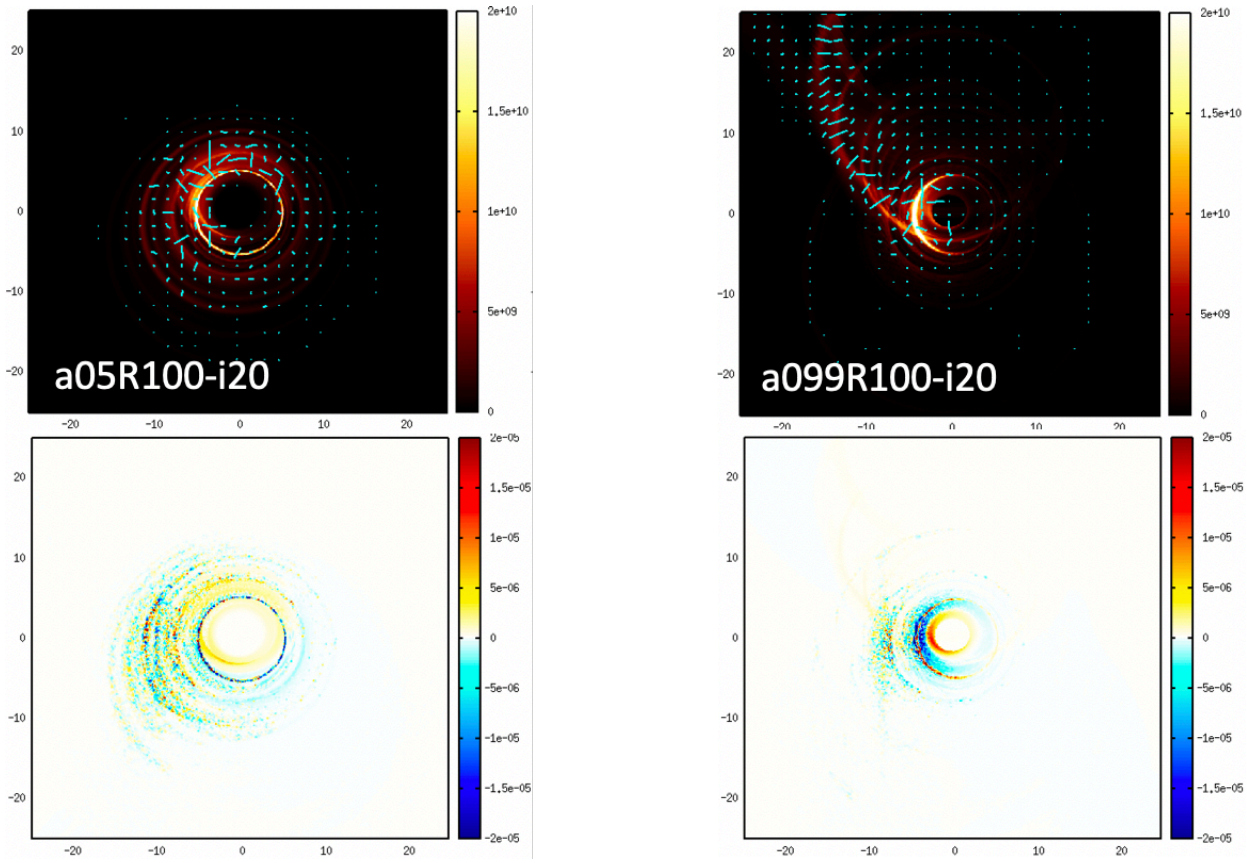

Fig. 3.14: Same as figure 3.2 but for Model a05R100-i20 (left panels) and for Model a099R100-i20 (right panels), respectively.

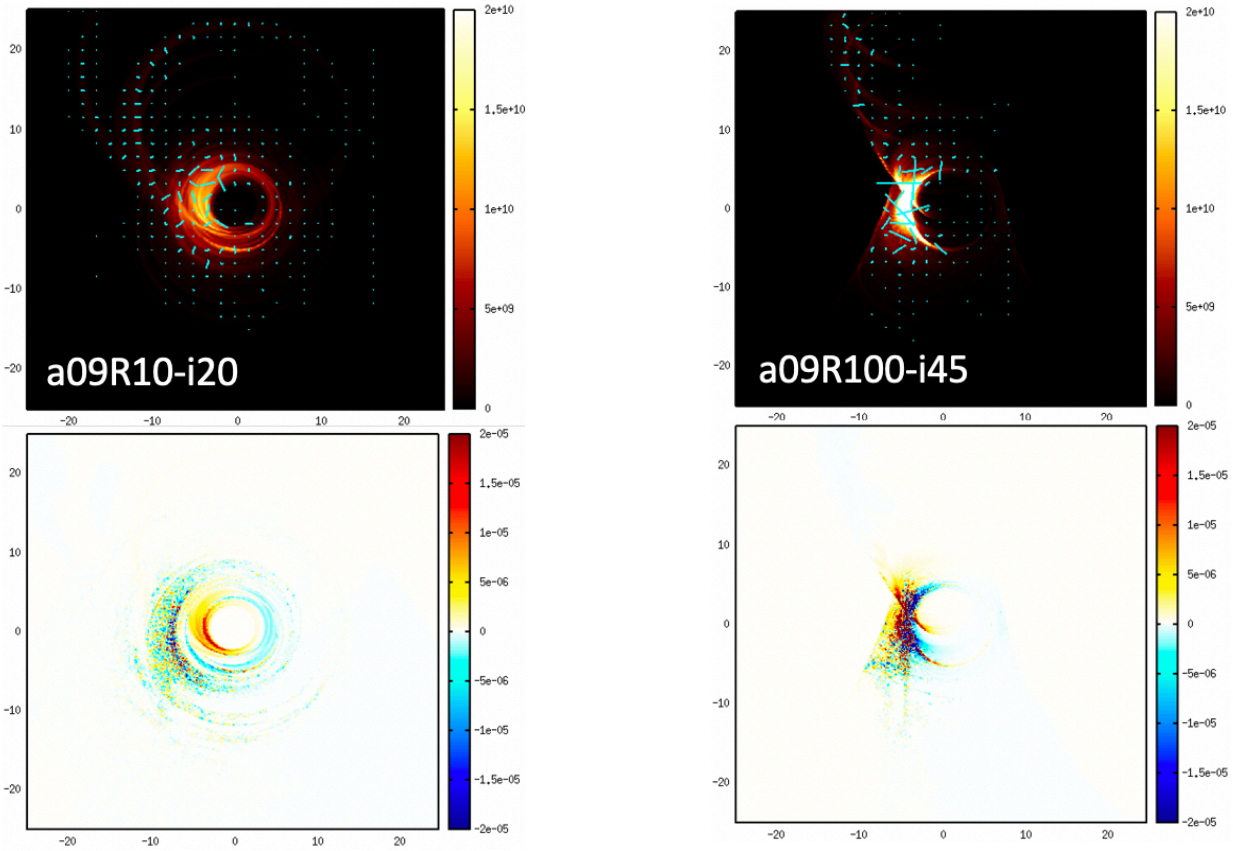

Fig. 3.15: Same as figure 3.2 but for Model a09R10-i20 (left panels) and for Model a09R100-i45 (right panels), respectively.

3.7 Conclusion

We performed general relativistic, polarimetric radiative transfer calculations based on the axisymmetric GRMHD simulation data by Nakamura et al. (2018) and made polarization images in the event-horizon scale to compare with future EHT polarimetry to elucidate the roles of magnetic fields for launching jets and outflow. Our results can be summarized in the following way:

- The calculated images at 230 GHz are sensitive to the black hole spin. Our fiducial model with the black hole spin of $a_{\rm BH} = 0.9M_{\rm BH}$, can reproduce the asymmetric crescent-shape photon ring and absence of jet features as are observed in the recent EHT observations of M87.

- We calculated linear and circular polarization maps. We found in all models that the linear polarization vectors, that can be seen at a distant observer, could be significantly modified by the Faraday rotation and depolarized so that the original information regarding the magnetic field properties may be lost at least partly. We also find that the circular polarization can grow via Faraday conversion of the linear polarization in the hot plasmas threaded by ordered magnetic fields, thus the circular polarization images provide information regarding the direction of magnetic field lines.

- We compare our results with the polarimetry of M87 core at 230 GHz in terms of rotation measure (RM) and the estimated mass accretion rate, finding that the fiducial model with $a = 0.9M_{\rm BH}$ are again favored over other models with $a = 0.5M_{\rm BH}$ or $0.99M_{\rm BH}$.

- One of the most outstanding issues is to compare the polarization images obtained by highly-resolved polarimetry of M87 and LLAGNs, to elucidate the magnetic field structures and the origins of jet eruption near the SMBH.

Chapter 4

Polarization Images of Sgr A*: Sign-Flipping and Helical Magnetic Field

Part of text in this chapter was published in Tsunetoe et al. (2021) (Tsunetoe, Y., Mineshige, S., Ohsuga, K., Kawashima, T., & Akiyama, K., *PASJ, 73, 912 (2021)*), titled as "*Polarization images of accretion flow around supermassive black holes: imprints of toroidal field structure*".

In this chapter, we calculate polarized radiative transfer of 'semi-MAD' models, with the dimensionless magnetic flux of $\phi \sim 10$ (Nakamura et al. 2018), for disk dominant case, whereas in the last chapter we studied the magnetic structure in the base region of M87 jets using jet dominated models. We use the parameters of Sgr A* and test the validity of the models by comparing it with polarization observations. Further, we will discuss the morphology of the LP and CP images due to the dominant disk through the Faraday effects (rotation and conversion) and will investigate what and to what extent we can constrain through future polarimetries, considering the interstellar scattering effect unique to Sgr A*.

The plan of this chapter is as follows: we will explain methods to obtain polarization images in section 4.1. Resultant images for three models will be shown in section 4.2, and remarkable features on them and physical processes involved there are described there. We will discuss possible effects of the interstellar scattering in future observations with EHT in subsection 4.3.1 and 4.3.2, and comparison with past observations and with other models with different inclinations and black hole spin in subsection 4.3.4 and in subsection 4.3.5 and 4.3.6, respectively.

4.1 Models

Numerical procedures of our study are in two parts: (1) GRMHD simulations with data taken from Nakamura et al. (2018), (2) polarized GRRT calculations.

Reference name	i	LP_{230}	CP_{230}	$\mathrm{RM}_{\sim 230}$ [rad/m^2]	Remarks	Figures
i30	30°	4.0%	0.8%	1.4×10^5	Face-on model	4.2, 4.7 top
i60	60°	5.8%	0.6%	-1.4×10^5	Intermediate model	4.6, 4.7 bottom
i90	90°	2.1%	−0.8%	-3.2×10^4	Edge-on model	4.5, 4.7 center
i120	120°	4.6%	0.4%	-1.2×10^5	Intermediate from below	-
i150	150°	2.0%	−3.3%	1.4×10^6	Face-on from below	4.10
a05-i60	60°	0.6%	−1.5%	-7.2×10^5	Slow spin case	-
a05-i120	120°	2.6%	−0.9%	5.4×10^5	Slow spin from below	4.12

Table 4.1: Calculated models and calculated mass accretion rate, $\dot{M}$, total LP fraction, LP $= \sqrt{Q^2+U^2}/I$, total CP fraction with sign,CP $= V/I$, where (I, Q, U, V) are the Stokes parameters, and rotation measure (RM) calculated from 230 & 235 GHz simulations. In all models we fix the black hole mass and spin to be $M_{\rm BH} = 4.5 \times 10^6 M_\odot$ and $a = 0.9 M_{\rm BH}$. In determination of electron temperature, we set $R_{\rm high} = 2$ and $R_{\rm low} = 1$ in the relation with proton temperature. Only free parameter is inclination angle i, for the top five models. We take a parameter set of $a_{\rm BH} = 0.5$ and $R_{\rm high} = 1$ for the slow-spin model in the bottom row. The mass accretion rate $\dot{M}$ of $4.0 \times 10^{-10} M_\odot$/yr ($3.5 \times 10^{-8} M_\odot$/yr) for models with $a = 0.9 M_{\rm BH}$ ($a = 0.5 M_{\rm BH}$) is a scaling parameter to the 230 GHz observed flux of Sgr A*, $\approx$ 3Jy.

4.1.1 GRMHD models of LLAGNs with weak jet

We adopted the distributions of particle density, proton temperature, magnetic field, and velocity field obtained in axi-symmetric GRMHD simulations by Nakamura et al. (2018) for our code to calculate polarized radiative transfer, as in the last chapter. The synchrotron electron temperature $T_{\rm e}$ is determined from the proton temperature $T_{\rm p}$, using the proton-to-electron temperature ratio relationship by plasma-β($\equiv 2P_{\rm gas}/B^2$) and two parameters $R_{\rm high}$ and $R_{\rm low}$ introduced in Mościbrodzka et al. (2016),

$$\frac{T_{\rm p}}{T_{\rm e}} = R_{\rm high} \frac{\beta^2}{1+\beta^2} + R_{\rm low} \frac{1}{1+\beta^2}, \tag{4.1}$$

as in the last chapter. Since the factors to convert the density and magnetic field from the GRMHD simulation's unit to the cgs unit depend on the black hole mass $M_{\rm BH}$ and mass accretion rate onto the black hole $\dot{M}$, in this study we use a commonly adopted value of $M_{\rm BH} = 4.5 \times 10^6 M_\odot$ and the distance of 8.1 kpc for Sgr A*, and scale $\dot{M}$ to reproduce its total flux of $\sim$ 3 Jy.

The purpose of the present study is to study the polarization properties of the LLAGNs which show no visible jets, in the context of disk dominant case for semi-MAD models with strong and ordered magnetic field. For this reason, we relatively suppress the jet emission (compared with the disk emission) by assigning a low value for $R_{\rm high}$. The BH spin is $a = 0.9 M_{\rm BH}$ (and $0.5 M_{\rm BH}$, see subsection 4.3.6,) and the temperature ratios in the disk and jet

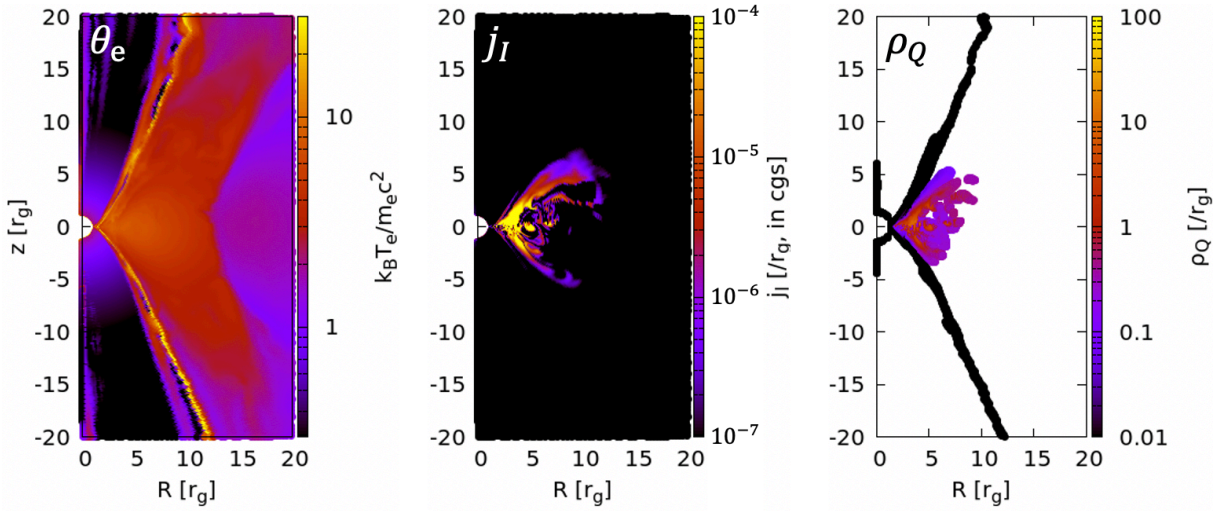

Fig. 4.1: Two-dimensional distributions of some physical quantities to be used in the polarimetric transfer simulation. Left: map of dimensionless electron temperature $\theta_{\rm e} \equiv \frac{k_{\rm B}T_{\rm e}}{m_{\rm e}c^2}$. Here, $k_{\rm B}$ is the Boltzmann constant, $T_{\rm e}$ is electron temperature, $m_{\rm e}$ is mass of electron, and c is the speed of light. Note that $\theta_{\rm e} = 1$ corresponds to $T_{\rm e} \simeq 6 \times 10^9$ K. Center: map of synchrotron emissivity j_I (in the covariant form, in cgs unit) roughly estimated from electron density, temperature, and magnetic strength. Right: that of the Faraday conversion coefficient ρ_Q (and ρ_U, also in the covariant form), but only the region where $|\rho_Q/\rho_V| > 0.01$ (ρ_V is a covariant coefficient of the Faraday rotation) is plotted. See also figures 3.9 and 3.10 of the last chapter for more details.

region are $R_{\rm high} = 2$ and $R_{\rm low} = 1$. Typical electron temperature is $\sim 10^{10}$ K in the inner disk region while $\lesssim 10^9$ K in the jet region, as seen in the left panel of figure 4.1. These parameter values are fixed in this study unless noted. Since full-array EHT data for Sgr A* are not yet available, we do not restrict ourselves to Sgr A* only, but present a typical parameter case of disk dominance and investigate to what extent the results are similar and what differences they exhibit, compared with the previous ones (the last chapter). The disk-dominated emission model is also motivated by a possible inefficient injection of the plasma inside the jet funnel in Sgr A*, which is suggested by Broderick & Tchekhovskoy (2015).

4.1.2 Polarized radiative transfer calculation

The method of full-polarimetric radiative transfer calculation is the same as that in the last chapter. We adopted the viewing angles of the spin axis of $i = 30°, 60°, 90°$, as seen in table 4.1, and the observational frequency of 230 GHz.

Here, we note about the numerical setting. In the GRMHD model, some remnant features of the initial torus, which was introduced for the sake of calculation convenience, are left in the outer part of the simulation box. In the last chapter, they do not affect the results, since the disk temperature was low and the inclination angles were mostly large ($i = 160°$) except for some special cases. In the present case with hot disk and small inclination angles, however, the

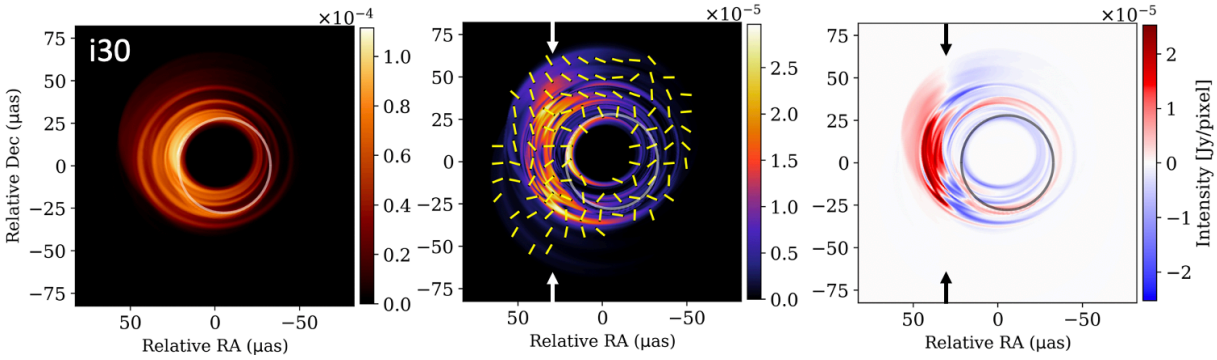

Fig. 4.2: Polarization images of Model i30. Left: total intensity (Stokes I) image. Center: Linear polarization (LP) map with color contour of LP intensity (Stokes $\sqrt{Q^2+U^2}$) and LP vectors in EVPA (electric vector position angle). Right: circular polarization (CP) image with color contour of CP intensity with sign (Stokes V). The spin axis of the black hole points upwards in the figures. Solid circles in the images correspond to the photon ring analytically obtained for the BH spin and the inclination angle (Takahashi 2004; Johannsen 2013; Wong 2021; Kawashima et al. 2021a). Two arrows in the top and bottom of the LP map and CP image indicate the position of the "separatrix" line (i.e., it lies in between the two arrows) described in subsubsection 4.2.1.1 and 4.2.1.2.

calculated images are significantly affected or sometimes dominated by such artificial features, as long as the synchrotron emission, the self-absorption effect or the Faraday effects in the initial torus are not ignored. In order to avoid this, we calculate the radiative transfer only in the limited range of $r\sin\theta \leq 10r_{\rm g}$. We confirmed that the total flux did not significantly change ($\approx$ 8% for Model i30) from the case in which the calculation was performed for the whole region $r \leq 100r_{\rm g}$, the values of polarization fraction and rotation measure (RM) varied only by a small factor ($\approx$ 1.2 for Model i30). We thus safely conclude that the omission of the outer zone in the transfer simulation does not change the main outcomes of this paper.

4.2 Results

In this section, we will show our results of polarimetric transfer simulations. We will show that the appearance of the LP vector maps and the CP images, as well as the total intensity maps, are sensitive to the inclination angle; that is, they look distinctively for edge-on and face-on observers.

4.2.1 Face-on model

Figure 4.2 shows the total intensity map, the LP vector fields, and the CP image for Model i30 from the left to the right, respectively. We take a small inclination angle, $i = 30°$; that is, we see the equatorial plane or accretion disk from nearly the face-on direction. The total intensity image is similar to those seen in the previous calculation for M87* (see, e.g., figure 2 of the last

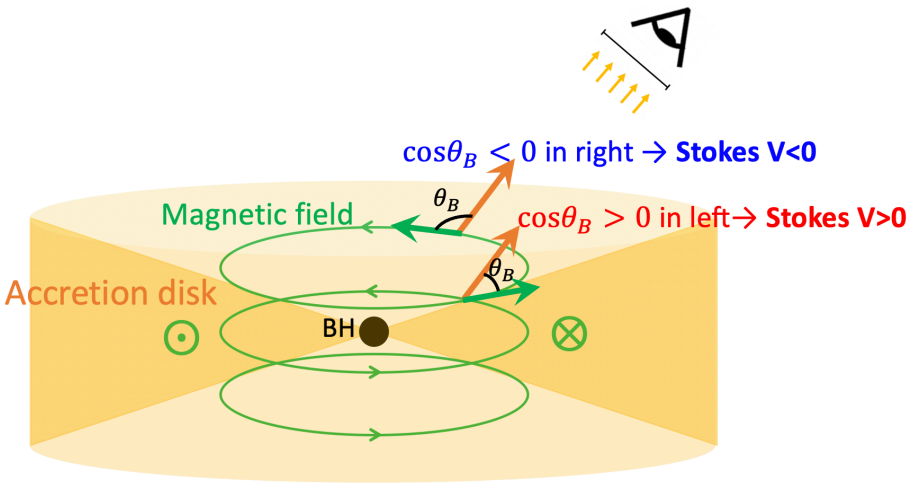

Fig. 4.3: Schematic picture of helical magnetic fields and a resultant sign-flipping CP image. Since the increased CP components here follow $V \propto \cos\theta_B$ through the Faraday rotation-induced conversion, their signs depend on whether the direction of light propagation and magnetic field line are close to parallel ($0 \leq \theta_B < \pi/2$) or anti-parallel ($\pi/2 < \theta_B \leq \pi$). Thus, in the present model with toroidally-dominant magnetic fields in the inner disk, the CP components become positive (or negative) on the left (right) side of the image.

chapter), showing a photon ring of a diameter of ~ 50 μas formed by light rays passing through close proximity of the black hole horizon, and multiple ring-like features besides the photon ring due to emissions from axi-symmetric intermittent components in the inner disk. Especially, the innermost ring-shaped feature corresponds to emission frrom the inner boundary of the disk, i.e. the innermost stable circular orbit of the particle (ISCO; Bardeen et al. 1972). The left side of the multiple rings corresponds to the approaching side of the rotational disk, and therefore is brighter than the other side because of relativistic beaming effects.

The LP image is vertically elongated and much brighter on the left side. The contrast between the left and right parts is much more enhanced in the LP image than in the total intensity image. Such a different tendency from the total intensity is due to the results of significant Faraday rotation. The LP vectors are very well ordered locally, compared with those in the last chapter (see figure 3.2). The CP image is also characterized by a ring-like feature, as seen in the last chapter. However, there is a sign change across the line of $x_{\rm image}$ (Relative RA) ~ 30 μas. We will discuss these features in detail below.

4.2.1.1 Sign reversal in the CP image

In equation 3.8 of the last chapter, we demonstrated that, CP component can be linearly amplified in synchrotron emitting, Faraday thick and optically thin plasma with ordered magnetic field as

$$V(s) \sim \frac{1}{2}\frac{\rho_Q \rho_V}{\rho_Q^2 + \rho_V^2} j_Q s, \tag{4.2}$$

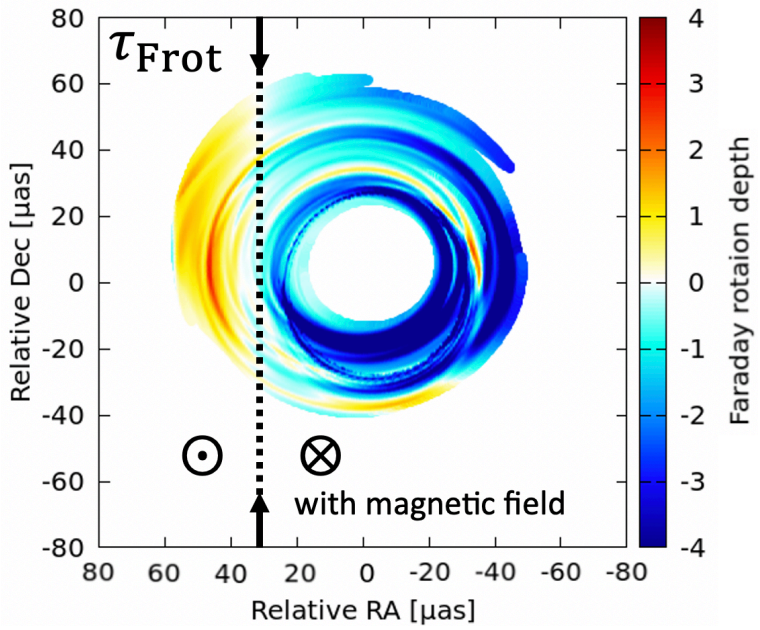

Fig. 4.4: Image map of Faraday rotation depth $\tau_{\rm Frot} \equiv \int \rho_V {\rm d}\lambda$ for Face-on model. Only light rays with $\tau_{\rm Fcon} \equiv \int \sqrt{{\rho_Q}^2 + {\rho_U}^2}{\rm d}\lambda > 0.2$ are plotted, focusing on the rays whose CP components can significantly be amplified.

where ρ_Q and ρ_V are coefficients of the Faraday conversion and rotation, and j_Q is emissivity of LP component. As shown in the central and right panels of figure 4.1, the region where synchrotron emission and well-balanced Faraday effects occurs are distributed in the inner disk near the black hole ($\lesssim 5r_{\rm g}$), more widely than in the last chapter. Thus the CP amplification significantly occurs here. In a previous work, Homan et al. (2009) introduced a combination of Faraday rotation and conversion to model the CP observed in a quasar 3C 279, mentioned it as 'rotation-driven conversion'. Equation (4.2) is an approximate form, ignoring oscillation terms, of the one derived by Dexter (2016) (see their appendix C).

Since the CP is amplified through the relation, $V(s) \propto \rho_V \propto \cos\theta_B$, an important key factor of amplification is $\theta_{\rm B}$, angle between the line of sight and the direction of magnetic field lines. This means that the sign (or direction) of the CP amplification depends on whether the line of sight and the direction of magnetic field line are close to parallel ($0 \leq \theta_B < \pi/2$) or anti-parallel ($\pi/2 < \theta_B \leq \pi$). In the present model, magnetic field in the amplification region (i.e., the inner disk) is toroidally dominated, so that the sign of $\cos\theta_B$ should be positive (or negative) on the left (right) side of the observational screen, as pictured in figure **??**. Here, we define the depth of the Faraday rotation as $\tau_{\rm Frot} \equiv \int \rho_V {\rm d}\lambda$, where λ is an affine parameter of a light path, and illustrate the Faraday rotation map for Model i30 in figure 4.4. We find in this figure that the positive and negative sign reversal occurs across the line of $x_{\rm image} \approx 30\ \mu$as[1]. In

[1]The border is not at $x_{\rm image} = 0$, because of the parallax (aberration) effects of special relativity by bulk motion of plasma. See subsection 4.4 for details.

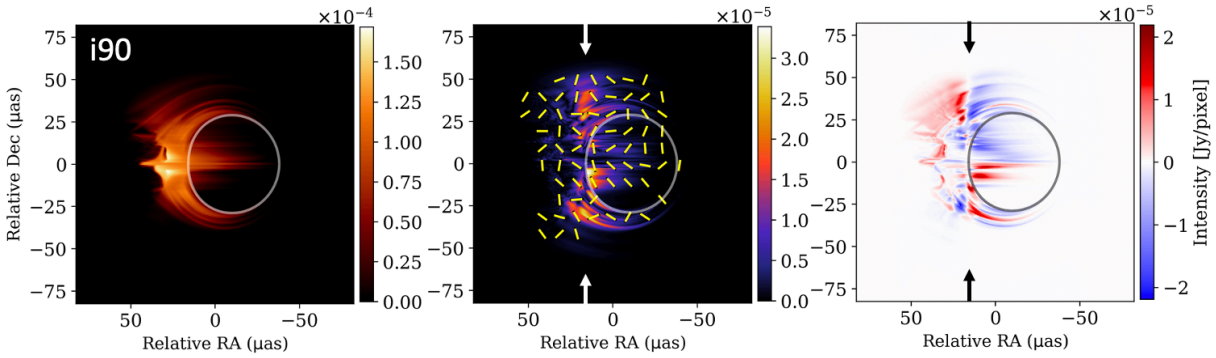

Fig. 4.5: Same as Fig. 4.2 but for Model i90.

the CP image shown in the right panel of figure 4.2, the CP component changes its sign across the line at $x_{\rm image} \approx 30$ μas, although there are some exceptional contaminants. We can thus concluded that the sign reversal on the CP image traces the direction of Faraday rotation on the screen, and reflects the toroidal magnetic structure in the inner disk.

4.2.1.2 The LP flux on the CP separatrix

The LP image in the central panel of figure 4.2 has the vertically elongated feature, as mentioned above, at $x_{\rm image} \approx 30$ μas, where the CP components changes its sign in the right panel. Thus, the LP flux tends to be enhanced where the CP flux vanishes. This brightened LP flux on the "separatrix" of the CP component can be easily explained in relation to the above statement about the angle dependence of the Faraday rotation.

As seen in figure 4.4, the Faraday rotation becomes very weak ($\tau_{\rm Frot} \ll 1$) in the case where the toroidal magnetic field becomes perpendicular with the line of sight at $x_{\rm image} \approx 30$ μas. Thus LP components are not Faraday-rotated so that the CP component should vanish around the vertical line of $x_{\rm image} \approx 30$ μas. In other regions on the image, the Faraday rotation depths are relatively high ($|\tau_{\rm Frot}| \sim 1$) regardless of their sign, thus the LP vectors are Faraday-depolarized and decline their polarized fractions. There, CP components are amplified to positive (or negative) values on the left (right) side of the separatrix as a consequence of the Faraday rotation. In other words, the sign reversal of the CP components and the large values of the LP component are mutually related; the Faraday depolarization processes are inefficient around the separatrix (where $\theta_B \approx \pi/2$), which results in large LP components and negligible CP components. Therefore, these features on the polarimetric images suggest that, we can expect to give a strong constraint to the configuration of magnetic structure, through comparison between linear and circular polarimetry in future observations.

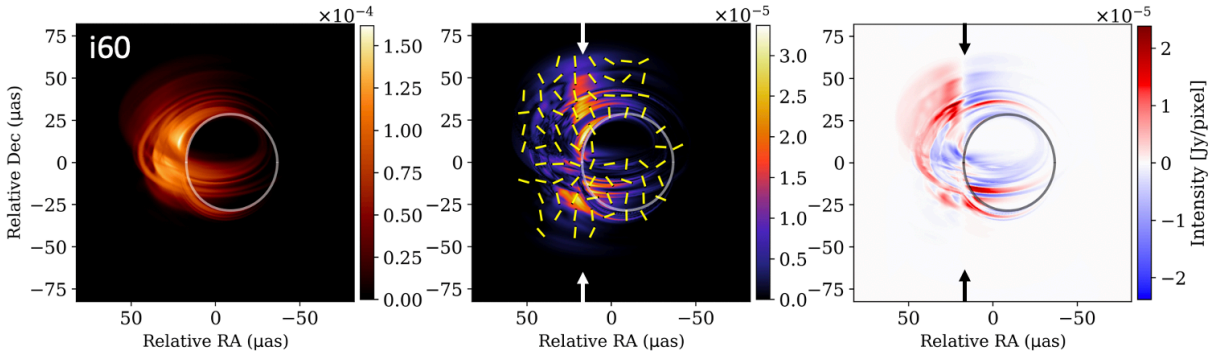

Fig. 4.6: Same as Fig. 4.2 but for Model i60.

4.2.2 Edge-on model

Figures 4.5 illustrate the results of Model i90 with a $i = 90°$ inclination, i.e., the disk is seen from an edge-on observer. Total intensity image in the left panel shows a triple-forked shape. Note that the image is brighter on the left side, while the ring-like part is fainter. This is because the optically thick disk with high electron temperature and density appears on the image near the equatorial plane, when seen from the edge-on direction. Further, the relativistic beaming effect due to the Keplerian rotation gives an asymmetric feature of the "crescent"-shaped shadow, in addition to the foreground disk component. Similar fork-like features due to the asymmetric shadow and the foreground disk can also be seen in edge-on cases in previous works (Mościbrodzka et al. 2014; Pu & Broderick 2018; Anantua et al. 2020).

The LP components in the central panel are also brighter on the left side, but fainter at the 'root' of the triple-forked, which is the brightest in the total intensity image. The LP vectors have different orientations in the upper and lower branches of the triple-forked image, indicating an asymmetry in the Faraday rotation effects. The CP image in the right panel is bright tracing the fork and contains the sign reversal at around $x_{\rm image} \approx 15$ μas. In addition, it is interesting to note another sign reversal occurring in the upper and lower portions across the line of $y_{\rm image} = 0$. This latter sign reversal in vertical direction reflects the fact that the direction of magnetic field is opposite above and below the equatorial plane, because the magnetic field lines are frame-dragged by the rotational motion of the disk. Comparing LP and CP images, we also see the features due to the helical field structure, described in the previous section for the face-on model. In both of the above and below the equatorial plane, the bright LP flux region is vertically elongated at around $x_{\rm image} \approx 15$ μas, where the signs of the CP components change.

4.2.3 Intermediate model

Figure 4.6 shows the results of the cases with $i = 60°$, which is often used as a 'conservative' value for Sgr A*. In short, the resultant images and polarization features are just in between the nearly face-on case (Figure 4.2) and the edge-on case (Figure 4.5). We can see in the total

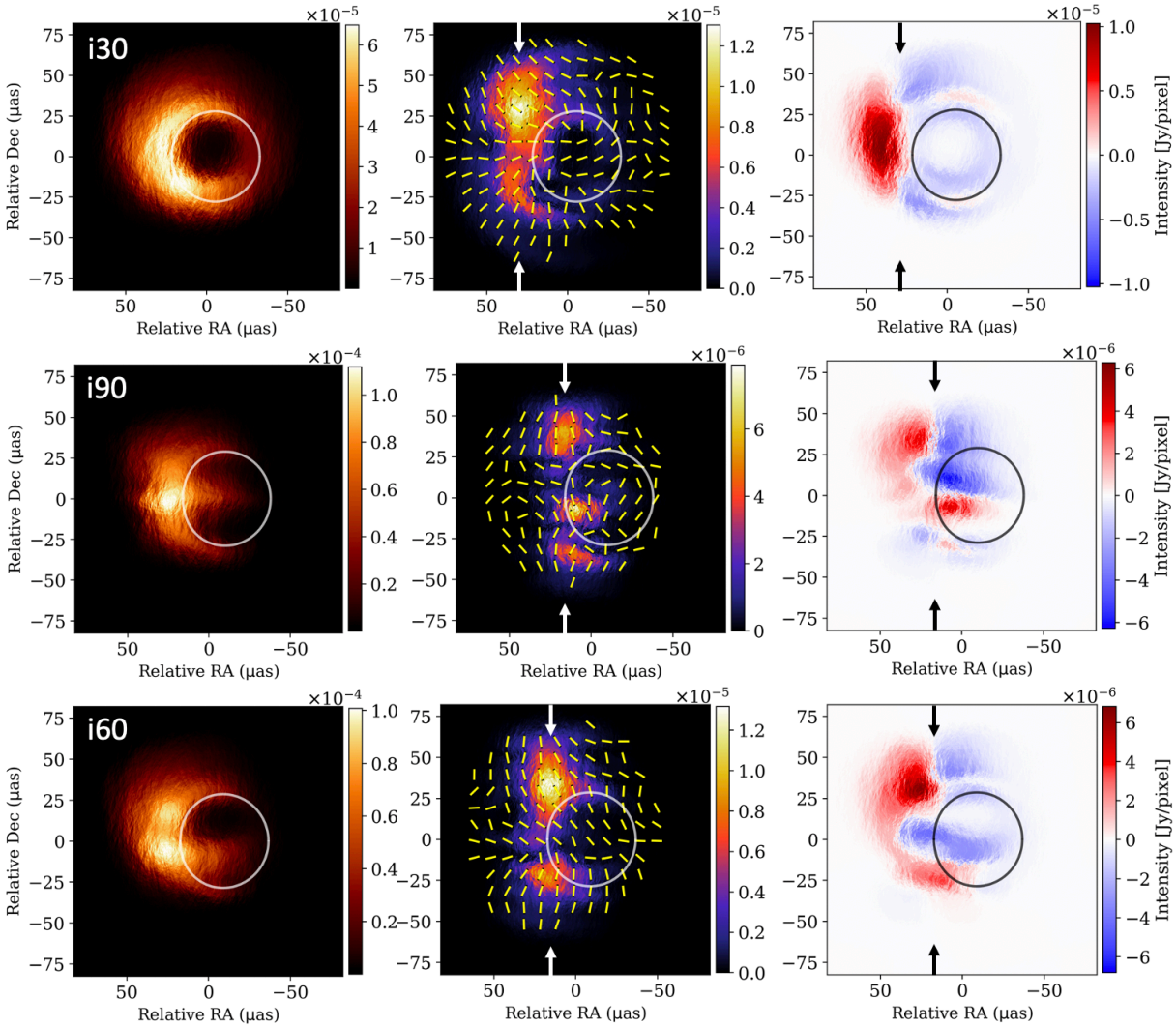

Fig. 4.7: Top to bottom: scatttered images of Face-on (i30), Edge-on (i90), and Intermediate (i60) model, respectively. Left to Right: the total intensity images, the LP maps, and the CP images. Two arrows on the top and bottom of the LP maps and the CP images correspond to those in the raw images in Fig. 4.2, 4.5, and 4.6.

intensity map both of a ring shape and a dim disk feature. This image is consistent with their images for SANE models by a previous work by Chael et al. (2018), in terms of composition of the photon ring and foreground disk relativistically beamed in the left side on the image.

The LP intensity is brighter on the left side, but fainter near the base of the fork-like, as in the edge-on model. The polarization vectors are well ordered in the upper half of the image, but are relatively disordered in the lower half. This LP map can be clearly compared with those in Jiménez-Rosales & Dexter (2018), since it has the base of an axi-symmetric GRMHD model and a moderate inclination in common with theirs. Our LP map of Model i60 resembles the bottom right panel of their figure 2 in the ordered upper-half of the image and the disordered lower-half, as described above, in addition to the Stokes I image consisting of the photon ring and the disk. Note that their LP maps comprise of the color contour of Stokes I and the LP vectors. Next we focus on their models with total flux of $F_\nu = 3\mathrm{Jy}$ and a temperature parameter of $\mu = 2$ to compare the model parameters, noting that the latter μ corresponds with our $R_{\rm high}$. They found accretion rates of $\dot{M} \simeq 4 \times 10^{-10} - 5 \times 10^9 M_\odot \mathrm{yr}^{-1}$, image-averaged Faraday rotation depths of $\langle \tau_{\rm Frot} \rangle \simeq 1 - 10$, and the net linear polarization fractions of $\pi \leq 5\%$. All of these ranges of values are consistent with ours for Model i60.

The CP tends to be respectively positive and negative on the left and right side of the border at $x_{\rm image} \approx 15\ \mu\mathrm{as}$, similarly to the above models, although there exist minor exceptional components. These 'contaminants' appear due to the violation of the conditions for the CP amplifications (see subsubsection 4.2.1.1); that is, due to large optical depth and/or significant turbulent field configurations.

In the central panels of figures 4.2, 4.5, and 4.6, the LP flux is weaker on the photon ring than otherwise. There are two main reasons for these depolarizations: (1) Light rays are strongly bundled around the photon ring so that they become Faraday thick ($\tau_{\rm Frot} \sim 5 - 10$) at 230 GHz because of long path lengths, while they are moderately thin ($\tau_{\rm Frot} \sim 1$) other area on the images (see figure 4.4 for Model i30). Therefore, the LP components are strongly depolarized on the photon ring. (2) The rays emitted from distinct areas with different magnetic field configurations (producing different polarization components) are mixed together due to the photon sphere effects, leading to the cancellation of LP components. We wish to remind that the polarization angles vary between the direct ($n = 0$; n is the number of half-orbits) and indirect ($n = 1, 2, 3, ...$) images (see Himwich et al. 2020). In fact, Jiménez-Rosales et al. (2021) reported the depolarization of the photon ring by a factor of ~ 2 by subtracting the LP flux from the total flux in each pixel. Note that the depolarization of the LP flux can occur due to the second effect, even if the plasma is Faraday thin and the magnetic fields are ordered (which may occur, for example, at higher frequencies).

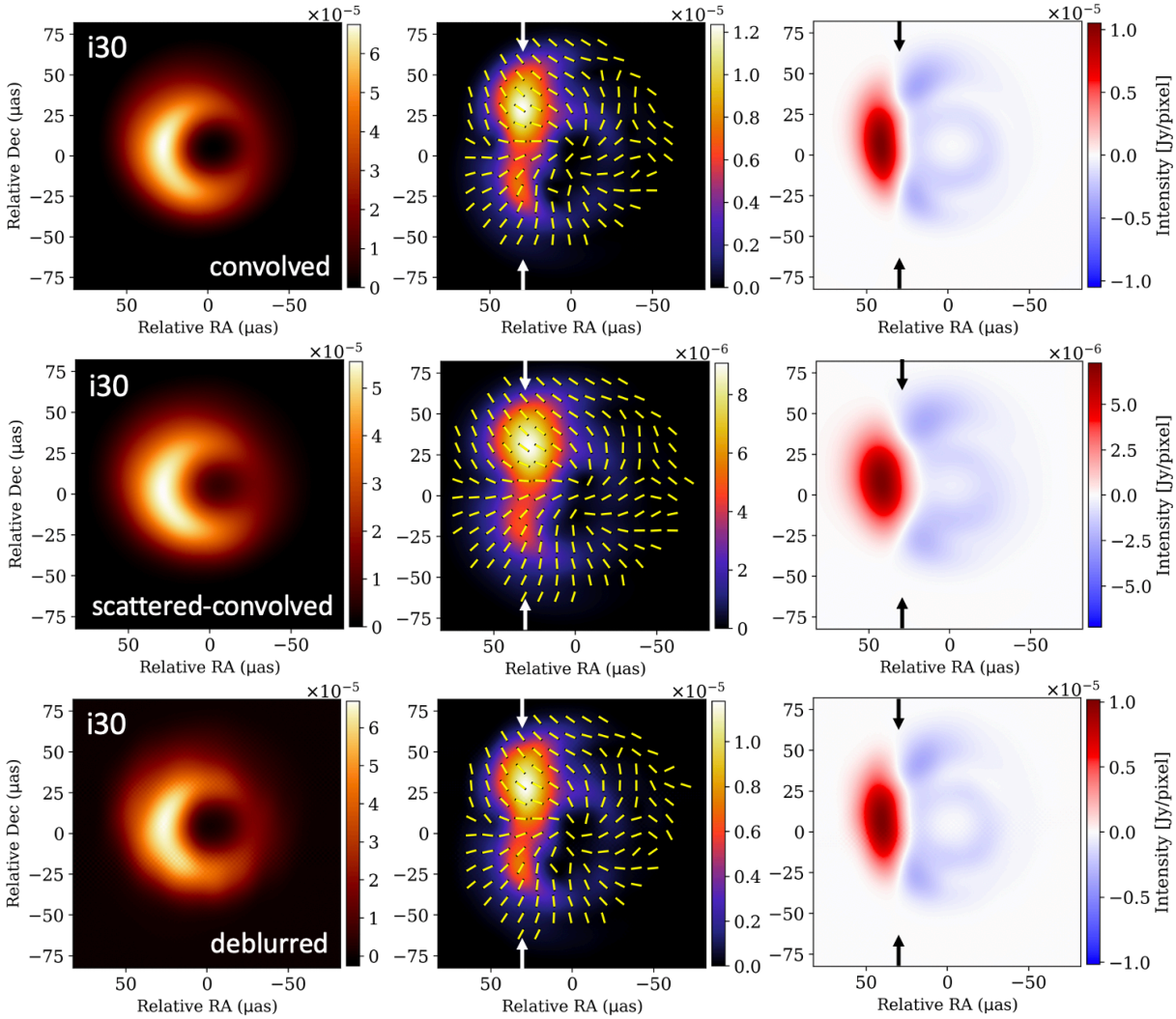

Fig. 4.8: Top: unreal images for Model i30 convolved with Gaussian beam of 17 μas without the scattering effects. Middle: mock-observational images scattered and Gaussian-convolved. Bottom: scattered, convolved, and deblurred images. Left to Right: the total intensity images, the LP maps, and the CP images. Two arrows on the top and bottom of the LP maps and the CP images correspond to those in the raw and scattered images.

4.3 Discussion

4.3.1 Scattering effects in interstellar medium

In the previous section, we presented the 'raw' polarization images from radiative transfer calculations and explained the physical processes producing the notable features. However, in actual observations of Sgr A* it is known that the tenuous interstellar plasma along the light of sights scatters its radio waves from the object, affecting its appearance in radio wavelengths (Davies et al. 1976). The scattering effects on Sgr A* is in the regime of the strong scattering (e.g. Narayan 1992), where their image distortion is well described with two subdominant effects, diffractive and refractive scattering (Blandford & Narayan 1985; Narayan & Goodman 1989; Goodman & Narayan 1989). Diffractive scattering will cause the angular broadening, described as the blurring convolution of the image with a scattering kernel (e.g. Fish et al. 2014). On the other hand, refractive scattering will create stochastic compact substructures on the image (Johnson et al. 2015; Johnson & Narayan 2016; Psaltis et al. 2018; Johnson et al. 2018). In the present work, we implement these scattering effects into our polarimetric images with two software libraries `SMILI` (Akiyama et al. 2017a, b) and `eht-imaging` (Chael et al. 2016; 2018).

4.3.1.1 Ring-like versus fork-like features in Stokes I images

In figure 4.7, we show scattered images of all three models shown in section 4.2. The images at 230 GHz are blurred with the diffractive kernel of $\sim 10\mu$as. In addition, the refractive effects introduce substructures into the images, although they do not affect the features discussed here. The scattered images in the left column, of total intensity, give the feature referred below as ring-like and fork-like for the face-on model i30 and edge-on model i90, respectively. In the intermediate model i60, the image has the intermediate feature of the small shadow in the upper half and the foreground disk in the lower half. These results imply that we may constrain the inclination angle for Sgr A* through morphology of the image, with the ring extraction from the image (Psaltis et al. 2015; Kuramochi et al. 2018; Event Horizon Telescope Collaboration et al. 2019d), although their dependence on the time-variability and three-dimensional features in the flaring and non-flaring states should be checked in future works.

4.3.1.2 Morphology of linear and circular polarimetric images

As shown in the images in the right column of figures 4.7, the scattered CP images still retain the characteristic separatrix features; the CP component is positive (or negative) in the left (right) parts. Rather, these features in the scattered images are simpler and even more enhanced than in the raw CP images (see figures 4.2, 4.5, and 4.6), because the additional minor features tend to be erased by the diffractive blurring effect. The scattered LP images in the central column of figures 4.7 clearly exhibit the brightened-on-separatrix features explained in subsubsection

4.2.1.2. Namely, we see that the LP component flux reaches its maximum, while the sign of the CP component is reversed. We thus conclude that the information of magnetic field structures around the black hole will be mostly preserved even with the scattering effects. If we find the separatrix feature, in particular, that will be a good indicator of toroidal-dominated field structures. In Gold et al. (2017), the LP and CP images (also including the scattering effects) for two SANE models shows similar features (see their figure 7). Especially, their `SANE_dipole-jet` model, with inclination of $i = 126^\circ$ and spin of $a = 0.92M_{\rm BH}$, gives the CP image with the vertical separatrix at $x_{\rm image} \approx 15 - 20\ \mu$as and the LP component brightened along the separatrix.

4.3.2 Capture of the polarimetric features in future observations

In the last subsection, we demonstrated that the major features in our raw polarization images (so intrinsic to plasma and radiative physics in the object Sgr A*) are resilient to scattering effects. Here, we will discuss the feasibilities for us to capture the features at the angular resolution of the EHT, by blurring the images of our representative Model i30. Here, we adopt a blurring Gaussian beam size of 17 μas, a resolution expected in recent and future EHT observations for Sgr A* at 230 GHz (Event Horizon Telescope Collaboration et al. 2019e).

Here, we show three types of processed images to demonstrate how scattering and its popular mitigation work on our simulation images. First, we give beam-convolved unscattered images (i.e. figure 2 images convolved with the beam) in the top of Figure 7, for an ideal observed image without scattering effects. Second, we yield beam-convolved scattered images to show images with full observing effects (i.e. we convolve the scattered images in the top of figure 4.7) in the middle of figure 4.8. We finally show beam-convolved images with the mitigation of diffractive scattering effects by de-blurring the scattered images with the diffractive scattering kernel (Fish et al. 2014; Johnson et al. 2015).

Comparing the top and middle row of figure 4.8, we see at first glance that the two results make no large difference because the kernel of diffractive scattering is comparable or less than the observational resolution, and also because the substracture of refractive scattering is not dominant and washed out at the EHT's resolution. Carefully watching them, we can point out that there exist some deviations in small scale, such as in the 'separatrix' on the CP image, but subsequently find out that these discrepancy on the observation are resolved through the deblurring process in the bottom row of figure 4.8. The good agreement between in the top and bottom row implies that even the refractive effect, which is not invertible with deblurring (Johnson & Gwinn 2015), is faint and compact enough to significantly affect the polarimetric images in the observations at present, although it may be problematic and require the direct modeling of refractive phase screens (Johnson 2016) in future observations with higher resolutions.

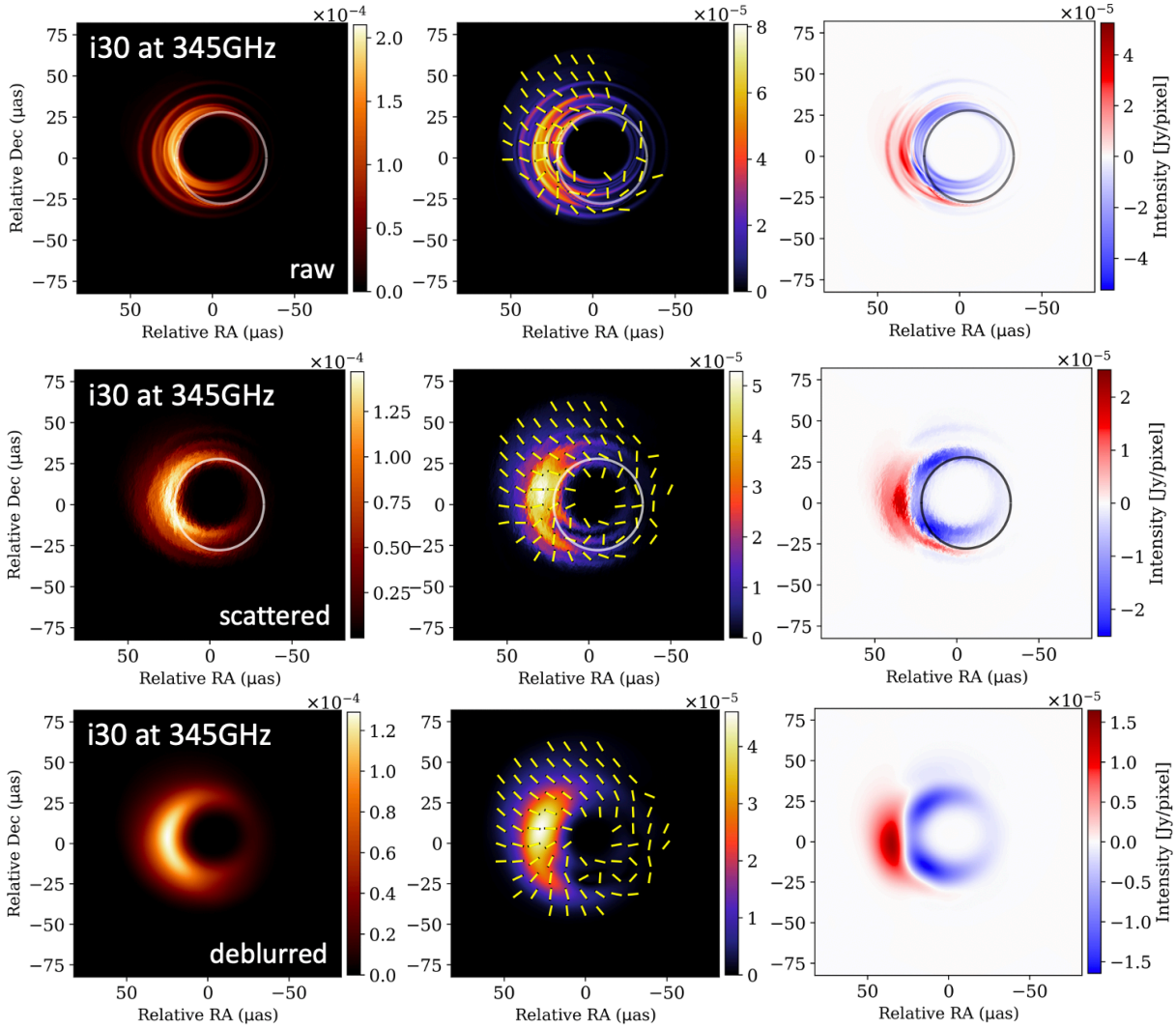

Fig. 4.9: Top to bottom: raw, scattered, and observational (deblurred) images at 345 GHz for Model i30, respectively. Left to Right: the total intensity images, the LP maps, and the CP images.

4.3.3 Polarimetric images at 345 GHz

With future observations at higher frequency in mind, we also present polarimetric images at 345 GHz for Model i30 in figure 4.9. The raw images in the top row show the more compact emissions near the black hole in the left, more ordered LP vectors in the center, and weaker CP components in the right than the raw images at 230 GHz in figure 4.2, because both of the synchrotron self-absorption and the Faraday effects (rotation and conversion) are weaker at shorter wavelengths. That is, the photosphere of synchrotron emissions locates near the black hole and the LP vectors can keep the original information about the magnetic fields in the emission region, although the amplified CP components with the separatrix of their sign can be seen to some extent.

We can see that these polarimetric features survive from the interstellar scattering in the images in the central row, because both diffractive and refractive scattering effects are also weaker at shorter wavelength (e.g. blurring kernel size $\propto \lambda^2$ at submillimeters; Johnson et al. 2018). Further, since the resolution is improved at short wavelengths, we can expect that the directly-interpretable images will be obtained at 345 GHz, as in the observational (deblurred after scattered and convolved with beam of 11 μas) in the bottom row.

4.3.4 Comparison with existing observations

Here we test the validity of the models by comparing them with existing observations. There have been many polarimetric observation of Sgr A* at 230 GHz mainly since 00s (Aitken et al. 2000; Bower et al. 2003). During about twenty years, the LP fraction of $\sim 10\%$ (Bower et al. 2018) and CP fraction of $\lesssim 1\%$ (Muñoz et al. 2012) have been detected with some long-term variabilities. On the basis of these observations, a previous study Dexter et al. (2020) imposed constraints of $LP = 2 - 8\%$ and $|CP| = 0.5 - 2\%$ on their radiative transfer models. Checked by their criteria for polarization fractions, our three models of i30, i60 and i90 pass the tests for both of the LP and CP, as seen in table 4.1. In addition, Sgr A* at around 230 GHz has shown the RM of about $10^5 - 10^6 \mathrm{rad/m^2}$ (Marrone et al. 2007). This RM has been thought to originate in the extended accretion flow up to the scale of $\sim 10^5 r_\mathrm{g}$ ('external' RM), while RMs obtained from our models in table 4.1 are due to the Faraday rotation within $\sim 10 r_\mathrm{g}$ near the emission region ('internal' RM). Thus we use the observational RM value as a rough upper limit estimated in order of magnitudes. In this sense, all the three models also pass the limitation test, and are consistent with the RM observations. In this way, we demonstrated that our three models can reproduce the features in polarimetric observations at 230 GHz, whereas some models additionally introduced below violate these constraints.

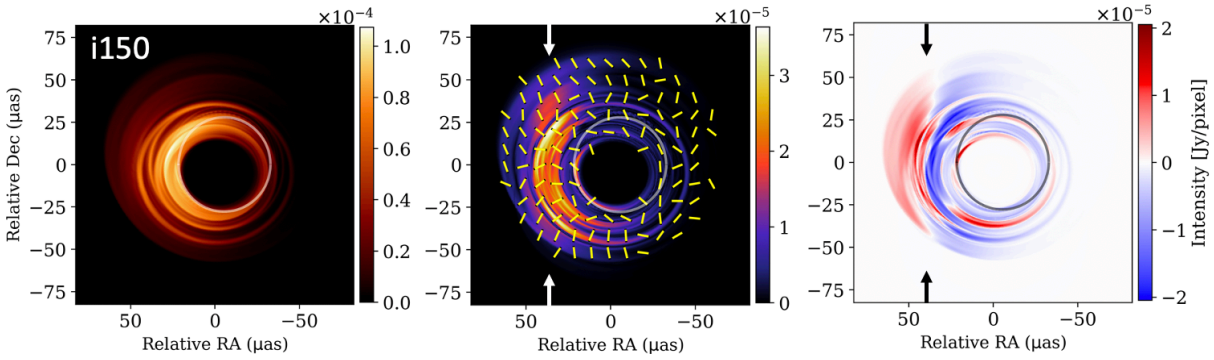

Fig. 4.10: Same as figure 4.2 but for Model i150.

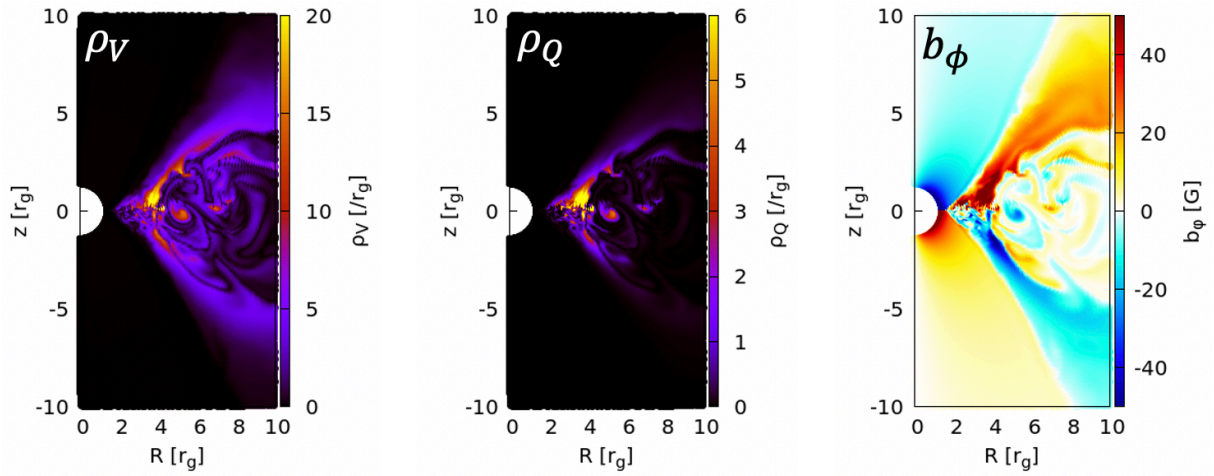

Fig. 4.11: Left: map of the Faraday conversion coefficient ρ_Q in linear-scale, roughly estimated from electron density, temperature, and magnetic strength. Center: that of the Faraday rotation coefficient ρ_V. Right: map of toroidal component of magnetic field in Gauss.

4.3.5 Comments on possible asymmetric structure

During the course of the present simulation study, we noticed an asymmetric structural features above and below the equatorial plane in the GRMHD model (in both of gas dynamics and field configurations). This means, the images may differ, if we see the disk from the totally opposite direction. We thus repeated the same calculations but with the inclination angle of $i = 120^\circ$ and 150°, instead of 60° and 30°, respectively. As a result, we found a different feature on the CP image between Model i150 and i30, while no large differences on the images between Model i120 and i60. In figure 4.10 we plot the images for the former i150, the counterpart of those in figure 4.2.

The CP image in the right of figure 4.10 shows the same tendency as in the right of figures 4.2, not the opposite to them, although the direction of toroidal-dominant magnetic fields are opposite on the two sides of the equatorial plane, as mentioned in subsection 4.2.2. To survey the apparently inconsistent result, we investigate where the Faraday conversion and rotation occur in the left and central panel of figures 4.11. Here we see that these Faraday effects are stronger on the north side than on the south side, as well as the synchrotron emission mentioned above. This is because the magnetic field strengths near the black hole are larger in the north at the moment of our plasma models (see the right panel of figures 4.11). As a result, observed polarization components reflect the magnetic field configuration in the north side, even when observing from the below (south side of) the equatorial plane, and gives the same sign reversal as in the case observing from the above (north side). Nevertheless, the right image of figures 4.10 for Model i150 has a feature that negative components are stronger around the border of sign change (the separatrix of $x_{\rm image} \approx 40\ \mu$as), different from Model i30, implying the Faraday effects on the south side and the gravitational lensing effect. In addition, Model i150 gives CP much higher than Model i30 in total polarization fraction, shown in table 4.1, reflecting the stronger Faraday effects in the dense disk to polarization components from the north side.

Model i120 and i60 give similar values of rotation measure (RM) with the same sign (see table 4.1). This also reflects the fact that the Faraday effects mainly occur on the north side. By contrast, Model i150 and i30 show RMs with the same sign but with different magnitudes by one order, because of the strong Faraday rotation in the long way from the north to south. Mościbrodzka et al. (2017) and Ricarte et al. (2020) demonstrated with M87* in mind that, the Faraday rotation and depolarization mainly occur in the disk rather than the jet, while emission from the foreground jet dominates observed LP flux and RM in their models. In our cases, Model i30 is relatively close to their M87* models, where emission on the foreground (on the north side) disk is dominant. Thus the LP flux survives from the Faraday depolarization, and total RM is suppressed. In contrast, emission on the background (on the north side) disk is dominated in Model i150 and the LP flux experiences strong Faraday rotation in the disk, as described above, and gives the much larger RM.

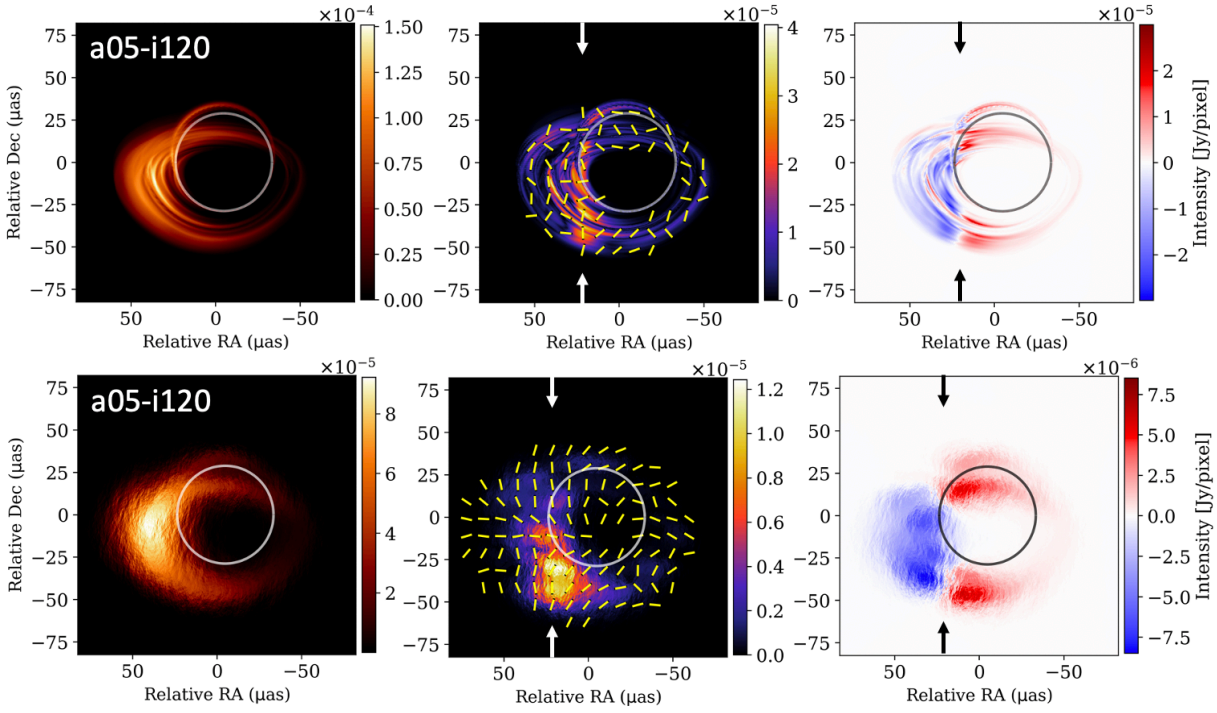

Fig. 4.12: Top: the intensity image (left), the LP map (middle), and the CP image (right) for the Model a05-i120. Bottom: same as in the top panel but their scattered images. The positions of the CP separatrix are indicated by the arrows.

4.3.6 Slow spin case

As mentioned in subsection 1.4.2, some previous works suggest the fast-spinning black hole and highly magnetized plasma around it (MAD case) to reproduce existing observations of Sgr A*. In our study above, we also adjusted models with fast spin of $a = 0.9M_{\rm BH}$ and semi-MAD plasma. Here we consider other possibility, a model with slow spin of $a = 0.5M_{\rm BH}$ and SANE-like plasma.

As seen in the bottom row of table 4.1, we can reproduce observed total LP and CP flux by adjusting $R_{\rm high} = 1$, $i = 120°$ and $\dot{M} = 3.5 \times 10^{-8} M_{\odot}/{\rm yr}$. That is, the electron temperatures are equal to the proton temperature in all over the region. In addition, there also exists plasma asymmetry above and below the equatorial plane, as was described in the previous subsection and can be seen through the comparison between Model a05-i60 and a05-i120 in table 4.1.

The resultant images for a05-i120 are shown in figures 4.12. The total intensity image in the top left panel consists of the beamed disk and the photon ring, similarly to Models i60 and i120 for $a = 0.9M_{\rm BH}$ case. The LP image in the top central panel is vertically elongated at $x_{\rm image} \sim 20\ \mu$as, where the CP image in the top right changes signs of its components. The scattered total image in the bottom left panel shows a horizontally-elongated structure because of the extended disk component. In the bottom central and right panels, we can see the sign reversal of CP components and bright LP flux on the CP separatrix, suggesting that these features can also be

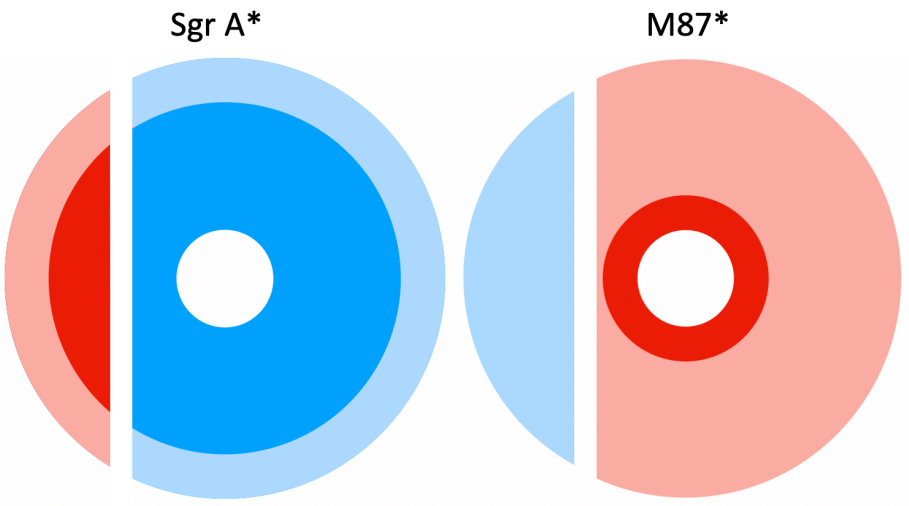

Fig. 4.13: Schematic view explaining the different CP images obtained for Model i30 in the present study (left panel) and for Model a09R100 in Paper 1 (right panel). The red and blue colors display the region with the circular polarization $V > 0$ and < 0 in the observer screen, respectively. The deep and light colors represent the high and low $|V|$ regions in the screen, repectively. The red and blue colors are reversed between Sgr A* and M87* because the viewing angles are $i < 90$ deg and $i > 90$ deg in the comparing models, respectively, and because of the difference in the emission region. In the CP image of M87*, the bright region on the image is limited to the right side of the separatrix described in subsubsection 4.2.1.1, so that the separatrix does not appear in the observed image.

captured for the SANE-like plasma with the slow spin if there is toroidally-dominant magnetic field.

4.3.7 Comparison with the case in M87*

In the last chapter, we obtained the CP ring feature with uniform sign for the fiducial model and other models with low-temperature disk as seen, for example, their figure 3.2. In the context of the CP separatrix described above, here we consider why the CP images for M87* do not show the sign-changing feature and re-interpret them.

In the fiducial model in the last chapter with $a = 0.9M_{\rm BH}$, $R_{\rm high} = 100$ and $i = 160°$, both of the synchrotron emission region and the CP amplification region are concentrated to the jet rim at $\sim 5r_{\rm g}$ from the jet axis (cf. their figure 3.10). In addition, the optical depth of the plasma surrounding the BH is less than unity at 230 GHz, so that only the photon ring and its neighborhood shows bright images of Stokes I and V.

Therefore, the total image and the CP image give compact features around the photon ring ($-5r_{\rm g} \lesssim x \lesssim 5r_{\rm g}$ in the image coordinate), compared with those in this work ($-10r_{\rm g} \lesssim x \lesssim 10r_{\rm g}$ in the image coordinate, here $1\ \mu{\rm as} \approx 5r_{\rm g}$ for Sgr A*). As a result, the ring feature in the CP image is entirely limited to the right side of the CP separatrix, as seen in a schematic picture of figure 4.13.

It should be noted that the features of the image of CP is qualitatively not affected by changing the choose of the magnitude of sigma cut, i.e., the upper limit of the magnetization σ ($\equiv B^2/4\pi\rho c^2$) by which the region solved by the polarized GRRT is restricted, as shown in section 3.5 in the last chapter. In this work, we confirmed for Model i30 that the restriction of $\sigma < 1$ does not significantly affect the results and discussions introduced above, and therefore set no sigma-cut as in the fiducial calculations in the last chapter.

There is also a possibility that we can explain the observations of Sgr A* by models with the strong jets like the case of M87*, especially if we observe the jet at low inclination to 'hide' the jet (Mościbrodzka et al. 2014; Davelaar et al. 2018). To verify this possibility, we performed a calculation with $i = 20^\circ$ and $R_{\rm high} = 25$ by using our GRMHD model with $a = 0.9M_{\rm BH}$, and obtained an image consistent with the previous works; that is, the image consists of beamed foreground-jet and dim background-jet components while the disk or the photon ring feature are absent.

4.3.8 Future prospects

In the present work, we adopted the axisymmetric GRMHD models to calculate radiative transfer and obtained the polarization images of Sgr A* as a snapshot with the "fast light" approximation. We have confirmed in the GRMHD simulation data that the flow structure is in a quasi-steady state; that is, the physical quantities do not show large temporal variation but only show rapid, small spatial scale fluctuations occurring on the dynamical timescale. Thus we can calculate the observational images by using one snapshot fluid model as a representative one in the quasi-steady state[2]. In addition, since the Keplerian orbital period near the SMBH in Sgr A* ($\sim$ 10 min.) is shorter than the observational time of the EHT array ($\sim$ 10 hrs), we can expect that the non-axisymmetric features will be smoothed if averaged over the ϕ-direction by the Keplerian motion.

Meanwhile, more "MAD" models often show much more radical variability and can give variable images in short timescale. In future works, we will further research the short-time variabilities and small-scale structure on images for Sgr A* and M87* through time-dependent simulations with 3D GRMHD models, bearing future observations with high resolution in mind. There, we will also survey the dependence of the polarimetric features, introduced in this work, on the SANE vs. MAD regime and magnetic field configurations in the disk and the jet.

4.4 Why is the position of the CP separatrix shifted?

In subsubsection 4.2.1.1, we mentioned that the positional shift of the CP separatrix (to $x_{\rm image} \approx 30\ \mu$as) is due to the relativistic parallax effects of plasma bulk motion. To demonstrate that

[2] Ricarte et al. (2021) took up the time-averaged CP images. They show images giving the sign-flipping feature after time-averaged, even in the case where the snapshot image gives turbulent feature.

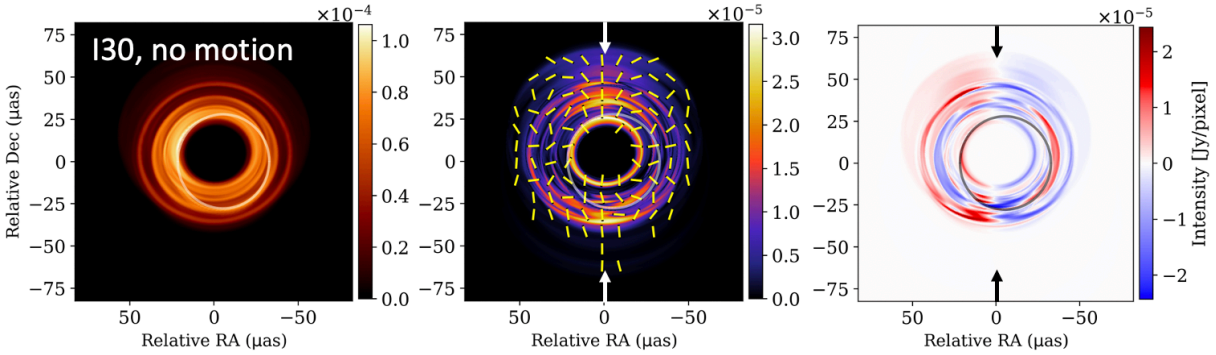

Fig. 4.14: Same as Fig. 4.2 but for the case without plasma bulk motions.

this is actually the case, we performed the same simulation but the case without the plasma bulk motion; i.e., we put the 4-velocity of plasma $u^\mu = (\alpha^{-1}, 0, 0, \alpha^{-1}\omega)$ and thus $u_\mu = (-\alpha, 0, 0, 0)$. That is, we take a position of a zero angular momentum observer (Bardeen et al. 1972). Here, α is the lapse function and ω is the shift vector in ϕ-direction with minus sign.

The resultant images are shown in figure 4.14 for the inclination angle of $i = 30°$. As expected, the separatrix in the CP image and the vertically-brightened region in the LP map appear at around $x_{\rm image} \approx 0$. This result reflects the toroidal-dominant magnetic fields, because in this case the angles θ_B are determined only by the magnetic field and light path's vector (line of sight). We can thus prove that the asymmetry in the LP and CP images are caused by the special relativistic effects due to plasma bulk motion, and not by the general relativistic effects of the black hole.

4.5 Conclusion

We performed full polarimetric radiative transfer simulations based on the semi-MAD models using axisymmetric GRMHD data by Nakamura et al. (2018), and obtained expected linear and circular polarization images in the horizon-scale, bearing EHT observations of Sgr A* in mind. For modeling the LLAGN without visible jets, we here assumed a low ratio of the proton temperature and the electron temperature in the disk, and discussed the relationship between the polarimetric features and magnetic field configurations around the SMBH, taking the interstellar scattering effects into account. Our results are summarized as follows:

- The Stokes I images show the ring-like or the fork-like features for the face-on (Model i30) or the edge-on (Model i90) cases, respectively. The moderate inclination case (Model i60) gives the intermediate feature in between.

- In all the three models, the circular polarization images show sign reversals, the so-called "separatrix" structure, since the CP amplification through the Faraday effects is proportional to $\cos\theta_B$ where θ_B is the angle between the line of sight and the direction of toroidally-dominant magnetic fields. For the same reason (that is, the Faraday rotation is weak for the linear polarization vectors on the separatrix on the images), the linear polarization fluxes are not depolarized and is brightest along the CP separatrix. These polarimetric features on the linear and circular polarization images can be double evidence of toroidal magnetic fields near the SMBH.

- The above features on Stokes I and polarization images still remain, even after undergoing interstellar diffractive and refractive scattering. Further we demonstrated that the angular resolution in present and future EHT observation for Sgr A* at 230 GHz is enough to capture the features described above, and the mitigation of diffractive scattering effects make the situation better.

- When the EHT observations at 345 GHz are available in a near future, we can expect to capture a smaller-scale structure and to directly interpret the polarimetric images in relation to the magnetic field configurations, because all of the synchrotron self-absorption, the Faraday effects, and the interstellar scattering effects are weaker at higher frequency.

Chapter 5

LP-CP Flux Separation in M87: the Disk-Jet Structure Close to the SMBH

Part of text in this chapter was published in Tsunetoe et al. (2022a) (Tsunetoe, Y., Mineshige, S., Ohsuga, K., Kawashima, T., Akiyama, K., & Takahashi, H. R., *ApJ, 931, 25 (2022)*), titled as "*Investigating the Disk-Jet Structure in M87 through Flux Separation in the Linear and Circular Polarization Images*".

We suggested in the previous chapters that the circular polarization (CP) can be amplified by Faraday conversion (Jones & O'Dell 1977) from the LP in hot and dense plasma near the black hole, up to the extent comparable with the LP (Tsunetoe et al. 2020, 2021). We there introduced an amplification process of the CP through combination of Faraday conversion and rotation (the rotation-induced conversion), which produces the CP components with signs imprinting the magnetic fields configuration.

Along this line, we here analyze and quantify the relationship among the polarization components on theoretical polarization images of M87* using correlation functions, focusing on the radiative processes in the jet-disk structure. We calculate auto- and cross- correlations among the total, LP and CP intensities on ray-traced images obtained from GRRT calculation through GRMHD models, in an attempt to understand their relations to the Faraday rotation, the Faraday conversion, the synchrotron self-absorption (SSA), and the underlying plasma properties in the jet-disk structure in M87.

This chapter is organized as follows: We outline the methodology for computing theoretical polarization images in section 5.1. We show our resultant images (5.2.1), correlation analyses (5.2.2), and an example of "LP-CP separation", a separation along the jet direction between LP and CP intensity distributions (5.2.3). We examine the separation for various electron-temperature parameters in the disk in subsecion 5.3.1. The dependence on frequency is presented in 5.3.2. Other possibilities for the inclination angle and models with different mass accretion rates from M87* are discussed in 5.3.4 and 5.3.5, respectively. We compare the results with existing observations and discuss prospects for future observations in 5.3.6. Section

5.10 presents our conclusion.

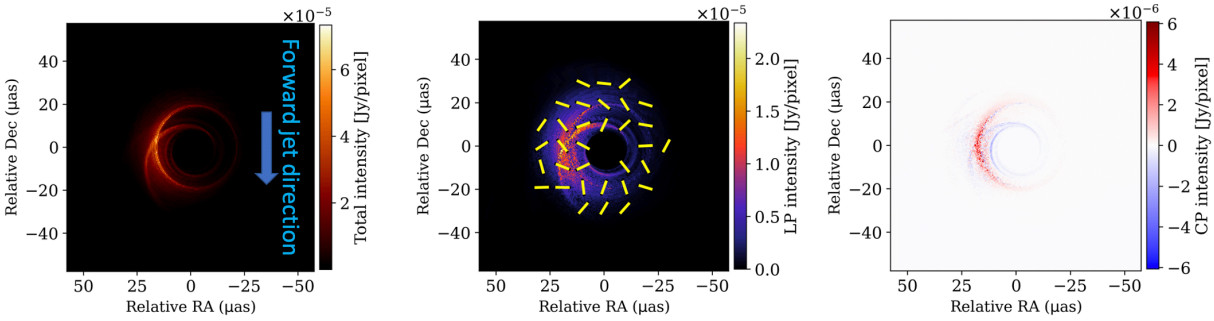

Fig. 5.1: Polarimetric images at 230 GHz obtained by the radiative transfer calculation for our fiducial model with an inclination angle of $i = 160°$. Left: total intensity (Stokes I) image, which consists of the photon ring feature and dim jet components. Center: linear polarization (LP) map with color contour of the LP intensity (Stokes $\sqrt{Q^2 + U^2}$) and overplotted LP vectors in EVPA (electric vector position angle). The LP vectors are scrambled by the Faraday rotation after the synchrotron emission and show a disordered pattern. Right: circular polarization (CP) image with color contour of the CP intensity with sign (Stokes V). The CP components around the photon ring are amplified by the Faraday conversion process in hot region near the black hole. The black hole is located in the center of the images. The spin axis of the black hole points upwards in the images, and the approaching jet extends downwards (as shown by a blue arrow in the left image) though it is dim on the images. The images consist of 600×600 pixels.

5.1 Models

5.1.1 GRMHD model and proton-electron coupling

We performed three-dimensional GRMHD simulation of RIAF around a Kerr black hole (BH) with a dimensionless spin parameter of the black hole $a = 0.9375$ by using GR-Radiation-MHD code `UWABAMI` (Takahashi et al. 2016, 2018a), where the radiative effects are turned off (Kawashima et al. 2021a) in order to avoid any inconsistency possibly caused by its current one-temperature-fluid approximation. The modified Kerr-Schild coordinate (e.g., Gammie 2004) is employed in the simulation. The inner- and outer-outflow boundaries are located at $0.96r_{\rm H} \simeq 1.29r_{\rm g}$ and $3.33 \times 10^3 r_{\rm g}$, respectively, where $r_{\rm g} \equiv GM_\bullet/c^2$ is the gravitational radius, G is the gravitational constant, $M_\bullet$, black hole mass, c is the speed of light, and $r_{\rm H} (= (1+\sqrt{1-a^2})r_{\rm g} \simeq 1.35r_{\rm g})$ is the outer horizon of the black hole. The simulation domain is devited into $r \times \theta \times \phi = 200 \times 128 \times 64$ meshes.

Initially, we set an isentropic hydroequilibrium torus rotating around the Kerr BH (Fishbone & Moncrief 1976) with the single-loop magnetic field configuration, which is embeded in a hot, static, uniform, and non-magnetized ambient gas. The position of the inner edge and the pressure maximum of the torus are set at $r = 20r_{\rm g}$ and $r = 33r_{\rm g}$ on the equatorial plane,

respectively. The specific heat ratio is assumed to be $\gamma_{\rm heat} = 13/9$. We use a snapshot of the simulation data at $t = 9 \times 10^3 r_{\rm g}/c$, at which the accretion flow in a quasi-steady state after the sufficient mass supply from the initial torus via the growth of the magneto-rotational instability (MRI) (Balbus & Hawley 1991). We calculate the MRI quality factor Q-factors, the numbers of the cells across a wavelength of the fastest-growing MRI mode in each direction (Hawley et al. 2011), and obtain $(Q_r, Q_\theta, Q_\phi) = (3.23, 3.97, 11.0)$ in the zero-angular momentum observer frame, averaging over $r \lesssim 20 r_{\rm g}$ and $60^\circ \lesssim \theta \lesssim 120^\circ$. (see subsection 5.3.7 for discussion about resolution of the MRI modes.)

GRMHD models are often categorized into two major groups, the MAD and SANE, which are divided by their strength of the dimensionless magnetic flux near the event horizon $\phi \equiv \Phi_{\rm BH}/\sqrt{\dot{M} r_{\rm g} c^2}$, where $\Phi_{\rm BH} = (1/2)\int_\theta \int_\varphi |B^r| {\rm d}A_{\theta\varphi}$. The MADs, which typically show the saturation of $\phi \gtrsim 50$ (in Gaussian units), are characterized by the strong, dynamically important magnetic flux near the black hole, while the SANEs ($\phi \leq 5$) have the weak magnetic flux. Our GRMHD simulation shows $\phi \approx 18$, so that the magnitude of ϕ is between the typical values of MAD and SANE and this state is sometimes referred to as semi-MAD.

Since the GRMHD simulation only gives temperature for protons, we have to determine electron temperature by post-process to calculate synchrotron radiation transfer. As in chapters 3 and 4, and previous works including Event Horizon Telescope Collaboration et al. (2019c, 2021b), we implement a relation equation between proton and electron temperature with the plasma $\beta \equiv p_{\rm gas}/p_{\rm mag}$, the gas-magnetic pressure ratio, and two parameters $R_{\rm low}$ and $R_{\rm high}$,

$$\frac{T_{\rm i}}{T_{\rm e}} = R_{\rm low} \frac{1}{1+\beta^2} + R_{\rm high} \frac{\beta^2}{1+\beta^2}, \tag{5.1}$$

which was introduced in Mościbrodzka et al. (2016). In this scheme, $T_{\rm e} \simeq T_{\rm i}/R_{\rm low}$ in the strongly magnetized region such as in the jets, while $T_{\rm e} \simeq T_{\rm i}/R_{\rm high}$ in the weakly magnetized, gas pressure dominant region such as in the midplane disk. Here, we adopt parameters of $R_{\rm low} = 1$ and $R_{\rm high} = 73$ for our fiducial model, corresponding with relatively high (or low) electron temperature in the jet (disk) region.[1]

While the electron temperature are thought to be lower in the disk than in the jet from comparison with spectral energy distributions and RMs (Mościbrodzka & Falcke 2013; Mościbrodzka et al. 2017) and with two-temperature calculations (Howes 2010; Ryan et al. 2018; Kawazura et al. 2019; Chael et al. 2019), a wide range of the proton-electron temperature ratio both in the disk and in the jet is suggested. As far as the radiative cooling is not incorporated, recently, Mizuno et al. (2021) demonstrated that this $R-\beta$ prescription and choice of parameters ($R_{\rm low} = 1$, $R_{\rm high} = 1 - 160$) are consistent with the turbulent- and magnetic reconnection-heating prescriptions in GRMHD simulations with electron thermodynamics, in comparison of images at 230 GHz obtained from GRRT calculations based on them. We discuss other choices for $R_{\rm high}$ in sub-subsection 5.3.1, focusing on the difference between the low-$T_{\rm e}$ and high-$T_{\rm e}$

[1] See Fig. 5.19 for maps of physical quantities including the electron temperature in our GRMHD model.

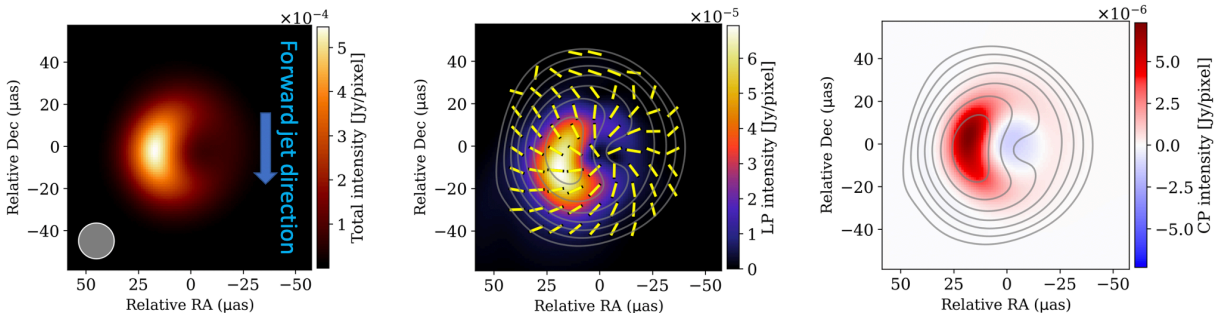

Fig. 5.2: Same as Fig. 5.1 but for the convolved images with Gaussian beam of 17 μas. The beam size is shown in the bottom left in the left image. Line contour of the total intensity is overplotted on the LP and CP images. The total image shows an asymmetric ring feature with no visible jet feature. Although the LP fraction is not so large ($\approx 10-20\%$), compared with those of the raw image, the LP vectors show a much more ordered pattern. The CP image gives a ring feature, consisting of significant components ($\gtrsim 1\%$ in fraction) with positive signs. Note that the images consist of 100×100 pixels, more coarsely than those in Fig. 5.1.

disks.

5.1.2 Polarimetric radiative transfer in Kerr metric

We perform full polarimetric radiative transfer with the Stokes parameters $(\mathcal{I}, \mathcal{Q}, \mathcal{U}, \mathcal{V})$ along light paths in Kerr metric determined by the general relativistic ray-tracing method, using our code developed and implemented in the last two chapters. The polarized radiative coefficients for the ultrarelativisic thermal distribution of electrons, the synchrotron emissivities (j_I, j_Q, j_U, j_V), synchrotron self absorption $(\alpha_I, \alpha_Q, \alpha_U, \alpha_V)$ and Faraday effects (ρ_Q, ρ_U, ρ_V), are implemented into the code, based on previous works (Mahadevan et al. 1996; Shcherbakov 2008; Dexter 2016). Further, the coefficient of Faraday rotation ρ_V is modified for accurate descriptions in the low temperature and frequency ratio region, as discussed in Dexter et al. (2020); Ricarte et al. (2020).

We adopt a black hole mass of $M_\bullet = 6.5 \times 10^9 M_\odot$ and a distance of 16.7 Mpc for M87* (Mei et al. 2007; Gebhardt et al. 2011; Event Horizon Telescope Collaboration et al. 2019c), which give an angular diameter of $\simeq 3.8$ μas on the celestial sphere corresponding with the gravitational radius r_g. An inclination angle i of the camera is set to $160°$, nearly face-on to the midplane disk, while other inclinations are also discussed in subsection 5.3.4. We set the camera at $r = 10^4 r_g$ and calculate radiative transfer within $r \leq 100 r_g$,[2] to present snapshot images with the "fast-light" approximation. We also scale a mass accretion rate onto the black hole $\dot{M}$ to reproduce the observed flux of ≈ 0.5 Jy at 230 GHz (Event Horizon Telescope Collaboration et al. 2019d). $\dot{M} = 6 \times 10^{-4} M_\odot/\mathrm{yr}$ for our fiducial model, which is comparable with those in

[2]We confirmed that significant radiative processes occur within $r \leq 100 r_g$ for our models. (see, e.g., Fig. 5.20 for estimation maps of the radiative coefficients.)

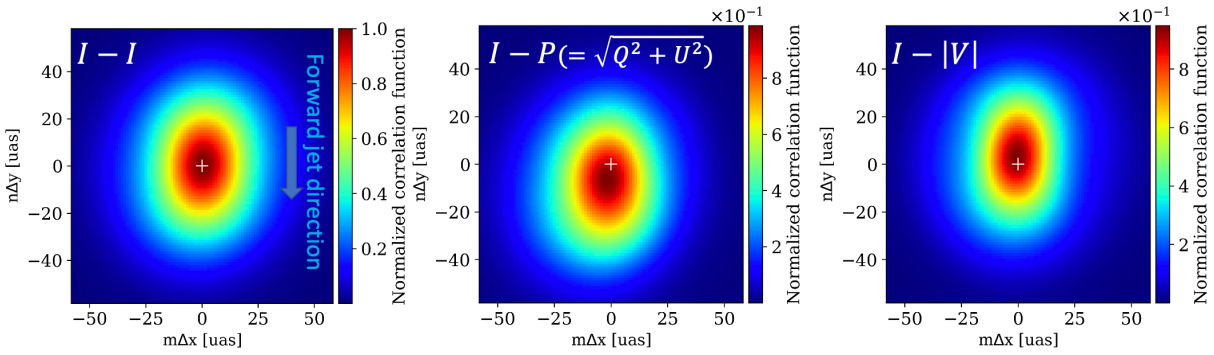

Fig. 5.3: Two-dimensional auto- and cross-correlation functions for the total, LP, and CP images in Fig. 5.2. White "+" in the maps indicates the centroid position of the map, where we set $(m\Delta x, n\Delta y) = (0, 0)$. Left: auto-correlation of total intensity, Stokes I, with a peak at the origin by definition. Center: cross-correlation between I and the LP intensity $P = \sqrt{Q^2 + U^2}$. The position of the correlation maximum is shifted downwards with respect to the centroid position, reflecting the LP intensities distributed downwards relatively to the total intensities on the image. Right: cross-correlation between I and the absolute CP intensity $|V|$. In contrast to $I - P$, it gives a peak in the upwards due to the CP intensities located upwards relatively to the total intensities. Three maps are normalized by the definition of the correlation coefficient, so that the auto-correlation of Stokes I yields 1 at the origin.

the "passed" MAD models in Event Horizon Telescope Collaboration et al. (2021b).

In the whole of this work, the sigma cut-off of $\sigma_{\rm cutoff} = 1$, removing the region with the plasma magnetization $\sigma \equiv B^2/4\pi\rho c^2 > \sigma_{\rm cutoff}$ in radiative transfer calculation, is adopted in order to avoid unphysical effects arising because of low density floors set in the MHD simulation. In subsection 5.3.7, we discuss the validity of our results with the sigma cutoff comparing to a case without the cutoff.

5.2 LP-CP flux separation

5.2.1 Polarization images

The raw images of the total intensity (I), the LP intensity (Q, U), and the CP intensity (V) at 230 GHz obtained by the polarimetric radiative transfer calculation are shown in the left to right panels in Fig. 5.1, respectively. The total intensity (Stokes I) image in the left panel gives the photon ring, which is a circle with a radius of ≈ 20 μas and is beamed in the left side due to the gravity of the spinning black hole and to the relativistic beaming effect by helical motion of plasma. In addition, a hint of tail-like jet extends downwards in the image.

In the central panel, the LP intensity (Stokes $\sqrt{Q^2 + U^2}$) distributes tracing the total intensity, with fractions of $\sqrt{Q^2 + U^2}/I \sim 50\%$ in individual pixels. The noteworthy features are that the LP vectors are not ordered but show chaotic features because of the Faraday rotation occurring within the disk. The CP (Stokes V) image in the right panel shows an asymmetric

ring-like feature with positive sign, which traces the photon ring in the total intensity image. The CP components with a fraction up to $|V|/I \sim 10\%$ in individual pixels are significantly stronger than those of the synchrotron emission ($|V|/I \lesssim 1\%$), implying that these result from an amplification process through the Faraday conversion in hot region ($T_{\rm e} \gtrsim 10^{10}$ K) near the black hole, as was firstly demonstrated in Tsunetoe et al. (2020) (see chapter 3). These features of rotation of the LP vectors and amplified CP components in individual pixels agree well with the results in chapter 3, based on two-dimensional semi-MAD models. Such monochromatic (uniform in +/- signs) CP ring features are also seen in the theoretical models in Bronzwaer et al. (2020); Mościbrodzka et al. (2021); Ricarte et al. (2021); Emami et al. (2021).[3]

At the same time of calculating of the images, we also calculate the intensity-weighted optical depths for each light ray to see the two Faraday effects and SSA; e.g.,

$$\tau_{{\rm Frot},I} \equiv \int \rho_V I(s) {\rm d}s / I_{\rm fin} \tag{5.2}$$

for Faraday rotation depth, where $I_{\rm fin}$ is a final value of Stokes I in each pixel (Event Horizon Telescope Collaboration et al. 2021b). We further average them over the image, weighting by the total intensity in each pixel, and obtain the image-averaged, intensity-weighted optical depths, $\langle \tau_{{\rm Frot},I} \rangle \simeq 1.7 \times 10^2$, $\langle \tau_{{\rm Fcon},I} \rangle \simeq 1.1$, and $\langle \tau_{{\rm SSA},I} \rangle \simeq 0.1$. (Here $\tau_{{\rm Fcon},I} \equiv \int \sqrt{\rho_Q^2 + \rho_U^2} I(s) {\rm d}s / I_{\rm fin}$, $\tau_{{\rm SSA},I} \equiv \int \alpha_I I(s) {\rm d}s / I_{\rm fin}$.) From these we understand that plasma near the black hole is optically thick for the Faraday effects but thin for the SSA for the lights at 230 GHz, typically. As a result, we obtained clear photon-ring image but dim foreground jet image, the scrambled LP vectors, and the amplified CP components (see section 5.5 for GRRT process for a pixel on the image).

Next, we show convolved (or blurred) images by Gaussian beam with size of 17 μas in Fig. 5.2. We have chosen this beam size, bearing the EHT observation at 230 GHz in mind. In the central panel, we can see an asymmetric ring feature without extended jet components, which is consistent with the EHT observation of M87* in 2017 (Event Horizon Telescope Collaboration et al. 2019a,c).

While the Gaussian convolution on the whole tends to reduce the LP fraction in the central panel, with values of $\sim 10 - 20\%$, it recovers a "hidden" ordered structure of the LP vectors in a hybrid pattern of azimuthal and radial ones, reflecting (i.e. being perpendicular with) the magnetic field configurations at synchrotron emission. (Note that the magnetic field configuration is toroidally dominated in the disk region, while it has significant poloidal components in the jet region, roughly.) Further, a distribution of the LP intensity is shifted downwards by $\lesssim 10$ μas in the image, compared with those of the total intensity. This is because the LP vectors which originate in the downstream region of the approaching jet are not affected by the Faraday rotation because of small Faraday rotation depth, and thus keep a well-ordered structure in emission. Those originating from the upstream or the photon ring are, by contrast, chaotically rotated in

[3] See also Ricarte et al. (2021) for a discussion about the sign-flipping sub-rings.

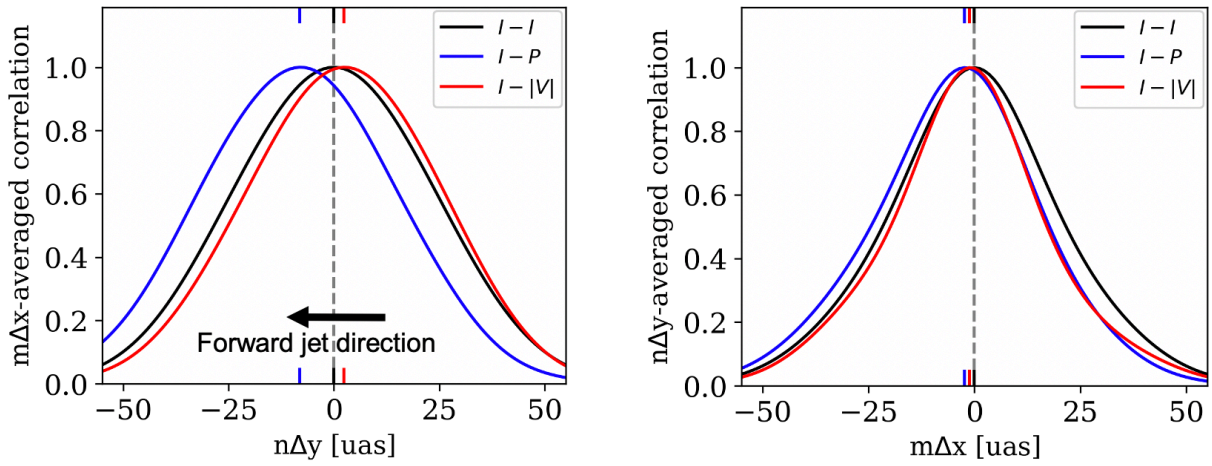

Fig. 5.4: One-dimensional auto- and cross- correlation functions calculated by integrating the two dimensional correlation functions in the x- (left) and y- (right) directions. The former corresponds to the vertical direction along the jet and BH spin axis, while the latter the horizontal direction perpendicular with the jet. Hatches in the upper and lower axes demarcate the places of the maximum correlation, the relative offsets between two kinds of intensity distributions. Each profile is normalized by its maximum value.

the disk region (see also Mościbrodzka et al. 2017; Ricarte et al. 2020) and drastically decrease their intensity by the convolution of observational beam (the beam depolarization). Such features as those seen in the convolved LP map agree with the observations of M87* in Event Horizon Telescope Collaboration et al. (2021a), where the downward direction on the images in this work corresponds to the north-east on their observational images.

Meanwhile, the CP intensity in the left panel is distributed around the photon ring in the total intensity image, with fractions of $|V|/I \sim$ a few percent. The centroid of the CP intensity is slightly shifted upwards by $\lesssim 5$ μas, compared with that of the total intensity. This is because only those around the photon ring and from the receding jet can be amplified in energetic region near the black hole through the Faraday conversion from the LP components, and the emission from more background is more effectively converted with larger optical depth for the Faraday conversion.

Further, we confirmed that these 230 GHz images give the net LP fraction of 2.6 %, the average LP fraction of 10.4 % when convolved with 20 μas Gaussian beam, and the net CP fraction of 0.76 %. All of these fractions satisfy the observational constraints in the model scoring in Event Horizon Telescope Collaboration et al. (2021b).

Next, we describe the results for the total, LP and CP intensities to the nearly-face-on observer and their origin in subsection 5.2.3.

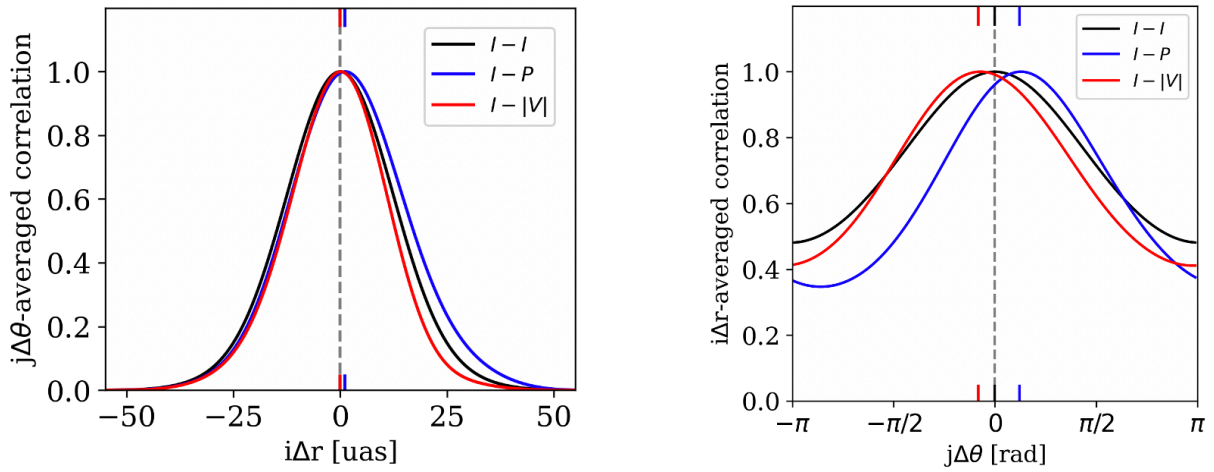

Fig. 5.5: Same as the one-dimensional correlation profiles in Fig. 5.4 but in the polar coordinates. The left panel shows the correlations in the radial direction, while the right one shows those in the azimuthal angle. Hatches in the upper and lower axes demarcate the places of the maximum correlation, the relative offsets between two kinds of intensity distributions. Two-dimensional polar correlation maps are shown in section 5.6.

5.2.2 Correlation functions for the images

5.2.2.1 Correlations in the Cartesian coordinates (x, y)

In Fig. 5.3, we show correlation functions in the Cartesian coordinates (x, y); that is, auto-correlation of total intensity (Stokes I), cross-correlations between I and the LP intensity P ($\equiv \sqrt{Q^2 + U^2}$), and between I and the absolute CP intensity ($|V|$), which are calculated from the convolved images in Fig. 5.2. The correlation functions are calculated for a pair of I and S ($= I$, P, or $|V|$) at each pixel of $(x_i, y_j) = (i\Delta x, j\Delta y)$ by the following way:

$$\{I - S\}(m\Delta x, n\Delta y) \equiv \frac{\{I - S\}_{\rm num}(m\Delta x, n\Delta y)}{\{I - S\}_{\rm den}} \quad (m, n = 0, \pm1, \pm2, ...), \tag{5.3}$$

where:

$$\{I - S\}_{\rm num}(m\Delta x, n\Delta y) \equiv \sum_{i=1}^{N}\sum_{j=1}^{N} I(x_i, y_j)S(x_{i+m}, y_{j+n}), \tag{5.4}$$

and:

$$\{I - S\}_{\rm den} \equiv \sqrt{\left\{\sum_{i=1}^{N}\sum_{j=1}^{N}[I(x_i, y_j)]^2\right\}\left\{\sum_{i=1}^{N}\sum_{j=1}^{N}[S(x_i, y_j)]^2\right\}}, \tag{5.5}$$

so that $\{I - I\}(0, 0) = 1$. Here Δx and Δy are the size of pixels in the x- (horizontal) and y- (vertical) direction, respectively, $N = 100$ is the number of pixels in each direction.[4]

[4]Here, we take more coarse pixel composition in the convolved images than in the raw images in Fig. 5.1 for faster calculation of the correlation functions. This does not change the results significantly because the size of convolutional beam is much larger than the pixel size.

Frequency	$I-P$ shift	$I-\|V\|$ shift	$P_{\rm tot}/I_{\rm tot}$	$\|V_{\rm tot}\|/I_{\rm tot}$	$\langle\tau_{{\rm Frot},I}\rangle$	$\langle\tau_{{\rm Fcon},I}\rangle$	Figs.
230 GHz	-8 μas	$+2$ μas	2.6%	0.76%	1.7×10^2	1.1	5.2, 5.3, 5.4
86 GHz	-25 μas	$+17$ μas	4.2%	0.64%	1.3×10^3	12	5.8, 5.9, 5.10

Table 5.1: Comparison between the various polarization quantities at 230 GHz and at 86 GHz; the vertical peak shifts of cross-correlation functions $I-P$ and $I-|V|$, the total LP and CP fractions, $P_{\rm tot}/I_{\rm tot}$ and $|V_{\rm tot}|/I_{\rm tot}$, and the image-averaged intensity-weighted optical depths for the Faraday rotation and conversion, $\langle\tau_{{\rm Frot},I}\rangle$ and $\langle\tau_{{\rm Fcon},I}\rangle$, from the left to the right.

The left panel in Fig. 5.3 represents the two-dimensional auto-correlation functions of Stokes I. We see that the correlation lengths (at half maximum $= 0.5$) of $20-30$ μas in various directions on the $(m\Delta x, n\Delta y)$-plane, and that they show a vertically elongated shape. This reflects the vertically elongated emission profile in the left side of the ring (see the left panel of Fig. 5.2). The cross-correlation between the total and LP intensities, $I-P$, in the central panel shows a shape similar to that of the auto-correlation $I-I$ in the left, but with a peak vertically shifted and at ~ -8 μas, meaning that the LP flux has a tendency to distribute downwards by ~ 8 μas relatively to the total flux (see Fig. 5.2, see also the statements in subsection 5.2.1). In the right panel, conversely, the cross-correlation map between the total and CP intensities $I-|V|$ yields a peak at $\sim +2$ μas upwards in the $n\Delta y$-direction. This is because the CP flux originates from the vicinity of the black hole and the counter-side (background) jet region, compared with the total flux (and LP flux). In this way, we can quantitatively assess the distinction between the total, LP, and CP intensity distributions through the cross-correlation analyses.

In order to more clearly examine the auto- and cross- correlation functions, we display in Fig. 5.4 one-dimensional cross sections of the two-dimensional correlation functions displayed in Fig. 5.3 in the vertical (left panel) and horizontal directions (right panel), respectively. The quantities are normalized by their maximum values. In the left panel, the cross-correlations of $I-P$ and $I-|V|$ have their peaks at negative and positive $n\Delta y$ values (corresponding to the downward and upward direction), respectively, while those in the $m\Delta x$-direction in the right panel do not show significant deviation from the auto-correlation profile, except a small transition of $I-P$ to the left side corresponding to the tendency of the LP flux left-leaning relative to the total flux. The autocorrelation profiles of $I-I$ in both of two panels have their peaks at the center of $(n\Delta y, m\Delta x) = (0,0)$ by definition.

5.2.2.2 Correlations in the polar coordinates (r,θ)

In the previous subsection, we analyzed the correlations in the Cartesian coordinates (x,y) on the images. This choice is reasonable for the M87 jet, because the direction, or position angle, of the approaching jet has been accurately constrained and established for a wide spatial range (from $\sim$ μas- to $\sim$ kpc- scale) through multi-wavelength observations (e.g., EHT MWL

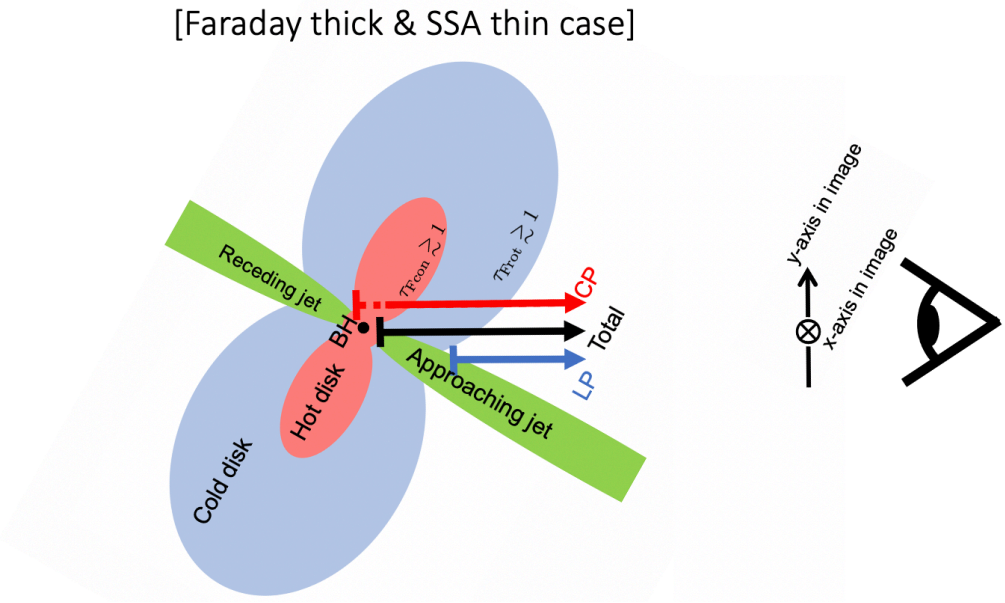

Fig. 5.6: A schematic picture displaying the rough locations where the total, LP and CP fluxes are generated and their main propagation path to a distant observer located at the far right position. This illustrates the case where the system is Faraday thick but SSA thin (e.g., at 230 GHz for our fiducial model; see section 5.5 for estimation maps of synchrotron emission and two Faraday effects). Here, the total flux is dominated by the emission from the jet base (green) and the inner hot disk (red) and the LP flux originates from the foreground jet, whereas the CP flux is dominated by the emission from the inner hot disk via the Faraday conversion (see subsection 5.2.3 for detail). Note that the original LP flux emitted from the inner hot disk and the background jet is strongly depolarized by the Faraday rotation when propagating through the inner hot, and the outer cold disk (blue). The LP-CP separation becomes more enhanced at lower frequencies (say, 86 GHz; see also subsubsection 5.3.2.1 and Fig. 5.13) or for higher mass accretion rates (see also subsection 5.3.5).

Science Working Group et al. 2021). It can be, however, advantageous o use a polar coordinate system when performing this type of cross correlation analysis on a single epoch images of ring like features. With this in mind, here we introduce correlation analyses in the polar coordinates (r, θ) on the images with the origin at $(x, y) = (0, 0)$. This is particularly useful for the M87* images at 230 GHz, because these total intensity images show ring-like features, symmetrical about the origin of the images, as seen in Fig. 5.2 or the actual observations by Event Horizon Telescope Collaboration et al. (2019a, 2021a). The correlation functions in the polar coordinates are calculated from the Stokes parameters at each pixel of $(r_k, \theta_l) = (k\Delta r, l\Delta\theta)$ in the following way:

$$\{I - S\}(i\Delta r, j\Delta\theta) \equiv \frac{\sum_{k=1}^{N}\sum_{l=1}^{N} r_k r_{k+i} I(r_k, y_l) S(r_{k+i}, y_{l+j})}{\sqrt{\left\{\sum_{k,l=1}^{N} r_k^2 I(r_k, \theta_l)^2\right\}\left\{\sum_{k,l=1}^{N} r_k^2 S(r_k, \theta_l)^2\right\}}} \quad (5.6)$$
$$(i, j = 0, \pm 1, \pm 2, ...),$$

so that $\{I - I\}(0, 0) = 1$. Here Δr and $\Delta\theta$ are the size of pixels in the r- and θ- directions, respectively. The factors of r_k and r_{k+i} in the summation come from the area element in the two-dimensional polar coordinates, $r\mathrm{d}r\mathrm{d}\theta$.

We show the auto- and cross- correlations in the polar coordinates in Fig. 5.5, respectively[5]. Autocorrelation $I - I$ has peaks at $(i\Delta r, j\Delta\theta) = (0, 0)$ by definition. In the left panel, two cross-correlations show similar profiles to that of the auto-correlation with correlation length (at half maximum) of $\sim$ 15 μas, although the cross-correlation $I - P$ is slightly shifted in the larger $i\Delta r$-direction. We can see, in the right panel, narrow $I - P$ profile with its peak at $j\Delta\theta \sim +\pi/8$ and wide $I - |V|$ profile with its peak at $j\Delta\theta \sim -\pi/16$. Here positive (or negative) $j\Delta\theta$ corresponds to the clockwise (counter-clockwise) direction around the center of the images. Therefore, these results in polar coordinates quantitatively describe the fact that the total, LP and CP fluxes on the images in Fig. 5.2 are located roughly on the same circle in the order of the LP, total, and CP intensities, in the clockwise direction, if starting from 0 o'clock (i.e. y-axis on the images).

5.2.3 Schematic of the Faraday rotation and conversion around the black hole

In the previous subsections, we found a separation of the LP and CP intensities. This is because the LP (or CP) components are mainly from the downward (upward) position with respect to the bright part of the total intensity distribution. Here, we interpret these polarimetric features by using a schematic picture of the Faraday rotation and conversion effects around the black hole.

Fig. 5.6 illustrates the case, in which the system is Faraday thick but SSA thin, as in the case that we encounter in subsection 5.2.1 (see upper row of Table 5.1 for the Faraday optical depths at 230 GHz, see also section 5.5 for estimation maps of synchrotron emission and two Faraday effects). Here, the total flux is dominated by the emission from the jet base (green) and the inner hot disk (red) around the black hole. As for polarization components, the contribution to the LP components from the downstream of the approaching (foreground) jet dominates over that from the receding (background) jet, since the latter is suppressed by strong Faraday rotation and depolarization when propagating through the inner hot and the outer cold parts of the disk. Meanwhile, the CP image is dominated by the components from the receding jet or the inner hot disk near the black hole, which are converted over larger Faraday conversion depths than those from the approaching jet. Compared with the total intensity distribution, therefore, the LP flux is distributed in the downstream side of the jet, whereas the CP flux is distributed in the counter-side jet or around the photon ring.

As introduced above, we find that the separation of the LP and CP components from the total intensity distribution can be understood in terms of the Faraday rotation and conversion in

[5] See section 5.6 for two-dimensional correlation maps in polar coordinates.

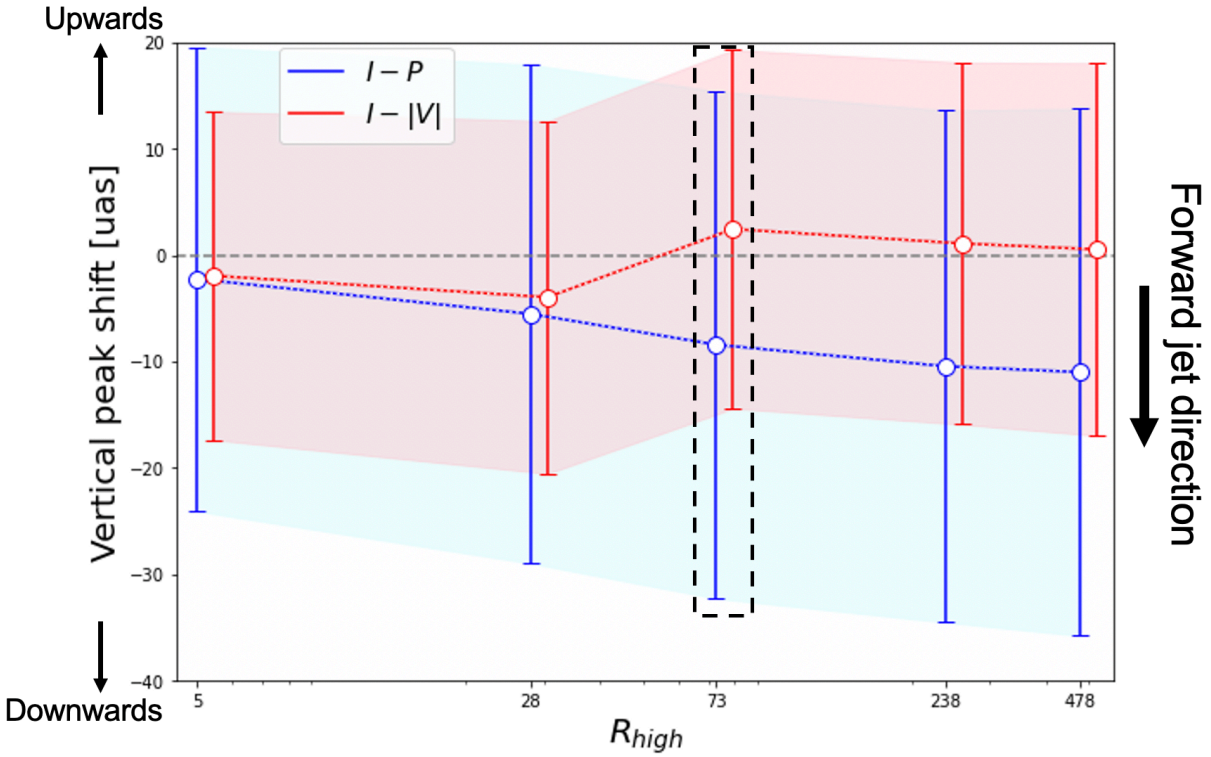

Fig. 5.7: Vertical peak shifts of cross-correlation functions $I - P$ and $I - |V|$ at 230 GHz for five electron-temperature parameters in the disk, $R_{\rm high} = 5, 28, 73, 238$, and 478. Circles correspond to the peaks, and bars the 1σ ranges of fitted Gaussian functions. The one boxed with dotted line corresponds to the peak and width of the cross-correlation profiles our fiducial model in Fig. 5.4. All of the based profiles are shown in Fig. 5.25 in section 5.8.

the jet-disk structure around the black hole. In the following section, we survey such a LP-CP flux separation for plasma and observational parameters.

5.3 Conditions for the LP-CP flux separation

5.3.1 Dependence on the electron-temperature parameter $R_{\rm high}$

In the model discussed so far, we fixed the parameters of $(R_{\rm low}, R_{\rm high}) = (1, 73)$ as our fiducial ones to describe proton-electron coupling in the jet-disk structure (see Eq. 5.1). While this choice seems reasonable in view of the recent GRMHD simulations including electron thermodynamics (Mizuno et al. 2021), a large range of $R_{\rm high}$ values are also suggested. To see how the results depend on this particular choice of the parameter, we calculate the images at 230 GHz for five models with $R_{\rm high} = 5,\ 28,\ 73\,({\rm fiducial}),\ 238,\ 478$, for which we scale the mass accretion rate of $\dot{M} = (\,1.2,\ 4,\ 6,\ 10,\ 12\,) \times 10^{-4} M_\odot/{\rm yr}$ to reproduce the total flux of 0.5 Jy in M87*, respectively, and analyze their cross-correlation functions $I - P$ and $I - |V|$.

In Fig. 5.7, we show vertical peak separation of the cross-correlations $I - P$ and $I - |V|$ as functions of $R_{\rm high}$. We also fit the vertical profiles with Gaussian function and plot their 1σ

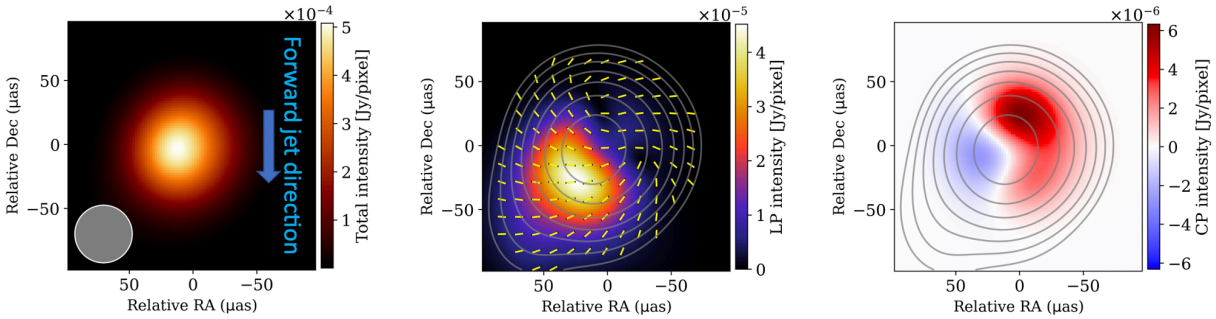

Fig. 5.8: Same as the convolved images in Fig. 5.2 but at 86 GHz with a larger field of view, being convolved with Gaussian beam of 45 μas (shown in the bottom-left of the left image). The beam size is a bit smaller than those in the present global VLBI observations at 86 GHz such as GMVA, (e.g., $123 \times 51 \mu$as; Kim et al. (2018)) with future observations in mind.

ranges as error bars on the figure (see section 5.8 for the raw profiles of the cross-correlations). The peak positions of the $I - P$ correlation shift downwards (in the downstream of the jet) by up to $\sim$ 10 μas, as $R_{\rm high}$ increases. This is because the higher $R_{\rm high}$ is, the lower becomes electron temperature in the disk (with high plasma-β). The higher $R_{\rm high}$ value, hence, requires higher mass accretion rate to reproduce the observed flux. As a result, such lower temperature and higher mass accretion give rise to stronger Faraday rotation in the disk (since $\tau_{\rm Frot} \propto nBT_{\rm e}^{-2} \propto \dot{M}^{3/2} R_{\rm high}^2$ in the disk, as pointed out by Mościbrodzka et al. (2017)). Therefore, the LP intensities originate in a more downstream region for higher $R_{\rm high}$, as shown in the picture of Fig. 5.6.

In contrast, the CP intensity distributions exhibit somewhat distinct trend; that is, the peak positions of the $I - |V|$ correlation behave irregularly for varying $R_{\rm high}$ values. This is because, unlike the Faraday rotation, the Faraday conversion is more enhanced for higher temperature and higher accretion rate, (since $\tau_{\rm Fcon} \propto nB^2T_{\rm e} \propto \dot{M}^2 R_{\rm high}^{-1}$ in the disk, see also subsection 3.3.3) so that higher $R_{\rm high}$ and $\dot{M}$ values may not necessarily yield stronger Faraday conversion. In two models with the higher $R_{\rm high}$ values (238 and 478), therefore, smaller separations are seen in the red bars in Fig. 5.7, almost down to zero for $R_{\rm high} = 478$ (which contrast the $I - P$ correlations shown in blue bars). In two models with low $R_{\rm high}$ values (5 and 28), conversely, break the tendency of the upwards CP relative to the total intensity, with the $I - |V|$ peaks in $n\Delta y > 0$. We can attribute these results to the fact that in these high electron-temperature models, the polarized emission from the broad, high-temperature disk around the midplane, which has relatively turbulent magnetic structure, becomes comparable with that from the approaching and receding jets, and the description of the emission from the twin jets and inner disk is no longer applicable (see also Fig. 5.24 in section 5.7 for cases where we observe the object from behind about the z-axis, with $\phi_{\rm camera} = 180°$).

These disk temperature survey in our model suggest that, if both the LP and CP separations would be observed in future observations, we could associate it with weaker proton-electron coupling (leading lower electron temperature) in the disk than in the jet. In the following sub-

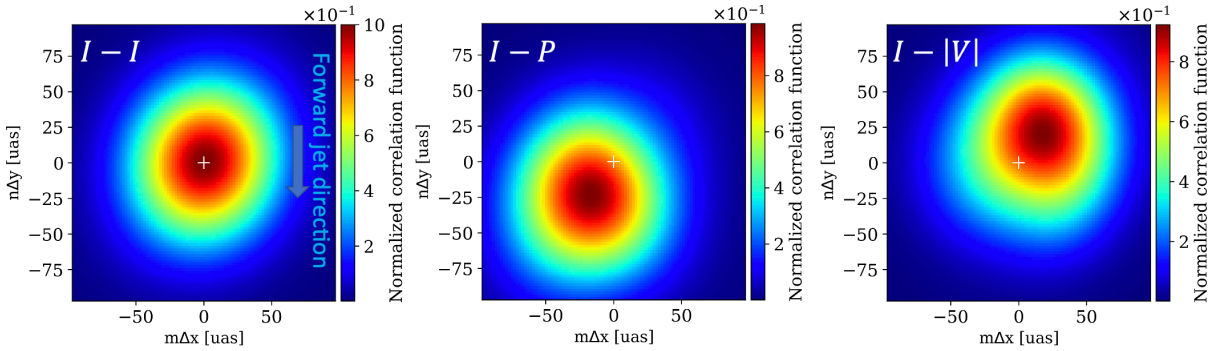

Fig. 5.9: Same as the correlation maps of Fig. 5.3 but for the images at 86 GHz in Fig. 5.8.

sections, we further survey the dependence of the LP-CP separation on observational frequencies ν, observer's inclination angles i, and accretion rates onto the black hole $\dot{M}$, for our fiducial model $(R_{\rm low}, R_{\rm high}) = (1, 73)$ with the low electron-temperature disk.

5.3.2 The LP and CP separations at multi-frequencies

So far we have seen clear tendencies in the cross-correlation functions between the total intensities and the LP or CP intensities for our fiducial model. These are caused by the Faraday effects which occur when radiation passes through the magnetized plasmas in the disk region, as described in subsection 5.2.3. Since the Faraday effects are known to be more enhanced for lower frequency (longer wavelength) observations ($\rho_V \propto \nu^{-2} \sim \lambda^2$ for the Faraday rotation and $\rho_{Q,U} \propto \nu^{-3} \sim \lambda^3$ for the Faraday conversion; see, for example, Shcherbakov 2008), we can expect that the LP-CP separation which we found at 230 GHz should be even clearer at lower frequencies, e.g., at 86 GHz. Therefore, we next survey the wavelength-dependence of the polarimetric correlations on the images, based on an angular resolution of global VLBI observations.

5.3.2.1 Correlation maps of the images at 86 GHz

We show the convolved polarimetric images at 86 GHz in Fig. 5.8, as an example at a lower frequency. The size of Gaussian-beam, or angular resolution in VLBI observations, is assumed to be 45×45 μas, which is extrapolated from the one by the EHT at 230 GHz with the scale rule of the diffraction limit, $\propto \lambda/D$, and a little optimistic compared with the existing VLBI observations at 86 GHz (e.g., 0.123×0.051 mas $= 123 \times 51$ μas; Kim et al. 2018). The total intensity image in the left panel shows a round-shaped emission profile in the left side on a linear scale, due to round-shaped, larger-sized Gaussian beam profile and to the relativistic beaming effect. In the central panel, we can see the LP intensity distributed in the bottom-left area on the image, which is obviously located in the downward region, compared with that of the total intensity. Note that the typical LP fraction is $\sim 20\%$. The CP components in the right panel shows a broad feature by Faraday conversion and the leftward "separatrix" due to the

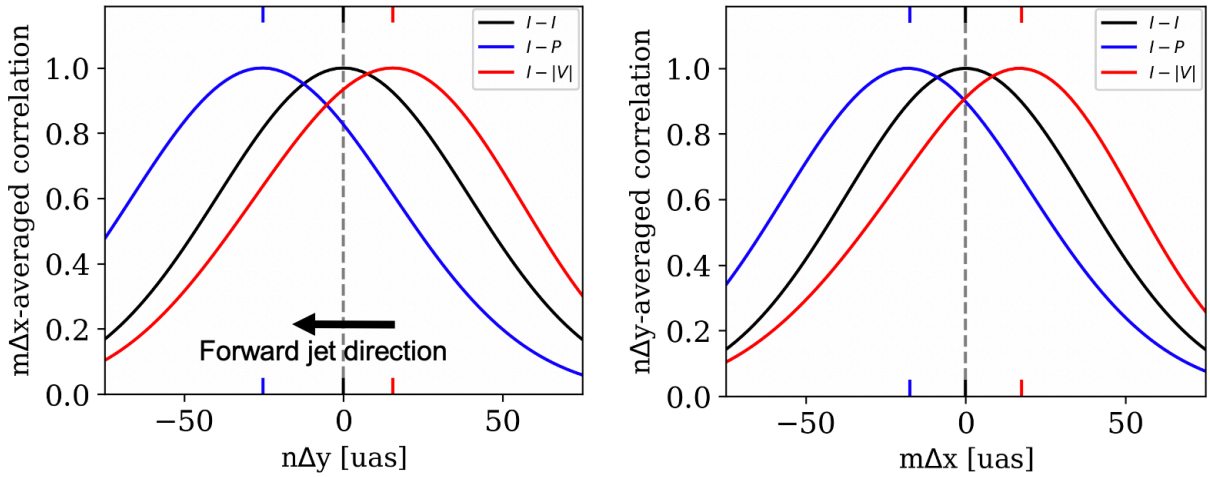

Fig. 5.10: Same as the correlation profile of Fig. 5.4 but for the images at 86 GHz in Fig. 5.8. Hatches in the upper and lower axes demarcate the places of the maximum correlation, the relative offsets between two kinds of intensity distributions.

helical magnetic field configuration and the relativistic aberration effect, at which a sign reversal occurs from negative (in the left side) to positive sign (in the right side). The existence of such a separatrix was first noted by Tsunetoe et al. (2021) (see chapter 4), although the separatrix is here overwritten and bent by the component from the approaching (foreground) jet around the origin. In absolute values, the positive CP components in the upper-right are brighter than other regions on the image.

Next, the two-dimensional correlation maps and their one-dimensional profiles in the Cartesian coordinates are shown in Figs. 5.9 and 5.10, respectively. As mentioned above, we see that the peak shifts are larger at 86 GHz, compared with those at 230 GHz, because of the stronger Faraday effects. That is, the locations of the correlation peak in the left panel of Fig. 5.10 are more separated from each other; peaks at ~ -25 μas (more downwards) for $I - P$ and at $\sim +16$ μas (more upwards) for $I - |V|$. In addition, the right panel of Fig. 5.10 also shows a separated structure of $I - P$ with a peak at ~ -17 μas (left-leaning) and $I - |V|$ with a peak at $\sim +17$ μas (right-leaning). These results are direct consequences of the features seen in Fig. 5.8 that the LP (CP) intensity is located in the bottom-left (upper-right) area, relatively to the total intensity.

We summarize the results of the correlation analyses at 230 and 86 GHz in Table 5.1 with the total LP and CP fractions and the image-averaged, intensity-weighted optical depths for the Faraday rotation and conversion. As was explained above, the stronger Faraday rotation (conversion) at 86 GHz results in the larger separation between the total and LP (CP) intensities, than at 230 GHz. Meanwhile, giving the higher total LP fraction and lower total CP fraction at 86 GHz in spite of the stronger Faraday rotation (depolarization) and conversion, the total polarization fractions do not predict the average Faraday depths, as also pointed out by Jiménez-Rosales & Dexter (2018) for the LP maps at 230 GHz of Sgr A*.

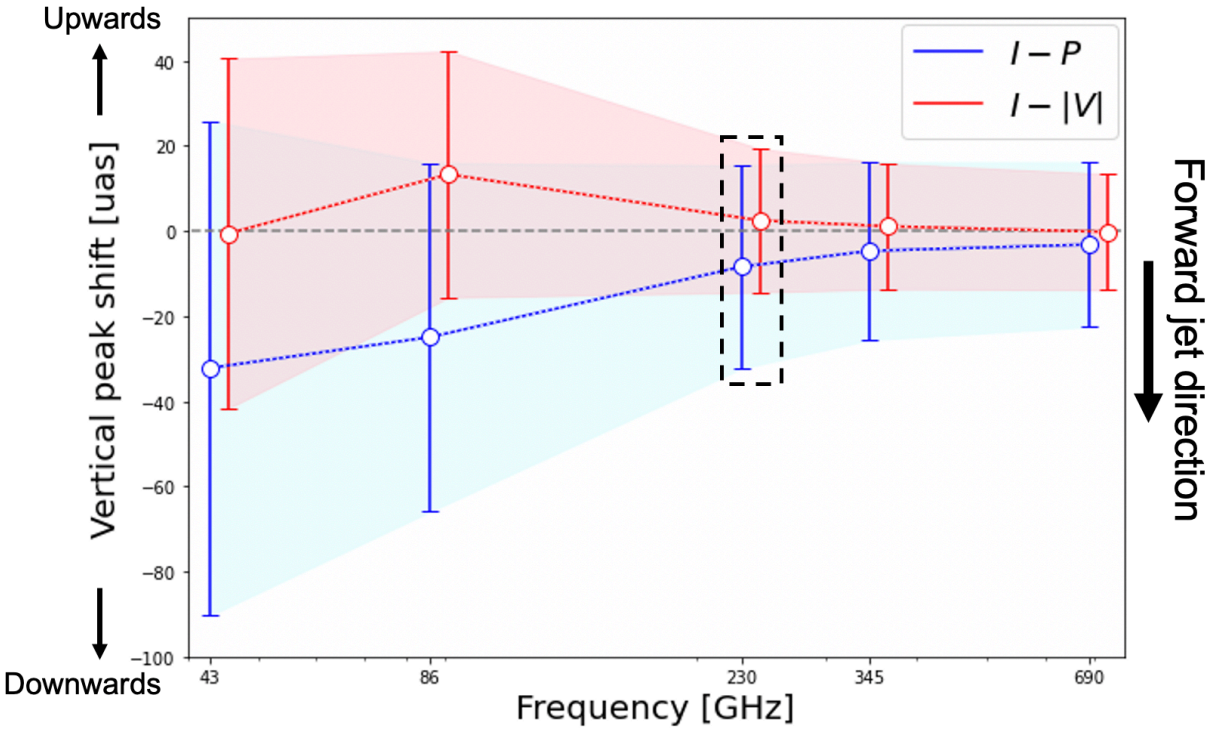

Fig. 5.11: Same as the vertical shifts of the cross-correlations in Fig. 5.7, but at five frequencies of 43, 86, 230, 345, and 690 GHz. The one boxed with dotted line corresponds to the image at 230 GHz in Fig. 5.4. While both of LP and CP show larger separations from the total intensity at lower frequency, the CP image at 43 GHz gives no separation because of strong SSA effect. See Fig. 5.26 in section 5.8 for the correlation function profiles which are based on making this figure.

5.3.2.2 Dependence on frequencies

We show the frequency-dependence of the vertical peak shifts in Fig. 5.11; at 43, 86, 230, 345, and 690 GHz, which are calculated by assuming Gaussian beam of 90, 45, 17, 10, and 5 μas, respectively.

As expected, the cross-correlation profiles at lower frequency show the larger tendency of the separation of the LP and CP components. That is, peaks of the cross-correlations $I - P$ (blue) leave off to the bottom-left up to $n\Delta y \sim 35$ μas (and $m\Delta x \sim 25$ μas; see section 5.8 for more detailed information and figures) as the frequency decreases, which demonstrate that the LP flux distribution is more shifted towards the bottom-left corner of the image along the beamed part of the approaching jet at lower frequency. Likewise, peaks of $I - |V|$ (red) tend to leave off to the top ($n\Delta y \sim 15$ μas), meaning that the CP flux at lower frequency down to 86 GHz is more separated from the total flux in the vertical direction. Exceptionally, the peak of the cross-correlation $I - |V|$ at 43 GHz behaves irregularly in the figure, showing coincidence of the total and CP intensity distributions (i.e., their cross-correlation show a peak at $n\Delta y \sim 0$). In the following subsection, we interpret these results in terms of the depths of the Faraday rotation and conversion, and of the SSA in radiative transfer process near the black hole.

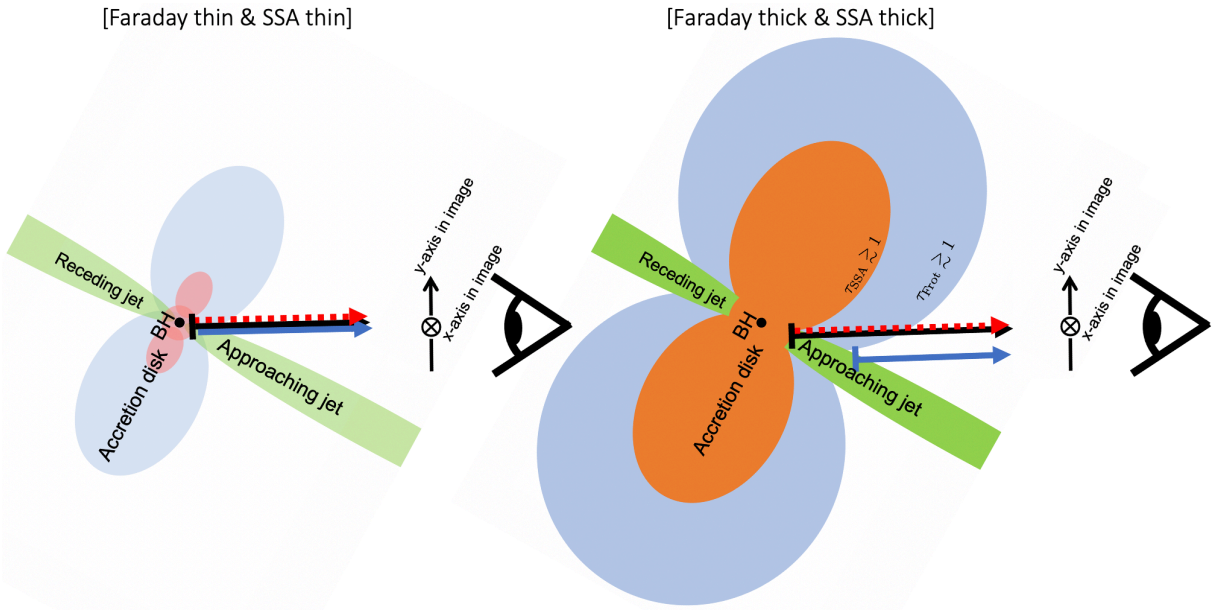

Fig. 5.12: Same as the schematic picture of Fig. 5.6 but for the optically thin (left) and thick (right) cases for the Faraday rotation and conversion effects and the SSA. The left picture illustrates the case where the plasma near the black hole is optically thin both for the Faraday effects and for synchrotron self-absorption (SSA), at higher frequencies (say, 345 and 690 GHz; see also Fig. 5.13) or for lower mass accretion rates. In this case, all of the total, strong LP and weak CP intensities at synchrotron emission directly come from near the black hole. The right picture illustrates the case where the system is Faraday thick and SSA thick at even lower frequencies (say, 43 GHz; see also Fig. 5.13) or for even higher mass accretion rates. Here the total intensity and weak CP intensity originates from the surface of the photosphere (orange) of the disk-jet structure, while the LP flux is depolarized in the outer Faraday (rotation) thick plasma (blue) and is dominated by those from the downstream of the foreground jet. See subsection 5.3.3 for detail description.

5.3.3 Why CP separation disappears at 43 GHz?

In the previous subsection, we saw the relationship between the polarized intensity distributions and that of the total intensity at multi-frequencies, finding peak separation increasing towards lower frequencies. We, however, noticed that such general tendency disappears for CPs at 43 GHz, why? Here, we describe how we understand these results by using two schematic pictures of Fig. 5.12, in comparison with Fig. 5.6.

The left picture in Fig. 5.12 illustrates the case, in which the disk-jet system is optically thin both for the Faraday effects (rotation and conversion) and for the SSA. This corresponds to the cases when the observed frequency is high (say, 345 or 690 GHz) and/or when the accretion rate is relatively low (e.g., $\langle \tau_{\mathrm{Frot},I} \rangle \simeq 19$ and $\langle \tau_{\mathrm{Fcon},I} \rangle \simeq 0.05$ at 690 GHz; see also the frequency-dependence of the three optical depths shown in Fig. 5.13). Here, the inner hot disk (with $\gtrsim 10^{10}$K), outer cold disk (with $\lesssim 10^{9}$K), and the jet are indicated by the red, light blue, and green colors, respectively. We then see that all of the total, strong LP and weak CP intensities at synchrotron emission directly come from the region near the black hole without being affected

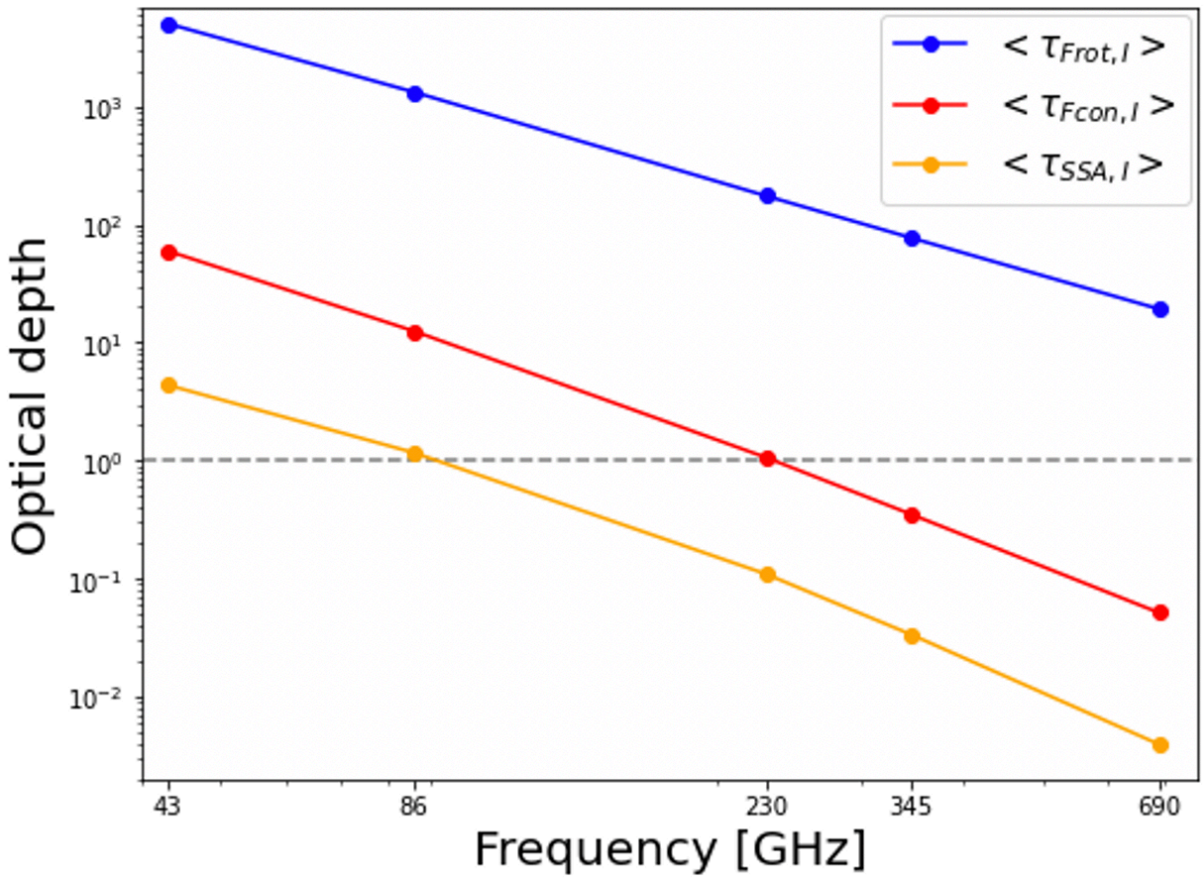

Fig. 5.13: Frequency-dependence of the image-averaged intensity-weighted optical depths for the Faraday rotation and conversion, and the synchrotron self-absorption, $\langle\tau_{\rm Frot,I}\rangle$, $\langle\tau_{\rm Fcon,I}\rangle$, and $\langle\tau_{\rm SSA,I}\rangle$. The grey dashed line corresponds to $\tau = 1$. $\langle\tau_{\rm Frot,I}\rangle$ and $\langle\tau_{\rm Fcon,I}\rangle$ roughly follow the rules of $\tau_{\rm Frot,I} \propto \nu^{-2}$ and $\tau_{\rm Fcon,I} \propto \nu^{-3}$, which reflect dependence of coefficients of the Faraday effects, $\rho_V \propto \nu^{-2}$ and $\rho_Q \propto \nu^{-3}$.

by the Faraday effects nor the SSA, to reach the observer's camera. We thus understand that all of the total, LP and CP intensities originate in the same or close place, so that the peaks of cross-correlations $I - P$ and $I - |V|$ should be at zero shift; i.e., $(m\Delta x, n\Delta y) = (0, 0)$ as the frequency becomes higher in Fig. 5.11.

Conversely, the right picture in Fig. 5.12 shows the case, in which the disk-jet system is Faraday thick and SSA thick. This corresponds to the cases when the observed frequency is low (say, 43 GHz) or when the accretion rate is relatively high, as was mentioned in subsection 5.3.2.2 and will be introduced in subsection 5.3.5 (e.g., the image-averaged intensity-weighted SSA depth is $\langle\tau_{{\rm SSA},I}\rangle \simeq 4.4$ at 43 GHz, while $\simeq 0.11$ at 230 GHz; see also Fig. 5.13). Here, we can understand the exceptional behavior at 43 GHz on Fig. 5.11 which arises because of a very large SSA depth near the black hole. In such a case, the polarized emissions come only from the surface of the photosphere (indicated by the orange color). Therefore, the emitted CP intensity is not amplified and is distributed in the similar way to the total intensity, while the LP intensity is depolarized by Faraday rotation in the outer cold disk (blue) and is dominated by

those from the downstream of the approaching jet.

We also calculated the images and correlation functions at 22 GHz with circular convolution beam of 90 μas same as at 43 GHz, because the beam size of 180 μas extrapolated from the diffraction limit is too large compared to the field of view of $\approx 185\mu$as for safe analyses. The resultant images at 22 GHz show downward LPs but no upward CPs as in those at 43 GHz, which are also consistent with the description in the Faraday- and SSA- thick case. Meanwhile, they give a little smaller separation between the total and LP intensities compared to those at 43 GHz. This can be because the SSA photosphere (orange) drastically expands and approaches to the sphere of the Faraday-rotation thick disk (blue) at 22 GHz.

In summary, we classify the behavior of the total, LP and CP intensity distributions on the images as seen in Fig. 5.11 into three regimes based on the optical depths, as pictured in Figs. 5.6 and 5.12. At high frequencies at which the plasma is optically thin both for the Faraday effects and for the SSA, all of the total, dominant LP, and weak CP intensities are distributed in the similar way. At low frequencies at which the plasma is optically thick for the Faraday rotation and conversion, the LP distribution shifts upwards while the amplified CP components are distributed downwards compared with the total intensity distribution. At even lower frequencies at which the plasma is optically thick both for the Faraday effects and for the SSA, the CPs become distributed similarly to the total intensities while the LPs keep being distributed upwards relatively to the total intensity.

5.3.4 Dependence on the inclination angle i

In the context described above, one may intuitively expect that the spatial gaps among the total, LP, and CP intensities should depend on the inclination angle (viewing angle) of the observer. That is, the larger (or smaller) is the inclination, or the closer is an observer to the edge-on (face-on) direction, the more (less) separated are among the total, LP, and CP intensity distribution, since the longer (shorter) becomes the distance projected on the observer's screen.

To examine the inclination angle-dependence of the correlations, we show the vertical shifts of the peaks of the correlation profiles for inclinations of $i = 150°$ and $170°$ in Figs. 5.14 (see section 5.8 for the profiles). Comparing with our fiducial model with $i = 160°$ displayed in Fig. 5.4, we notice similar tendencies for other cases with different inclination angles; that is, downward (or upward) shift of the cross-correlations with LP (CP), but the larger (smaller) separations for the larger (smaller) inclination, demonstrating the above intuition. We summarize these results for the inclination angle-dependence in Table 5.2.

We can thus conclude that *the polarimetric correlation analyses are potentially important methods to give constraints on the inclination angle of the approaching jet in its base region*, through the analyses of the separated polarization components on the images around the black hole, comparing the values constrained by observations of the larger-scaled jet at multi-frequencies (e.g., $i \approx 162° - 163°$ ($17° - 18°$) in Mertens et al. 2016 and Walker et al.

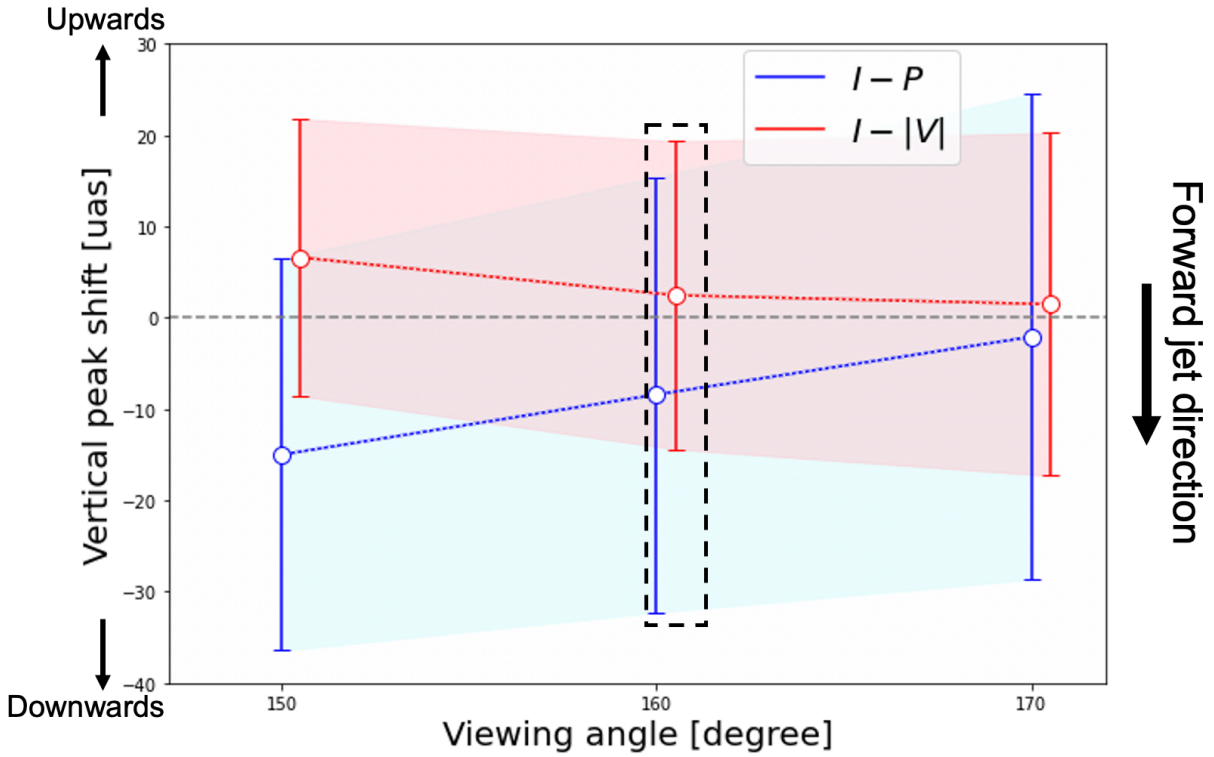

Fig. 5.14: Same as the vertical shifts of the cross-correlations in Fig. 5.7, but for three inclination (viewing) angles of observer, $i = 150, 160, 170°$. The one boxed with dotted line corresponds to our fiducial model in Fig. 5.4. The based profiles are shown in Fig. 5.27 and 5.28 in section 5.8.

2018).

5.3.5 Dependence on accretion rates onto the black hole $\dot{M}$

In subsection 5.3.1, we changed the parameter $R_{\rm high}$ and accordingly scaled the mass accretion rate onto the black hole, $\dot{M}$, to reproduce the observed flux of M87*. Here, we only change the accretion rate $\dot{M}$ for a fixed $R_{\rm high}$ $(= 73)$, bearing application to a variety of LLAGN jets in mind.

We calculate the images for $\dot{M} = 6 \times 10^{-3} M_{\odot}/{\rm yr}$, ten times higher accretion rate than our fiducial model, and show the convolved images with 17 μas Gaussian beam in Fig. 5.15.

Inclination angle	$I - P$ peak	$I - \|V\|$ peak	Fig. number
150°	-15 μas	$+7$ μas	Fig. 5.27
160°	-8 μas	$+2$ μas	Figs. 5.1, 5.2, 5.4
170°	-1 μas	$+1$ μas	Fig. 5.28

Table 5.2: Comparison among the different inclination angles; the vertical peak shifts of cross-correlation functions $I - P$ and $I - |V|$, and corresponding figures, from the left to the right.

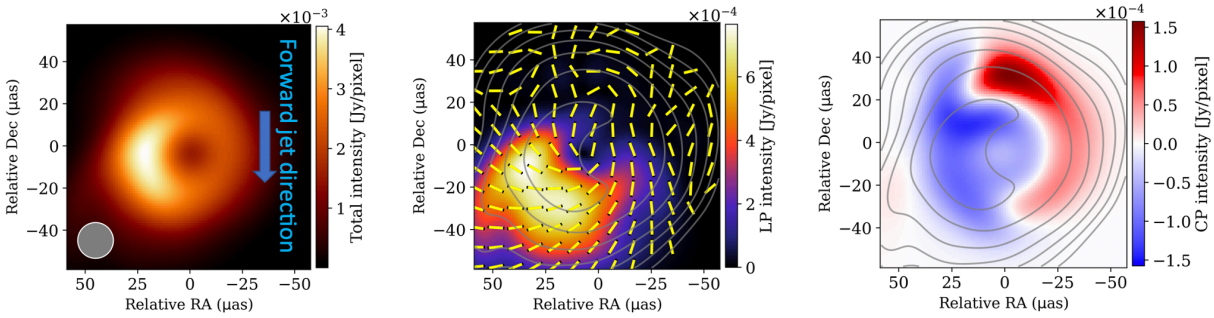

Fig. 5.15: Same as the convolved images in Fig. 5.2 but for a model with ten times higher accretion rate of $\dot{M} = 6 \times 10^{-3} M_\odot/\mathrm{yr}$.

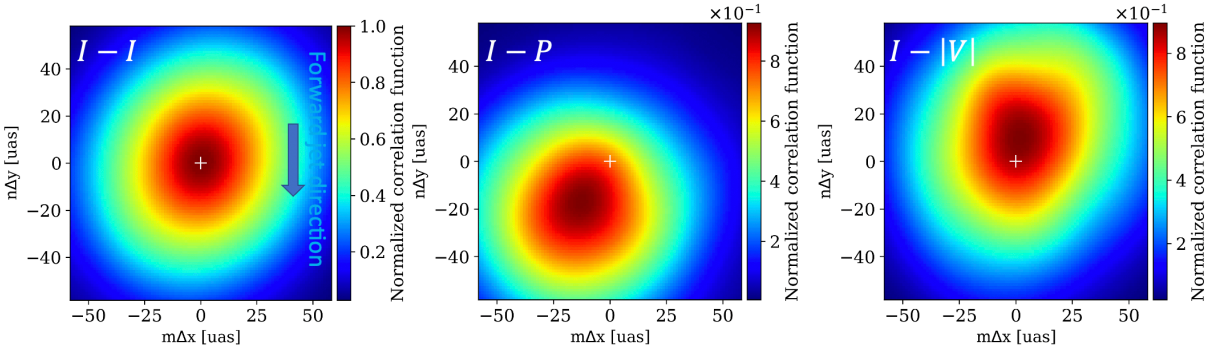

Fig. 5.16: Same as the correlation maps of Fig. 5.3 but for the images for high accretion model in Fig. 5.15.

Compared with Fig. 5.2, they show a broader emission profile consisting of the photon ring and the foreground jet, dominance of the LP intensity in the jet, and stronger CP components in the photon ring and from the background jet with the sign-flipping separatrix (see in Fig. 5.8 for the images at 86 GHz, see also chapter 4). We also show three maps of the auto- and cross- correlation functions in Fig. 5.16. They reflect the polarimetric features described above and give larger separation between the total and LP and between the total and CP intensity distributions, than our fiducial model displayed in Fig. 5.3.

In Fig. 5.17, we show the vertical shifts of the peaks of the cross-correlation functions $I-P$ and $I-|V|$ for four mass accretion rates, $\dot{M} = (3,\ 6,\ 20,\ 60,\ 300) \times 10^{-4} M_\odot/\mathrm{yr}$. Both of $I-P$ and $I-|V|$ give monotonic increases in their peaks as the accretion rate increase, demonstrating that the LP (or CP) intensity on the image for higher accretion rate originates from in more downward (upward) regions, relative to the total intensity emitting region (see Fig. 5.6 and the left picture in Fig. 5.12, see also their explanation in subsections 5.2.3 and 5.3.3). This is because higher mass accretion rate $\dot{M}$ leads to higher particle density and stronger magnetic fields in non-radiative GRMHD simulations with a fixed black hole mass $M_\bullet$, giving rise to stronger Faraday effects, as was shown in subsection 5.3.1 ($\tau_{\mathrm{Frot}} \propto \dot{M}^{3/2}$ and $\tau_{\mathrm{Fcon}} \propto \dot{M}^2$). The highest accretion-rate model with $\dot{M} = 3 \times 10^{-2} M_\odot/\mathrm{yr}$ shows a somewhat different behavior, that is, it gives a small peak shift in $I-|V|$. This is because the highly accreted plasma becomes

optically thick not only for the Faraday effects but also for the SSA, with $\langle \tau_{\mathrm{SSA},I} \rangle \simeq 21$, and the polarized images are dominated by emission from the foreground photosphere (see the case at 43 GHz in Fig. 5.11, see also the right picture in Fig. 5.12 and its explanation in subsection 5.3.3).

The above results show that higher-mass accretion rates give larger LP-CP separations, but even higher mass accretion suppresses the separation of the CPs due to SSA effect, if the other parameters are fixed to those of M87*. This can be analogous with the LLAGNs with large-scale jets, such as 3C 279 or Cen A, because we here assume that the electrons are hotter in the jet than in the disk and emission in the jet dominates over that in the disk. Meanwhile, we should be careful to apply these discussion to the LLAGNs without large jet, like Sgr A*. Such LLAGNs can be modeled with the hotter disk, so that the disk emission becomes dominant. Our M87 models with higher disk temperature, as shown in subsection 4.1, do not necessarily present the separation of CPs. In future works, we should statistically check the hot disk cases with various BH masses and inclination angles, bearing a variety of LLAGNs in mind.

5.3.6 Comparison with observations

Here, we compare our results at multi-wavelengths with existing observations including linear-polarimetry. As mentioned in subsection 5.2.1 and also pointed out in Event Horizon Telescope Collaboration et al. (2021a), the linear-polarimetric images at 230 GHz obtained by the EHT persistently show strong LP components in the south-west region on the ring feature. This region corresponds to the downstream side of the large-scale jet, extending from the bright region (south part of the asymmetric ring) in total intensity image of our study, as pictured in Fig. 5.18 (see the middle panel of Fig. 5.2; note that the jet direction is downward in this plot). In this sense, our simulated images at 230 GHz are consistent with the observational features as was already discussed (see, e.g., subsection 5.2.1). (Note, however, that it is observationally unclear if this region really corresponds to a jet.)

We furthermore infer that this region may extend to the north-west jet, which was observed at lower frequencies (e.g. at 86 GHz). Hada et al. (2016) observed M87 jet at 86 GHz by the Very Long Baseline Array (VLBA) and the Green Bank Telescope, and presented the first 86 GHz polarimetric image in their Figure 10. They detected a polarized feature at ≈ 0.1 mas ($= 100$ μas) downstream from the M87 core with LP fraction of $3 - 4$ %. Walker et al. (2018) presented the LP maps of M87 jet at 43 GHz by VLBA in their Figure 15, showing the peak of LP intensity at ≈ 0.15mas ($= 150$ μas) southwest of the core with fractional LP of $1 - 4$ %. Kravchenko et al. (2020) also gave the LP maps at 43 (and 24) GHz by VLBA in their Figure 1, with the LP emission peaks at $\sim 0.1 - 0.2$mas ($= 100 - 200$ μas) downstream with LP fraction of $2 - 3$ % over a long period (2007 - 2018).

Our results at 86 GHz (and at 43 GHz) in subsection 5.3.2 suggests that the LP intensities are distributed left-downward by $25 - 30$ μas ($30 - 40$ μas) relatively to the total intensity, with

LP fraction of ≈ 20 %. These are qualitatively consistent with the observations in that the LP maps at lower frequencies give larger separations from the total intensity images, suggesting that the LP components at multi-wavelengths from near the black hole and the base region of the extended jet can be unifiedly explained by a persistent description, as pictured in Fig. 5.12. Meanwhile, the values of distances and LP fractions differ by factors from the observations. These deviations can be resolved by future observations with higher resolution, since we here assumed smaller beam size than existing observations (e.g., 45×45 μas at 86 GHz)[6]. Furthermore, combination between the linear- and circular-polarimetry in future observations will improve the situation.

In Johnson et al. (2014) and Johnson et al. (2015), they showed that the offset between the centroids of the total and linearly polarized flux can be estimated from the visibility on a short baseline. Thus we can expect to extract the information about the separation of polarized fluxes from even a single or a few interferometric baselines in present and future observations, to give a constraint on the plasma properties by the description introduced above.

5.3.7 Future prospects

Whereas we adapt the $R - \beta$ prescription by Eq. 5.1 in determination of the electron temperature distribution, Event Horizon Telescope Collaboration et al. (2021b) pointed out that the temperature ratio is not necessarily well described by this prescription in comparison with their fully radiative simulations.

Actually, the polarization components from near the black hole should be affected by the temperature prescription in the jet-disk region through the Faraday effects. In future works, we should verify the validity of the present results through comparison with those based on the fluid calculation incorporating the radiative cooling effect, which should significantly affect both of the ion and electron temperature distribution.

Related to the above discussion, Event Horizon Telescope Collaboration et al. (2021b) also suggested $R_{\rm low} > 1$, characterized as low electron-temperature in the jet region, for M87* from radiative simulations. To survey this parameter domain, we calculate a same model as the above but with $R_{\rm low} = 10$. We confirm the LP-CP separation feature at 230 GHz with an increased mass accretion rate of $\dot{M} = 1.5 \times 10^{-3} M_\odot/{\rm yr}$.

To examine the uncertainty in the sigma cutoff $\sigma_{\rm cutoff} < 1$, we also calculated a test model without the sigma cutoff. The resultant images at 230 GHz give only the downward LPs but not the upward CPs, because a lower mass accretion rate of $\dot{M} = 2.5 \times 10^{-4} M_\odot/{\rm yr}$ leads to small Faraday conversion depths, $\langle \tau_{\rm Fcon,I} \rangle \sim 0.1$. Meanwhile, the images at 86 GHz show both of the LP and CP separations due to large Faraday rotation and conversion depths.

[6]We can point out that the total (image-integrated) LP fractions in our model of 4.2% at 86 GHz and 4.6% at 43 GHz are comparable with the observed values in the peak LP regions.

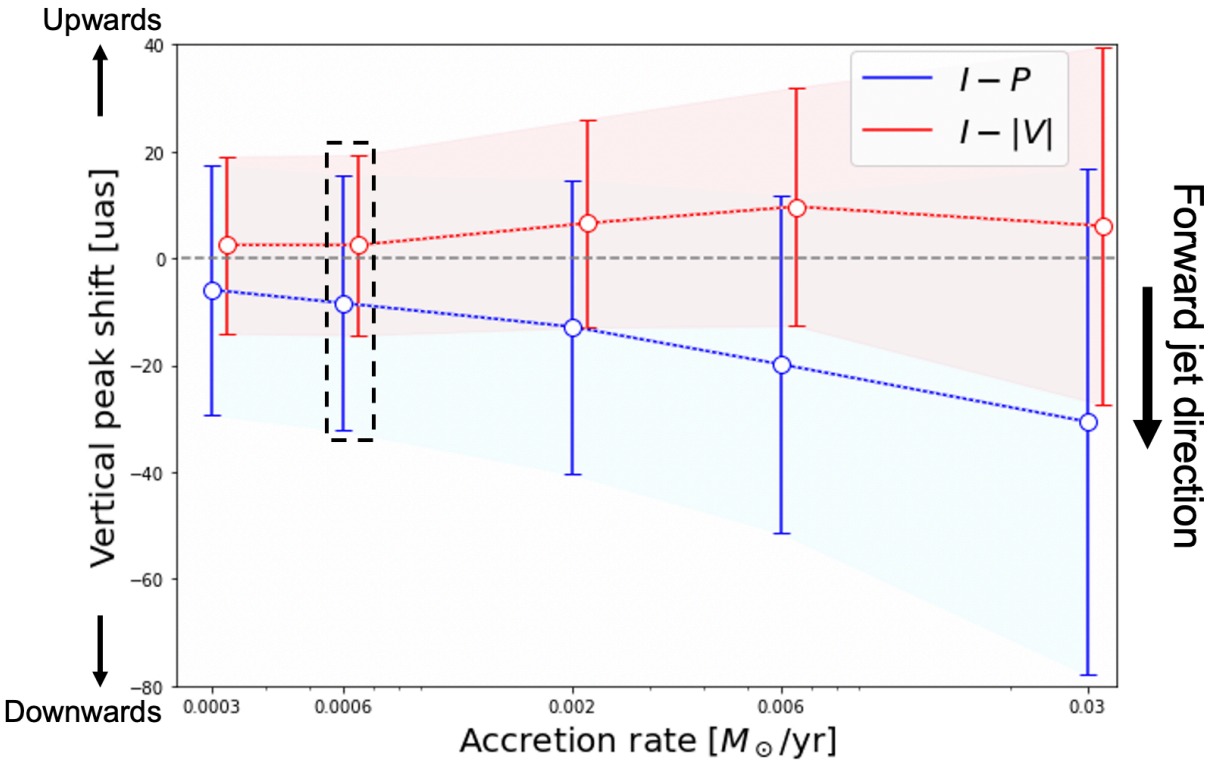

Fig. 5.17: Same as the vertical peak shifts of cross-correlations in Fig. 5.7 but for four mass accretion rates onto the black holes $\dot{M} = (3, 6, 20, 60, 300) \times 10^{-4} M_\odot/\mathrm{yr}$. The one boxed with dotted line corresponds to our fiducial model in Fig. 5.4. While both of LP and CP show larger separations from the total intensity for larger mass accretion rate, the CP image for $\dot{M} = 3 \times 10^{-2} M_\odot/\mathrm{yr}$ gives a small separation because of strong SSA effect. The based profiles are shown in Fig. 5.30 in section 5.8.

In regards to the fluid model, we showed the MRI Q-values of $(Q_r, Q_\theta, Q_\phi) = (3.23, 3.97, 11.0)$ in subsection 5.1.1. The Q_ϕ seems sufficient compared with the fiducial value $Q \sim 6$ in Sano et al. (2004), although Q_r and Q_θ seem a bit insufficient. Meanwhile, these three values are insufficient compared to $Q_z \sim 10$ and $Q_\phi \sim 20$ in Hawley et al. (2011). Based on that depolarization by turbulent magnetic fields in small scale can make quantitative difference, we will perform highly resolved GRMHD simulations and polarized GRRT, and quantitatively analyze the results in future work.

In this work, we suggested the LP-CP separation features for the images based on semi-MAD models. It should be checked in future works whether and to what extent the LP-CP separation would be obtained for SANE or MAD models. The tendency of the LP-CP separation might be complicated by two conflicting factors: (1) We could assume that SANE models might give larger separations due to the larger Faraday depth with a higher mass accretion rate to reproduce the flux of M87*, while MADs might show smaller ones because of a lower mass accretion. (2) In contrast, another possibility is that the stronger magnetic field and higher jet velocity in MADs could result in the stronger LP flux in the approaching jet, i.e., larger LP-CP separation, which could be expected from fig.4 in EHTC (2021b; paper VIII). In addition

to those mentioned above, the separations can also be affected by the jet-disk structure and its time-variability, in particular to the MADs. Thus, it should be statistically tested both for the SANE-MAD regime and for various model parameters such as the BH spin, the electron-temperature prescription, observer's inclination angle.

Finally, all of the results and discussions above are based on one snapshot of the GRMHD model with different parameters at multi-frequencies. To check the validity of the results for the choice of GRMHD snapshot[7], we newly pick up three snapshots in the quasi-steady state, in addition to the above one. Here, we calculate these four models for four different azimuthal angles of the observer's camera, $\phi_{\rm camera} = 0, 90°, 180°$, and $270°$, thus sixteen images at 230 GHz in total.

As a result, we confirm the LP-CP separation with the shifts of up to $\sim 15\mu as$ in 13 out of 16 images, while the remaining three images show only $I - P$ peak shift but give the both of LP and CP separation in the images at 86 GHz. (See also Fig. 5.31 in section 5.9 for a scatter diagram with histogram of $I - P$ and $I - |V|$ for these images.) Thus, we conclude that the results are robust for the choice of the GRMHD snapshot, although more statistical analyses including the time-variability should be performed in future works.

5.4 Maps of plasma quantities in the GRMHD model

In Fig. 5.19, we show the poloidal maps of four plasma quantities for our fiducial model, the plasma density ρ in $\mathrm{g/cm^3}$, the dimensionless electron temperature $\theta_{\rm e} \equiv k_{\rm B}T_{\rm e}/m_{\rm e}c^2$, the plasma-$\beta$ parameter, and the plasma magnetization σ. The particle density is scaled with the black hole mass $M_\bullet = 6.5 \times 10^9 M_\odot$ and the accretion rate $\dot{M} = 6 \times 10^{-4} M_\odot/\mathrm{yr}$. We take $(R_{\rm low}, R_{\rm high}) = (1, 73)$ in the determination of the electron temperature by Eq. 5.1. The other two quantities are independent of the model parameters.

5.5 Radiative coefficient maps and transfer plots along a light path

We show three maps of the synchrotron emissivity j_I, and coefficients of Faraday conversion and rotation, ρ_Q and ρ_V at 230 GHz in Fig. 5.20, which are estimated from the plasma density, electron temperature, and magnetic field strength. They consist of no sigma cutoff case in the left half ($\phi = \pi$) and sigma cutoff case in the right half ($\phi = 0$). These estimation maps demonstrate that emissions in the edge of jet within a range of $-5r_{\rm g} < z < 5r_{\rm g}$ dominate over those in the disk, except the region in the vicinity of the black hole $r \lesssim 3r_{\rm g}$, even with

[7] We here distinguish the term of "choice of snapshot" from "time-variability", in that we adapt different scaling factor from simulation- to cgs- units for each snapshot to reproduce the M87* flux of 0.5 Jy in 2017.

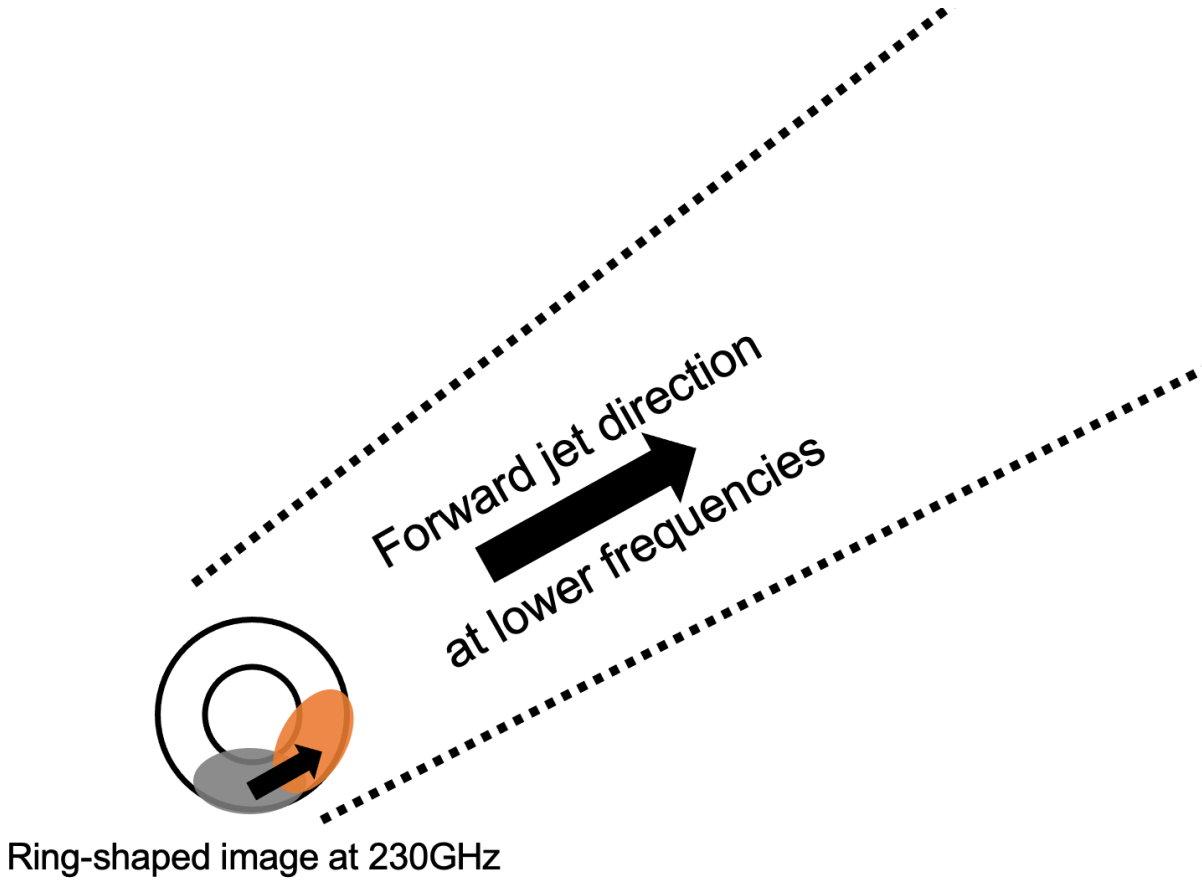

Fig. 5.18: A schematic picture showing the relationship between the total intensity and LP images at 230 GHz and the total intensity image at lower frequencies (e.g. 86 GHz) with our interpretation. The ring in the lower-left corner corresponds to the EHT image at 230 GHz and the brightest region in the total intensity image and that in the LP map are indicated by the grey color (in the south part of the ring) and by the orange color (in the south-west part), respectively. The jet, which is observed at lower frequencies, is indicated by the two dotted lines extending to the north-west direction (the downward direction in our images; see, e.g., Fig. 5.2 and 5.8). Thus, we can interpret that the LP flux is mainly distributed in the downstream side of the jet, compared with the total flux distribution.

the sigma cutoff, while Faraday conversion and rotation are strong in the inner and outer disk, respectively, as pictured in Fig. 5.6.

Further, we pick up a pixel pointed by a white "x" in the left image of Fig. 5.21, and show the radiative transfer plots along the light path (shown in the central and right panel of of Fig. 5.21) in Fig. 5.22. The pixel is located in the brightest region in the total intensity image, and around a "cross-section" between the photon ring and the tail-like jet feature.

We can follow up the radiative transfer plot lines of Stokes parameters in Fig. 5.22 by four steps, referring the radiative coefficients in Fig. 5.20, as follows:

(1) the synchrotron emission occurs in the jet-edge in the north ($z > 0$) side simultaneously with the Faraday rotation and conversion processes. Combination of these effects leads to increase of both LP ($\sqrt{Q^2 + U^2}$) and CP (V), in addition to the total intensity (I), as

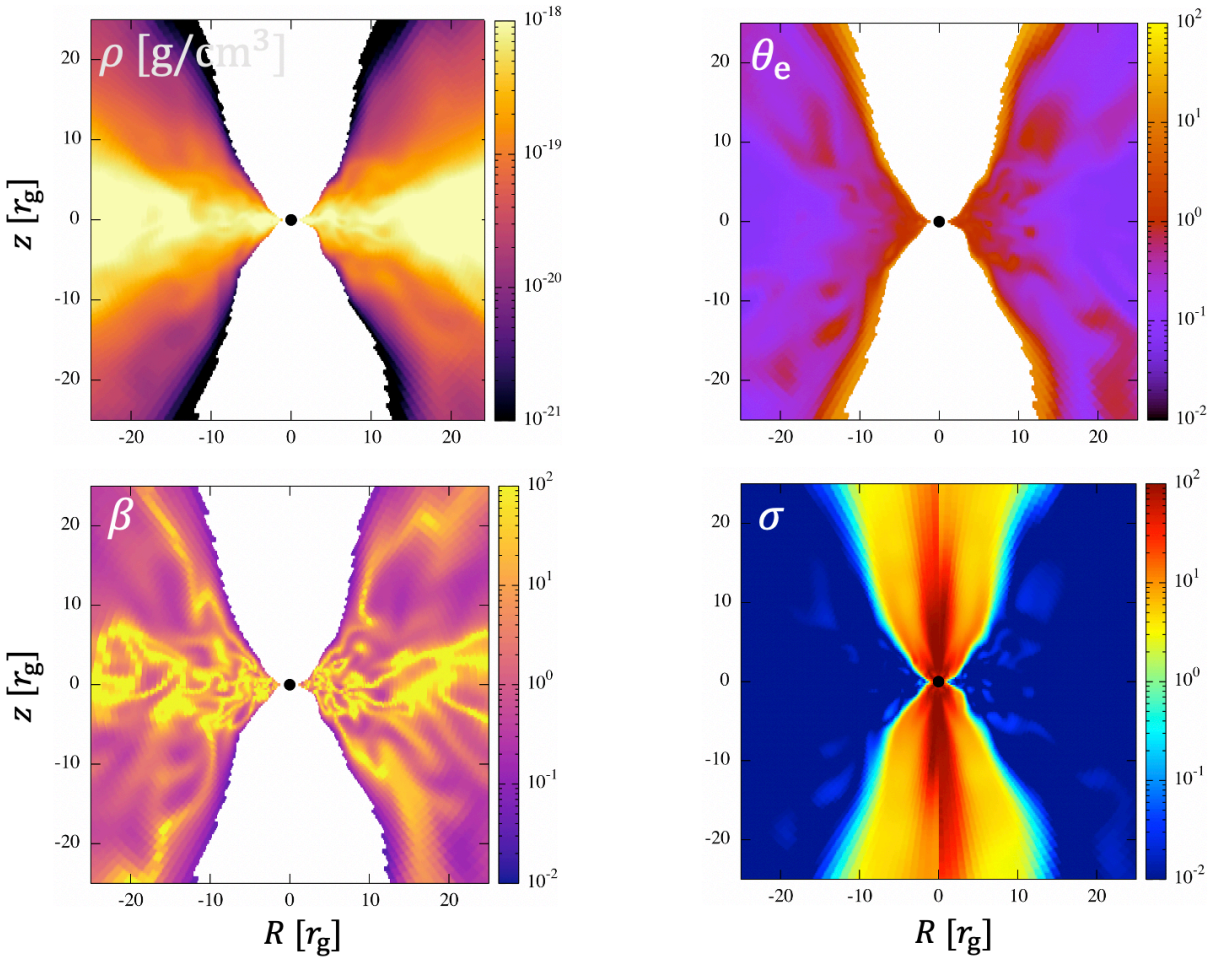

Fig. 5.19: Maps of four plasma quantities in our GRMHD model with $R_{\rm low} = 1, R_{\rm high} = 73$. Upper-left: the plasma density ρ in $\mathrm{g/cm^3}$. Upper-right: the dimensionless electron temperature $\theta_{\rm e} \equiv k_{\rm B}T_{\rm e}/m_{\rm e}c^2$. Bottom-left: the plasma-β parameter. Bottom-right: the plasma magnetization σ. Each map consists of a snapshot at $t = 9000t_{\rm g}$ for $\phi = \pi$ in the left half and for $\phi = 0$ in the right half. In the former three maps, only the region with $\sigma < \sigma_{\rm cutoff} = 1$ is plotted.

we also introduced in chapter 3.

(2) Entering the disk region around the equatorial plane, Faraday rotation becomes dominant. Thus, the LP vector is drastically rotated, giving rise to rapid oscillations of Q and U.

(3) In the jet-edge in the south ($z < 0$) side, the emission arises again. While the total intensity increases, the rotated LP vector are partly canceled out with the new emission component. The CP does not change significantly due to weak Faraday conversion, because the light is now passing through the outer or downstream region relatively to the prior northern jet-edge. After leaving this region, the light enters the sigma cutoff region in the southern funnel region.

(4) There is a low-σ region in the funnel distributed in a spiral shape in the three-dimensional fluid model. This feature can be seen, for example, as a “hump”-like feature along the jet-

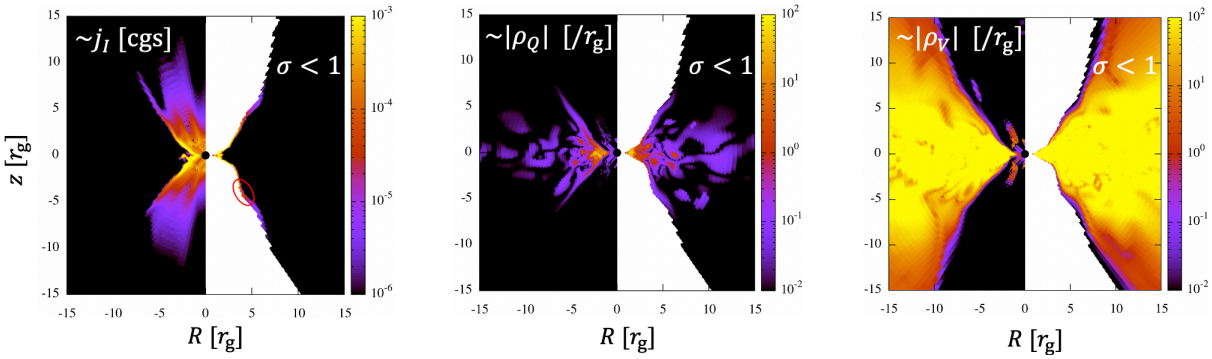

Fig. 5.20: Three maps of the synchrotron emissivity j_I, Faraday conversion coefficient ρ_V, and Faraday rotation coefficient ρ_Q at 230 GHz, left to right. The values are estimated from the plasma density, electron temperature, and magnetic strength at $t = 9000t_g$, ignoring the relativistic effects and the angle effect between the light path and magnetic field. Each map consists of no sigma cutoff case in the left half ($\phi = \pi$) and sigma cutoff case in the right half ($\phi = 0$). The jet emission is dominant over the disk emission, except the region in the vicinity of the BH $r \lesssim 3r_g$. The Faraday effects are stronger in the disk than in the jet. A red circle in the left panel corresponds to the "hump"-like feature introduced in step (4) in Fig. 5.22 and section 5.5.

edge around $(5r_g, -5r_g)$ in the left panel of Fig. 5.20. Here, the total intensity increases and the LP is overwritten in similar way to (3) in the south jet-edge, since the synchrotron emission occurs again.

As a result, we obtain the total intensity increased in the inner jet-edges and the downstream spiral low-σ component, which can be seen as the photon ring and the tail-like jet on the image. Further, the obtained LP vector consists of the rotated components from the north (counter-side) jet-edge and the overwriting emission from the south (approaching) jet-edge. Finally, the obtained CP is originated from those increased in the north (counter-side) jet-edge. Therefore, the LP map is dominated by the contributions from the approaching jet while the CP image by those from the counter-side jet, after the observational beam convolution. In this way, we demonstrate that the scenario pictured in Fig. 5.6 actually occurs in the radiative transfer calculation.

5.6 Correlation maps in polar coordinates

In Fig. 5.23, we show three maps of auto- and cross- correlation functions $I - I$, $I - P$, and $I - |V|$ for polar coordinates (r, θ) on the images at 230GHz, defined by Eq. 5.6. The positive (negative) $j\Delta\theta$ corresponds to counterclockwise (clockwise) direction on the images. The maps have a period of 2π in the $j\Delta\theta$ direction, so that they have same values in the top ($j\Delta\theta = +\pi$) and bottom ($j\Delta\theta = -\pi$).

The auto correlation for the total intensity, $I - I$ has a peak at $(r, \theta) = (0, 0)$ by definition. In the radial, $i\Delta r$- direction, two cross-correlations $I - P$ and $I - |V|$ have little deviations from the center, reflecting the fact that most of the total, LP and CP intensities are distributed

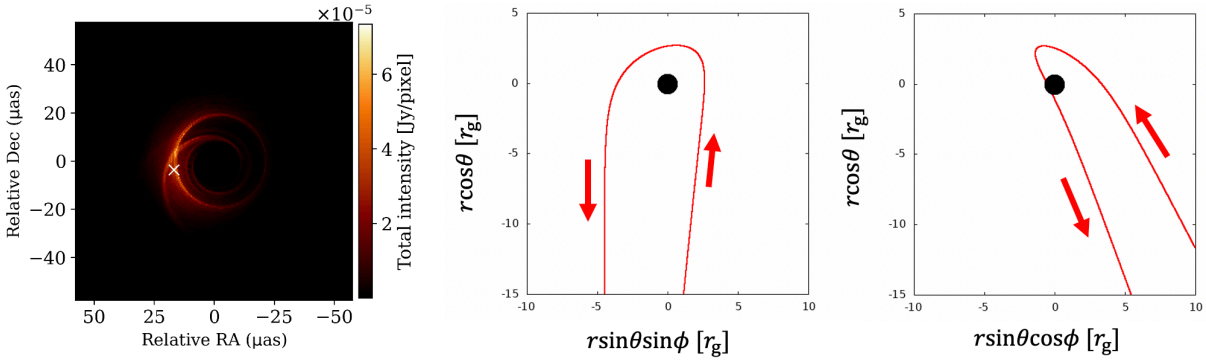

Fig. 5.21: Left: The total intensity image at 230 GHz of our fiducial model (same with the left panel of Fig. 5.1). We pick up a pixel around the "cross-section" between the photon ring and the tail-like jet feature, shown by a white "x". Center and right: the light path corresponding to the pixel, projected to the y-z and x-z plane in the simulation coordinates, respectively.

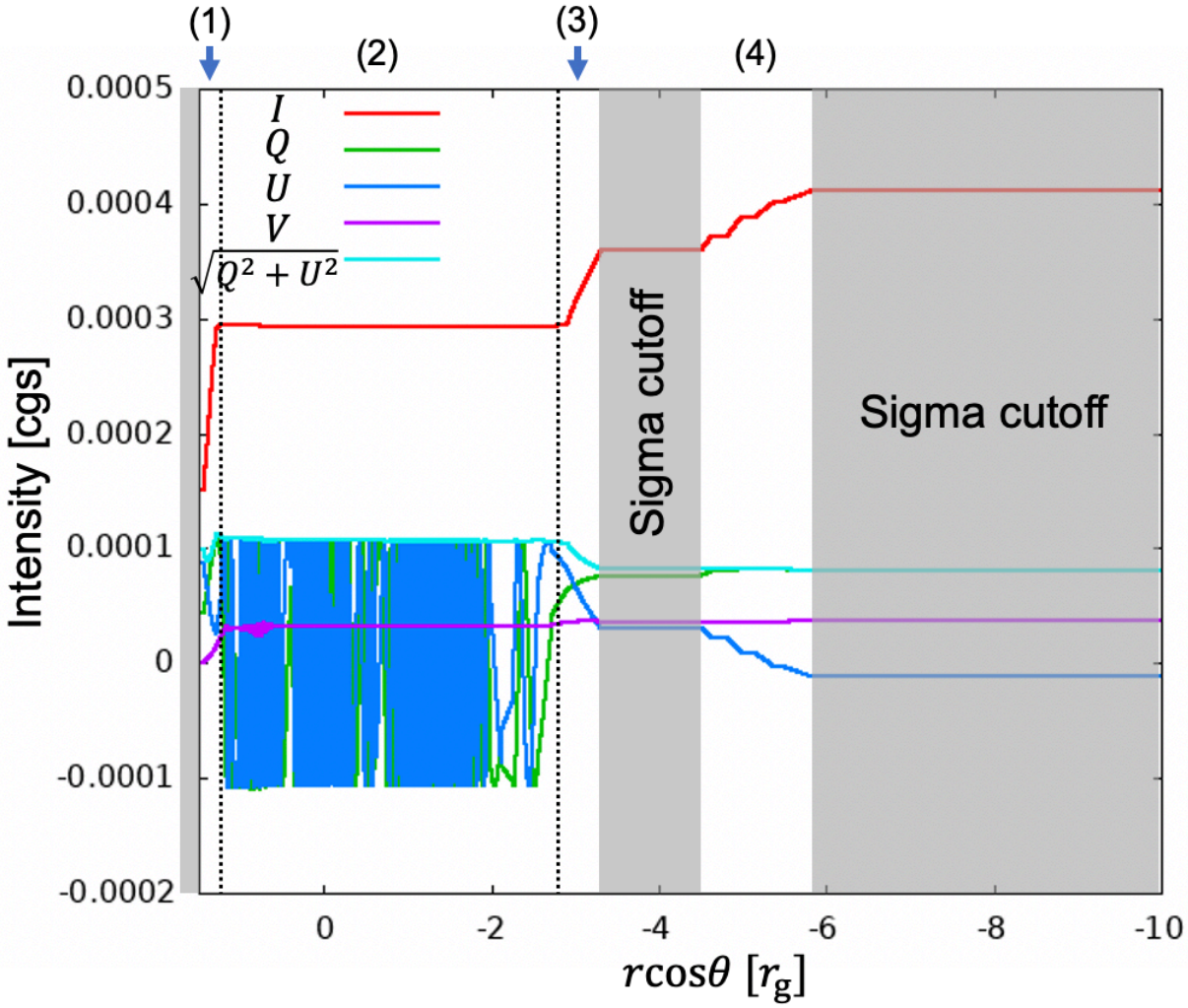

Fig. 5.22: The radiative transfer plots of Stokes parameters (I, Q, U, V) and $\sqrt{Q^2+U^2}$ along the z-coordinate of the light path in Fig. 5.21. The areas skipped by the sigma cutoff are marked with grey. The radiative process can be followed up by four steps (1) - (4), as described in section 5.5.

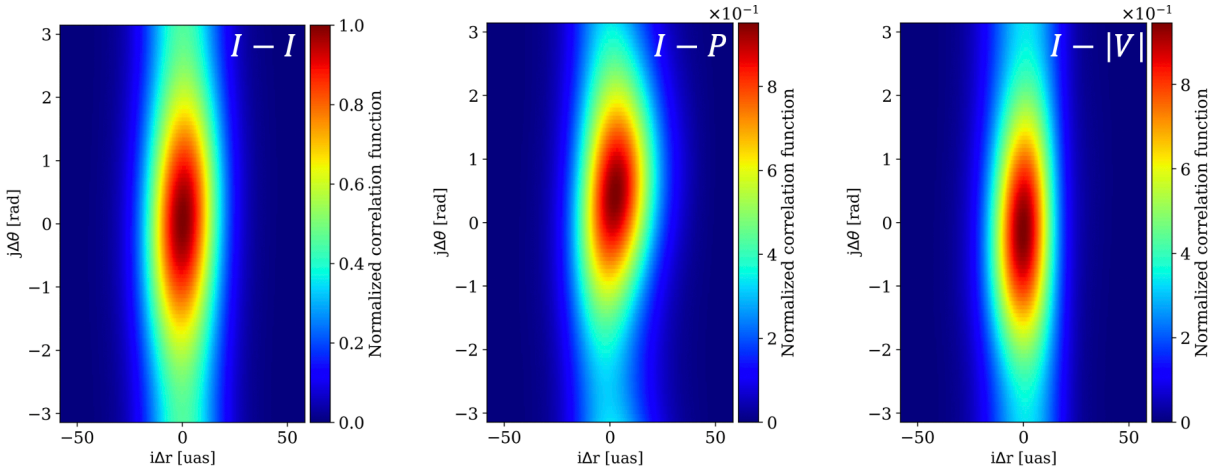

Fig. 5.23: Distribution maps of correlation functions in polar coordinates (r, θ), for the polarization images in Fig. 5.2. Right: auto-correlation of Stokes I. Center: cross-correlation between I and $P = \sqrt{Q^2 + U^2}$. Right: cross-correlation between I and $|V|$. Three maps are normalized so that auto-correlation of Stokes I yields 1 in the origin. We average the central and right maps in vertical (horizontal) direction and show them as $i\Delta r$- ($j\Delta\theta$-) profile in Fig. 5.5.

on the common ring. Meanwhile, $I - P$ ($I - |V|$) gives a peak at positive (negative) region in the azimuthal, $j\Delta\theta$- direction. Now the total intensity image is brighter in the left side of the asymmetric ring feature, so this results quantify the tendency that the LP (CP) intensities are distributed in the lower-left (upper-left) of the common ring.

5.7 Vertical peak shifts of $I - P$ and $I - |V|$ for the cases seeing from behind

In Fig. 5.24, We show the vertical peak shifts of the cross-correlation functions for different $R_{\rm high}$ parameters, as in Fig. 5.7, but for the azimuthal angle position of the camera $\phi_{\rm camera} = 180°$, which corresponds to the observer in the opposite side with respect to the jet (z-) axis.

5.8 Vertical and horizontal profiles of cross-correlation functions $I - P$ and $I - |V|$ for different model parameters

In the text, we showed only the vertical peak shifts of the correlation functions at the higher and lower frequencies except 230 and 86 GHz, and for various model parameters except a high accretion model with $\dot{M} = 6 \times 10^{-3} M_\odot/{\rm yr}$. Here, we show the vertical (y-) and horizontal (x-) profiles of the correlation functions, in Figs.5.25 to 5.30.

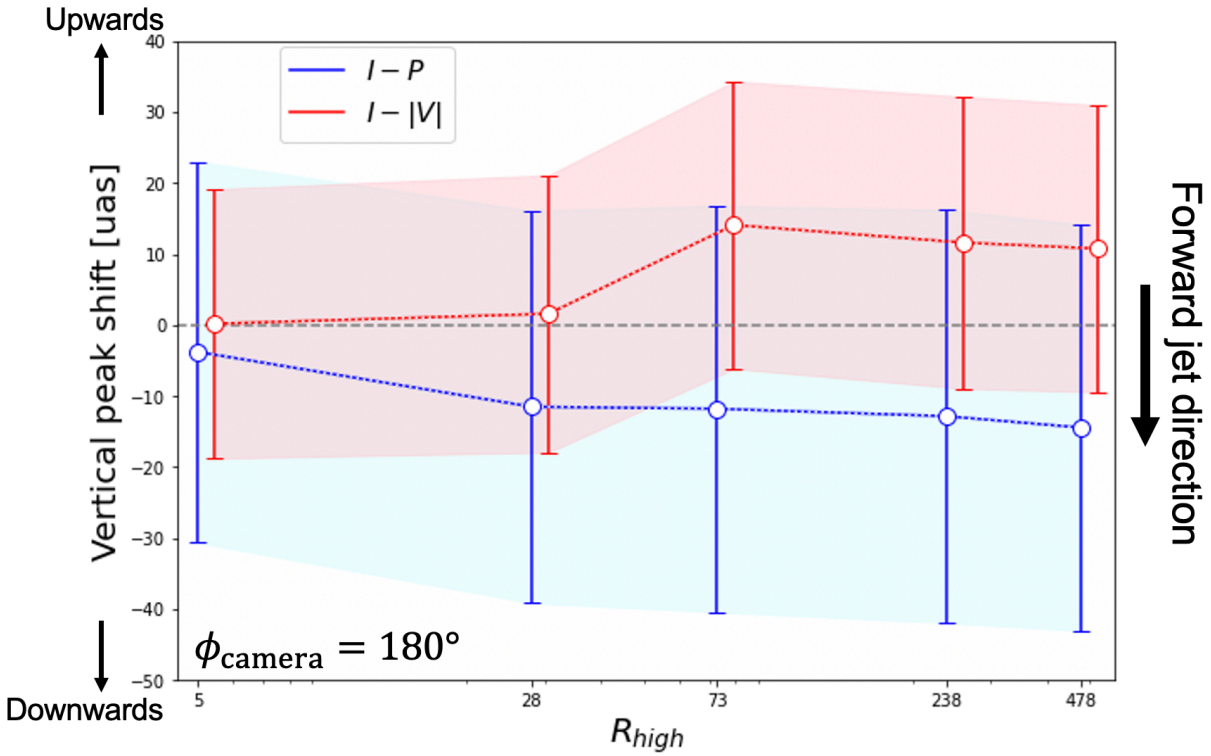

Fig. 5.24: Same as Fig. 5.7 but for the cases with $\phi_{\mathrm{camera}} = 180°$.

5.9 A scatter diagram with histogram of $I - P$ and $I - |V|$ vertical peaks for sixteen images

In Fig. 5.31, we show a scatter diagram with histogram of the peak shifts of $I-P$ and $I-|V|$ on the sixteen images introduced in subsection 5.3.7, where 13 out of 16 images show the LP-CP separation (in the yellow-marked region in the diagram). It also shows that 9 of 16 images give $I - P$ shifts larger than 10 μas, while 5 images yield $I - |V|$ peak shift larger than 5 μas.

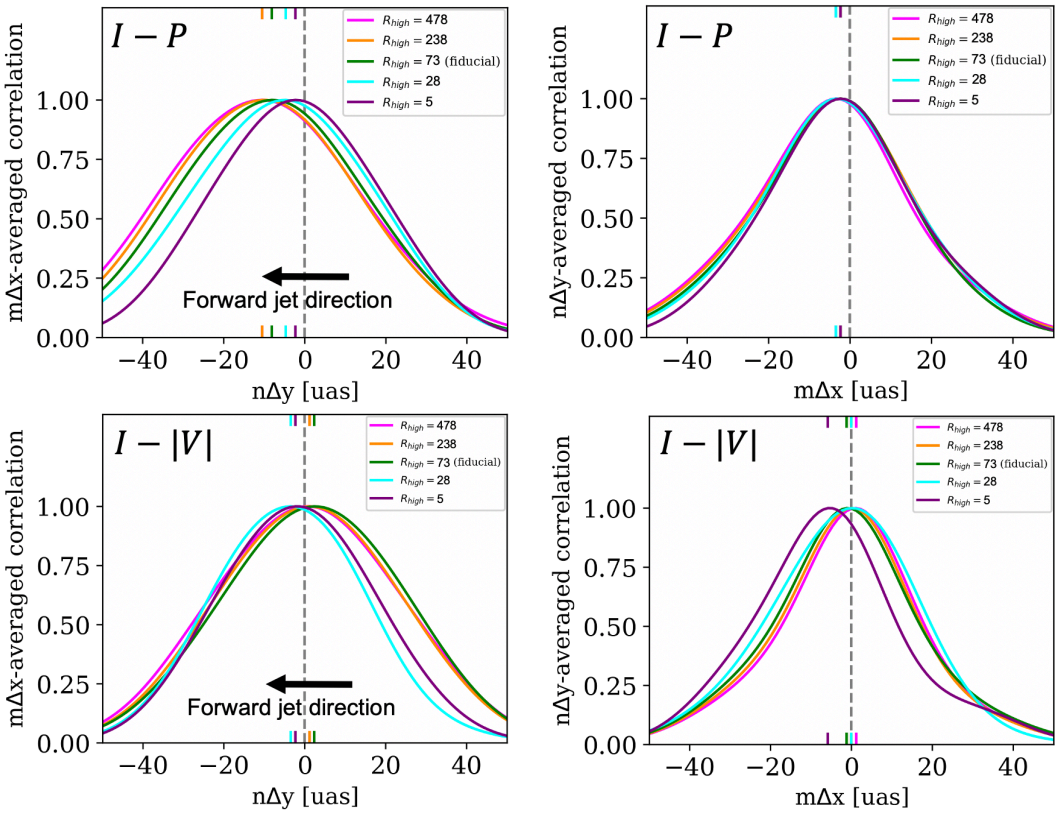

Fig. 5.25: $n\Delta y$- (left) and $m\Delta x$- (right) profiles of cross-correlations $I - P$ (top) and $I - |V|$ (bottom) for five parameters $R_{\rm high} = 5, 28, 73, 238$, and 476.

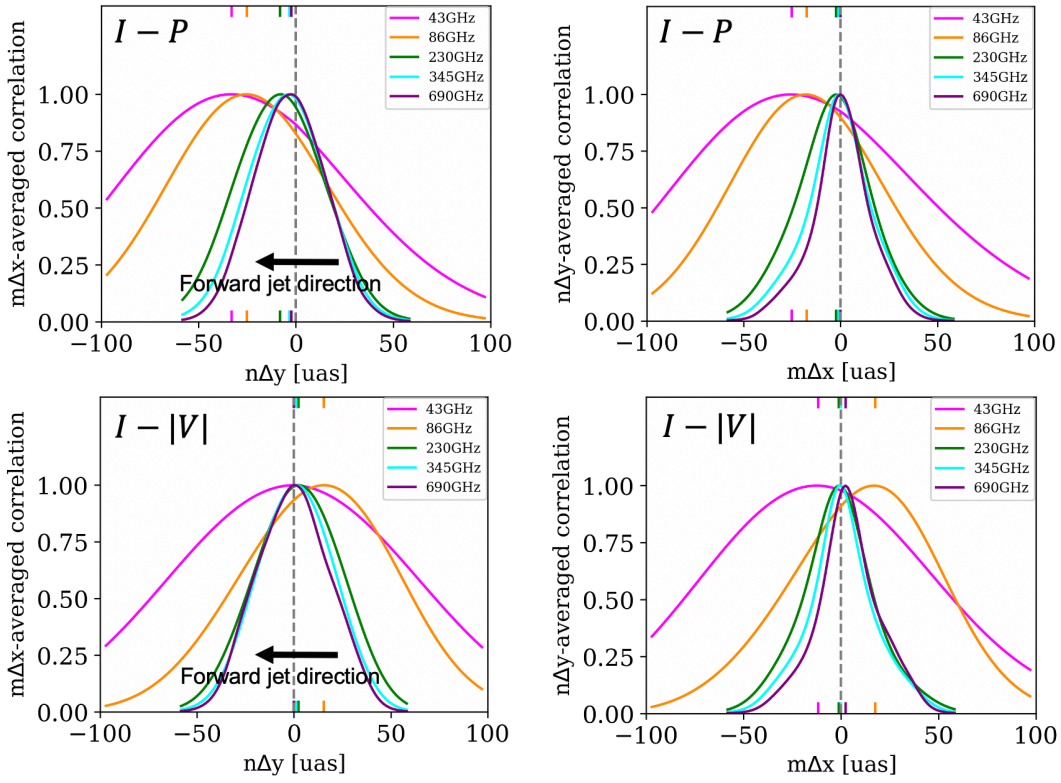

Fig. 5.26: Same as Fig. 5.25 but at five wavelengths of 43, 86, 230, 345, and 690 GHz.

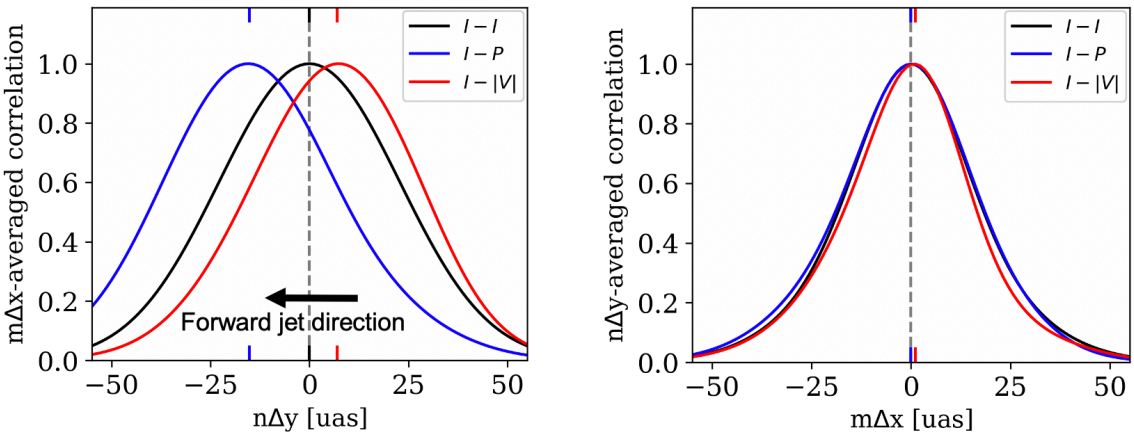

Fig. 5.27: Same as Fig. 5.4 but for a high inclination angle of $i = 150°$.

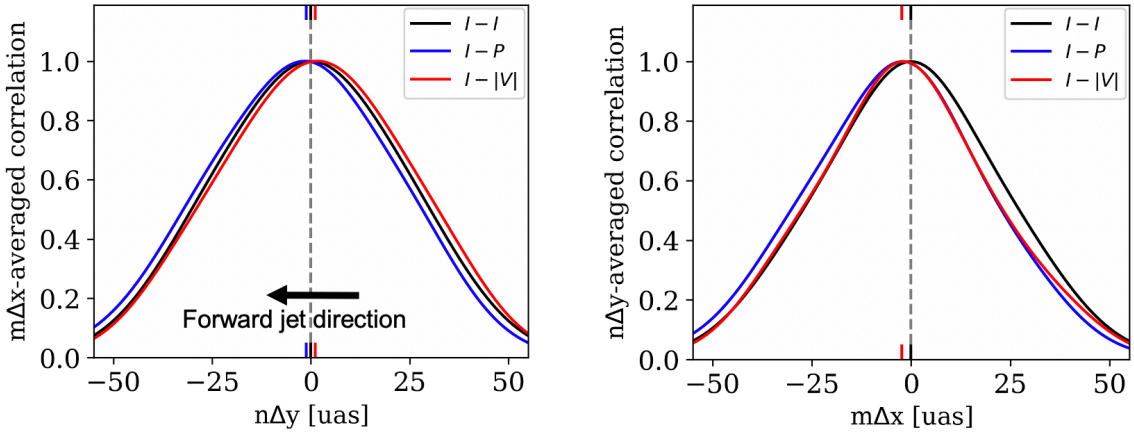

Fig. 5.28: Same as Fig. 5.4 but for a low inclination angle of $i = 170°$.

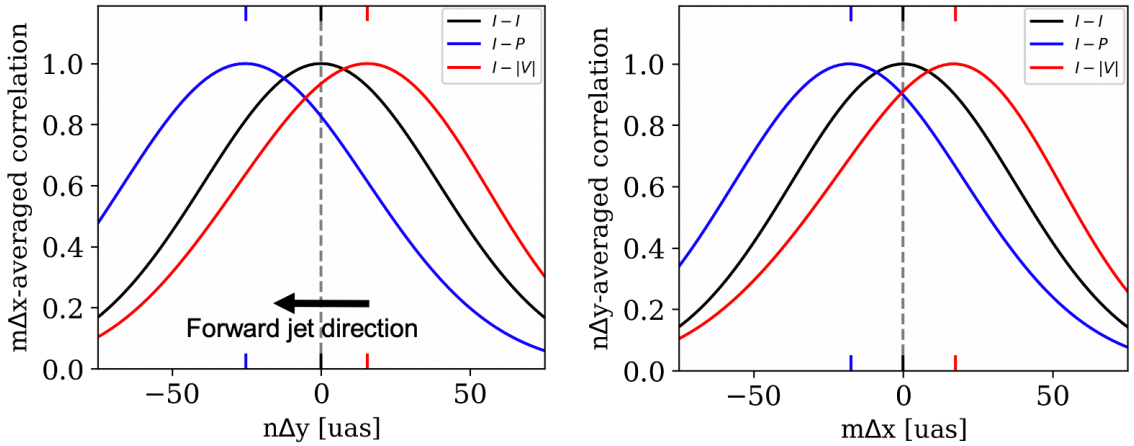

Fig. 5.29: Same as Fig. 5.4 but for the images for high accretion model in Fig. 5.15.

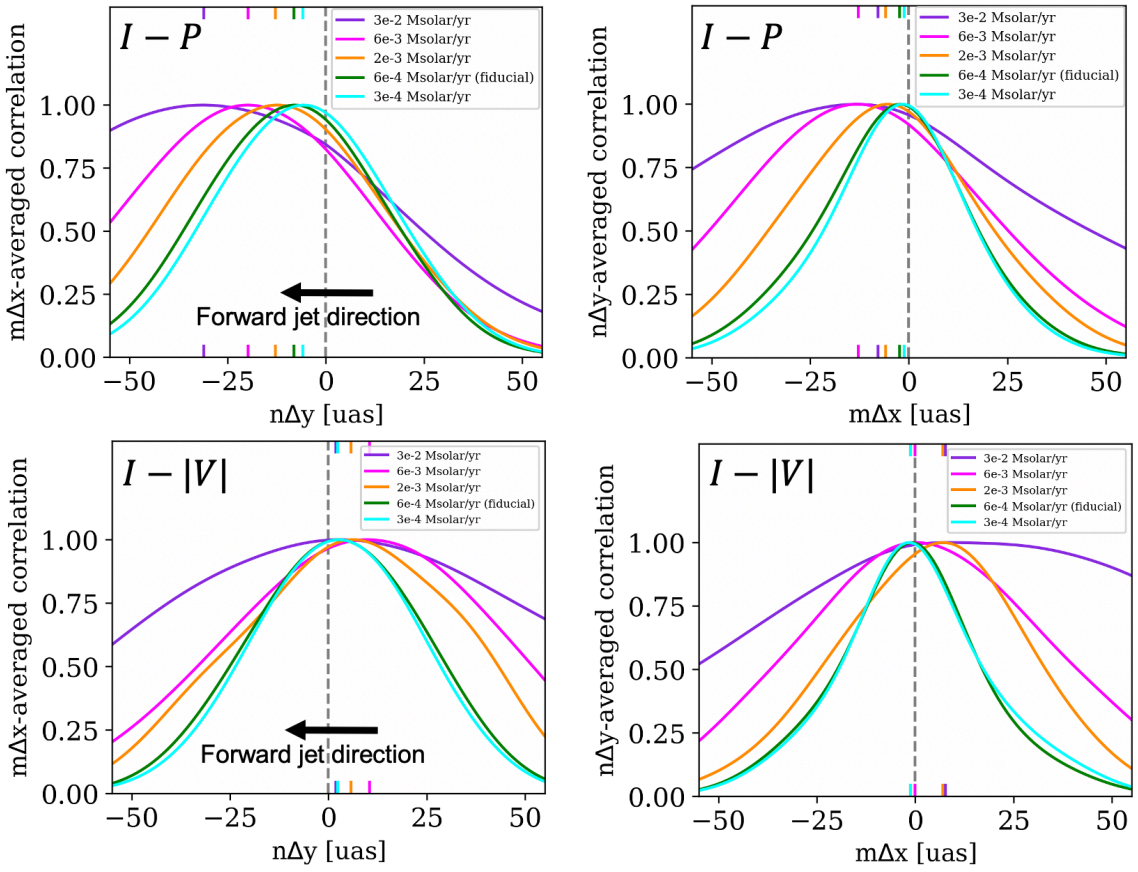

Fig. 5.30: $n\Delta y$- (left) and $m\Delta x$- (right) profiles of cross-correlations $I - P$ (top) and $I - |V|$ (bottom) for five mass accretion rates onto the black holes of $\dot{M} = (3, 6, 20, 60, 300) \times 10^{-4} M_{\odot}/\mathrm{yr}$.

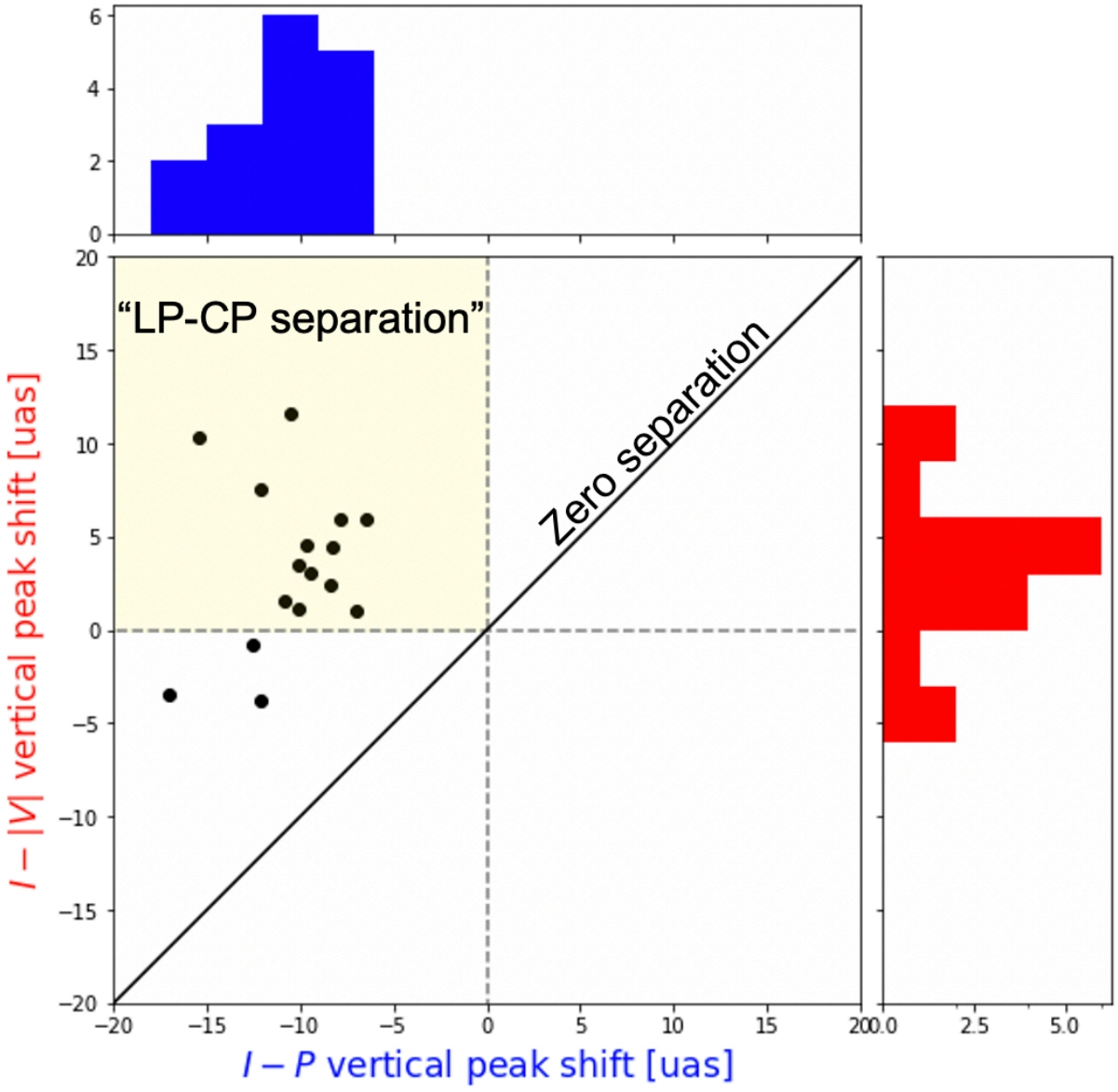

Fig. 5.31: A scatter diagram with histogram of vertical peak shifts of cross-correlations $I-P$ and $I-|V|$ on 16 images, for four snapshots (at $t = 9000t_{\rm g}, 9500t_{\rm g}, 10000t_{\rm g}$, and $11000t_{\rm g}$) and for four observer's azimuthal angles ($\phi_{\rm camera} = 0°, 90°, 180°$, and $270°$). Thirteen out of sixteen images show the LP-CP separation (i.e., positive $I-P$ peak and negative $I-|V|$ peak; yellow-marked region in the diagram), while the remaining three images do not present negative $I-|V|$ peak shifts. Furthermore, nine images give $I-P$ peak shifts larger than 10 μas, while five images yield $I-|V|$ peak shift larger than 5 μas.

5.10 Conclusion

While the LP and CP emissions from near the black hole and the base region of the jet can be a good tool to survey the magnetic field configuration possibly driving the LLAGN jets such as M87, both of observational and theoretical studies have suggested that they can be affected by the Faraday effects in magnetized plasma. In particular to M87 jet with a nearly face-on viewing angle ($i \approx 160°$) assumed, the LP vectors, especially from the background (receding) jet, can be scrambled by the Faraday rotation in the midplane disk, as pointed out by Mościbrodzka et al. (2017); Ricarte et al. (2020). In addition, the CP components can be amplified by the Faraday conversion in energetic region near the black hole through the medium of the Faraday rotation and twist of the fields, imprinting the direction and configuration of the magnetic fields (Tsunetoe et al. 2020, 2021; Mościbrodzka et al. 2021; Ricarte et al. 2021).

To examine and quantify the relationship between these polarization components and the plasma properties near the black hole, we calculated theoretical polarization images based on a moderately-magnetized (semi-MAD) GRMHD model (with a magnetic flux in the intermediate range of $5 \lesssim \phi \lesssim 50$ which was not explicitly examined in Event Horizon Telescope Collaboration et al. (2021b)), and analyzed the correlation relations among the total intensity, LP, and CP components on the images. By surveying the peak shifts of correlation functions at multi-wavelengths and for different model parameters, we established a unified description by three schematic pictures as in Figs. 5.6 and 5.12:

- **Faraday thin and SSA thin case**: at higher frequencies (say, 345 and 690 GHz for our fiducial model) and for lower mass accretion onto the black hole, the polarized synchrotron emission reaches to us without suffering the Faraday effects because both of the Faraday rotation and conversion are weaker. As a result, we observe the intrinsic polarization components consisting of dominant LP and weak CP with a distribution similar to the total intensity image.

- **Faraday thick and SSA thin case**: the LP vectors from the background jet and the inner disk are strongly scrambled by the Faraday rotation in the disk and are depolarized after convolved by observational beam, while the CP components are amplified by the Faraday conversion near the black hole. As a result, the LP components from the downstream of the foreground (approaching) jet dominate over those from the upstream, the counter-side jet or the photon ring, whereas the CP components are distributed around the photon ring and the counter-side jet. Thus, the downwards LPs and upwards CPs, relatively to the total intensity distribution, are observed on the images (e.g., at 230 and 86 GHz for our fiducial model). These tendencies become more enhanced at lower frequency or for higher mass accretion rate, as long as the SSA is not significant.

- **Faraday thick and SSA thick case**: at even lower frequencies (say 43 GHz for our fiducial model) or for even higher mass accretion rate, the SSA becomes significant in

addition to the Faraday effects. In this case, the polarized emission comes from the surface of the photosphere. Therefore, the intrinsic CPs are observed in similar distribution to the total intensities, while the LPs are depolarized in the outer disk and are dominated by those from the downstream.

We found that high electron-temperature disk (low $R_{\rm high}$) models also show a downwards LP distribution, but do not necessarily give an upwards CP distribution. This is because the emission from the midplane disk, where the plasma structure is relatively turbulent, is dominant in these models, and thus the CP image is affected by the disk structure in small scale rather than the up- and down- stream structure of the jet. Thus we can propose the LP-CP separation feature as a possible test of the proton-electron coupling in the jet-disk structure. We also confirmed that larger viewing angle (i.e. more edge-on observer) gives larger separation among the total, LP and CP intensities because of larger projected distance on the screen.

Comparing these results with existing observations of M87 by the EHT and other VLBIs, we can see a persistent tendency at multi-frequencies of the LP components distributed in the downstream of the jet. We can further expect that future observations including both of the linear and circular polarimetries with high angular resolution at a large range of frequencies will give a strong constraint on the plasma properties such as the optical thickness for the Faraday effects and the SSA, the density/temperature distribution and magnetic field structure near the black hole and the jet base region.

In future works, we will examine the description obtained in this work in the context of the time-variable fluid model. As a precursor, we calculated the images of different snapshots with different azimuthal angles of the camera $\phi_{\rm camera} = 0 - 360^\circ$ (rotating the camera about the z-axis), and obtained the features variable but qualitatively consistent with the description for our fiducial one (e.g., Figs. 5.24 or 5.31 in section 5.9, see also a discussion in subsection 5.3.7). The contribution of non-thermal electrons to the synchrotron emission should be also discussed in future works, which is thought to be important especially for the images at lower frequencies. In addition, we should also verify the validity of the determination of the electron temperature, here by the $R - \beta$ prescription, through comparison with fluid calculations incorporating the radiative cooling.

This page intentionally left blank.

Chapter 6

Survey of Diverse Polarimetric Features: Towards a Unified View of AGN Jets

Part of text in this chapter was published in Tsunetoe et al. (2022b) (Tsunetoe, Y., Mineshige, S., Ohsuga, K., Kawashima, T., Akiyama, K., & Takahashi, H. R., *Galaxies, 10, 103 (2022)*), titled as "*Diverse Polarimetric Features of AGN Jets from Various Viewing Angles: Towards a Unified View*".

In the previous chapter, we confirmed on the basis of our moderately magnetized models with a hot jet and cold disk, a scenario where the polarized emissions produced in the jet experience the Faraday rotation and conversion effects in the disk. In this description of the emitting jet and Faraday-thick disk, we found that the LP (or CP) intensities are mainly distributed in the downstream (upstream) side of the approaching jet for nearly face-on observers. In this work, we survey polarimetric features for different inclination angles between the black hole's spin-axis and an observer, to expand and develop the discussions. Here, we bear in mind observations of a diverse range of AGN jets at 230 GHz by the EHT and other very long baseline interferometers (VLBIs). Furthermore, we think of applying them to the interpretation of the disk precession around SMBHs (e.g., Ressler et al. 2020; Liska et al. 2021).

6.1 Models

We follow the model parameters adopted in the fiducial model in the last chapter. Here, we use a three-dimensional GRMHD model simulated with `UWABAMI` code (Takahashi et al. 2016; Kawashima et al. 2021a), which is categorized into the intermediary area between a magnetically arrested disk (MAD; Narayan et al. 2003) and standard and normal evolution (SANE; Narayan et al. 2012), and is thus called semi-MAD. The $R-\beta$ model is adopted for the determination of electron temperature, where the proton–electron temperature ratio ($T_{\rm i}/T_{\rm e}$) is given at each point in the fluid model by a function of plasma-β ($\equiv p_{\rm gas}/p_{\rm mag}$; gas–magnetic-pressure

Parameter	Value
BH mass $M_\bullet$	$6.5 \times 10^9 M_\odot$
BH spin parameter a	0.9375
Magnetic flux on the horizon ϕ	≈18 (semi-MAD)
T_e-parameter R_{low}	1
T_e-parameter R_{high}	73
Mass accretion rate onto BH $\dot{M}$	$6 \times 10^{-4}\ M_\odot \mathrm{yr}^{-1}$ (at the moment of snapshot)
Distance to observer D	16.7 Mpc
Observational frequency ν	230 GHz

Table 6.1: Parameters in our GRMHD and GRRT model, following a fiducial model in the last chapter except the observer's inclination angle. Here, $M_\odot$ is the solar mass. $\phi \equiv \Phi_{\rm BH}/\sqrt{\dot{M} r_{\rm g} c^2}$ is a strength of dimensionless magnetic flux on the event horizon of SMBH, where $r_{\rm g} \equiv GM_\bullet/c^2$ and $\Phi_{\rm BH} = (1/2)\int\int |B^r| {\rm d}A_{\theta\phi}$. G and c are the gravitational constant and speed of light, respectively.

ratio) and two parameters $R_{\rm low}$ and $R_{\rm high}$ (Mościbrodzka et al. 2016) as follows:

$$\frac{T_{\rm i}}{T_{\rm e}} = R_{\rm low}\frac{1}{1+\beta^2} + R_{\rm high}\frac{\beta^2}{1+\beta^2}. \tag{6.1}$$

The model parameters are summarized in Table 6.1. GRRT calculation is performed by a code implemented in chapters 3, 4, and 5 with a sigma cutoff of $\sigma_{\rm cutoff} = 1$, and fast-light approximation is performed for a snapshot fluid model. Here, we use a snapshot at $t = 9000 t_{\rm g}$ (here, $t_{\rm g} \equiv r_{\rm g}/c$) in the quasi-steady state as a main model, while three other snapshots are surveyed and discussed in Section 6.3.2. The mass accretion rate onto the black hole is fixed so that we reproduce the 230GHz observed flux of M87 in Event Horizon Telescope Collaboration et al. (2019a), ≈0.5 Jy, for the case with $i = 160°$. Under these assumptions, we calculate the total, LP, and CP images, varying the observer's inclination (viewing) angle $i = 0° - 180°$ by $10°$ as pictured in Figure 6.1.

6.2 Results

6.2.1 Polarization Images

In Figure 6.2, we show resultant polarization images at 230 GHz for three inclination angles of $i = 20°, 50°$, and $90°$ as examples of the nearly face-on, intermediate, and edge-on cases, respectively. The observers for the first and third cases are pictured by arrows and eyeballs in Figure 6.1 (A movie of all of the images for $i = 0° - 180°$ can be found on `https://youtu.be/065qAx6Tff0`; accessed on October 19, 2022). The $i = 20°$ case in the top panels shows polarimetric features following the fiducial image in the last chapter for $i = 160°$; that is, the total intensity showing a photon ring and dim tail-like jet component overlapped

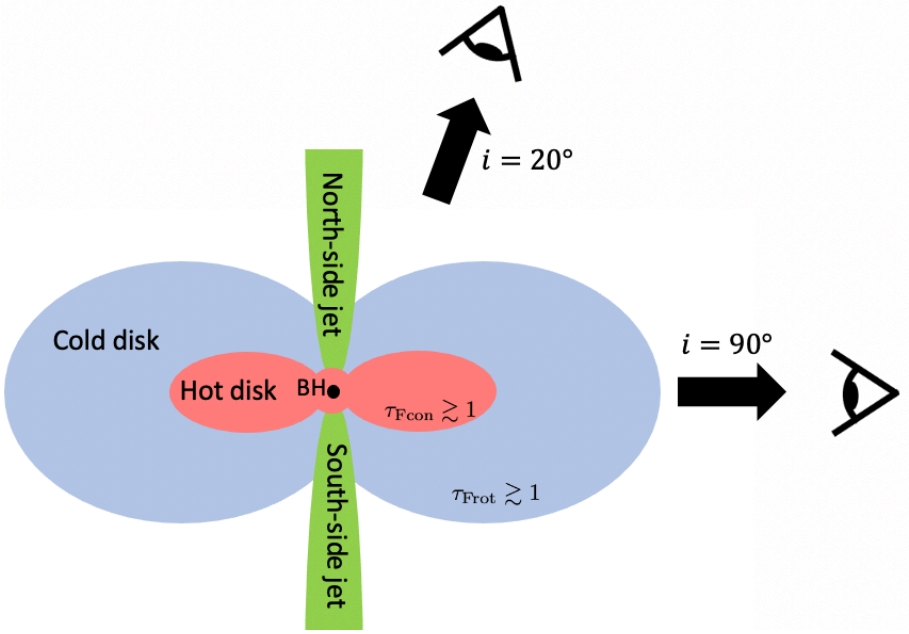

Fig. 6.1: A schematic picture of the jet–disk structure (adopted from the last chapter). In our model, synchrotron emission is predominantly produced in the funnel jet (green). After the emission, the polarized lights experience Faraday conversion in the inner hot disk (red) and Faraday rotation in the outer cold disk (blue) on the way to the observer (eyeball), respectively. See the last chapter for poloidal-slice maps of typical values of the emissivity and Faraday coefficients.

on the ring, the LP map with partly scrambled vectors, and the CP image giving a bright, negative ring.

Here, we see a reversal of the CP ring's sign compared to that for $i = 160°$ in the last chapter (which shows a positive ring), including the fine "second sub-ring" (see Ricarte et al. 2021) and the tail-like jet on the ring with positive signs (which were negative for $i = 160°$). These are attributed to the helicity of the magnetic fields, which is flipped between the northern and southern part about the equatorial plane in our model. This is because of the frame-dragging effect of a rotating BH (for detailed discussion on CP's sign, see also chapter 4 or Tsunetoe et al. 2021; and Ricarte et al. 2021). A similar sign-reversal of CP rings for two observers in the north and south side of the BH was also reported by Mościbrodzka et al. (2021).

The edge-on images in the bottom panels of Figure 6.2 exhibit distinct morphological features compared to the nearly face-on ones. The total intensity image shows a crescent-shaped BH shadow broken at the equator, which is caused by a synchrotron self-absorption (SSA) effect in the optically thick disk. This broken crescent is qualitatively different from a three-forked shadow in chapter 4, where we modeled Sgr A* with a hot disk, implying the effect of the disk temperature on the shape of the BH shadow.

The edge-on LP maps give a scrambled vector pattern (which will also be shown by a total LP fraction in the next subsection), whereas the CP image follows a total image with flipping signs in four parts of the image divided by the left-leaning (relativistically beamed) vertical line

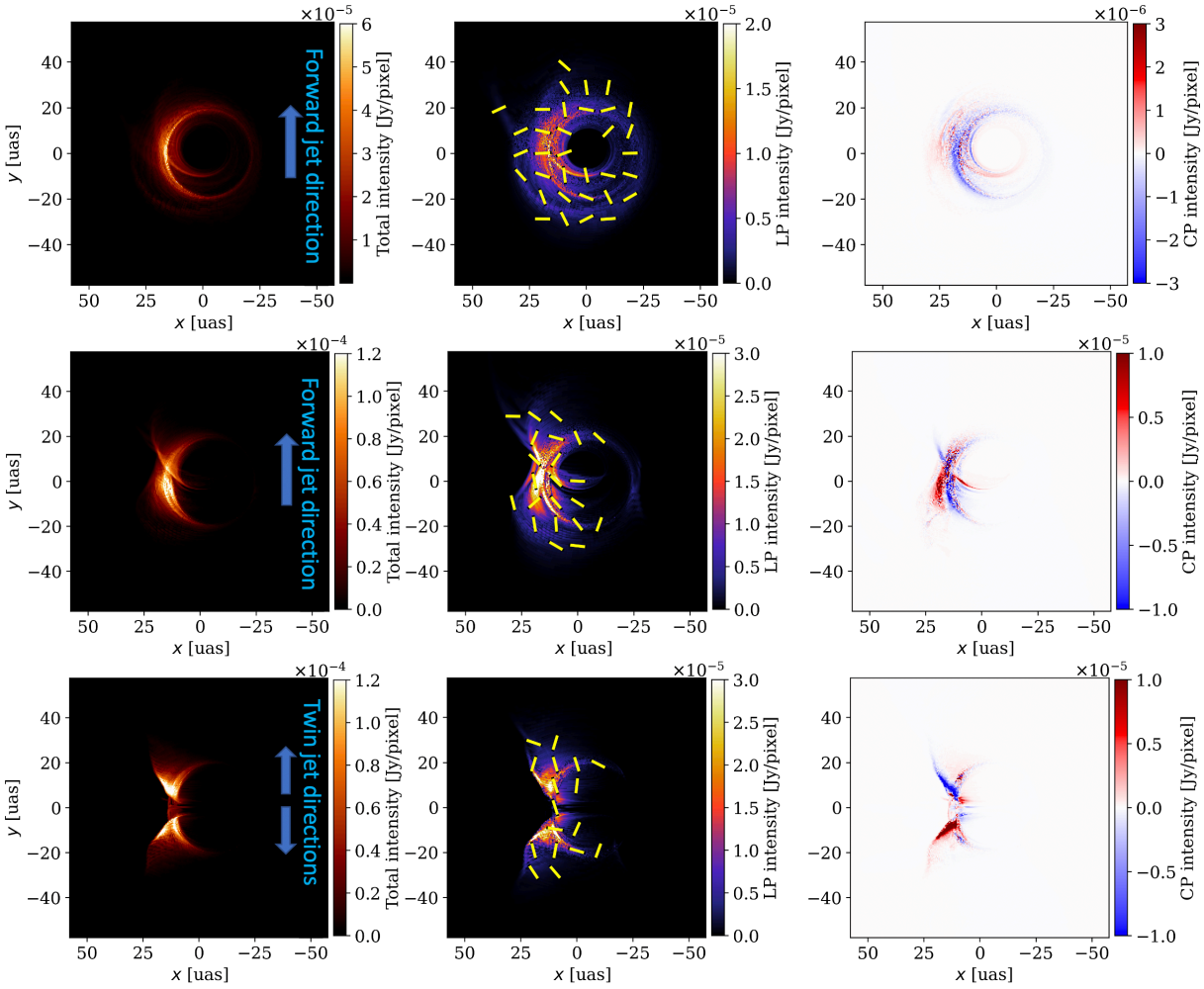

Fig. 6.2: A calculated polarization images at 230 GHz for three viewing angles of $i = 20°$ (nearly face-on), $50°$ (intermediate), and $90°$ (edge-on), top to bottom. (**Left**) Total intensity (Stokes I) image. Each image consists of 600×600 pixels. The forward jet extends upward on the image. (**Center**) LP map. The LP intensity is shown by the color contour, with LP vectors in electric vector position angle (EVPA) overwritten. (**Right**) CP image. The CP intensity (Stokes V) is shown by the color contour with sign. A movie of all the images for $i = 0° - 180°$ can be found on https://youtu.be/065qAx6Tff0 (accessed on October 19, 2022).

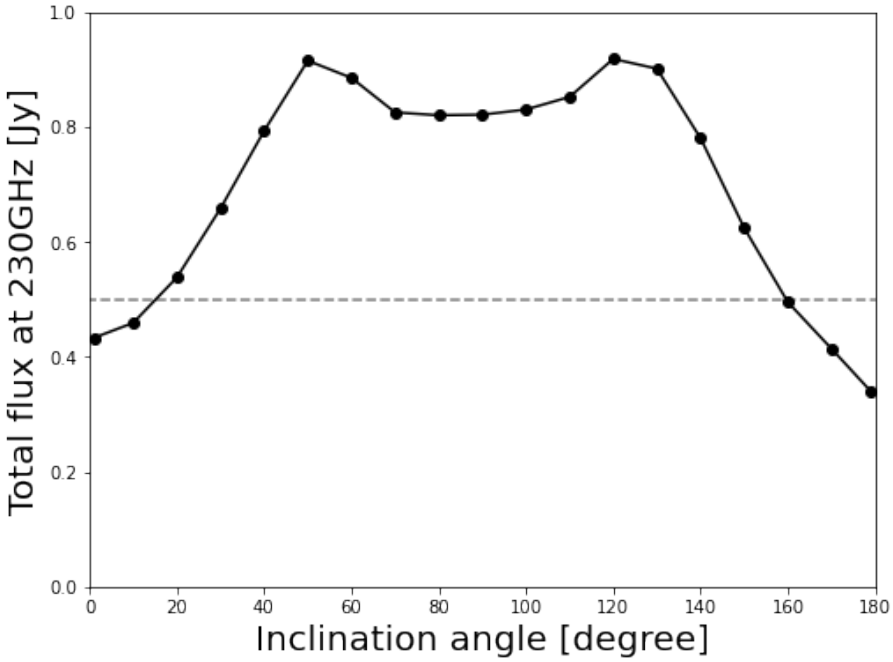

Fig. 6.3: Diagram of the total (image-integrated) fluxes at 230 GHz for different inclination angles, assuming the distance to M87. Gray dash line corresponds to 0.5 Jy.

and the equatorial line. This CP sign-reversal in the four parts is due to the intrinsic emission and the Faraday-rotation-induced conversion with the reversal of the magnetic field helicity about the equatorial plane (see chapter 4 or Tsunetoe et al. 2021, and also Ricarte et al. 2021).

Further, we show the images for $i = 50°$ in middle panels of Figure 6.2 as an example of intermediate inclination cases. The images show intermediate features between the face-on case and edge-on case, giving a crescent-shaped shadow and tail-like emission from the approaching jet. In the CP image, we can also see both a blue, ring-like feature and a sign-flipping feature on the jet-edge.

6.2.2 Unresolved Polarimetric Features

For a more comprehensive survey of inclination angles, we next show a diagrams of the total (image-integrated) intensity flux, $I_{\rm total} = \sum_{\rm pixels} I$, in Figure 6.3. (Note that, here, we assume a distance to M87 of $D = 16.7$ Mpc for all cases.) The profile is steep for nearly face-on cases and flat for nearly edge-on cases, and has a symmetry of the total flux about the equatorial plane (the edge-on case) with two peaks at $i \approx 50°$ and $\approx 130°$.

Next, a diagram of the total LP and CP fractions, $\sqrt{Q^2_{\rm total} + U^2_{\rm total}}/I_{\rm total}$ and $V_{\rm total}/I_{\rm total}$ (here, (I, Q, U, V) are the Stokes parameters), is shown in Figure 6.4. Here, we find a roughly symmetric feature in the LP fractional profile with higher fractions in more face-on like cases. In contrast, the CP fractional profile shows an antisymmetric profile about the $i \approx 90°$ case with three peaks and bottoms.

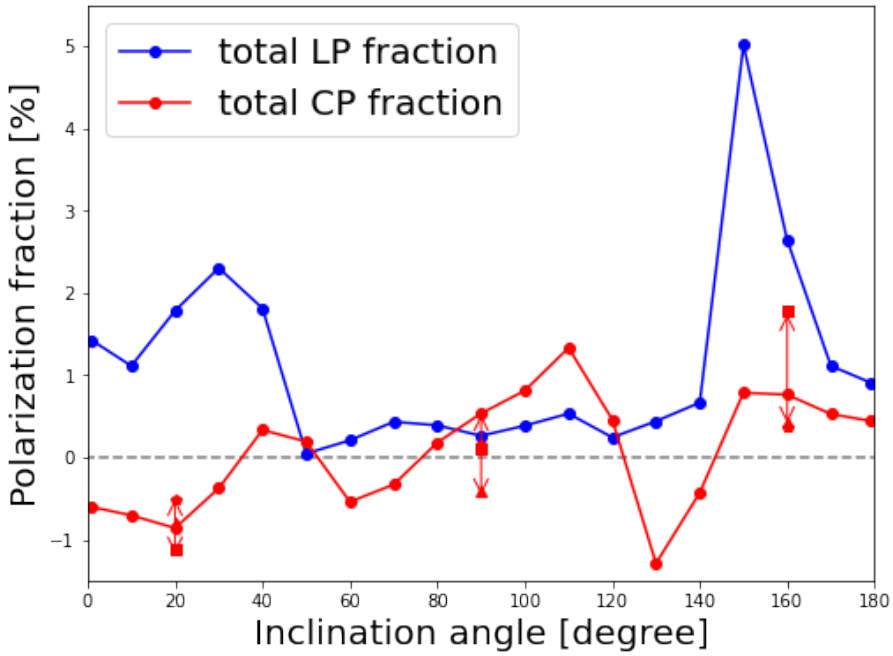

Fig. 6.4: Diagram of the total LP and CP fractions at 230 GHz for different inclination angles. For $i = 20°, 90°$, and $160°$ cases, we additionally plotted the values for other three snapshots in the GRMHD model. $t = 9500t_g$ (triangle), $10{,}000t_g$ (square), and $11{,}000t_g$ (pentagon), whereas $t = 9000t_g$ (circle) for the fiducial model. The arrows indicate the time variations of the CP fractions.

6.3 Discussion

In this section, we will pick up representative polarimetric features that appear in the images and total (unresolved) values obtained in the last section, and discuss their relationship with the magnetic field configuration and plasma structure around the SMBH.

6.3.1 Total Flux Suppression for the Edge-On Like Cases

We see a two-hump feature at $i \approx 50°$ and $\approx 130°$ in the total flux profiles in Figure 6.3. This can be attributed to the opening angle of the funnel jet region around the black hole, where the emissions are predominantly produced (see also figure 5.20 in the last chapter). In the case where the observer's inclination is smaller than the opening angle of the jet, as $i \leq 50°$, $130° \leq i$, the emissions go through the sparse funnel region. Otherwise, as $60° \leq i \leq 120°$, the emissions go through the dense disk and experience a significant SSA effect in the disk.

In Figure 6.5, we show an inclination diagram of a typical (image-integrated and intensity-weighted) optical depths for Faraday rotation/conversion and SSA (see the last chapter for a definition and introduction of these optical depths). In fact, typical optical depths for the SSA (orange profile) approach $\sim$1 at $i = 50°$ and $130°$, where the plasma transit between optically thin and thick states. As a result, the intensities are saturated in the foregrounded colder plasma and suppressed in the edge-on-like cases.

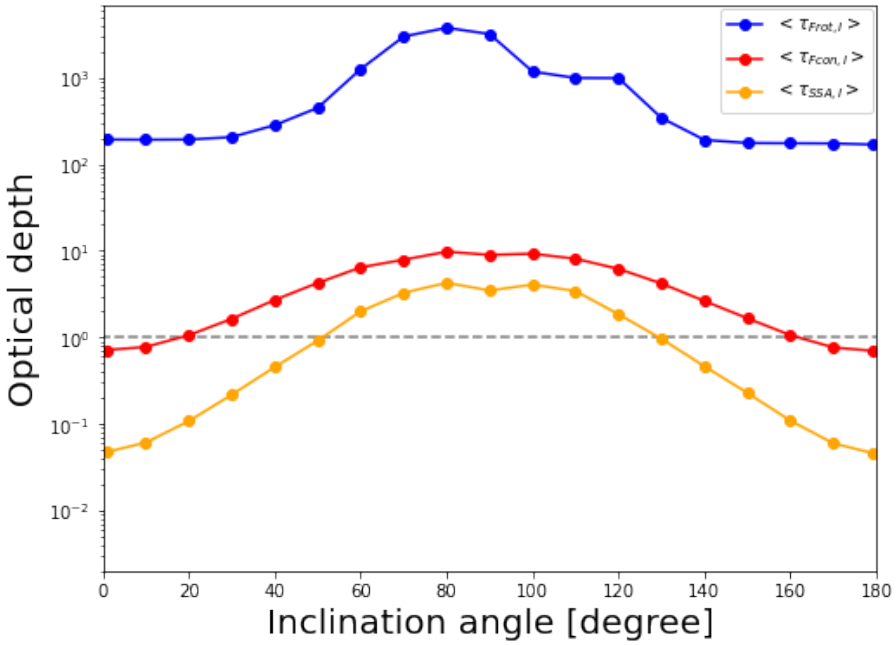

Fig. 6.5: Diagram of the image-integrated intensity-weighted optical depths for Faraday rotation and conversion, and SSA at 230 GHz for different inclination angles. Gray dashed line corresponds to $\tau = 1$.

6.3.2 Reversal of Unresolved CP Signs

In Figure 6.4, we find a reversal of CP signs for face-on like cases in the north and south side of the SMBH; that is, $i \approx 0° - 30°$ cases persistently give negative CP fractions whereas $i \approx 150° - 180°$ show positive ones. These persistent CP signs result from integrating the CP images that consist of a monochromatic photon ring (e.g., the left panel in Figure 6.2), which are unique to the face-on-like cases and are due to the helicity of magnetic fields.

We additionally plot points of CP fractions for the other three snapshots (at $t = 9500t_{\rm g}$, $10{,}000t_{\rm g}$, and $11{,}000t_{\rm g}$) for $i = 20°, 90°$, and $160°$ in Figure 6.4. They show persistent signs of time-variable CP fractions for two face-on-like cases, while their absolute values can vary by a factor. Meanwhile, the CP fractions for the edge-on case change their sign for time-variability and are relatively small in their absolute values. This is because CP intensities with both signs comparably contribute to the unresolved CP flux (see the bottom-right panel in Figure 6.1). Due to the cancellation of its sign, the CP fraction is small and the time-variable emission can easily change the sign of the total CP flux. These results suggest that we can survey the magnetic field configuration around the SMBH through the circular polarimetry, even for unresolved sources.

From stimulated CP observations of AGNs, the following facts have been established; if some AGNs show significant positive (or negative) CP fluxes, they continue to show positive (negative) CP fluxes over timescale of decades. The same is true for those AGNs that do not show significant CPs (Wardle & Homan 2001). For example, Sgr A* are known to continue to show negative CP fluxes at centimeter to submillimeter wavelengths (Bower et al. 1999, 2018).

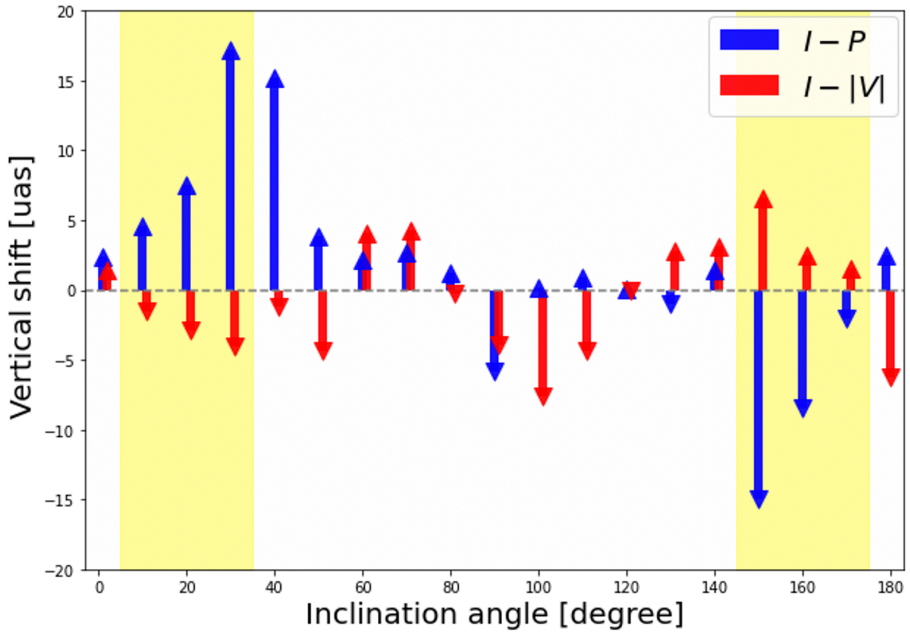

Fig. 6.6: Diagram of separations in y-direction in Figure 6.2 (the direction of projected SMBH spin axis) between total and LP (or CP) intensities at 230 GHz for different inclination angles. The LP (or CP) intensities tend to be distributed downstream (upstream) of the jet for Faraday thick cases. Arrows point to the distances of separations in the vertical direction of the images between total and LP (or CP) intensity distribution in blue (or red) color. The separations are calculated from cross-correlation function between two kinds of intensities on the images. See chapter 5 for introduction and definition of the correlation analyses.

In contrast, quasar 3C 279 always shows positive CPs as a whole (Homan & Lister 2006; Homan et al. 2009).

We can interpret these observational results in relation to our calculated values for the face-on-like cases, which are consistent with the low inclination angle interpretation favored for these two objects (Jorstad et al. 2004; GRAVITY Collaboration et al. 2018b; Event Horizon Telescope Collaboration et al. 2022b). However, we should note that the "core" emission in large beam-sized observations of low-inclination objects can degenerate the distant, downstream jet/outflow components, which would be resolved as "knots" at a higher resolution, with the emission from around the central SMBH.

6.3.3 Symmetry of the LP-CP Separation along the Jet

Here, we survey the separation features among the total, LP, and CP intensity distributions on the images. In the last chapter, we demonstrated that the LP components (or CP components) are distributed in the downstream (or upstream/counter-side) of the approaching jet on the images for $i = 160°$ due to Faraday conversion in the inner hot disk and rotation in the outer cold disk as pictured in Figure 6.1.

We apply these analyses to the cases with different inclination angles. The separations

between total and LP (or CP) intensities are shown in Figure 6.6, in which, the peak separations of the cross-correlation function between two kinds of intensities $I - P$ and $I - |V|$ are plotted (see the last chapter for detail). Here, we convolve the images with a circular Gaussian beam of 17 μas, bearing present and near-future EHT observations in mind.

We can clearly see the LP-CP separations along the jet in the face-on-like cases both from the north ($i = 10° - 30°$) and south side ($i = 150° - 170°$), which are yellow-marked, introduced at the beginning of this section. We showed in the last chapter that the larger the inclination angle, the large the LP-CP separations become due to the longer projected distance on the screen, by using the latter three cases. Here, we also confirm this tendency in the northern face-on-like cases, where the directions of separation are reversed for the north-side cases because the approaching (north-side) jet extends upward on the images.

These results demonstrate that the description of the synchrotron-emitting jet and Faraday-thick disk, as pictured in the last chapter and Figure 6.1, can be applied to the face-on cases both in north and south sides. In fact, it is shown in Figure 6.5 that typical optical depths for Faraday rotation (blue) and conversion (red) have a symmetric structure for the face-on-like observers in the north and south sides.

6.3.4 Oscillation of CP Signs

Next, we examine an oscillation feature of CP signs in edge-on-like cases. In Figure 6.4, we see a hint of flipping CP signs that oscillate for two cycles in a range of $i \approx 40° - 140°$. This can be interpreted with a combination of polarimetric features introduced so far. In the following descriptions, we distinguish two cases, observed from the north side and from the south side. Figure 6.2 shows the former cases (i.e., $i \leq 90°$).

First, the CP images in edge-on-like cases are characterized by changing signs between the neighboring quadrants, as seen in the bottom-right panel in Figure 6.2. We confirm the validity of this description for edge-on "like" (not only $i = 90°$) cases.[1] In particular, the CP intensities in the **second and third quadrants** are brighter due to the relativistic beaming effect (see the bottom-right of Figure 6.2), and are dominant for the image-integrated, unresolved CP flux. Second, the unresolved CP fluxes in lower inclination cases are predominantly contributed from the counter-side jet (as shown in Section 6.3.3); the stronger CP intensities are found in the **third quadrant** (or **second quadrant**) side for the north (south) side observers. Third, the SSA effect becomes significant for a large inclination angle, as shown in Figure 6.5. Then, the CP emissions from the counter-side jet are suppressed because of large optical depths, and yield their dominance to those from the foreground-side jet (**second quadrant** for north and **third quadrant** for south). This is also shown by upward and downward $I - |V|$ arrows for north and south side cases in Figure 6.6, respectively.

[1] Refer to the movie of all of the images for $i = 0° - 180°$ on https://youtu.be/065qAx6Tff0 (accessed on October 19, 2022).

As a result, the dominant part for the CPs changes in order of the negative ring (face-on cases in the north), **third quadrant** (positive), **second quadrant** (negative), ($i = 90°$; crossing the equatorial plane,) **third quadrant** (positive), **second quadrant** (negative), and the positive ring (face-on in the south), if starting from $i = 0°$ to $180°$. In this way, the oscillation of the total CPs is explained with the monochromatic rings and quadranted images.

Ricarte et al. (2021), using MAD and SANE models, also calculated profiles of unresolved CP fractions for inclination angles. Their profiles give negative and positive values for face-on-like cases in the north and south side, respectively, in a similar way to ours. Meanwhile, they show a sign-changing feature for edge-on cases but for one cycle (cf. two cycles in our case). The difference may be explained by removing our third sign-changing factor above: the change in the bright region. Where the emission, Faraday rotation/conversion, and SSA occur depends on many factors, such as the magnetic strength and electron temperature and density. Thus, the difference in the MAD-SANE regime and the electron temperature prescription can drastically affect the morphology of the images and integrated CP fractions.

The total CP fraction is a product from integrating an image consisting of the intrinsic emission and rotation- and twisted-field-driven conversion, which have different dependencies on the plasma and observational properties to each other. Thus, it may be difficult to access the characteristics of the system through this unresolved quantity alone (Ricarte et al. 2021). One straightforward application is to combine it with the total LP, which we will discuss in the next subsection.

6.3.5 Combination of the Unresolved LP and CP Fractions

Finally, we focus on the relationship between the unresolved LP and CP fractions. The unresolved LP fractions in Figure 6.4 give a symmetric-like profile with high ($\gtrsim 1\%$) and low ($\lesssim 1\%$) values in face-on and edge-on-like cases, respectively. This result is due to a larger optical depth for Faraday rotation for larger inclination angles. As pictured in Figure 6.1, the emitted LP vectors to the more edge-on-like observer experience a larger Faraday rotation in the outer cold disk. In fact, the typical optical depths for Faraday rotation are larger in the edge-on cases by approximately one order of magnitude than in the face-on cases.

If we combine this with the discussion in Section 6.3.2, we can conclude that the unresolved LP and CP fractions are characterized by relatively strong LPs and sign-persistent CPs in the face-on-like cases, and weak LPs and time-variable CPs in the edge-on cases. Precisely speaking, the CP signs are time-varying in the edge-on-like cases (see Figure 6.4).

M87(*) has been known to show strong LP and weak CP flux at radio wavelengths (Kuo et al. 2014; Event Horizon Telescope Collaboration et al. 2022a; Goddi et al. 2021). If we apply the model constraints for the total LP and CP fractions from Event Horizon Telescope Collaboration et al. (2021b), the face-on like models are favored, which is consistent with the well-known large-scaled M87 jet. Future stimulating resolved/unresolved LPs and CPs will

become a good tool for investigating the system of SMBH and plasma in M87 itself, and for applying knowledge of M87 to other AGN jets.

In contrast, M81* has been reported to show larger CP fractions than LP fractions (Bower et al. 2002; Brunthaler et al. 2006). These observation may be explained by our edge-on-like $i \approx 40^\circ - 140^\circ$ cases with low LPs due to strong Faraday rotation, which is also consistent with high inclination angles referred for radio galaxies.

Whether and how source types, such as blazars, quasars, and radio galaxies, are related to the LP and CP fractions has also been discussed (e.g., Rayner et al. 2000; Homan & Lister 2006). Coupled with more statistical data from the future resolved/unresolved spectro-polarimetry of various targets, a survey of inclination angles can give a clue for accessing a unified description of a diversity of AGNs.

6.3.6 Future Prospects

In this work, we focused our discussion on the diverse appearance of AGN jets, using the same fluid model, to demonstrate how jets are observed differently depending on the viewing angle. Meanwhile, it should be surveyed whether the results based on the semi-MAD model are common even for other fluid models, such as more SANE- or MAD-like models, and/or with different electron-temperature prescriptions, including the time-variability. More statistical surveys for various fluid models and long time durations is the scope of our future works.

This page intentionally left blank.

Chapter 7

Concluding Remarks

To investigate the enigmatic mechanism of the magnetically driven jets and a supermassive black hole (SMBH) in active galactic nuclei (AGN), we performed the polarized general relativistic radiative transfer (GRRT) calculations based on fluid models by the general relativistic magnetohydrodynamics (GRMHD) simulations. Through the calculated linear and circular polarimetric images in the event horizon scale with observations by the Event Horizon Telescope (EHT) and other global-scale VLBIs in mind, we produced predictions about the magnetic field and plasma structure in the jet and accretion disk close to the supermassive black hole, and its possible observational features. Our results can be summarized in the following:

- Using the axisymmetric GRMHD simulation models by Nakamura et al. (2018), which successfully reproduce the shape of M87 jet at multiwavelengths, we found in the horizon scale that the linear polarization (LP) vectors are significantly scrambled and depolarized by the Faraday rotation so that the original information regarding the magnetic field properties may be lost partly. We also found that the circular polarization (CP) components can grow via Faraday conversion of the linear polarization, which is driven by Faraday rotation (rotation-induced conversion), in the innermost hot plasma threaded by ordered magnetic fields. Thus the CP images provide information regarding the degree of alignment and order of magnetic field lines close to the SMBH. In addition, the fiducial model with a spin of $a = 0.9$ and low disk electron-temperature, which produce a crescent-shaped ring and absence of extending jet component on the horizon-scale image, was favored in comparison with existing unresolved LP observations.

- To model our Galactic center Sgr A*, without observable outstanding jet, by the same GRMHD simulation models above, we adopted high disk electron-temperature models to make the disk emissive relatively to the jet. The total intensity images show a variety

of morphological features depending on the observer's viewing angle, like the ring-like for the face-on observer or the three-fork-like image for the edge-on observer to the disk. In all the models, the CP images show a sign reversal feature with a vertical border line, which we termed as the "separatrix". This is because the CP components increased via the rotation-induced conversion has a sign proportional to $\cos\theta_B$, where θ_B is the angle between the propagating light path and the direction of (here toroidally-dominant) magnetic field. For the same reason (that is, the Faraday rotation $\propto \cos\theta_B$ is weak to the LP vectors on the CP separatrix), the LP fluxes on the separatrix are not depolarized and are brighter on the image. These LP and CP features can be double evidence of toroidal magnetic fields near the black hole. Further, we confirmed that the above non-polarimetric and polarimetric features still remain even after undergoing the interstellar scattering unique to Sgr A*. We also demonstrated that the angular resolution in present and future EHT observation for Sgr A* at 230 GHz and 345 GHz is enough to capture the features.

- Based on the above results of the rotated LP vectors and the converted CP components by the Faraday effects, we investigated the disk and jet structure around the SMBH, as the "site" of the Faraday rotation and conversion, through the polarimetric images based on the three-dimensional, semi-MAD (magnetically arrested disk) GRMHD simulation model by `UWABAMI` code (Takahashi et al. 2016; Kawashima et al. 2021a). To examine and quantify the relationship between these polarization components and the plasma properties near the black hole, we analyzed the correlation relations among the total, LP and CP intensity distributions on the images. By surveying the peak shifts of correlation functions at multi-wavelengths and for different model parameters, we established a unified description of three regimes;

  - **Faraday thin and SSA thin case**: at higher frequencies (say, 345 and 690 GHz for our fiducial model) and for lower mass accretion onto the black hole, the polarized synchrotron emission reaches to us without suffering the Faraday effects since both of the Faraday rotation and conversion are weak. As a result, we observe the intrinsic synchrotron polarization consisting of dominant LP and weak CP components with similar distributions to the total intensity image.
  - **Faraday thick and SSA thin case**: the LP vectors from the background jet and the upstream of the foreground (approaching) jet are scrambled by the Faraday rotation in the outer disk and are depolarized after convolved by observational beam, while the CP components are increased by the Faraday conversion in the innermost hot disk. As a result, the LP components from the downstream of the foreground jet dominate over those from the upstream and the backgroung jet, or those on the photon ring, whereas the CP components are distributed around the photon ring and

the background jet. Thus, the downwards LP and upwards CP components, relatively to the total intensity distribution, are observed on the images (e.g., at 230 and 86 GHz for our fiducial model). These tendencies become more enhanced at lower frequency or for higher mass accretion rate, as long as the SSA is not significant.

– **Faraday thick and SSA thick case**: at even lower frequencies (say 43 GHz for our fiducial model) or for even higher mass accretion rate, the SSA becomes significant in addition to the Faraday effects. In this case, the polarized emission comes from the surface of the photosphere. Therefore, the intrinsic CP components are observed in similar distribution to the total intensities, while the LP vectors are depolarized in the outer cold disk and are again dominated by those from the downstream.

Further, we found that high electron-temperature disk models also show a downwards LP distribution, but do not necessarily give an upwards CP distribution. This is because the emission from the midplane disk, where the plasma structure is relatively turbulent, is dominant in these models, and thus the CP image is affected by the disk structure in small scale rather than the up- and down- stream structure of the jet. Thus we can propose the LP-CP separation feature as a possible test of the proton-electron coupling in the jet-disk structure close to the SMBH. Comparing these results with existing observations of M87 by the EHT and other VLBIs, we can see a persistent tendency at multi-frequencies of the LP components distributed in the downstream of the jet. We can further expect that future observations including both of the linear and circular polarimetries will give a strong constraint on the plasma properties such as the optical thickness for the Faraday effects and the SSA, the density/temperature distribution and magnetic field structure near the SMBH.

- To apply these description to a diversity of AGN jets, we surveyed the polarimetric images based on the same 3D GRMHD model for various observer's viewing angles. We confirmed a consistent, typical scenario where polarized synchrotron emissions from the funnel jet experience Faraday rotation and conversion in the equatorial disk. We found that the LP vectors are inevitably depolarized for edge-on like observers, whereas a portion of vectors survive and reach the observers in face-on like cases. For the face-on like cases, it was also confirmed that the larger viewing angle gives the larger separation among the total, LP and CP intensity distributions because of the larger projected distance along the jet on the screen. We also found that the unresolved CP fluxes have persistent signs in the face-on cases and changing signs in the edge-on cases, and that these features are smoothly connected via intermediate viewing-angle cases. These diverse results are due to Faraday rotation and conversion for different viewing angles, and suggest that a combination of linear and circular polarimetry should give a constraint on the inclination

between the observer and SMBH's (and/or accretion disk's) rotating-axis and magnetic field and plasma properties in the disk-jet structure. These can also lead to more statistical and unified interpretation for a diversity of AGN jets.

This page intentionally left blank.

Appendix A

Polarized Radiative Transfer Coefficients

Here, we introduce the coefficients in polarized radiative transfer, as mentioned in subsections 1.5.1 and 1.5.2 in the Introduction chapter and section 2.2 in the Method chapter; polarized synchrotron emissivities, the coefficients in transfer matrix of synchrotron self-absorption, Faraday rotation and conversion. The coefficients are implemented into our code for two kinds of electron distribution, basically following Dexter (2016) who review these in their appendix. One is the relativistic thermal (Maxwell-Jüttner) distribution,

$$N(\gamma) = \frac{n_{\rm e}\gamma(\gamma^2-1)^{1/2}}{\theta_{\rm e}K_2(1/\theta_{\rm e})}\exp\left(-\frac{\gamma}{\theta_{\rm e}}\right), \tag{A.1}$$

and another is the power-law distribution,

$$N(\gamma) = \begin{cases} \frac{n_{\rm e}(p-1)}{(\gamma_1^{1-p}-\gamma_2^{1-p})}\gamma^{-p} & \gamma_1 < \gamma < \gamma_2 \\ 0 & \text{otherwise} \end{cases} \tag{A.2}$$

where p, γ_1 and γ_2 are the power-law index, the low- and high- energy cutoff of the distribution, respectively.

A.1 Polarized Synchrotron Emissivities and Self-Absorption Coefficients

Thermal Electron Distribution

First, we look at the polarized synchrotron emissivities in the plasma rest frame for the ultrarelativistic thermal electron distribution ($\theta_{\rm e} \gg 1$). Substituting A.1 into 1.15 and then into 1.16,

one obtains, by the approximation of $K_2(z) \approx 2z^2$ for small z,

$$j_I(\nu, \theta_B) = \frac{n_{\rm e} e^2 \nu}{2\sqrt{3} c\, \theta_{\rm e}^2} I_I(x), \tag{A.3}$$

$$j_Q(\nu, \theta_B) = \frac{n_{\rm e} e^2 \nu}{2\sqrt{3} c\, \theta_{\rm e}^2} I_Q(x), \tag{A.4}$$

$$j_V(\nu, \theta_B) = \frac{2 n_{\rm e} e^2 \nu \cot\,\theta_B}{3\sqrt{3} c\, \theta_{\rm e}^3} I_I(x), \tag{A.5}$$

where $x \equiv \nu/\nu_{\rm c}$ and here $\nu_{\rm c} = (3/2)\nu_B \theta_{\rm e}^2 \sin\,\theta_B$, and

$$I_I(x) = \frac{1}{x}\int_0^\infty {\rm d}z z^2 \exp(-z) F\left(\frac{x}{z^2}\right), \tag{A.6}$$

$$I_Q(x) = \frac{1}{x}\int_0^\infty {\rm d}z z^2 \exp(-z) G\left(\frac{x}{z^2}\right), \tag{A.7}$$

$$I_V(x) = \frac{1}{x}\int_0^\infty {\rm d}z z^2 \exp(-z) H\left(\frac{x}{z^2}\right). \tag{A.8}$$

Here the functions F, G, and H are given in equation 1.12 (Sazonov 1969; Mahadevan et al. 1996; Huang et al. 2009). The analytical approximations of these integrals are calculated with high accuracy by fitting with polynomials (Mahadevan et al. 1996; Dexter 2016);

$$I_I(x) = 2.5651(1 + 1.92x^{-1/3} + 0.9977x^{-2/3})\exp(-1.8899x^{1/3}), \tag{A.9}$$

$$I_Q(x) = 2.5651(1 + 0.932x^{-1/3} + 0.4998x^{-2/3})\exp(-1.8899x^{1/3}), \tag{A.10}$$

$$I_V(x) = (1.8138x^{-1} + 3.423x^{-2/3} + 0.02955x^{-1/2} + 2.0377x^{-1/3})\exp(-1.8899x^{1/3}). \tag{A.11}$$

These fitting formulae are accurate to $\lesssim 20\%$ for parameters of our interest $\theta_{\rm e} > 3$ and $\nu/\nu_{\rm c} > 1$ (Dexter 2016; see also Pandya et al. 2016 for their numerical integrations), which correspond to $T_{\rm e} \gtrsim 10^{11}$ K close to the SMBH and centimeter, millimeter to submillimeter wavelengths $\nu \gtrsim 2$ GHz considering

$$\nu_{\rm c} \sim 2 \left(\frac{B}{10\ {\rm Gauss}}\right)\left(\frac{\theta_{\rm e}}{3}\right)^2\ {\rm GHz}. \tag{A.12}$$

As mentioned in subsection 1.5.1, the polarized SSA coefficients for the thermal electron distribution are calculated from Kirchoff's law $\alpha_{(I,Q,U,V)} = j_{(I,Q,U,V)}/B_\nu(T_{\rm e})$ with the Planck function $B_\nu(T)$, respectively (see, for example, Rybicki & Lightman 1979).

Power-Law Electron Distribution

Next, we have a look at the case of the power-law electron distribution. Substituting A.2 into 1.15 gives, with 1.16,

$$j_I(\nu,\theta_B) = \frac{(p-1)n_e e^2 \nu_c \gamma_1^{-(p+3)/2}}{2\sqrt{3}c(\gamma_1^{1-p}-\gamma_2^{1-p})}\left(\frac{\nu}{\nu_c}\right)^{-\frac{p-1}{2}}\{G_I(x_1)-G_I(x_2)\}, \tag{A.13}$$

$$j_Q(\nu,\theta_B) = \frac{(p-1)n_e e^2 \nu_c \gamma_1^{-(p+3)/2}}{2\sqrt{3}c(\gamma_1^{1-p}-\gamma_2^{1-p})}\left(\frac{\nu}{\nu_c}\right)^{-\frac{p-1}{2}}\{G_Q(x_1)-G_Q(x_2)\}, \tag{A.14}$$

$$j_V(\nu,\theta_B) = \frac{2(p-1)n_e e^2 \nu_c \gamma_1^{-(p+4)/2}\cot\theta_B}{3\sqrt{3}c(\gamma_1^{1-p}-\gamma_2^{1-p})}\left(\frac{\nu}{\nu_c}\right)^{-\frac{p}{2}}\{G_V(x_1)-G_V(x_2)\}, \tag{A.15}$$

where $\nu_c = (3/2)\nu_B\gamma_1^2\sin\theta_B$, and

$$G_I(x) = \int_x^\infty \mathrm{d}z z^{\frac{p-3}{2}} F(z), \tag{A.16}$$

$$G_Q(x) = \int_x^\infty \mathrm{d}z z^{\frac{p-3}{2}} G(z), \tag{A.17}$$

$$G_V(x) = \int_x^\infty \mathrm{d}z z^{\frac{p-2}{2}} H(z). \tag{A.18}$$

The power-law emissivities are implemented into our code by numerically tabulating these integrals[1] for each value of power-law index p.

At frequencies in the range of $\nu_c \ll \nu \ll \nu_c(\gamma_2^2/\gamma_1^2)$, the integrals are approximately calculated in analytic forms by limiting the integral interval $[x_1, x_2]$ to $[0,\infty]$ (see, for example, Legg & Westfold 1968; Jones & O'Dell 1977). Using the relationship between the modified Bessel and gamma functions, (Westfold 1959),

$$\int_0^\infty \mathrm{d}x x^s K_\alpha(x) = 2^{s-1}\Gamma\left(\frac{s+\alpha+1}{2}\right)\Gamma\left(\frac{s-\alpha+1}{2}\right), \tag{A.19}$$

the limited integral yield

$$G_I(0) = 2^{\frac{p-3}{2}}\frac{p+\frac{7}{3}}{p+1}\Gamma\left(\frac{p}{4}+\frac{7}{12}\right)\Gamma\left(\frac{p}{4}-\frac{1}{12}\right), \tag{A.20}$$

$$G_Q(0) = \frac{p+1}{p+\frac{7}{3}}G_I(0), \tag{A.21}$$

$$G_V(0) = 2^{\frac{p-2}{2}}\frac{p+2}{p}\Gamma\left(\frac{p}{4}+\frac{1}{3}\right)\Gamma\left(\frac{p}{4}+\frac{2}{3}\right), \tag{A.22}$$

and

$$G_I(\infty) = G_Q(\infty) = G_V(\infty) = 0. \tag{A.23}$$

These approximations gives, in particular, a LP fraction of non-thermal synchrotron emission,

$$\frac{j_{Q(\mathrm{approx})}}{j_{I(\mathrm{approx})}} = \frac{p+1}{p+\frac{7}{3}}, \tag{A.24}$$

[1] The tabulation process can be accelerated by a relation among modified Bessel functions (see Westfold 1959; Dexter 2016)

which is equal to 75% for the power-law index $p = 3$. However, we here should note that the critical synchrotron frequency of our interest (e.g., M87)

$$\nu_{\rm c} \sim 200 \left(\frac{B}{10\ {\rm Gauss}}\right)\left(\frac{\gamma_1}{30}\right)^2\ {\rm GHz} \tag{A.25}$$

is so close to submillimeter wavelengths (e.g., 230 GHz) that one cannot extend $\nu/\nu_c \to 0$ safely, and thus have to calculate the integrals numerically (see Huang & Shcherbakov 2011 and Figure A1 of Dexter (2016) for a deviation between the numerical integration and the approximate form).

The SSA coefficients for power-law (thus non-thermal) electrons do not follow Kirchoff's law, but are calculated in the analogous way with the power-law emissivities above. Substituting A.2 into 1.28, one obtains after calculation,

$$\alpha_I = \frac{(p-1)(p+2)n_{\rm e}e^2\gamma_1^{-(p+2)}}{4\sqrt{3}m_{\rm e}c\nu_{\rm c}(\gamma_1^{1-p}-\gamma_2^{1-p})}\left(\frac{\nu}{\nu_{\rm c}}\right)^{-\frac{p+4}{2}}\left\{Ga_I(x_1)-Ga_I(x_2)\right\}, \tag{A.26}$$

$$\alpha_Q = \frac{(p-1)(p+2)n_{\rm e}e^2\gamma_1^{-(p+2)}}{4\sqrt{3}m_{\rm e}c\nu_{\rm c}(\gamma_1^{1-p}-\gamma_2^{1-p})}\left(\frac{\nu}{\nu_{\rm c}}\right)^{-\frac{p+4}{2}}\left\{Ga_Q(x_1)-Ga_Q(x_2)\right\}, \tag{A.27}$$

$$\alpha_V = \frac{(p-1)(p+2)n_{\rm e}e^2\gamma_1^{-(p+3)}\cot\theta_B}{3\sqrt{3}m_{\rm e}c\nu_{\rm c}(\gamma_1^{1-p}-\gamma_2^{1-p})}\left(\frac{\nu}{\nu_{\rm c}}\right)^{-\frac{p+4}{2}}\left\{Ga_V(x_1)-Ga_V(x_2)\right\}, \tag{A.28}$$

where the integrals are

$$Ga_I(x) = \int_x^\infty {\rm d}z z^{\frac{p-2}{2}}F(z), \tag{A.29}$$

$$Ga_Q(x) = \int_x^\infty {\rm d}z z^{\frac{p-2}{2}}G(z), \tag{A.30}$$

$$Ga_V(x) = \int_x^\infty {\rm d}z z^{\frac{p-1}{2}}H(z). \tag{A.31}$$

These are implemented by tabulating the integrals.

If one limit the integral interval to $[0,\infty]$, the integrals are approximately calculated as

$$Ga_I(0) = 2^{\frac{p-2}{2}}\frac{p+\frac{10}{3}}{p+2}\Gamma\left(\frac{p}{4}+\frac{5}{6}\right)\Gamma\left(\frac{p}{4}+\frac{1}{6}\right), \tag{A.32}$$

$$Ga_Q(0) = \frac{p+2}{p+\frac{10}{3}}Ga_I(0), \tag{A.33}$$

$$Ga_V(0) = 2^{\frac{p-1}{2}}\frac{p+3}{p+1}\Gamma\left(\frac{p}{4}+\frac{7}{12}\right)\Gamma\left(\frac{p}{4}+\frac{11}{12}\right), \tag{A.34}$$

and

$$Ga_I(\infty) = Ga_Q(\infty) = Ga_V(\infty) = 0. \tag{A.35}$$

As mentioned in subsection 1.5.1, these approximate emissivities and absorption coefficients give the source function for the power-law electrons as $S^{\rm nth}_{\nu(I,Q,U,V)} \propto \nu^{5/2}$, which can be distinguishable in spectra from those for the thermal electrons $S^{\rm th}_{\nu(I,Q,U,V)} \propto \nu^2$ in the optically thick case.

A.2 Faraday Rotation and Conversion Coefficients

Thermal Electrons

As mentioned in subsection 1.5.2, the coefficients of Faraday rotation and conversion are calculated from the plasma response tensor. In Shcherbakov (2008), the approximate forms were given for the high frequency limit $\nu/\nu_{\rm c} \gg 1$ and all the temperature $\theta_{\rm e}$, and were also calculated with high accuracy for sufficiently high frequency $\nu/\nu_{\rm c} \gtrsim 10^{-1}$ and the relativistic temperature $\theta_{\rm e} \gtrsim 1$ by fitting formulae. Dexter (2016) modified their expressions by comparison with the numerical integration given in Jones & Hardee (1979), so that they keep accuracy over a wider range of the synchrotron limit $\nu/\nu_{\rm B} \gg 1$, as follows;

$$\rho_Q = \frac{n_{\rm e}e^2\nu_B^2}{m_{\rm e}c\nu^3}\sin^2\theta_B\, f_m(X)\left\{\frac{K_1(\theta_{\rm e}^{-1})}{K_2(\theta_{\rm e}^{-1})}+6\theta_{\rm e}\right\}, \tag{A.36}$$

$$\rho_V = \frac{2n_{\rm e}e^2\nu_B}{m_{\rm e}c\nu^2}\cos\theta_B\frac{K_0(\theta_{\rm e}^{-1})-{\rm Step}(\theta_{\rm e};1)\Delta J_5(X)}{K_2(\theta_{\rm e}^{-1})}, \tag{A.37}$$

where

$$X = \left(\frac{3}{2\sqrt{2}}10^{-3}\frac{\nu}{\nu_{\rm c}}\right)^{-1/2}, \tag{A.38}$$

$$f_m(X) = f(X) \tag{A.39}$$

$$+\frac{1}{2}\left\{0.011{\rm exp}\left(-\frac{X}{47.2}\right)-\frac{2^{-1/3}}{3^{23/6}}10^4\pi X^{-8/3}\right\}\left[1+\tanh\left\{10{\rm ln}\left(\frac{X}{120}\right)\right\}\right], \tag{A.40}$$

$$\Delta J_5(X) = 0.4379\,{\rm ln}(1+0.001858X^{1.503}), \tag{A.41}$$

${\rm Step}(\theta_{\rm e};1)$ is a smoothed step function at $\theta_{\rm e}=1$[2], and

$$f(X) = 2.011{\rm exp}\left(-\frac{X^{1.035}}{4.7}\right)-\cos\left(\frac{X}{2}\right){\rm exp}\left(-\frac{X^{1.2}}{2.73}\right)-0.011{\rm exp}\left(-\frac{X}{47.2}\right) \tag{A.42}$$

is the fitting function firstly introduced in Shcherbakov (2008). The synchrotron electron limit, $\nu \gg \nu_B \sim 0.2(B/10\ {\rm Gauss})$ GHz, is valid over a range of wavelengths of our interest.

Power-Law Electrons

The Faraday coefficients for the power-law distribution is given in appendix of Jones & O'Dell (1977) in the approximate form (see also Sazonov 1969), as

$$\rho_Q = \rho_\perp\frac{2}{p-2}\left(\frac{2\nu_{\rm c}}{3\nu}\right)^3\gamma_1^{-(p+4)}\left\{1-\left(\frac{2\nu_{\rm c}}{3\nu}\right)^{(p-2)/2}\right\}, \tag{A.43}$$

$$\rho_V = 2\rho_\perp\frac{p+2}{p+1}\left(\frac{2\nu_{\rm c}}{3\nu}\right)^2\gamma_1^{-(p+5)}{\rm ln}\,\gamma_1\cot\theta_B, \tag{A.44}$$

[2]This is introduced in appendix of Dexter et al. (2020) to suppress the $\Delta J_5(X)$ term in the cold, non-relativistic electron limit $\theta_{\rm e} \ll 1$, so that the ρ_V converges into the familiar form of $\rho_V^{\rm NR} = 2n_{\rm e}e^2\nu_B\cos\theta_B/m_{\rm e}c\nu^2 \propto n_{\rm e}B\cos\theta_B$, for example, in the context of Faraday rotation measure (RM; e.g., Rybicki & Lightman 1979).

where

$$\rho_{\perp} = (p-1)\frac{3n_{\rm e}e^2\gamma_1^2}{2m_{\rm e}c\nu_c(\gamma_1^{1-p}-\gamma_2^{1-p})}. \tag{A.45}$$

These are complemented into our code. Huang & Shcherbakov (2011) confirmed by a comparison with the numerical integrations in the response tensor that the approximate ρ_Q is relatively accurate for $\gamma_1 \lesssim 100$ while the approximate ρ_V works accurately for $\gamma_1 \gtrsim 10$. The superposed accurate range covers the minimum non-thermal energy of our interest.

Appendix B

Code Performance Tests

In this dissertation, we performed polarized GRRT calculations with a code newly implemented by ourselves. To evaluate the performance of the code, we firstly did the same tests as those employed by Dexter (2016). First, we numerically solved the transfer equations with the typical step size in our GRRT calculation, assuming uniform emission and absorption for Stokes I and Q components (see his appendix C).

$$\frac{\mathrm{d}}{\mathrm{d}s}\begin{pmatrix} I \\ Q \end{pmatrix} = \begin{pmatrix} j_I \\ j_Q \end{pmatrix} - \begin{pmatrix} \alpha_I & \alpha_Q \\ \alpha_Q & \alpha_I \end{pmatrix}\begin{pmatrix} I \\ Q \end{pmatrix}, \tag{B.1}$$

and compared the results with the analytic solutions, his (C2) and (C3), in the left panels of figure B.1. We find good agreement between them.

Second, we compared the numerical and analytic solutions of equation with uniform polarized emission and Faraday effects for Stokes (Q, U, V),

$$\frac{\mathrm{d}}{\mathrm{d}s}\begin{pmatrix} Q \\ U \\ V \end{pmatrix} = \begin{pmatrix} j_Q \\ j_U \\ j_V \end{pmatrix} - \begin{pmatrix} 0 & \rho_V & 0 \\ -\rho_V & 0 & \rho_Q \\ 0 & -\rho_Q & 0 \end{pmatrix}\begin{pmatrix} Q \\ U \\ V \end{pmatrix}, \tag{B.2}$$

which is the same as equation (3.3) in the present paper (cf. his (C5-7); see also Appendix C in this thesis), and showed them and its residues from the analytical results (see equation (3.4)) in the right panels of figure B.1, which are small enough for our interest.

To test the GR transfer of both the polarization intensities and vectors, we also made a 345 GHz linear polarization map of semi-analytical force-free jet model introduced by Broderick & Loeb (2009a), and show it in figure B.2, which corresponds to their figure 7 (M0) and figure 6 of Dexter (2016). We find good agreement between them, in terms of asymmetric, branches-like brightened structure by helical bulk motion of plasma, and well-ordered polarization vectors.

Further, we execute the analytic model image tests in Gold et al. (2020), in which the authors compare the GRRT schemes in the EHT Collaboration. We show our resultant images in figure B.3. In any case with/without the rotation of BH/disk and with/without significant absorption,

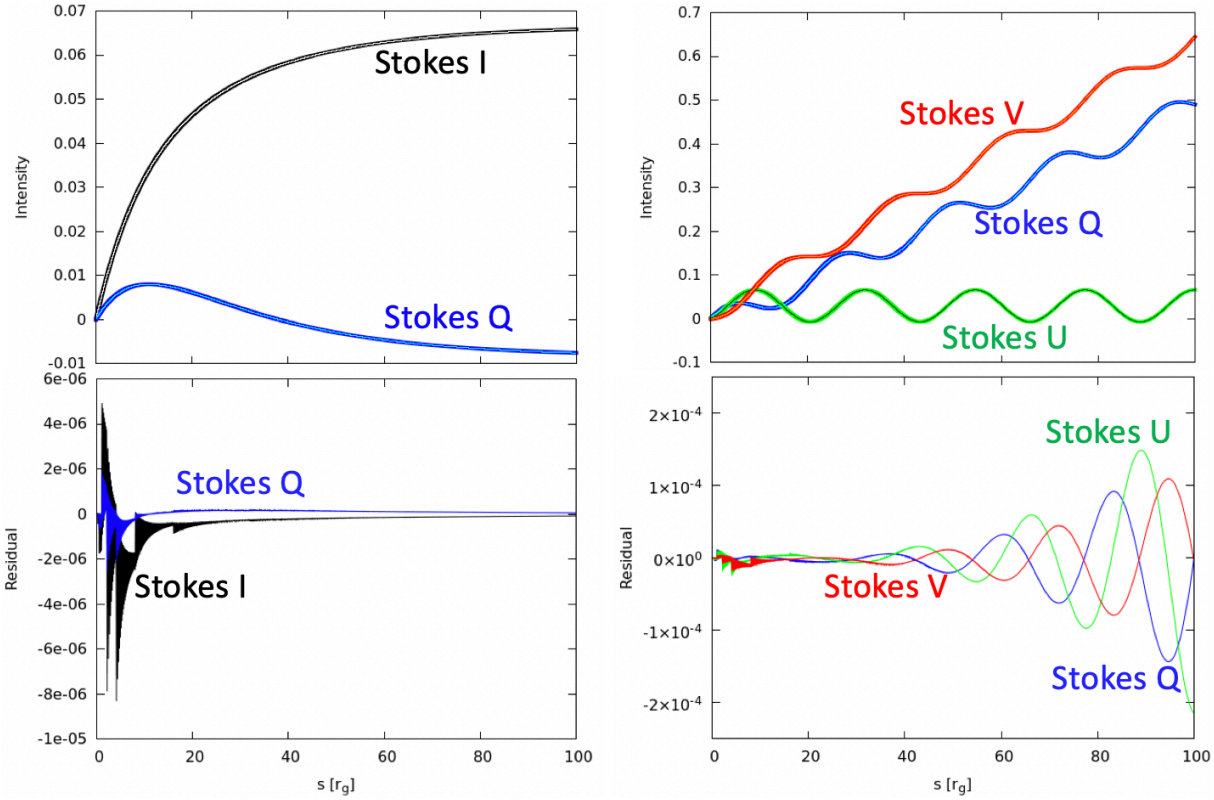

Fig. B.1: Top left: Evolution of Stokes I and Q for a test problem of equations (B.1), with numerical solutions (bold) by our code with a typical step size in our GRRT calculation and analytic ones (fine). Bottom left: Evolution of each of residual for equations (B.1). Top right: Evolution of Stokes (Q, U, V) for a test problem of equations (3.3), as the top left. Bottom right: Evolution of residuals for equations (3.3).

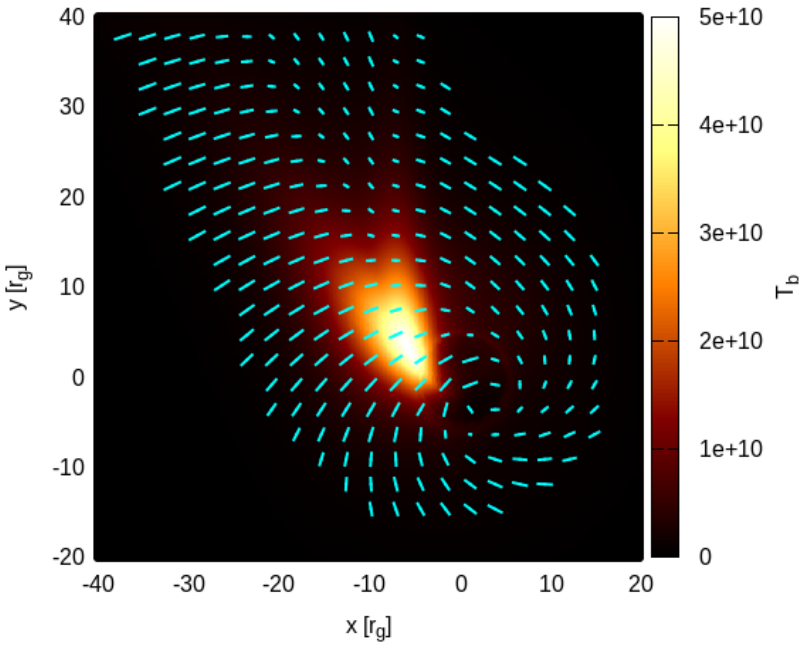

Fig. B.2: 345 GHz linear polarization map (brightness temperature in color contour, in linear scale, and polarization vectors by EVPA in ticks) of semi-analytical force-free jet model for M87 by Broderick & Loeb (2009a). This corresponds to their figure 7 (for their model M0) and figure 6 of Dexter (2016).

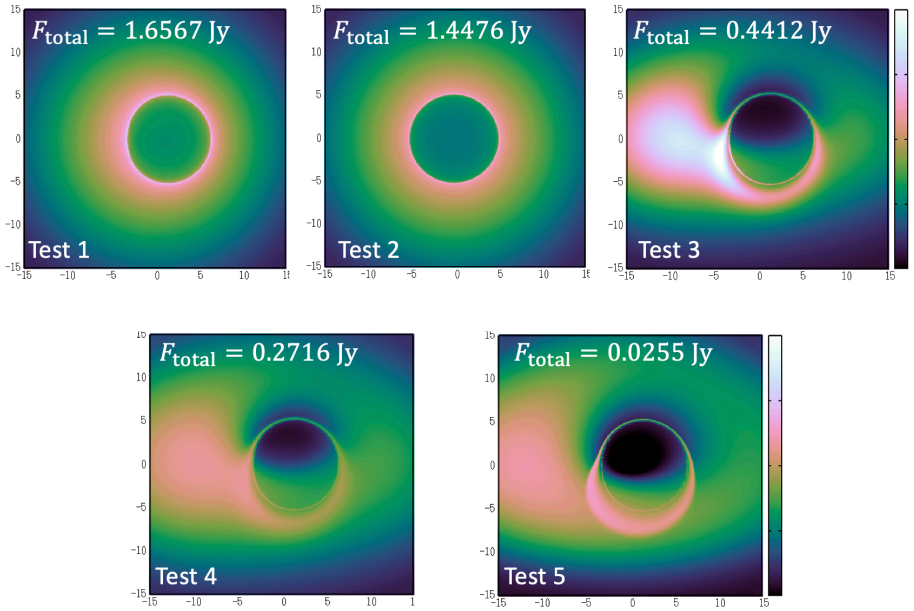

Fig. B.3: Images at 230 GHz for five analytic model tests as in Gold et al. (2020), which correspond to their figure 2.

our image features agree with theirs (in figure 2 in their paper) with the total flux deviations $< 1\%$ from the exact solutions, which are within equivalent accuracy with their codes.

Finally, we also implemented an analytic, one-dimensional jet model in Mościbrodzka (2019), to check polarized (non-GR)RT calculation and radiative coefficients at a range of wavelengths. We successfully reproduced the linear- and circular- polarimetric spectral energy distribution in the range of $10^9 - 10^{14}$ GHz (their Figure 2) and the path propagation of polarization at 225 and 241 GHz (their Figure 3).

Appendix C

Analytic Solution to Polarized Radiative Transfer Equation with Constant Coefficients

In the case with polarized emissivities and Faraday rotation and conversion coefficients (without absorption), the radiative transfer equation can be divided into two parts:

$$\frac{\mathrm{d}I}{\mathrm{d}s} = j_I \tag{C.1}$$

and

$$\frac{\mathrm{d}}{\mathrm{d}s}\begin{pmatrix} Q \\ U \\ V \end{pmatrix} = \begin{pmatrix} j_Q \\ j_U \\ j_V \end{pmatrix} - \begin{pmatrix} 0 & \rho_V & -\rho_U \\ -\rho_V & 0 & \rho_Q \\ \rho_U & -\rho_Q & 0 \end{pmatrix}\begin{pmatrix} Q \\ U \\ V \end{pmatrix}. \tag{C.2}$$

Let us think of the case that all the radiative coefficients are constant. The former for the total specific intensity I can be explicitly integrated as $I(s) = I_0 + j_I s$, where $I_0 \equiv I(0)$ is initial value. The latter for the polarization components, if expressing as

$$\frac{\mathrm{d}\boldsymbol{I}}{\mathrm{d}s} = \boldsymbol{j} - \boldsymbol{K}\boldsymbol{I}, \tag{C.3}$$

can also be integrated in analogy with the case of unpolarized radiative transfer equation $\mathrm{d}I/\mathrm{d}s = j - \alpha I$ (see, for example, Rybicki & Lightman 1979) with the properties of matrix exponential:

$$\boldsymbol{I}(s) = \exp(-\boldsymbol{K}s)\boldsymbol{I}_0 + \int_0^s \exp\left\{-\boldsymbol{K}(s-s')\right\}\mathrm{d}s'\,\boldsymbol{j}. \tag{C.4}$$

Then, one obtains the analytic solution after calculation of the exponential components and its integration by the diagonalization of the transfer matrix $\boldsymbol{K}$.

In a special case with initial Stokes components and no emission, vanishing the second term in equation C.4,

$$I(s) = I_0,$$

$$\begin{pmatrix} Q(s) \\ U(s) \\ V(s) \end{pmatrix} =$$
$$\frac{1}{\rho^2}\begin{pmatrix} \rho_Q^2+\rho_U^2\cos^2\rho s+\rho_V^2\cos^2\rho s & \rho_Q\rho_U(1-\cos\rho s)-\rho\rho_V\sin\rho s & \rho_V\rho_Q(1-\cos\rho s)+\rho\rho_U\sin\rho s \\ \rho_Q\rho_U(1-\cos\rho s)+\rho\rho_V\sin\rho s & \rho_Q^2\cos^2\rho s+\rho_U^2+\rho_V^2\cos^2\rho s & \rho_U\rho_V(1-\cos\rho s)-\rho\rho_Q\sin\rho s \\ \rho_V\rho_Q(1-\cos\rho s)-\rho\rho_U\sin\rho s & \rho_U\rho_V(1-\cos\rho s)+\rho\rho_Q\sin\rho s & \rho_Q^2\cos^2\rho s+\rho_U^2\cos^2\rho s+\rho_V^2 \end{pmatrix}\begin{pmatrix} Q_0 \\ U_0 \\ V_0 \end{pmatrix}, \tag{C.5}$$

where $\rho \equiv \sqrt{\rho_Q^2+\rho_U^2+\rho_V^2}$. This agree with the one shown in Appendix of Mościbrodzka & Gammie (2018).

In the case of zero initial components with emission, erasing the first term in equation C.4,

$$I(s) = j_I s,$$

$$\begin{pmatrix} Q(s) \\ U(s) \\ V(s) \end{pmatrix} =$$
$$\frac{1}{\rho^2}\begin{pmatrix} \rho_Q^2 s+\frac{\rho_U^2+\rho_V^2}{\rho}\sin\rho s & \frac{\rho_Q\rho_U}{\rho}(\rho s-\sin\rho s)-\rho_V(1-\cos\rho s) & \frac{\rho_V\rho_Q}{\rho}(\rho s-\sin\rho s)+\rho_U(1-\cos\rho s) \\ \frac{\rho_Q\rho_U}{\rho}(\rho s-\sin\rho s)+\rho_V(1-\cos\rho s) & \rho_U^2 s+\frac{\rho_V^2+\rho_Q^2}{\rho}\sin\rho s & \frac{\rho_U\rho_V}{\rho}(\rho s-\sin\rho s)-\rho_Q(1-\cos\rho s) \\ \frac{\rho_V\rho_Q}{\rho}(\rho s-\sin\rho s)-\rho_U(1-\cos\rho s) & \frac{\rho_U\rho_V}{\rho}(\rho s-\sin\rho s)+\rho_Q(1-\cos\rho s) & \rho_V^2 s+\frac{\rho_Q^2+\rho_U^2}{\rho}\sin\rho s \end{pmatrix}\begin{pmatrix} j_Q \\ j_U \\ j_V \end{pmatrix}. \tag{C.6}$$

Taking $\rho_U = 0$, this coincides with equation B.2 as shown in Appendix of Dexter (2016). In chapter 3 and 4, the amplification processes of CP component (Stokes V) are discussed in relation with this form.

In the general case with non-zero initial polarization components, emission and Faraday effects, the solution is given as the sum of C.5 and C.6.

This page intentionally left blank.

List of Figures

List of Tables

References

Abbott, B. P., Abbott, R., Abbott, T. D., et al. 2016, Phys. Rev. Lett., 116, 061102, doi: 10.1103/PhysRevLett.116.061102

Abramowicz, M. A., Calvani, M., & Nobili, L. 1980, ApJ, 242, 772, doi: 10.1086/158512

Abramowicz, M. A., Chen, X., Kato, S., Lasota, J.-P., & Regev, O. 1995, ApJ, 438, L37, doi: 10.1086/187709

Abramowski, A., Acero, F., Aharonian, F., et al. 2012, ApJ, 746, 151, doi: 10.1088/0004-637X/746/2/151

Aharonian, F., Akhperjanian, A. G., Bazer-Bachi, A. R., et al. 2006, Science, 314, 1424, doi: 10.1126/science.1134408

Aitken, D. K., Greaves, J., Chrysostomou, A., et al. 2000, ApJ, 534, L173, doi: 10.1086/312685

Akiyama, K., Lu, R.-S., Fish, V. L., et al. 2015, ApJ, 807, 150, doi: 10.1088/0004-637X/807/2/150

Akiyama, K., Kuramochi, K., Ikeda, S., et al. 2017a, ApJ, 838, 1, doi: 10.3847/1538-4357/aa6305

Akiyama, K., Ikeda, S., Pleau, M., et al. 2017b, AJ, 153, 159, doi: 10.3847/1538-3881/aa6302

Algaba, J. C., Asada, K., & Nakamura, M. 2016, ApJ, 823, 86, doi: 10.3847/0004-637X/823/2/86

Anantua, R., Emami, R., Loeb, A., & Chael, A. 2020, ApJ, 896, 30, doi: 10.3847/1538-4357/ab9103

Antonucci, R. 1993, ARA&A, 31, 473, doi: 10.1146/annurev.aa.31.090193.002353

Asada, K., & Nakamura, M. 2012, ApJ, 745, L28, doi: 10.1088/2041-8205/745/2/L28

Baade, W., & Minkowski, R. 1954, ApJ, 119, 215, doi: 10.1086/145813

Baade, W., & Zwicky, F. 1934, Physical Review, 46, 76, doi: 10.1103/PhysRev.46.76.2

Baganoff, F. K., Bautz, M. W., Brandt, W. N., et al. 2001, Nature, 413, 45, doi: 10.1038/35092510

Baganoff, F. K., Maeda, Y., Morris, M., et al. 2003, ApJ, 591, 891, doi: 10.1086/375145

Balbus, S. A., & Hawley, J. F. 1991, ApJ, 376, 214, doi: 10.1086/170270

—. 1992, ApJ, 400, 610, doi: 10.1086/172022

—. 1998, Reviews of Modern Physics, 70, 1, doi: 10.1103/RevModPhys.70.1

Balick, B., & Brown, R. L. 1974, ApJ, 194, 265, doi: 10.1086/153242

Bardeen, J. M. 1973, in Black Holes (Les Astres Occlus), 215–239

Bardeen, J. M., Press, W. H., & Teukolsky, S. A. 1972, ApJ, 178, 347, doi: 10.1086/151796

Barthel, P. D. 1989, ApJ, 336, 606, doi: 10.1086/167038

Beckwith, K., Hawley, J. F., & Krolik, J. H. 2008, ApJ, 678, 1180, doi: 10.1086/533492

Begelman, M. C., McKee, C. F., & Shields, G. A. 1983, ApJ, 271, 70, doi: 10.1086/161178

Biretta, J. A., Zhou, F., & Owen, F. N. 1995, ApJ, 447, 582, doi: 10.1086/175901

Blandford, R., & Globus, N. 2022, MNRAS, 514, 5141, doi: 10.1093/mnras/stac1682

Blandford, R., & Narayan, R. 1985, MNRAS, 213, 591, doi: 10.1093/mnras/213.3.591

Blandford, R. D., & Begelman, M. C. 1999, MNRAS, 303, L1, doi: 10.1046/j.1365-8711.1999.02358.x

Blandford, R. D., & Königl, A. 1979, ApJ, 232, 34, doi: 10.1086/157262

Blandford, R. D., & Payne, D. G. 1982, MNRAS, 199, 883, doi: 10.1093/mnras/199.4.883

Blandford, R. D., & Rees, M. J. 1974, MNRAS, 169, 395, doi: 10.1093/mnras/169.3.395

Blandford, R. D., & Znajek, R. L. 1977, MNRAS, 179, 433, doi: 10.1093/mnras/179.3.433

Bolton, C. T. 1975, ApJ, 200, 269, doi: 10.1086/153785

Bondi, H. 1952, MNRAS, 112, 195, doi: 10.1093/mnras/112.2.195

Bower, G. C., Falcke, H., & Backer, D. C. 1999, ApJ, 523, L29, doi: 10.1086/312246

Bower, G. C., Falcke, H., & Mellon, R. R. 2002, ApJ, 578, L103, doi: 10.1086/344607

Bower, G. C., Wright, M. C. H., Falcke, H., & Backer, D. C. 2003, ApJ, 588, 331, doi: 10.1086/373989

Bower, G. C., Broderick, A., Dexter, J., et al. 2018, ApJ, 868, 101, doi: 10.3847/1538-4357/aae983

Boyer, R. H., & Lindquist, R. W. 1967, Journal of Mathematical Physics, 8, 265, doi: 10.1063/1.1705193

Brandenburg, A., Nordlund, A., Stein, R. F., & Torkelsson, U. 1995, ApJ, 446, 741, doi: 10.1086/175831

Bridle, A. H., & Perley, R. A. 1984, ARA&A, 22, 319, doi: 10.1146/annurev.aa.22.090184.001535

Broderick, A. E., & Loeb, A. 2006, MNRAS, 367, 905, doi: 10.1111/j.1365-2966.2006.10152.x

—. 2009a, ApJ, 697, 1164, doi: 10.1088/0004-637X/697/2/1164

—. 2009b, ApJ, 703, L104, doi: 10.1088/0004-637X/703/2/L104

Broderick, A. E., & McKinney, J. C. 2010, ApJ, 725, 750, doi: 10.1088/0004-637X/725/1/750

Broderick, A. E., Narayan, R., Kormendy, J., et al. 2015, ApJ, 805, 179, doi: 10.1088/0004-637X/805/2/179

Broderick, A. E., & Tchekhovskoy, A. 2015, ApJ, 809, 97, doi: 10.1088/0004-637X/809/1/97

Bronzwaer, T., Younsi, Z., Davelaar, J., & Falcke, H. 2020, A&A, 641, A126, doi: 10.1051/0004-6361/202038573

Brunthaler, A., Bower, G. C., & Falcke, H. 2006, A&A, 451, 845, doi: 10.1051/0004-6361:20054790

Byram, E. T., Chubb, T. A., & Friedman, H. 1966, Science, 152, 66, doi: 10.1126/science.152.3718.66

Carter, B. 1968, Physical Review, 174, 1559, doi: 10.1103/PhysRev.174.1559

—. 1971, Phys. Rev. Lett., 26, 331, doi: 10.1103/PhysRevLett.26.331

Chael, A., Narayan, R., & Johnson, M. D. 2019, MNRAS, 486, 2873, doi: 10.1093/mnras/stz988

Chael, A., Rowan, M., Narayan, R., Johnson, M., & Sironi, L. 2018, MNRAS, 478, 5209, doi: 10.1093/mnras/sty1261

Chael, A. A., Johnson, M. D., Narayan, R., et al. 2016, ApJ, 829, 11, doi: 10.3847/0004-637X/829/1/11

Chan, C.-K., Psaltis, D., Özel, F., Narayan, R., & Sądowski, A. 2015, ApJ, 799, 1, doi: 10.1088/0004-637X/799/1/1

Chandrasekhar, S. 1931, ApJ, 74, 81, doi: 10.1086/143324

—. 1980, Highlights of Astronomy, 5, 45

—. 1983, The mathematical theory of black holes

Connors, P. A., Piran, T., & Stark, R. F. 1980, ApJ, 235, 224, doi: 10.1086/157627

Cruz-Osorio, A., Fromm, C. M., Mizuno, Y., et al. 2022, Nature Astronomy, 6, 103, doi: 10.1038/s41550-021-01506-w

Curtis, H. D. 1918, Publications of Lick Observatory, 13, 9

Davelaar, J., Mościbrodzka, M., Bronzwaer, T., & Falcke, H. 2018, A&A, 612, A34, doi: 10.1051/0004-6361/201732025

Davelaar, J., Olivares, H., Porth, O., et al. 2019, A&A, 632, A2, doi: 10.1051/0004-6361/201936150

Davies, R. D., Walsh, D., & Booth, R. S. 1976, MNRAS, 177, 319, doi: 10.1093/mnras/177.2.319

Daylan, T., Finkbeiner, D. P., Hooper, D., et al. 2016, Physics of the Dark Universe, 12, 1, doi: 10.1016/j.dark.2015.12.005

De Villiers, J.-P., & Hawley, J. F. 2003, ApJ, 592, 1060, doi: 10.1086/375866

De Villiers, J.-P., Hawley, J. F., & Krolik, J. H. 2003, ApJ, 599, 1238, doi: 10.1086/379509

Dexter, J. 2016, MNRAS, 462, 115, doi: 10.1093/mnras/stw1526

Dexter, J., Agol, E., Fragile, P. C., & McKinney, J. C. 2010, ApJ, 717, 1092, doi: 10.1088/0004-637X/717/2/1092

Dexter, J., McKinney, J. C., & Agol, E. 2012, MNRAS, 421, 1517, doi: 10.1111/j.1365-2966.2012.20409.x

Dexter, J., Jiménez-Rosales, A., Ressler, S. M., et al. 2020, MNRAS, 494, 4168, doi: 10.1093/mnras/staa922

Di Matteo, T., Allen, S. W., Fabian, A. C., Wilson, A. S., & Young, A. J. 2003, ApJ, 582, 133, doi: 10.1086/344504

Dihingia, I. K., Vaidya, B., & Fendt, C. 2021, MNRAS, 505, 3596, doi: 10.1093/mnras/stab1512

Doeleman, S. S., Weintroub, J., Rogers, A. E. E., et al. 2008, Nature, 455, 78, doi: 10.1038/nature07245

Doeleman, S. S., Fish, V. L., Schenck, D. E., et al. 2012, Science, 338, 355, doi: 10.1126/science.1224768

Eckart, A., Baganoff, F. K., Morris, M., et al. 2004, A&A, 427, 1, doi: 10.1051/0004-6361:20040495

EHT MWL Science Working Group, Algaba, J. C., Anczarski, J., et al. 2021, ApJ, 911, L11, doi: 10.3847/2041-8213/abef71

Einstein, A. 1915, Sitzungsberichte der Königlich Preussischen Akademie der Wissenschaften, 844

—. 1916, Sitzungsberichte der Königlich Preussischen Akademie der Wissenschaften, 688

Emami, R., Anantua, R., Chael, A. A., & Loeb, A. 2021, arXiv e-prints, arXiv:2101.05327. https://arxiv.org/abs/2101.05327

Enßlin, T. A. 2003, A&A, 401, 499, doi: 10.1051/0004-6361:20030162

Event Horizon Telescope Collaboration, Akiyama, K., Alberdi, A., et al. 2019a, ApJ, 875, L1, doi: 10.3847/2041-8213/ab0ec7

—. 2019b, ApJ, 875, L6, doi: 10.3847/2041-8213/ab1141

—. 2019c, ApJ, 875, L5, doi: 10.3847/2041-8213/ab0f43

—. 2019d, ApJ, 875, L4, doi: 10.3847/2041-8213/ab0e85

—. 2019e, ApJ, 875, L2, doi: 10.3847/2041-8213/ab0c96

Event Horizon Telescope Collaboration, Akiyama, K., Algaba, J. C., et al. 2021a, ApJ, 910, L12, doi: 10.3847/2041-8213/abe71d

—. 2021b, ApJ, 910, L13, doi: 10.3847/2041-8213/abe4de

Event Horizon Telescope Collaboration, Akiyama, K., Alberdi, A., et al. 2022a, ApJ, 930, L12, doi: 10.3847/2041-8213/ac6674

—. 2022b, ApJ, 930, L16, doi: 10.3847/2041-8213/ac6672

Falcke, H., Mannheim, K., & Biermann, P. L. 1993, A&A, 278, L1. https://arxiv.org/abs/astro-ph/9308031

Falcke, H., Melia, F., & Agol, E. 2000, ApJ, 528, L13, doi: 10.1086/312423

Feng, J., Wu, Q., & Lu, R.-S. 2016, ApJ, 830, 6, doi: 10.3847/0004-637X/830/1/6

Fish, V. L., Doeleman, S. S., Beaudoin, C., et al. 2011, ApJ, 727, L36, doi: 10.1088/2041-8205/727/2/L36

Fish, V. L., Johnson, M. D., Lu, R.-S., et al. 2014, ApJ, 795, 134, doi: 10.1088/0004-637X/795/2/134

Fishbone, L. G., & Moncrief, V. 1976, ApJ, 207, 962, doi: 10.1086/154565

Ford, H. C., Harms, R. J., Tsvetanov, Z. I., et al. 1994, ApJ, 435, L27, doi: 10.1086/187586

Gabuzda, D. C., Vitrishchak, V. M., Mahmud, M., & O'Sullivan, S. P. 2008, MNRAS, 384, 1003, doi: 10.1111/j.1365-2966.2007.12773.x

Gammie, C. F. 2004, ApJ, 614, 309, doi: 10.1086/423443

Gammie, C. F., McKinney, J. C., & Tóth, G. 2003, ApJ, 589, 444, doi: 10.1086/374594

Gebhardt, K., Adams, J., Richstone, D., et al. 2011, ApJ, 729, 119, doi: 10.1088/0004-637X/729/2/119

Ghez, A. M., Duchêne, G., Matthews, K., et al. 2003, ApJ, 586, L127, doi: 10.1086/374804

Gillessen, S., Eisenhauer, F., Fritz, T. K., et al. 2009, ApJ, 707, L114, doi: 10.1088/0004-637X/707/2/L114

Gillessen, S., Plewa, P. M., Eisenhauer, F., et al. 2017, ApJ, 837, 30, doi: 10.3847/1538-4357/aa5c41

Goddi, C., Martí-Vidal, I., Messias, H., et al. 2021, ApJ, 910, L14, doi: 10.3847/2041-8213/abee6a

Gold, R., McKinney, J. C., Johnson, M. D., & Doeleman, S. S. 2017, ApJ, 837, 180, doi: 10.3847/1538-4357/aa6193

Gold, R., Broderick, A. E., Younsi, Z., et al. 2020, ApJ, 897, 148, doi: 10.3847/1538-4357/ab96c6

Goodman, J., & Narayan, R. 1989, MNRAS, 238, 995, doi: 10.1093/mnras/238.3.995

GRAVITY Collaboration, Abuter, R., Amorim, A., et al. 2018a, A&A, 615, L15, doi: 10.1051/0004-6361/201833718

—. 2018b, A&A, 618, L10, doi: 10.1051/0004-6361/201834294

—. 2019, A&A, 625, L10, doi: 10.1051/0004-6361/201935656

Hada, K., Doi, A., Kino, M., et al. 2011, Nature, 477, 185, doi: 10.1038/nature10387

Hada, K., Kino, M., Doi, A., et al. 2013, ApJ, 775, 70, doi: 10.1088/0004-637X/775/1/70

—. 2016, ApJ, 817, 131, doi: 10.3847/0004-637X/817/2/131

Hamaker, J. P., & Bregman, J. D. 1996, A&AS, 117, 161

Hawking, S. W. 1974, Nature, 248, 30, doi: 10.1038/248030a0

Hawley, J. F., Guan, X., & Krolik, J. H. 2011, ApJ, 738, 84, doi: 10.1088/0004-637X/738/1/84

Hawley, J. F., & Krolik, J. H. 2002, ApJ, 566, 164, doi: 10.1086/338059

Hawley, J. F., Smarr, L. L., & Wilson, J. R. 1984, ApJ, 277, 296, doi: 10.1086/161696

Hilbert, D. 1917, Nachrichten von der Gesellschaft der Wissenschaften zu Göttingen, Mathematisch-Physikalische Klasse (Berlin: Weidmannsche Buchhandlung, Berlin)

Himwich, E., Johnson, M. D., Lupsasca, A., & Strominger, A. 2020, Phys. Rev. D, 101, 084020, doi: 10.1103/PhysRevD.101.084020

Ho, L. C., Filippenko, A. V., & Sargent, W. L. W. 1997, ApJS, 112, 315, doi: 10.1086/313041

Hodge, P. E. 1982, ApJ, 263, 595, doi: 10.1086/160530

Homan, D. C., & Lister, M. L. 2006, AJ, 131, 1262, doi: 10.1086/500256

Homan, D. C., Lister, M. L., Aller, H. D., Aller, M. F., & Wardle, J. F. C. 2009, ApJ, 696, 328, doi: 10.1088/0004-637X/696/1/328

Howes, G. G. 2010, MNRAS, 409, L104, doi: 10.1111/j.1745-3933.2010.00958.x

Huang, L., Liu, S., Shen, Z.-Q., et al. 2009, ApJ, 703, 557, doi: 10.1088/0004-637X/703/1/557

Huang, L., & Shcherbakov, R. V. 2011, MNRAS, 416, 2574, doi: 10.1111/j.1365-2966.2011.19207.x

Ichimaru, S. 1977, ApJ, 214, 840, doi: 10.1086/155314

Igumenshchev, I. V. 2008, ApJ, 677, 317, doi: 10.1086/529025

Igumenshchev, I. V., Narayan, R., & Abramowicz, M. A. 2003, ApJ, 592, 1042, doi: 10.1086/375769

Israel, W. 1967, Physical Review, 164, 1776, doi: 10.1103/PhysRev.164.1776

Issaoun, S., Johnson, M. D., Blackburn, L., et al. 2019, ApJ, 871, 30, doi: 10.3847/1538-4357/aaf732

Jennison, R. C., & Das Gupta, M. K. 1953, Nature, 172, 996, doi: 10.1038/172996a0

Jeter, B., Broderick, A. E., & Gold, R. 2020, MNRAS, 493, 5606, doi: 10.1093/mnras/staa679

Jiménez-Rosales, A., & Dexter, J. 2018, MNRAS, 478, 1875, doi: 10.1093/mnras/sty1210

Jiménez-Rosales, A., Dexter, J., Ressler, S. M., et al. 2021, MNRAS, 503, 4563, doi: 10.1093/mnras/stab784

Jin, C., Done, C., Ward, M., & Gardner, E. 2017, MNRAS, 471, 706, doi: 10.1093/mnras/stx1634

Johannsen, T. 2013, ApJ, 777, 170, doi: 10.1088/0004-637X/777/2/170

Johannsen, T., & Psaltis, D. 2010, ApJ, 718, 446, doi: 10.1088/0004-637X/718/1/446

Johnson, M. D. 2016, ApJ, 833, 74, doi: 10.3847/1538-4357/833/1/74

Johnson, M. D., Fish, V. L., Doeleman, S. S., et al. 2014, ApJ, 794, 150, doi: 10.1088/0004-637X/794/2/150

Johnson, M. D., & Gwinn, C. R. 2015, ApJ, 805, 180, doi: 10.1088/0004-637X/805/2/180

Johnson, M. D., & Narayan, R. 2016, ApJ, 826, 170, doi: 10.3847/0004-637X/826/2/170

Johnson, M. D., Fish, V. L., Doeleman, S. S., et al. 2015, Science, 350, 1242, doi: 10.1126/science.aac7087

Johnson, M. D., Narayan, R., Psaltis, D., et al. 2018, ApJ, 865, 104, doi: 10.3847/1538-4357/aadcff

Jones, T. W. 1988, ApJ, 332, 678, doi: 10.1086/166685

Jones, T. W., & Hardee, P. E. 1979, ApJ, 228, 268, doi: 10.1086/156843

Jones, T. W., & O'Dell, S. L. 1977, ApJ, 214, 522, doi: 10.1086/155278

Jones, T. W., O'Dell, S. L., & Stein, W. A. 1974, ApJ, 192, 261, doi: 10.1086/153057

Jorstad, S. G., Marscher, A. P., Lister, M. L., et al. 2004, AJ, 127, 3115, doi: 10.1086/420996

Junor, W., Biretta, J. A., & Livio, M. 1999, Nature, 401, 891, doi: 10.1038/44780

Kato, S., Fukue, J., & Mineshige, S. 2008, Black-Hole Accretion Disks — Towards a New Paradigm —

Kato, Y., Mineshige, S., & Shibata, K. 2004, ApJ, 605, 307, doi: 10.1086/381234

Kawashima, T., Kino, M., & Akiyama, K. 2019, ApJ, 878, 27, doi: 10.3847/1538-4357/ab19c0

Kawashima, T., Ohsuga, K., & Takahashi, H. R. 2021a, arXiv e-prints, arXiv:2108.05131. https://arxiv.org/abs/2108.05131

Kawashima, T., Toma, K., Kino, M., et al. 2021b, ApJ, 909, 168, doi: 10.3847/1538-4357/abd5bb

Kawazura, Y., Barnes, M., & Schekochihin, A. A. 2019, Proceedings of the National Academy of Science, 116, 771, doi: 10.1073/pnas.1812491116

Kerr, R. P. 1963, Phys. Rev. Lett., 11, 237, doi: 10.1103/PhysRevLett.11.237

Kim, J.-Y., Lu, R.-S., Krichbaum, T., et al. 2016, Galaxies, 4, 39, doi: 10.3390/galaxies4040039

Kim, J. Y., Krichbaum, T. P., Lu, R. S., et al. 2018, A&A, 616, A188, doi: 10.1051/0004-6361/201832921

Kino, M., Takahara, F., Hada, K., et al. 2015, ApJ, 803, 30, doi: 10.1088/0004-637X/803/1/30

Kino, M., Takahara, F., Hada, K., & Doi, A. 2014, ApJ, 786, 5, doi: 10.1088/0004-637X/786/1/5

Kitaki, T., Mineshige, S., Ohsuga, K., & Kawashima, T. 2021, PASJ, 73, 450, doi: 10.1093/pasj/psab011

Koide, S., Shibata, K., & Kudoh, T. 1999, ApJ, 522, 727, doi: 10.1086/307667

Koide, S., Shibata, K., Kudoh, T., & Meier, D. L. 2002, Science, 295, 1688, doi: 10.1126/science.1068240

Komissarov, S. S. 1999, MNRAS, 308, 1069, doi: 10.1046/j.1365-8711.1999.02783.x

Kormendy, J. 1988, ApJ, 325, 128, doi: 10.1086/165988

Kovalev, Y. Y., Lister, M. L., Homan, D. C., & Kellermann, K. I. 2007, ApJ, 668, L27, doi: 10.1086/522603

Kravchenko, E., Giroletti, M., Hada, K., et al. 2020, A&A, 637, L6, doi: 10.1051/0004-6361/201937315

Krolik, J. H., Hawley, J. F., & Hirose, S. 2005, ApJ, 622, 1008, doi: 10.1086/427932

Kruskal, M. D. 1960, Physical Review, 119, 1743, doi: 10.1103/PhysRev.119.1743

Kuo, C. Y., Asada, K., Rao, R., et al. 2014, ApJ, 783, L33, doi: 10.1088/2041-8205/783/2/L33

Kuramochi, K., Akiyama, K., Ikeda, S., et al. 2018, ApJ, 858, 56, doi: 10.3847/1538-4357/aab6b5

Landau, L. D., & Lifshitz, E. M. 1975, The classical theory of fields

—. 1980, Statistical physics. Pt.1, Pt.2

Laplace, P.-S. 1796, Exposition du système du monde, Vol. 11 (Paris, Courcier)

Legg, M. P. C., & Westfold, K. C. 1968, ApJ, 154, 499, doi: 10.1086/149777

Lemaître, G. 1933, Annales de la Société Scientifique de Bruxelles, 53, 51

Liska, M., Hesp, C., Tchekhovskoy, A., et al. 2021, MNRAS, 507, 983, doi: 10.1093/mnras/staa099

Lu, R.-S., Broderick, A. E., Baron, F., et al. 2014, ApJ, 788, 120, doi: 10.1088/0004-637X/788/2/120

Ly, C., Walker, R. C., & Junor, W. 2007, ApJ, 660, 200, doi: 10.1086/512846

Lynden-Bell, D. 1969, Nature, 223, 690, doi: 10.1038/223690a0

Macchetto, F., Marconi, A., Axon, D. J., et al. 1997, ApJ, 489, 579, doi: 10.1086/304823

Mahadevan, R. 1998, Nature, 394, 651, doi: 10.1038/29241

Mahadevan, R., Narayan, R., & Yi, I. 1996, ApJ, 465, 327, doi: 10.1086/177422

Manmoto, T., Mineshige, S., & Kusunose, M. 1997, ApJ, 489, 791, doi: 10.1086/304817

Marrone, D. P., Moran, J. M., Zhao, J.-H., & Rao, R. 2006, ApJ, 640, 308, doi: 10.1086/500106

—. 2007, ApJ, 654, L57, doi: 10.1086/510850

Marshall, H. L., Miller, B. P., Davis, D. S., et al. 2002, ApJ, 564, 683, doi: 10.1086/324396

McKinney, J. C. 2006, MNRAS, 368, 1561, doi: 10.1111/j.1365-2966.2006.10256.x

McKinney, J. C., & Blandford, R. D. 2009, MNRAS, 394, L126, doi: 10.1111/j.1745-3933.2009.00625.x

McKinney, J. C., & Gammie, C. F. 2004, ApJ, 611, 977, doi: 10.1086/422244

McKinney, J. C., Tchekhovskoy, A., & Blandford, R. D. 2012, MNRAS, 423, 3083, doi: 10.1111/j.1365-2966.2012.21074.x

Mei, S., Blakeslee, J. P., Côté, P., et al. 2007, ApJ, 655, 144, doi: 10.1086/509598

Meier, D. L. 1979, ApJ, 233, 664, doi: 10.1086/157428

Melrose, D. 2013, Quantum Plasmadynamics, Vol. 854, doi: 10.1007/978-1-4614-4045-1

Melrose, D. B. 1980, Plasma astrophysics: Nonthermal processes in diffuse magnetized plasmas. Volume 1 - The emission, absorption and transfer of waves in plasmas

—. 1997a, Journal of Plasma Physics, 57, 479, doi: 10.1017/S0022377896004989

—. 1997b, Journal of Plasma Physics, 58, 735, doi: 10.1017/S0022377897006284

Mertens, F., Lobanov, A. P., Walker, R. C., & Hardee, P. E. 2016, A&A, 595, A54, doi: 10.1051/0004-6361/201628829

Michell, J. 1784, Philosophical Transactions of the Royal Society of London Series I, 74, 35

Mihalas, D., & Mihalas, B. W. 1984, Foundations of radiation hydrodynamics

Mineshige, S., Kawaguchi, T., Takeuchi, M., & Hayashida, K. 2000, PASJ, 52, 499, doi: 10.1093/pasj/52.3.499

Misner, C. W., Thorne, K. S., & Wheeler, J. A. 1973, Gravitation

Miyoshi, M., Moran, J., Herrnstein, J., et al. 1995, Nature, 373, 127, doi: 10.1038/373127a0

Mizuno, Y. 2022, Universe, 8, 85, doi: 10.3390/universe8020085

Mizuno, Y., Fromm, C. M., Younsi, Z., et al. 2021, MNRAS, 506, 741, doi: 10.1093/mnras/stab1753

Mościbrodzka, M. 2019, A&A, 623, A152, doi: 10.1051/0004-6361/201834503

Mościbrodzka, M., Dexter, J., Davelaar, J., & Falcke, H. 2017, MNRAS, 468, 2214, doi: 10.1093/mnras/stx587

Mościbrodzka, M., & Falcke, H. 2013, A&A, 559, L3, doi: 10.1051/0004-6361/201322692

Mościbrodzka, M., Falcke, H., & Shiokawa, H. 2016, A&A, 586, A38, doi: 10.1051/0004-6361/201526630

Mościbrodzka, M., Falcke, H., Shiokawa, H., & Gammie, C. F. 2014, A&A, 570, A7, doi: 10.1051/0004-6361/201424358

Mościbrodzka, M., & Gammie, C. F. 2018, MNRAS, 475, 43, doi: 10.1093/mnras/stx3162

Mościbrodzka, M., Janiuk, A., & De Laurentis, M. 2021, MNRAS, 508, 4282, doi: 10.1093/mnras/stab2790

Muñoz, D. J., Marrone, D. P., Moran, J. M., & Rao, R. 2012, ApJ, 745, 115, doi: 10.1088/0004-637X/745/2/115

Nakamura, M., & Asada, K. 2013, ApJ, 775, 118, doi: 10.1088/0004-637X/775/2/118

Nakamura, M., Asada, K., Hada, K., et al. 2018, ApJ, 868, 146, doi: 10.3847/1538-4357/aaeb2d

Narayan, R. 1992, Philosophical Transactions of the Royal Society of London Series A, 341, 151, doi: 10.1098/rsta.1992.0090

Narayan, R., Chael, A., Chatterjee, K., Ricarte, A., & Curd, B. 2022, MNRAS, 511, 3795, doi: 10.1093/mnras/stac285

Narayan, R., & Goodman, J. 1989, MNRAS, 238, 963, doi: 10.1093/mnras/238.3.963

Narayan, R., Igumenshchev, I. V., & Abramowicz, M. A. 2003, PASJ, 55, L69, doi: 10.1093/pasj/55.6.L69

Narayan, R., Mahadevan, R., Grindlay, J. E., Popham, R. G., & Gammie, C. 1998, ApJ, 492, 554, doi: 10.1086/305070

Narayan, R., Quataert, E., Igumenshchev, I. V., & Abramowicz, M. A. 2002, ApJ, 577, 295, doi: 10.1086/342159

Narayan, R., SÄ dowski, A., Penna, R. F., & Kulkarni, A. K. 2012, MNRAS, 426, 3241, doi: 10.1111/j.1365-2966.2012.22002.x

Narayan, R., & Yi, I. 1994, ApJ, 428, L13, doi: 10.1086/187381

—. 1995, ApJ, 452, 710, doi: 10.1086/176343

Narayan, R., Yi, I., & Mahadevan, R. 1995, Nature, 374, 623, doi: 10.1038/374623a0

Narayan, R., Palumbo, D. C. M., Johnson, M. D., et al. 2021, ApJ, 912, 35, doi: 10.3847/1538-4357/abf117

Newman, E. T., Couch, E., Chinnapared, K., et al. 1965, Journal of Mathematical Physics, 6, 918, doi: 10.1063/1.1704351

Noble, S. C., Gammie, C. F., McKinney, J. C., & Del Zanna, L. 2006, ApJ, 641, 626, doi: 10.1086/500349

Novikov, I. D., & Thorne, K. S. 1973, in Black Holes (Les Astres Occlus), 343–450

Oda, M., Gorenstein, P., Gursky, H., et al. 1971, ApJ, 166, L1, doi: 10.1086/180726

Ohsuga, K., & Mineshige, S. 2011, ApJ, 736, 2, doi: 10.1088/0004-637X/736/1/2

Ohsuga, K., Mineshige, S., Mori, M., & Kato, Y. 2009, PASJ, 61, L7, doi: 10.1093/pasj/61.3.L7

Oppenheimer, J. R., & Volkoff, G. M. 1939, Physical Review, 55, 374, doi: 10.1103/PhysRev.55.374

Osterbrock, D. E., & Pogge, R. W. 1985, ApJ, 297, 166, doi: 10.1086/163513

Owen, F. N., Eilek, J. A., & Keel, W. C. 1990, ApJ, 362, 449, doi: 10.1086/169282

Owen, F. N., Hardee, P. E., & Cornwell, T. J. 1989, ApJ, 340, 698, doi: 10.1086/167430

Pandya, A., Zhang, Z., Chandra, M., & Gammie, C. F. 2016, ApJ, 822, 34, doi: 10.3847/0004-637X/822/1/34

Park, J., Hada, K., Kino, M., et al. 2019a, ApJ, 871, 257, doi: 10.3847/1538-4357/aaf9a9

—. 2019b, ApJ, 887, 147, doi: 10.3847/1538-4357/ab5584

Pearson, T. J., Unwin, S. C., Cohen, M. H., et al. 1981, Nature, 290, 365, doi: 10.1038/290365a0

Penrose, R., & Floyd, R. M. 1971, Nature Physical Science, 229, 177, doi: 10.1038/physci229177a0

Perley, R. A., Dreher, J. W., & Cowan, J. J. 1984, ApJ, 285, L35, doi: 10.1086/184360

Peterson, B. M., Wanders, I., Bertram, R., et al. 1998, ApJ, 501, 82, doi: 10.1086/305813

Porth, O., Mizuno, Y., Younsi, Z., & Fromm, C. M. 2021, MNRAS, 502, 2023, doi: 10.1093/mnras/stab163

Prieto, M. A., Fernández-Ontiveros, J. A., Markoff, S., Espada, D., & González-Martín, O. 2016, MNRAS, 457, 3801, doi: 10.1093/mnras/stw166

Pringle, J. E. 1981, ARA&A, 19, 137, doi: 10.1146/annurev.aa.19.090181.001033

Psaltis, D., Johnson, M., Narayan, R., et al. 2018, arXiv e-prints, arXiv:1805.01242. https://arxiv.org/abs/1805.01242

Psaltis, D., Özel, F., Chan, C.-K., & Marrone, D. P. 2015, ApJ, 814, 115, doi: 10.1088/0004-637X/814/2/115

Pu, H.-Y., & Broderick, A. E. 2018, ApJ, 863, 148, doi: 10.3847/1538-4357/aad086

Rayner, D. P., Norris, R. P., & Sault, R. J. 2000, MNRAS, 319, 484, doi: 10.1046/j.1365-8711.2000.03854.x

Rees, M. J. 1966, Nature, 211, 468, doi: 10.1038/211468a0

—. 1984, ARA&A, 22, 471, doi: 10.1146/annurev.aa.22.090184.002351

Rees, M. J., Begelman, M. C., Blandford, R. D., & Phinney, E. S. 1982, Nature, 295, 17, doi: 10.1038/295017a0

Ressler, S. M., Tchekhovskoy, A., Quataert, E., Chandra, M., & Gammie, C. F. 2015, MNRAS, 454, 1848, doi: 10.1093/mnras/stv2084

Ressler, S. M., White, C. J., Quataert, E., & Stone, J. M. 2020, ApJ, 896, L6, doi: 10.3847/2041-8213/ab9532

Ricarte, A., Prather, B. S., Wong, G. N., et al. 2020, MNRAS, 498, 5468, doi: 10.1093/mnras/staa2692

Ricarte, A., Qiu, R., & Narayan, R. 2021, MNRAS, 505, 523, doi: 10.1093/mnras/stab1289

Ripperda, B., Liska, M., Chatterjee, K., et al. 2022, ApJ, 924, L32, doi: 10.3847/2041-8213/ac46a1

Rowan, M. E., Sironi, L., & Narayan, R. 2017, ApJ, 850, 29, doi: 10.3847/1538-4357/aa9380

Ryan, B. R., Ressler, S. M., Dolence, J. C., Gammie, C., & Quataert, E. 2018, ApJ, 864, 126, doi: 10.3847/1538-4357/aad73a

Rybicki, G. B., & Lightman, A. P. 1979, Radiative processes in astrophysics

Sädowski, A., Narayan, R., Penna, R., & Zhu, Y. 2013, MNRAS, 436, 3856, doi: 10.1093/mnras/stt1881

Salpeter, E. E. 1964, ApJ, 140, 796, doi: 10.1086/147973

Sanders, D. B., Phinney, E. S., Neugebauer, G., Soifer, B. T., & Matthews, K. 1989, ApJ, 347, 29, doi: 10.1086/168094

Sano, T., Inutsuka, S.-i., Turner, N. J., & Stone, J. M. 2004, ApJ, 605, 321, doi: 10.1086/382184

Sazonov, V. N. 1969, Soviet Ast., 13, 396

Schmidt, M. 1963, Nature, 197, 1040, doi: 10.1038/1971040a0

Schödel, R., Ott, T., Genzel, R., et al. 2002, Nature, 419, 694, doi: 10.1038/nature01121

Schwarzschild, K. 1916, Sitzungsberichte der Königlich Preussischen Akademie der Wissenschaften, 189

Shain, C. A. 1958, Australian Journal of Physics, 11, 517, doi: 10.1071/PH580517

Shakura, N. I., & Sunyaev, R. A. 1973, A&A, 24, 337

Shcherbakov, R. V. 2008, ApJ, 688, 695, doi: 10.1086/592326

Shcherbakov, R. V., & Huang, L. 2011, MNRAS, 410, 1052, doi: 10.1111/j.1365-2966.2010.17502.x

Shcherbakov, R. V., Penna, R. F., & McKinney, J. C. 2012, ApJ, 755, 133, doi: 10.1088/0004-637X/755/2/133

Shibata, K., & Uchida, Y. 1985, PASJ, 37, 31

—. 1986, PASJ, 38, 631

Shiokawa, H., Dolence, J. C., Gammie, C. F., & Noble, S. C. 2012, ApJ, 744, 187, doi: 10.1088/0004-637X/744/2/187

Sikora, M., & Wilson, D. B. 1981, MNRAS, 197, 529, doi: 10.1093/mnras/197.3.529

Stone, J. M., & Pringle, J. E. 2001, MNRAS, 322, 461, doi: 10.1046/j.1365-8711.2001.04138.x

Sun, W.-H., & Malkan, M. A. 1989, ApJ, 346, 68, doi: 10.1086/167986

Takahashi, H. R., Mineshige, S., & Ohsuga, K. 2018a, ApJ, 853, 45, doi: 10.3847/1538-4357/aaa082

Takahashi, H. R., Ohsuga, K., Kawashima, T., & Sekiguchi, Y. 2016, ApJ, 826, 23, doi: 10.3847/0004-637X/826/1/23

Takahashi, K., Toma, K., Kino, M., Nakamura, M., & Hada, K. 2018b, ApJ, 868, 82, doi: 10.3847/1538-4357/aae832

Takahashi, M., Nitta, S., Tatematsu, Y., & Tomimatsu, A. 1990, ApJ, 363, 206, doi: 10.1086/169331

Takahashi, R. 2004, ApJ, 611, 996, doi: 10.1086/422403

Takeuchi, S., Ohsuga, K., & Mineshige, S. 2013, PASJ, 65, 88, doi: 10.1093/pasj/65.4.88

Tchekhovskoy, A., & McKinney, J. C. 2012, MNRAS, 423, L55, doi: 10.1111/j.1745-3933.2012.01256.x

Tchekhovskoy, A., Narayan, R., & McKinney, J. C. 2011, MNRAS, 418, L79, doi: 10.1111/j.1745-3933.2011.01147.x

Thorne, K. S., Price, R. H., & MacDonald, D. A. 1986, Black holes: The membrane paradigm

Tolman, R. C. 1939, Physical Review, 55, 364, doi: 10.1103/PhysRev.55.364

Trubnikov, B. A. 1958, PhD thesis, -

Tsunetoe, Y., Mineshige, S., Kawashima, T., et al. 2022a, ApJ, 931, 25, doi: 10.3847/1538-4357/ac66dd

—. 2022b, Galaxies, 10, 103, doi: 10.3390/galaxies10050103

Tsunetoe, Y., Mineshige, S., Ohsuga, K., Kawashima, T., & Akiyama, K. 2020, PASJ, 72, 32, doi: 10.1093/pasj/psaa008

—. 2021, PASJ, 73, 912, doi: 10.1093/pasj/psab054

Walker, M., & Penrose, R. 1970, Communications in Mathematical Physics, 18, 265, doi: 10.1007/BF01649445

Walker, R. C., Hardee, P. E., Davies, F. B., Ly, C., & Junor, W. 2018, ApJ, 855, 128, doi: 10.3847/1538-4357/aaafcc

Wardle, J. F. C., & Homan, D. C. 2001, in Astronomical Society of the Pacific Conference Series, Vol. 250, Particles and Fields in Radio Galaxies Conference, ed. R. A. Laing & K. M. Blundell, 152. https://arxiv.org/abs/astro-ph/0011515

Wardle, J. F. C., & Homan, D. C. 2003, Ap&SS, 288, 143, doi: 10.1023/B:ASTR.0000005001.80514.0c

Webster, B. L., & Murdin, P. 1972, Nature, 235, 37, doi: 10.1038/235037a0

Westfold, K. C. 1959, ApJ, 130, 241, doi: 10.1086/146713

Wong, G. N. 2021, ApJ, 909, 217, doi: 10.3847/1538-4357/abdd2d

Wong, G. N., Du, Y., Prather, B. S., & Gammie, C. F. 2021, ApJ, 914, 55, doi: 10.3847/1538-4357/abf8b8

Yuan, F., Markoff, S., & Falcke, H. 2002, A&A, 383, 854, doi: 10.1051/0004-6361:20011709

Yuan, F., & Narayan, R. 2014, ARA&A, 52, 529, doi: 10.1146/annurev-astro-082812-141003

Yuan, F., Quataert, E., & Narayan, R. 2003, ApJ, 598, 301, doi: 10.1086/378716

—. 2004, ApJ, 606, 894, doi: 10.1086/383117

Zavala, R. T., & Taylor, G. B. 2004, ApJ, 612, 749, doi: 10.1086/422741

Zensus, J. A. 1997, ARA&A, 35, 607, doi: 10.1146/annurev.astro.35.1.607

This page intentionally left blank.

This page intentionally left blank.